ICIAM 2019 SEMA SIMAI Springer Series 5

Manuel Cruz
Carlos Parés
Peregrina Quintela *Eds.*

Progress in Industrial Mathematics: Success Stories

The Industry and the Academia Points of View

Springer

SEMA SIMAI Springer Series

ICIAM 2019 SEMA SIMAI Springer Series

Volume 5

This sub-series of the SEMA SIMAI Springer Series aims to publish some of the most relevant results presented at the ICIAM 2019 conference held in Valencia in July 2019.

The sub-series is managed by an independent Editorial Board, and will include peer-reviewed content only, including the Invited Speakers volume as well as books resulting from mini-symposia and collateral workshops.

The series is aimed at providing useful reference material to academic and researchers at an international level.

More information about this subseries at http://www.springer.com/series/16499

Manuel Cruz • Carlos Parés • Peregrina Quintela
Editors

Progress in Industrial Mathematics: Success Stories

The Industry and the Academia Points of View

Springer

Editors
Manuel Cruz
Departamento de Matemática
Instituto Superior de Engenharia do Porto
Porto, Portugal

Carlos Parés
Departamento de Análisis Matemático,
Estadística e Investigación Operativa y
Matemática Aplicada
Universidad de Málaga
Málaga, Spain

Peregrina Quintela
ITMATI (Technological Institute for
Industrial Mathematics), R&D&i Unit,
Santiago de Compostela Spain; Red
Española Matemática-Industria (math-in),
Santiago de Compostela, Spain
Department of Applied Mathematics,
Universidade de Santiago de Compostela
Santiago de Compostela, Spain

ISSN 2199-3041 ISSN 2199-305X (electronic)
SEMA SIMAI Springer Series
ISSN 2662-7183 ISSN 2662-7191 (electronic)
ICIAM 2019 SEMA SIMAI Springer Series
ISBN 978-3-030-61843-8 ISBN 978-3-030-61844-5 (eBook)
https://doi.org/10.1007/978-3-030-61844-5

This Springer imprint is published by the registered company Springer Nature Switzerland AG.
The registered company address is: Gewerbestrasse 11, 6330 Cham, Switzerland

Foreword

That Mathematics is a key technology for the future of our societies and of industry does not have to be demonstrated anymore. It has become well-known and accepted that Mathematics can help in developing new processes and products that will make industrial work more robust, efficient, and successful, and above all, more innovative. The difference between processes using the intelligence of Mathematics and those without it is becoming more and more impressive. Mathematics is embedded in all kinds of industrial developments, it is all over the place, and some like to say "Mathematics is everywhere," but often hidden. The interaction has been more or less strong depending on the countries, kinds of companies, and academic communities, but in some places this is an old story. But, this old story has made huge progress in the last decades, with the boost given by high performance computing, and also from the capability to deal with huge amounts of data. Bridging data analytic methods with more classical modeling has sometimes led to extremely performant ways to deal with complex industrial or societal processes. The digital twins are a very good example of this kind of activity. All sides of the process, modeling, data analysis, and learning must continuously grow and develop new tools to be able to provide revolutionary solutions for new industrial and societal challenges.

Some say that artificial intelligence will kill traditional mathematical modeling, because all processes will be then designed through learning... Those who think or say so do not know that this could be a viable option only for some industrial processes, but not for the majority of them. But, what is clear is that modeling together with data, automatization, and learning will lead to revolutionary solutions for multiple industries. Collaboration between different technologies will mutually enhance their possibilities to give excellent answers to difficult questions.

Because Industrial Mathematics is one of the big pillars of ICIAM, the ICIAM 2019 Congress was a natural place to show once more that the link between Mathematics and Industry is becoming ubiquitous and essential. The project to include an Industry Day during the congress was almost a prerequisite for the congress organizers when they were chosen to do it. But, there was no need to pressure them, as they were already quite convinced of the need to do so. As it

should be, the weight of the Industry Day embedded in the ICIAM 2019 did rest not only on mathematicians but also on practitioners working in various companies, in Spain and elsewhere. This double approach was very important, since it is not enough that mathematicians show methods that they have devised to facilitate the resolution of industrial problems in an optimized way. It is also important to see and hear industrialists explaining how Mathematics has helped them to solve problems that are crucial for their companies, to make better products, and to do them in a more efficient, robust, and innovative way.

When the math-industry network EU-MATHS-IN was born, in 2013, most of the people related to it were university professors and researchers, working in collaboration with industry, and already involved in industrial mathematics in their respective countries. The idea was then to create a European network relating all the national efforts of the European continent, helping and advising each other, and getting better and more efficient in promoting the need of Mathematics for the society in general and for the industry in particular. But, as said above, at that time most of the people involved in the project were working in universities and in research centers. Since then, things have changed in the right direction, with more countries taking part in the network and above all, with an Industrial Core Team, a set of European companies supporting the EU-MATHS-IN network. This should have been there from the beginning, but it was not, because it was more difficult to organize; but, very quickly it was understood that it was badly missing. The Industry Day in the ICIAM 2019 Congress followed the trend, was well balanced, and showed the two sides of Industrial Mathematics.

On the industry side, there were presentations about digital twins, the mathematics of the blockchain, new management methods enabled by the use of Mathematics, the design of new algorithms to study material surfaces' properties, and new methods in mass spectroscopy in Chemistry. In all those presentations, the use of Mathematics was fundamental in the design of new and successful industrial techniques or processes. On the Mathematics side, some academic mathematicians working on industry- or society-related problems explained what their suggestions and work allowed to do and to improve. There we heard talks about batteries, tires, tsunamis, automotive spare parts, geographic information management, price modeling, wildfire resources, and multi-physics. All those subjects do not seem to have anything to do with Mathematics, but the methods developed to address issues in them do have a lot to do with Mathematics actually!

This volume tells us about all those contributions. They tell us about success stories, which are the best way to explain how Mathematics is a key technology for the future. All areas of Mathematics are important in the modeling of industrial processes, different areas for the different problems, and often, a mix is needed in order to address complex problems. But, not only there is a variety of Mathematical areas in industrial mathematics, there is also a great variety in the types of companies that can benefit from Mathematics. Small and large companies appear in the success stories, but also companies that belong to very different kinds of industry.

The ICIAM 2019 Congress was a big success, due mainly to the excellent work and support of the whole Spanish applied mathematical community. The organizers

did a great job! Its Industry Day was a particularly successful moment, thanks to the vitality of the Spanish network of industrial mathematics and their excellent collaborative inclusion in the international industrial mathematical community.

Senior Researcher at CNRS
Paris, France
Co-founder of EU-MATHS-IN
Past-president of ICIAM

Maria J. Esteban

Preface

This book contains a selection of works presented at the International Congress on Industrial and Applied Mathematics (ICIAM) held in Valencia, Spain, from 15 to 19 July 2019. As in previous editions of this series of congresses, the ICIAM 2019 was a showcase for the most recent advances in industrial and applied mathematics, covering interdisciplinary topics relating mathematics and other disciplines and demonstrating the applicability of this discipline to science, engineering, and industry.

The 2019 edition was the most attended congress of this series, gathering almost 4000 participants from 99 countries all over the 5 continents. The Opening Ceremony was presided by H.M. King Felipe VI, where he highlighted the importance of Industrial and Applied Mathematics in "serving as a vector for technological development and innovation regarding most of the major challenges in several areas," as well as the fundamental role of universities, "without whose capability to generate knowledge and transfer it to society, scientific and technological progress would simply not be possible."

An event with such a large magnitude addressed several fields of research, topics, and different goals. In fact, the 3660 scientific communications presented were partitioned into Invited Lectures, Special Panels, and Industrial Minisymposia and classified under 26 different topics. Beside this, for the first time in ICIAM congresses history, an Industry Day was promoted. Several books may result from such a panoply of high-quality resources. In fact, readers will find several volumes in this same collection as a result of the huge number of contributions made at the ICIAM 2019.The editors of this volume have made their choice based on showing specific success stories presented at the congress from the point of view of the researchers who have carried them out and that of the companies as end users. As a result, some talks presented at the "EU-MATHS-IN: Success Stories of Mathematics in Societal Challenges and Industry" minisymposium and at the Industry Day have been selected. The contributions that appear in this book intend to present an overview of both events as well as to highlight several real-world applications of industrial mathematics.

During the Industry Day, speakers from fourteen companies with a broad representation of the different sectors—such as banking, computing, materials, automotive, and energy, among others—showed to industrial and academic participants the high innovation potential of the mathematical tools, intending to open new channels of communication between researchers and potential users of these tools. The first part of this book contains five articles giving an industrial insight about the advantages of using mathematical tools and collaborating with mathematicians to tackle different industrial challenges. All of them were written by non-mathematician's managers, whose vision is provided from a different angle than that is usually presented on this type of publication. In the first part of the book, the reader will find the key role of maths in topics as diverse and actual as developing Digital Twins or novel block chain architectures, efficient and creative business and industry management, optimal mass spectral library searching, or simulation of locally reacting surfaces.

The second part of the book encompasses eight of the 16 success stories presented at the minisymposium promoted by the European Service Network of Mathematics for Industry and Innovation (EU-MATHS-IN). The main purpose of this organization, that was promoted by several European research networks following the recommendations of the European Science Foundation, is to increase the impact of mathematics on innovations in key technologies and to foster the development of new modeling, simulation, and optimization tools. The goal of this minisymposium was to present to the attendees some success stories of application of mathematical technologies in industry developed by researchers belonging to the national networks that are members of the EU-MATHS-IN. A broadband of industrial and societal sectors is being impacted by those applications of mathematics to solve real-world challenges. Most of them were tailor-made mathematical models, based upon several scientific fields, and developed to fulfill industrial or societal specific needs that were not satisfactorily addressed by the commercial software. In this book, some of these models are described with more details, impacting different subjects such as batteries, tires, tsunamis, spare parts, or wildfire resources, just to name a few.

We would like to address our warmest thanks and gratitude to all who have made this book possible: first of all, to all the speakers of the Industry Day and the minisymposium "EU-MATHS-IN: Success Stories of Mathematics in Societal Challenges and Industry" for their valuable contributions and, very specially, to those who accepted our invitation to contribute to this volume. Next, to the anonymous referees who helped the authors to improve the quality of the manuscripts. We also would like to thank the members of the Managing Board of EU-MATHS-IN for their support and help in the speakers' selection and the organization of both events. We would like to highlight the support of academic sponsors without whom Industry Day would not have been possible; in addition to the already mentioned EU-MATHS-IN, we are really grateful to the European Consortium for Mathematics in Industry (ECMI, Europe), the Institute of Mathematics for Industry (Japan), the MITACS (Canada), the Rede Portuguesa de Matemática para a Indústria e Inovação (PT-MATHS-IN, Portugal), the Sociedad Española de Matemática

Aplicada (SEMA, Spain), the Spanish Network for Mathematics & Industry (math-in, Spain), and the Technological Institute for Industrial Mathematics (ITMATI, Spain). Many thanks to the Scientific, Executive, and Organizing Committees of the ICIAM 2019 for having accepted our proposals and helped us with the organization of both events: in spite of the huge amount of work that the organization of such a big event implies, the answers to our questions and queries were always fast and kind. We would like to address our appreciation to the Editorial Board of the ICIAM 2019 subseries of the SEMA SIMAI series of Springer for having accepted our proposal of contributing with this book to the subseries, and very specially to the Editor in charge, our colleague Sebastià Xambó. We also thank the Springer staff for their help and support during the Edition process, and very specially to Francesca Bonadei, Executive Editor in charge. Finally, we would like to add that it is a pleasure and a honor for us to open this volume with the foreword of María Jesús Esteban, former president of ICIAM, who played a fundamental role in the Forward Look on Mathematics for Industry held in Europe and in the implementation of the EU-MATHS-IN network.

Porto, Portugal — Manuel Cruz
Málaga, Spain — Carlos Parés
Santiago de Compostela, Spain — Peregrina Quintela

Contents

Editors and Contributors

About the Editors

Manuel Cruz is Professor at the Instituto Superior de Engenharia do Porto and coordinator of the Mathematical Engineering Laboratory at the same institution. He was elected President of the Portuguese Mathematics Network for Industry and Innovation in 2016, and member of the European Service Network of Mathematics for Industry and Innovation executive board in 2019. He has a PhD in Applied Mathematics from the University of Porto and has participated in several challenges of technology transfer from Mathematics to Industry.

Carlos Parés is Professor of Applied Mathematics at the University of Málaga (Spain). He is a specialist in numerical methods for nonlinear hyperbolic systems of Partial Differential Equations. He promoted the creation and development of the group of research EDANYA, which is nowadays an international reference in the simulation of geophysical flows. He was among the promoters of the Spanish Network for Mathematics & Industry, and he was member of its Managing Board from 2011 to 2019.

Peregrina Quintela is president of the Spanish Network for Mathematics & Industry, director of the Technological Institute for Industrial Mathematics, and member of the European Service Network of Mathematics for Industry and Innovation Executive Board. She holds two PhDs in Mathematical Sciences from the Universidad Autónoma de Madrid and the Université Pierre et Marie Curie. She is Full Professor at the Universidade de Santiago de Compostela, specialized in modelling and simulation of industrial challenges.

Contributors

Elena Akhmatskaya Basque Center for Applied Mathematics, Bilbao, Spain
IKERBASQUE, Basque Foundation for Science, Bilbao, Spain

S. Barroso NORS, Porto, Portugal

Mauricio R. Bonilla Basque Center for Applied Mathematics, Bilbao, Spain

D. Cabo Microflown Technologies, Arnhem, Netherlands

Javier Carrasco Centre for Cooperative Research on Alternative Energies (CIC energiGUNE), Basque Research and Technology Alliance (BRTA), Alava Technology Park, Vitoria-Gasteiz, Spain

G. Carrillo Microflown Technologies, Arnhem, Netherlands

M. J. Castro Department of Mathematical Analysis, Statistics and Optical Research and Applied Mathematics, Faculty of Sciences, University of Málaga, Málaga, Spain

R. Costa NORS Group, Porto, Portugal

M. B. Cruz LEMA—Engineering Mathematics Laboratory, School of Engineering, Polytechnic of Porto, Porto, Portugal

M. de la Asunción Department of Mathematical Analysis, Statistics and Optical Research and Applied Mathematics, Faculty of Sciences, University of Málaga, Málaga, Spain

D. Fernández Microflown Technologies, Arnhem, Netherlands

Mario Fernández-Pendás Basque Center for Applied Mathematics, Bilbao, Spain Kimika Fakultatea, Euskal Herriko Unibertsitatea (UPV/EHU) and Donostia International Physics Center (DIPC), Donostia, Spain

Fabián A. García Daza Department of Chemical Engineering and Analytical Science, The University of Manchester, Manchester, UK

María José Ginzo Villamayor Department of Statistics, Mathematical Analysis and Optimization, Institute of Mathematics, IMAT, Technological Institute of Industrial Mathematics, ITMATI, Group of Optimization Models, Decision, Statistics and Applications, MODESTYA, University of Santiago de Compostela, Santiago, Spain

J. M. González-Vida Department of Applied Mathematics, Industrial Engineering School, University of Málaga, Málaga, Spain

Carlos Gorria Department of Applied Mathematics, Statistics and Operations Research, University of the Basque Country (UPV/EHU), Leioa, Spain

Dirk Hartmann Siemens Corporate Technology, Princeton, NJ, USA

Ghassan Karame NEC Laboratories Europe, Heidelberg, Germany

Anthony J. Kearsley National Institute of Standards and Technology, Gaithersburg, MD, USA

Michael Kolmbauer MathConsult GmbH, Linz, Austria

Mikel Lezaun Department of Applied Mathematics, Statistics and Operations Research, University of the Basque Country (UPV/EHU), Leioa, Spain

J. Macías Department of Mathematical Analysis, Statistics and Optical Research and Applied Mathematics, Faculty of Sciences, University of Málaga, Málaga, Spain

Arun S. Moorthy National Institute of Standards and Technology, Gaithersburg, MD, USA

Günter Offner AVL List GmbH, Graz, Austria

André Oliveira BitSight, R. de Campolide, Lisboa, Portugal

S. Ortega Department of Applied Mathematics, Industrial Engineering School, University of Málaga, Málaga, Spain

C. Parés Department of Mathematical Analysis, Statistics and Optical Research and Applied Mathematics, Faculty of Sciences, University of Málaga, Málaga, Spain

M. Pina NORS Group, Porto, Portugal

Bernhard Pöchtrager Radon Institute for Computational and Applied Mathematics (RICAM), Austrian Academy of Sciences, Linz, Austria

A. Prieto CITIC, Department of Mathematics, Universidade da Coruña, Coruña, Spain

S. F. Ramos LEMA—Engineering Mathematics Laboratory, School of Engineering, Polytechnic of Porto, Porto, Portugal
CEAUL—Faculty of Sciences, University of Lisbon, Lisbon, Portugal

Jorge Rodríguez Veiga Department of Statistics, Mathematical Analysis and Optimization, Institute of Mathematics, IMAT, Technological Institute of Industrial Mathematics, ITMATI, Group of Optimization Models, Decision, Statistics and Applications, MODESTYA, University of Santiago de Compostela, Santiago, Spain

José Luis Santos Department of Mathematics, University of Coimbra, CMUC, Coimbra, Portugal

Herman Van der Auweraer Siemens Industry Software NV, Leuven, Belgium

Balbina Virginia Casas Méndez Department of Statistics, Mathematical Analysis and Optimization, Institute of Mathematics, IMAT, Technological Institute of Industrial Mathematics, ITMATI, Group of Optimization Models, Decision, Statistics and Applications, MODESTYA, University of Santiago de Compostela, Santiago, Spain

Part I
The Industry Point of View

Digital Twins

Dirk Hartmann and Herman Van der Auweraer

Abstract Digital Twins are one of the hottest digital trends. In this contribution we review the concept of Digital Twins and the chances for novel industrial applications. Mathematics are a key enabler and the impact will be highlighted along four specific examples addressing Digital Product Twins democratizing Design, Digital Production Twins enabling robots to mill, Digital Production Twins driving industrialization of additive manufacturing, and Digital Performance Twins boosting operations. We conclude the article with an outlook on the next wave of Digital Twins, Executable Digital Twins, and will review the associated challenges and opportunities for mathematics.

1 Introduction

Complexity in today's industry is exploding. New production methods, miniaturization of electronics, novel sensor technologies, and last but not least the internet of things (IoT) have led to many disruptive development. Ultimately, this led to more and more complex products. On the one hand, this offers unique opportunities e.g. in terms of efficiency or autonomy of components, products, and complex systems. On the other hand, it challenges today's design, engineering, operation, and service paradigms mostly focusing on manual expert interaction, which can hardly, if at all, handle this enormous complexity.

At the same time digitization changes everything everywhere. With the rise of new technology trends, such as AI Foundations, Intelligent Things, Cloud to Edge, or Immersive Experiences [1], many of today's paradigms can be expected to be disrupted. Along these new technology trends are also Digital Twins, see e.g. [2].

D. Hartmann (✉)
Siemens Technology, Munich, Germany
e-mail: hartmann.dirk@siemens.com

H. Van der Auweraer
Siemens Industry Software NV, Leuven, Belgium
e-mail: herman.vanderauweraer@siemens.com

M. Cruz et al. (eds.), *Progress in Industrial Mathematics: Success Stories*,
SEMA SIMAI Springer Series 5, https://doi.org/10.1007/978-3-030-61844-5_1

The Digital Twin concept has been originally introduced in 2003 by Michael Grieves [3] and first put to public by the NASA in 2012 [4]. Digital Twins integrate all (electronic) information and knowledge generated during the life-time of a product, from the product definition and ideation to the end of its life. They bridge the virtual and real world with the goal to model, understand, predict, and optimize their corresponding real assets.[1]

Today, Digital Twins are considered so important to business, that they were named three years in a row among Gartner's Top 10 Strategic Technology Trends [5–7]. It is widely accepted that Digital Twins lead to high savings along the entire life-cycle and at the same time will allow for novel services such as on-site diagnostics, prescriptive maintenance or operation optimization [8, 9]. Ultimately the are expected to be a good for themselves enabling complex ecosystems [10].

Within this article we will review the concept of Digital Twins and relate the concept with opportunities for the mathematical sciences. In particular we will provide a set of examples where advanced mathematical methods have made a difference. Furthermore, we will outline challenges laid down by Digital Twins expecting to spur new mathematical research with impact for industrial applications [11].

Since the concept of Digital Twins is not new, we start with a short history of simulation (Sect. 2) before we introduce the concept of Digital Twins (Sect. 3). We then show it's opportunities along the four industrial examples of early design support, manufacturing parallel simulations, a specific manufacturing planning task, as well as operation-parallel simulations (Sect. 4). In all these cases, Digital Twins have allowed for paradigm shifts in their respective domains. Albeit these example prove the success of Digital Twins already today, we believe that they are just taking off. Thus we introduce the next generation concept of Executable Digital Twins in the following (Sect. 5) and conclude with the associated challenges.

For a very concise and more detailed review of on Digital Twins we would in particular like to refer to [12].

2 A Short History of Simulation

The concept of Digital Twins is not new (Fig. 1). Actually the concept goes back to the early 60s (or even earlier) when simulation developed as a key tool for understanding scientific phenomena. For example, albeit many physical phenomena and basic equations have been understood, it was simulation which allowed to handle complex systems such as rockets and space ships. The interactions and geometries were far too complex to be solved by analytical means. Actually, still

[1] For a more precise definition c.f. Sect. 3.

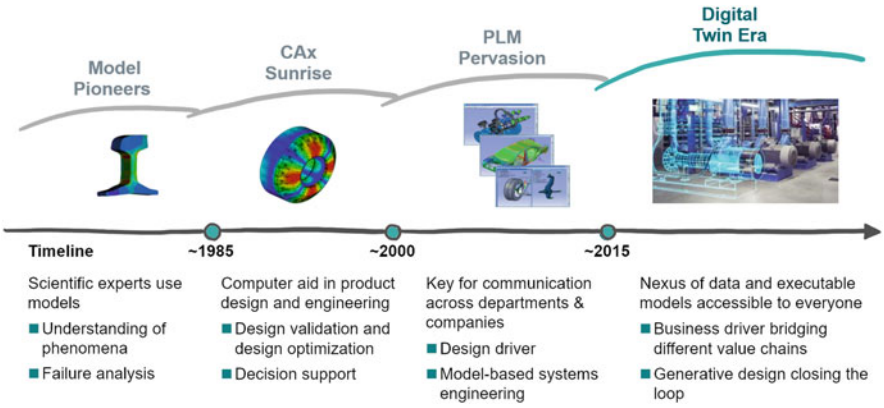

Fig. 1 Waves of simulation

a number of today's widely used simulation tools date back to these days, e.g. the NASA Structure Analysis software better known as NASTRAN.[2]

Simulation proved to be a very powerful if not the key tool to realize such complicated systems. Therefore, naturally simulation became a standard tool in many engineering disciplines[3] over the following decades. In particular, combined with optimization simulations matured from a trouble shooting tool to standard virtual validation tools and ultimately design driving tools (Generative Design tools).

With mathematical models and their simulations developing as a success story for all engineering disciplines, it was a logical step to democratize them across the complete development process. With the rise of the so-called model based systems engineering, models became the backbone of systems engineering allowing always up-to date virtual validation on all levels, from components to the system level, validating product requirements. Purely document based systems were set down for model-based philosophies.[4]

3 The Digital Twin Vision

With the evolution towards model-based (systems) engineering, the next logical step was to introduce the concept of Digital Twins extending model-based paradigms

[2]C.f. https://github.com/nasa/NASTRAN-95 or the corresponding commercial versions.

[3]Covering such divers fields as mechanics, electro-magnetic, fluid dynamics, thermodynamics, and many more.

[4]It is actually an ongoing process and only very few examples exist with complex model-based engineering philosophies.

along the complete life-cycle. Early definitions of these concepts can be traced back to the works of [3] or [4]. But since then a multitude of different concepts and definition have been introduced, see e.g. [12].

Digital Twins are expected to become a business imperative, covering the entire life-cycle of an asset or process and forming the foundation for connected products and services. Companies that fail to respond will be left behind. For example, it is predicted that companies who invest in Digital Twin technology will see a 30% improvement in cycle times of critical processes [13]. A potential market of 48bn Dollar per year associated to corresponding offerings is predicted for 2026, [14] e.g. via savings or enabling novel business opportunities such as model-based diagnostics, prescriptive maintenance, or optimized operations.

Let's us try to provide a very basic definition of Digital Twins:

Definition (Digital Twin)[5]: The Digital Twin integrates all data (test, operation data, ...), models (design drawings, engineering models, analyses, ...), and other information (requirements, orders, inspections, ...) of a physical asset generated along its life cycle that leverage business opportunities. The role of the Digital Twin is to predict and optimize performance. To this purpose simulation methods and/or data-based methods are used.

The Digital Twin itself however is only a central asset, if it can be used to make relevant predictions providing the right level of information at the right time. In this case, it bridges the physical and the virtual world and is a key tool to understand and model the assets performance, predicting its behavior, and optimize its operation and service. Since it spans the entire asset life-cycle continuous updating to mirror the reality is a central requirement.

3.1 Why Are Digital Twins Hot?

As stressed above, the concept of Digital Twins is not new but the natural extension of model-based philosophies across the complete life cycle. However, with the exponential advancement of a number of key technologies, such as computing hardware, mathematical algorithms, knowledge graphs, and semantic technologies as well as augmented and virtual reality device, we are entering a new era.

For example Moore's law has led over the past decades to an explosion of computational power [15]. And actually a continuous capability growth in computer and hardware architectures beyond scaling of chip performance and cloud is observed, e.g. graphics processing units (GPUs), re-configurable computing, or ubiquitous computing [16]. This is often referred to *More-than-Moore*'s law. At

[5]For a short explainer see also https://youtu.be/ObGhB9CCHP8.

the same time also major breakthrough in mathematics and computer science have been achieved. These have led to an exponential capability growth contributing significantly to efficiency, scalability, and usability of (simulation) model-based as well as data-based approaches [17]. However these enabling factors are often not recognized outside the Computational Science and Engineering community. Along with the growth of computational and algorithmic capabilities also the interaction with digital models has been simplified. In particular, virtual and mixed reality is entering the professional market ultimately driving democratization of formerly expert centric tools [18]. Furthermore the advancement of semantic standards and knowledge graphs, now entering rapidly the industrial domain, allows for efficient realization of ontologies. Semantic information access has reached a new level beyond general purpose inter-operable standards [19]. This in particular reduces the required manual efforts for many tasks.

Thanks to these technology leaps, it is not anymore about faster and more accurate simulations but rather we can rather democratize simulation across a wide range of application domains and the complete life-cycle. Thus it is absolutely justified to have named Digital Twins in three consecutive years as one of the top 10 technologies [5–7]. Or to quote the ASSESS community: *The Digital Twin approach will [..] make engineering simulation widely available appropriate to support improved decision making throughout the entire life-cycle of engineered products and processes.*[6]

3.2 Digital Twins—Model- and Data-Based Predictions

From a high level point of view, information included in Digital Twins can be split in two categories, pure data values with only little additional structure/knowledge associated, such as data gathered from sensors, and structured executable model-based data, in particular simulation models. Thus, Digital Twins bring together classical data based schemes with model-based approaches such as simulation and optimization. Albeit the scientific communities today are still very separated, we believe that only a combination of the two will enable the success of Digital Twins. Hybrid models combining the best of the two worlds (e.g. combining response-surface modeling with equation based models) are not new, but an explosion in terms of publications can be observed in particular in the last years (Fig. 2).

[6] https://www.assessinitiative.com/wp-content/uploads/Understanding-and-Enabling-the-Simulation-Revolution.pdf.

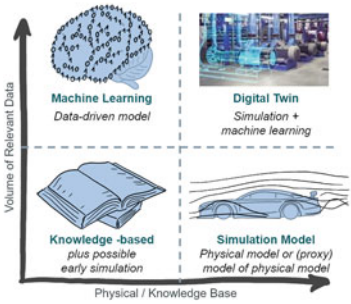

	Physical Models	Data Driven Models
Data Reliance	**Small data**	Big data
Domain Reliance	Deep domain expertise	**Little domain knowledge**
Fidelity & Robustness	**Highly non-linear and complex relations**	Limited to data and model complexity
Adaptability & Deployability	Complex and time consuming setup	**Rapidly adapt to a specific problem**
Interpretability	**Consistent physical meaningful**	Physics agnostics surrogate

Fig. 2 Digital Twins embrace model-based as well as data-based approaches (Inspired by Lior Horesh)

4 Digital Twins Enable the Impossible

As stated above, Digital Twins are key tools to address toady's industrial challenges. In many cases the offer a unique potential for higher efficiency and savings. For example in the case of predictive power trains the cost/efficiency ratio has been compared with different other measures [20]. But very often it is only Digital Twins which enable a novel solution or service at all—often tasks which have been considered to be impossible. To be more concrete we will review four applications below.

4.1 Interactive Design Tools

Typical industrial design processes today require the coordination of experts with different specialization. For example, in the case of the geometric design of a component at least a designer, creating and adapting the geometric design within a CAD tool, and an analyst/simulation engineer, validating and optimizing the design by means of physical simulations in a CAE tool, are required. Their interaction is typically iteratively with each step requiring hours to sometimes days (in particular for the analysis step). The required efforts therefore limit the potential design configurations to be investigated. Considering additive manufactured parts this is a severe limitation. Being constrained only by very few design constraints, the potential design space is quasi infinite. Thus the search for the optimum design is limited by the available time for the design process. Providing faster and more CAD-integrated analysis tools in particular for the very early concept design phase would allow to better exploit the potential design space. Not only would this reduce development costs but due to the opportunity to search even for more design options, this would at the same time also increase product performance.

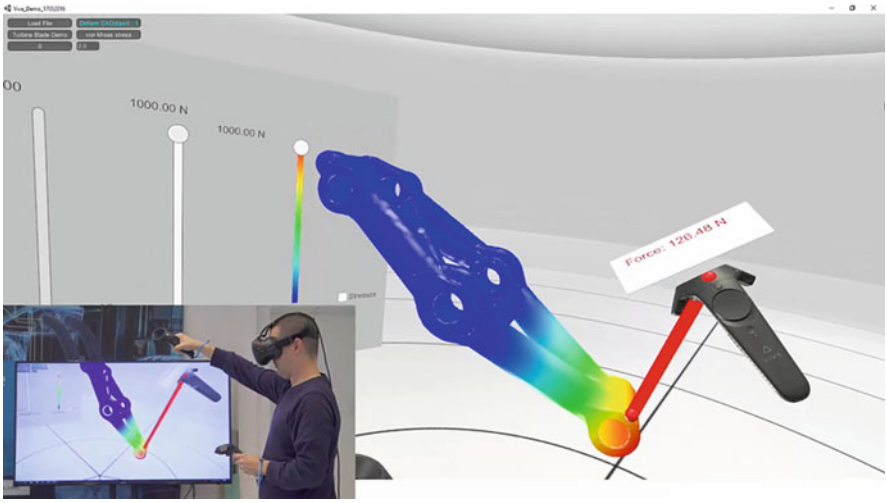

Fig. 3 Interactive 3d multi-physics FEM simulation in a virtual environment. Reproduced with permission. Copyright © Siemens AG

Combining

- **Efficient voxel-based discretization techniques** allowing lean codes, efficient memory access, easy parallelization, and fast transfer to novel compute architectures such as graphic processing units,
- **Geometric multi-grid solvers** enabling an optimal solution of linear systems in terms of complexity, and
- **Hardware-aware implementations** exploiting massively-parallel graphics processing units,

we have developed highly accelerated solvers ready for industrial use [21]. Depending on the use case the solvers outperform state-of-the-art solutions by several orders of magnitude while having an appropriate good enough accuracy. (In particular in the early design phase there are still a large number of uncertainties, such as the expected forces).

Potential applications range from accelerated topology optimization [21] to sufficiently accurate 3d physics simulations in virtual reality[7] [22]. Without sacrificing the achievable performance the concept phase can be accelerated up to 10 times. At the same time a much larger user base can be addressed with simulation tools leading to a democratization in terms of usage [23] (Fig. 3).

[7]Design concepts in VR https://youtu.be/ecg9JxsrNw8.

4.2 Robot Milling

Albeit the advancement of additive manufacturing technologies most parts are still produced by classical manufacturing technologies, such as subtractive manufacturing processes. Due to the high process forces in machining, in particular for metals, corresponding machine tools need to be extremely stiff such that they are not impacted by the high forces. Any deflection of the machine would lead to quality defects. Machining itself is typically split into two separate tasks: roughening removing the large part of the material and finishing of the surface. While roughening has accuracy requirements around 0.1 mm, finishing often requires accuracies below 0.01 mm. The corresponding high mechanical requirements are a key cost driver of machine tools.

Therefore, it is not surprising that machining has been considered as a use case for more flexible and versatile robots, e.g. robots could be also used for other tasks such as loading loading of machine tools and they have a significantly larger operating space while they are cheaper than machine tools. Today they are already used for soft material milling such as foams in industrial applications. However, the use for metal machining has not been considered realistic in terms of achievable accuracy.

Introducing

- **Novel voxel-based milling process force models** based on fine-resolution multiscale geometry models combined with simple heuristic force models and
- **Model predictive compensation solutions** offered by recent advancements in controls,[8]

we could show that the error for aluminium parts could be reduced from around 1.0 mm to 0.1 mm using standard robots without any mechanical modifications [24].

Digital Twins ultimately allowed to realize the application of robot milling[9] which was widely believed not to be possible satisfying industrial requirements for metal milling with conventional robots [25] (Fig. 4).

4.3 Robotic Cleaning of 3D Prints

Albeit additive manufacturing is a rather old technology it has only recently taken the barrier of industrialization. Among the many technologies, selective laser melting is one of the most widely adopted additive manufacturing technologies for metals. Thereby a powder bed is build up layer-wise and the different layers are welded together with a laser. The powder in between remains untouched and as

[8] Siemens SINUMERIK module Run MyCC/ROCO.

[9] Precise, Digital and Flexible https://youtu.be/2iIN-9Kno3o.

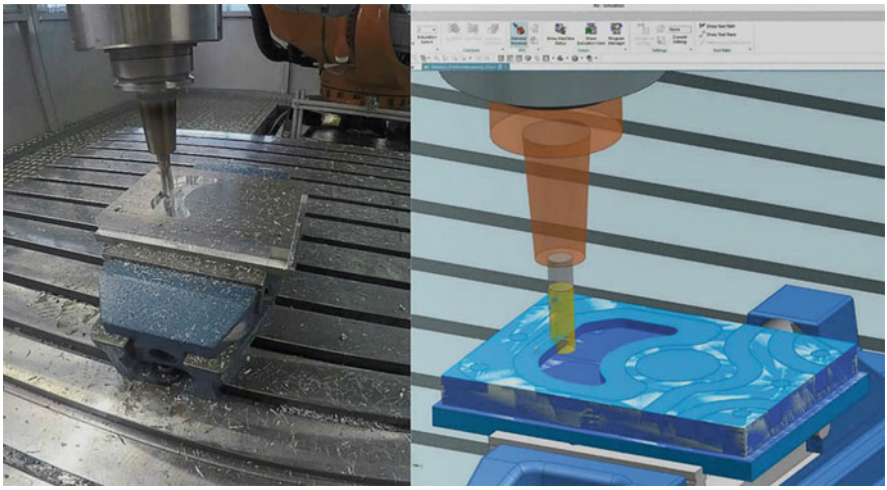

Fig. 4 Milling robot in action together with the corresponding digital twin. Reproduced with permission. Copyright © Siemens AG

such acts as a support structure for the next layer. Thus if the final part includes void volumes, these are filled with metal powered.

Before the actual use of the parts the metal powder needs to be removed, in particular due to its potential noxious effects. Since the corresponding shapes can be highly complex (c.f. Sect. 4.1) and are very often produced only in small lot numbers an automation of this process is not possible. Typically the cleaning of the additively manufactured parts is a manual process.

Using a combination of

- **A highly simplified discrete element method** representing coarse grained models of the metal powder,
- **Heuristic optimization algorithms** based on the Fast Marching Method for an efficient determination of emptying strategies, and
- **Automatic control code generation** which can be transferred seamlessly to automated de-powdering machines,

we have realized a robotic depowdering machine which can highly autonomously clean 3d printed parts requiring only the basic geometric information of void volumes [26]. The reduction of manual work, in particular in combination with potential health issues, is a key building block for industrialization of additive manufacturing. In addition less powder is lost providing a significant amount of savings (Fig. 5).

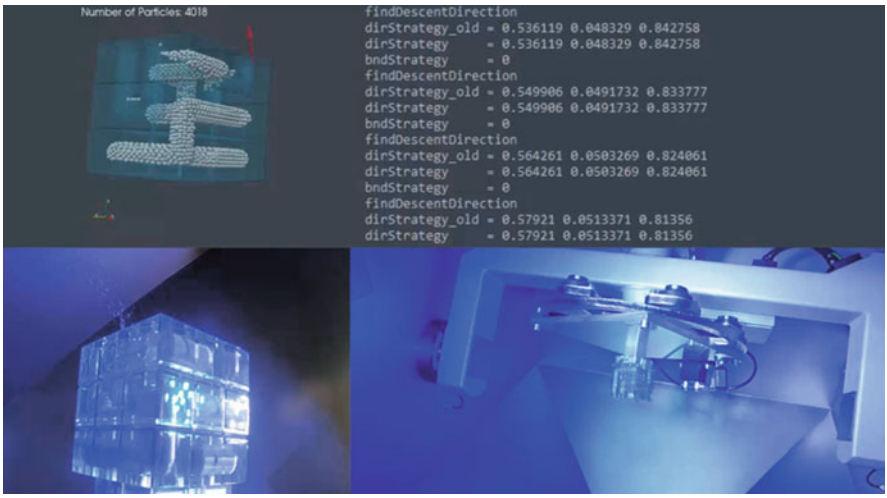

Fig. 5 Operation of a de-powdering machine and its corresponding digital twin. Reproduced with permission. Copyright © Siemens AG

4.4 Online 3D Virtual Temperature Sensors

Many machines today are limited by thermal effects, i.e. they could run too hot leading to sequent damage. For example, during startup large electrical machines can develop high temperatures at the rotor—limiting the operation. However, these can hardly be measured using cost-efficient sensor technology. To prevent corresponding damage, they are often subject to conservative operation conditions avoiding overheating. Since stator temperatures can easily be measured, rotor temperatures can be estimated. However this requires significant manual efforts to build corresponding thermal networks and to validated them. Limiting their applicability for certain types of machines.

Combining

- **Model order reduction** speeding up standard finite element models (FEM) from engineering by factors of up to 10,000,
- **Continuous calibration in the loop** of these models combined with uncertainty quantification to provide statistical information on the validity of the predictions, and
- **Immersed user experience** leveraging state-of-the-art mixed reality technologies with online simulations,

allow to 3d build virtual thermal sensors determining temperature distributions in the complete motor. By having efficient means to estimate critical rotor temperatures limiting operations today, higher availability of large electrical drives can be achieved. Having in mind that this can save costs of up to 200kEUR/h this is

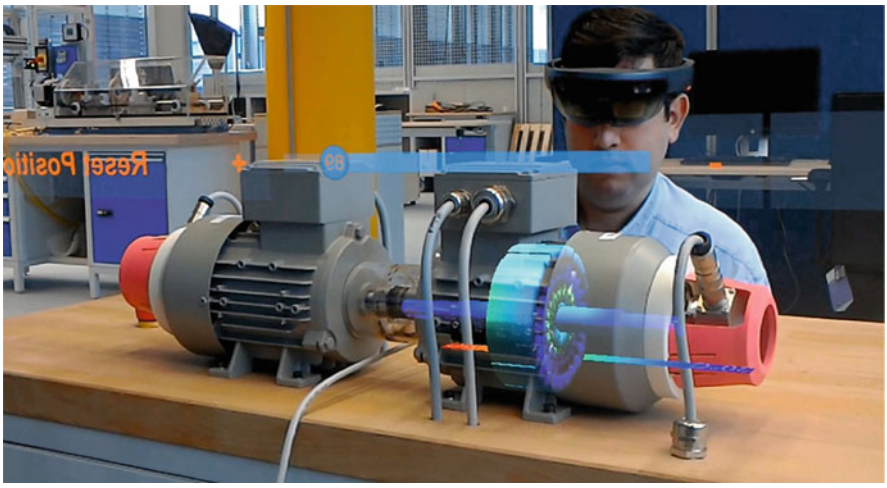

Fig. 6 Mixed reality setup allowing to measure spatial temperature distributions parallel to operations by means of online simulations. Reproduced with permission. Copyright © Siemens AG

a tremendous achievement [27]. At the same time using model order reduction technologies [28] the concept can be built directly on top of engineering models allowing to achieve the benefits with only little additional efforts. Mathematics enables quasi thermal X-rays for electrical motors allowing to monitor temperature distributions in real time (Fig. 6).[10]

5 The Next Wave—Executable Digital Twins

Albeit the previous section has shown four great examples of Digital Twins, a major limiting factor today is the manual work required to realize a Digital Twin, i.e. transfer of the corresponding models between different domains or life cycle phases. Most applications require to provide the models in the right execution environments with the right online capability in particular during the operations phase.

We therefore introduce the concept of an Executable Digital Twin, which will be from our point of view a key aspect in any future Digital Twin driven application.

Definition (Executable Digital Twin) An Executable Digital Twin is a specific encapsulated realization of a Digital Twin with its execution engines.[11] As such they enable the reuse of simulation models outside R&D. In order to do so, the

[10] Virtual X-ray for large motors https://youtu.be/86vkjykbHRM.

[11] Typically models today are distributed separately from their execution/simulation tools.

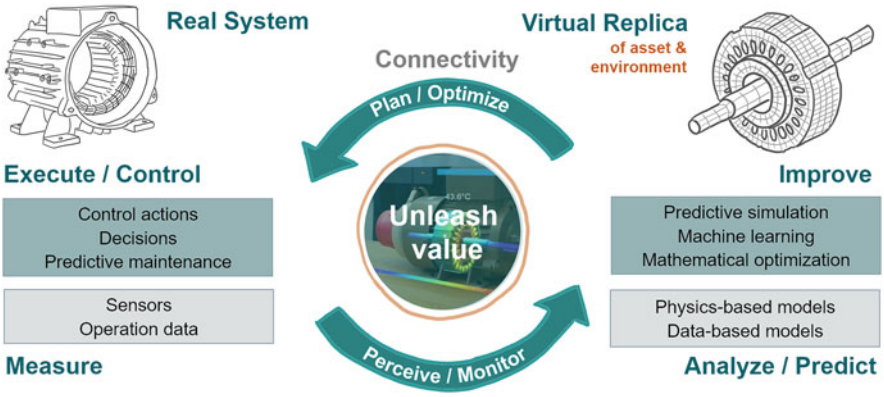

Fig. 7 Operation parallel Executable Digital Twin (Inspired by Wim Desmet)

Executable Digital Twin needs to be prepared suitably for a specific application out of existing data and models. In particular it must have the right accuracy and speed. The Executable Digital Twin can be instantiated on the edge, on premise, or in the cloud and used autonomously by a non-expert or a machine through a limited set of specific APIs (Fig. 7).

Executable Digital Twins are a key enabler for democratization of Digital Twins. Their use can span a wide range of scenarios:

- **System Integration:** Executable Digital Twins can be used for simulation models within a systems simulations. This could include scenarios of 3d solver coupling, the integration of 3d analysis within system simulations, or the integration of lumped system models. Thereby, the various models could originate from various parties in a complex ecosystem and also be based on different types of computational solvers. Applications can cover a wide range of scenarios, from sales support to sophisticated design and engineering tasks, such as virtual integration of a new component or subsystem, operating condition assessment, or performance limit evaluation.
- **Embedded Digital Twins:** Executable Digital Twins could be deployed on the edge within the embedded software stack to realize e.g. virtual sensors to enrich available information (c.f. Sect. 4.4) or to be used directly in model predictive control loops, Furthermore, they also allow for simplified X-in-the-loop simulations or controller tuning during commissioning.
- **Companion Digital Twins:** Executable Digital Twins could be further deployed on the edge, on premise, or in the cloud as an additional support in the context of complex Internet of Things (IoT) applications. This could span application fields from advanced monitoring and diagnostics, to asset optimization (e.g. via model predictive control) or predictive maintenance. Ultimately with the advancements of 5G, communication latency issues will be decrease allowing the convergence of the different compute locations from embedded to cloud.

In all these scenarios the creator and consumer of the Digital Twins will be separated, contrary to most applications of simulation today.[12] Ultimately, the creator and consumer can be connected through complex Digital Twin ecosystems [10]. Executable Digital Twins inherently support this democratization of simulation.

Today, most model-based approaches, and in particular simulation, are domain specific and mostly used during design and engineering. The core concept of the Digital Twin is to extend their usage along the complete life-cycle and to deliver new services providing the right information at the right place in an efficient way. Obviously the concept of Executable Digital Twins enforces sophisticated requirements in order to be successfully employed in standard industrial practice.

Requirements:

- **Interactivity**—Speed and accuracy define the value of simulation and Digital Twins. Being very accurate, today's model and simulation approaches are extremely time-consuming. Speeding them up, while retaining the right level of accuracy, is crucial for extending the use of Digital Twins.
- **Reliability**—Users of Digital Twins cannot be expected to be sophisticated experts, like it can be expected during the use in design and engineering. Thus, any prediction by the Digital Twin must be fail safe and/or provided along with confidence intervals such that no expertise is required to interpret the results or can be used autonomously, e.g. by controls. In particular Digital Twins must be self-aware and inform the user if they are used outside their validation and specification domain.
- **Usability**—Simulation tools are expert centric today. Expert resources are limited and thus the use of corresponding tools today is limited by the availability of experts. Therefore, any Digital Twin solutions must be accessible also for non-experts from a usability perspective. Similarly, efforts for their generation should be reduced as much as possible.
- **Security**—Many business models based on the Digital Twin will require to exchange Digital Twins between different parties. Reverse engineering must be prevented, such that no intellectual property is lost.
- **Deployability**—Digital Twins will be used different from the place where they have been created, e.g. on customer premises, in the cloud, or on controls. Thus, deployment must be easy to reduce barriers and efforts.
- **Synchronicity**—Digital Twins link the real with the digital world. Since each asset is typically unique, Digital Twins must be uniquely adapted and keep synchronous with their real world counter parts. This includes adaptation of models according to wear as well as updating the models due to reconfiguration or service replacements.

Many of these requirements have not yet today appropriate technical solutions. We believe that they all require sophisticated mathematical concepts ranging from model order reduction (Interactivity) and uncertainty quantification (Reliability) to

[12] In the context of Artificial Intelligence applications this separation is a fact already today.

block chain concepts (Security). Without further mathematical research the vision of Digital Twins and in particular Executable Digital Twins will not be successful.

Acknowledgments The authors greatly acknowledge the contributions of Utz Wever, Stefan Gavranovic, and Hans-Joachim Bungarz for the use case of interactive design tools (Sect. 4.1), Florian Schöes, Michael Zäh, Sven Tauchmann, Birgit Obst, and Frank Fischer for the use case of robot milling (Sect. 4.2), Christoph Kiener, Frank Fischer, and Meinhard Paffrath for the robotic cleaner (Sect. 4.3), and Utz Wever, Birgit Obst, Theo Papadopoulos, Wenrong Wen, and Philipp Stelzig for the virtual temperature sensors (Sect. 4.4): In particular also see the corresponding publications. Furthermore, we gratefully acknowledge the support of the Innovation Fund of the Siemens AG enabling the transfer of unique mathematical building blocks to industrial innovations.

References

1. Panetta, K.: Top 10 strategic technology trends for 2018 (2017). https://www.gartner.com/smarterwithgartner/gartner-top-10-strategic-technology-trends-for-2018/
2. NAFEMS: Digital twins - believe the hype? (2018). https://www.nafems.org/publications/benchmark/archive/april-2018/
3. Grieves, M.: White paper (2014)
4. Glaessgen, E., Stargel, D.: 53rd AIAA/ASME/ASCE/AHS/ASC Structures, Structural Dynamics and Materials Conference 20th AIAA/ASME/AHS Adaptive Structures Conference 14th AIAA (2012), p. 1818
5. Cearley, D., Velosa, A., Walker, M.: Top 10 strategic technology trends for 2017: Digital twins (2017). https://www.gartner.com/en/documents/3647717/top-10-strategic-technology-trends-for-2017-digital-twin/
6. Kerremans, M., Cearley, D., Velosa, A., Walker, M., Burke, B.: Top 10 strategic technology trends for 2018: Digital twins (2018). https://www.gartner.com/en/documents/3867164/top-10-strategic-technology-trends-for-2018-digital-twin
7. Kerremans, M., Cearley, D., Velosa, A., Walker, M.: Top 10 strategic technology trends for 2019: Digital twins (2019). https://www.gartner.com/en/documents/3904569/top-10-strategic-technology-trends-for-2019-digital-twin
8. Van Der Auweraer, H., Donders, S., Hartmann, D., Desmet, W.: Proceedings of ISMA 2018-International Conference on Noise and Vibration Engineering and USD 2018-International Conference on Uncertainty in Structural Dynamics, pp. 3547–3565 (2018)
9. Boschert, S., Rosen, R.: Mechatronic Futures, pp. 59–74. Springer, New York (2016)
10. Boschert, S., Heinrich, C., Rosen, R.: In: Horvath, I., Suarez Rivero, J.P., Hernandez Castellano, P.M. (eds.) Proceedings of TMCE, Las Palmas de Gran Canaria, Spain (2018)
11. Krull, F.: A passion for digital twins (2019). https://new.siemens.com/global/en/company/stories/research-technologies/digitaltwin/passion-for-digital-twins.html
12. Rasheed, A., San, O., Kvamsdal, T. (2019). Preprint. arXiv:1910.01719
13. Pettey, C.: Prepare for the impact of digital twins (2017). https://www.gartner.com/smarterwithgartner/prepare-for-the-impact-of-digital-twins/
14. Markets and Markets, Digital Twin Market by Technology, Type (Product, Process, and System), Application (predictive maintenance, and others), Industry (Aerospace & Defense, Automotive & Transportation, Healthcare, and others), and Geography - Global Forecast to 2026 (2020)
15. Schaller, R.R.: IEEE Spectrum **34**(6), 52 (1997)
16. Arden, W., Brillouët, M., Cogez, P., Graef, M., Huizing, B., Mahnkopf, R.: Version **2**, 14 (2010)
17. Rüde, U., Willcox, K., McInnes, L.C., De Sterck, H., Biros, G., Bungartz, H., Corones, J., Cramer, E., Crowley, J., Ghattas, O., et al. (2016). Preprint. arXiv:1610.02608

18. Bellini, H., Chen, W., Sugiyama, M., Shin, M., Alam, S., Takayama, D.: Profiles in innovation: virtual and augmented reality (2016). https://www.goldmansachs.com/insights/pages/technology-driving-innovation-folder/virtual-and-augmented-reality/report.pdf
19. Woods, D.: Is the enterprise knowledge graph finally going to make all data usable? (2018)
20. Haas, B.: Proceedings of the Automotive Powertrain Control Systems (2012)
21. Gavranovic, S., Hartmann, D., Wever, U.: Advances in Evolutionary and Deterministic Methods for Design, Optimization and Control in Engineering and Sciences, pp. 553–566. Springer, New York (2019)
22. Breuer, H.: Quick idea test (2019). https://new.siemens.com/global/en/company/stories/research-technologies/digitaltwin/digital-twins-improve-transformer-design.html
23. Hanna, K., Weinhold, I.: The democratization of CFD (2017). https://go.mentor.com/4RREr
24. Schnoes, F., Zaeh, M.: Procedia CIRP **82**, 497 (2019). In: 17th CIRP Conference on Modelling of Machining Operations (17th CIRP CMMO)
25. Krull, F.: Loading robots with a will to mill (2018). https://new.siemens.com/global/en/company/stories/research-technologies/digitaltwin/the-future-of-manufacturing-milling-robots.html
26. Breuer, H.: Following ariadne's thread through labyrinthine voids (2018). https://new.siemens.com/global/en/company/stories/research-technologies/digitaltwin/additive-manufacturing-cleaning-3d-printed-components.html
27. Barnard, S., ands Zistl, A.: Virtual sensor opens a world of efficiency for large motors (2018). https://new.siemens.com/global/en/company/stories/research-technologies/digitaltwin/virtual-sensor-opens-a-world-of-efficiency-for-large-motors.html
28. Hartmann, D., Herz, M., Wever, U.: Reduced-Order Modeling (ROM) for Simulation and Optimization, pp. 167–179. Springer, New York (2018)

Towards Scalable and Private Industrial Blockchains

Ghassan Karame

Abstract During the industry day of ICIAM 2019, we presented a novel blockchain architecture devised specifically to meet industrial standards. In this paper, we detail our proposal and discuss its advantages over existing blockchain proposals. Our proposal features a scalable and novel consensus protocol based on BFT consensus and leverages the notion of satellite chains that can privately run different consensus protocols in parallel-thereby considerably boosting the scalability premises of the system. Our solution also accounts for a "hands-off" regulator that oversees the entire network, enforces specific policies by means of smart contracts, etc. Our proposal is implemented and integrated with Hyperledger Fabric.

1 Introduction

The blockchain technology is rapidly gaining grounds as a key technology, especially in the financial and supply chain management sectors. This is largely due to the ability of the technology to (i) efficiently manage the sharing of digital resources between a large number of stakeholders and (ii) to efficiently manage disputes arising in the process.

In spite of its many advantages, experience with existing blockchain proposals reveals that there are still many challenges that need to be overcome prior to any large scale industrial adoption, namely:

Privacy Existing blockchain deployments rely on the availability of transactions and their order of execution to all nodes in the system. Clearly, this comes at odds with current industry practices which only restrict data sharing and distribution to the intended stakeholders. While some solutions propose to selectively encrypt transactions, such approaches require delicate key management infrastructure,

G. Karame (✉)
NEC Laboratories Europe, Heidelberg, Germany
e-mail: ghassan@karame.org

M. Cruz et al. (eds.), *Progress in Industrial Mathematics: Success Stories*,
SEMA SIMAI Springer Series 5, https://doi.org/10.1007/978-3-030-61844-5_2

and still allow the remaining nodes in the system to learn about the occurrence of a particular exchange in the system.

Scalability Existing permissionless blockchains (e.g., Bitcoin) are able to scale to a considerable number of nodes at the expense of attained throughput (e.g., Bitcoin can only achieve few transactions per second [3]). On the other hand, permission-based blockchains can achieve relatively higher throughput, but can only scale to few hundred nodes. However, one needs to cater for both performance and scalability to meet industrial standards.

Lack of Governance One of the main attractions of the blockchain lies in its decentralized aspects. However, organizations are typically not democratic entities, and want to retain control of their systems in order to enforce specific business logics and policies.

In this paper, we discuss a blockchain architecture devised specifically to meet industrial standards. Our architecture combines the use of the satellite chain architecture proposed in [5] and a novel Byzantine Fault Tolerant (BFT) consensus algorithm, called FastBFT [7].

More specifically, our proposal leverages the notion of *satellite chains* that form interconnected, but independent, subchains of a single blockchain system. Nodes join a given satellite chain if they want to transact with another set of particular nodes. Each satellite chain maintains its own private ledger, thus preventing any non-member node from receiving or accessing any given transaction in its ledger. Each satellite chain executes a novel scalable BFT protocol, FastBFT, to reach consensus. At the heart of FastBFT is a novel message aggregation technique that combines hardware-based trusted execution environments (TEEs) with lightweight secret sharing. Combining this technique with several other optimizations (i.e., optimistic execution, tree topology and failure detection), FastBFT achieves low latency and high throughput even for large scale networks [7].

Our solution supports an unbounded number of active chains at any time—thereby allowing for unprecedented levels of scalability in the system. Satellite chains can transfer assets among each other at any point in time without compromising the security and soundness guarantees in the system. Finally, our solution allows a *regulator* to oversee the entire network, enforce specific policies by means of smart contracts, etc.

2 Background

In what follows, we briefly overview a number of existing blockchain efforts.

2.1 Hyperledger Fabric

Hyperledger is an open source project, managed by the Linux foundation, comprising a number of major banks and IT firms. Hyperledger Fabric is a permission-based

blockchain that requires that all prospective members register and acquire an identity (i.e., an enrollment certificate) before attempting to connect to the network and submit transactions. The fabric's *Membership Services* handle both registration process and identity management.

The system comprises clients, peers, and orderers. Transactions are first sent by the clients to endorsing peers who execute the smart contracts (or chaincodes) to get endorsements. Then, the collected endorsements along with the transaction proposal are sent to the orderers to get ordered into blocks. Finally, the blocks are distributed back to all peers who have subscribed in the corresponding channel, and are validated and applied to the copy of ledger maintained by each peer.

2.2 Corda

Corda is a recent distributed ledger framework proposal that introduces the notion of *flows* to improve transaction privacy. Flows establish point-to-point connections between nodes that wish to carry out transactions. Thus, transactions will be only visible to the contracting nodes. Corda's transactions, following Bitcoin's UTXO model [8], are linked to each other in a consumer-producer model: they take current ledger's entries as inputs to produce new ledger's entries as outputs. Nodes then verify the entire transaction graph upon the receipt of a new transaction.

The consensus protocol in Corda is run by notaries, a cluster of nodes that maintains the ledger, and ensures that no conflicting transactions is included therein. There can be multiple notaries in the network, and nodes can choose by which notary cluster they want their transactions to be finalized. During the consensus process, notaries are required to receive and verify all the transactions of their "subscribed" nodes.

However, this approach achieves privacy only for message transmission, which is orthogonal to consensus realization in the network. Namely, notaries need to see transactions to check for double spending; when traversing the transaction graph to verify a newly received transaction, nodes learn about other transactions issued by other nodes.

2.3 Existing Byzantine Fault Tolerant Protocols

Byzantine fault-tolerant (BFT) protocols have not yet seen significant real-world deployment, due to their poor efficiency and scalability. In a system with n nodes, such protocols need to exchange $O(n^2)$ messages to reach consensus on a single operation [7].

We refer the readers to [7] for a thorough treatment of the different categories of existing BFT protocols, and their respective performance.

3 Our Approach

In this section, we present and detail our proposed architecture. To this end, we start by introducing our system model, after which we introduce the concept of satellite chains, and discuss how to enable asset transfer among satellite chains.

3.1 System Model

We consider a permission-based blockchain network comprising of registered stakeholders. The platform supports smart contracts in the form of distributed applications such as those found in Ethereum [10] and Fabric [4].

Our system consists of a number of nodes that can take any of the following roles: *clients* that just send transactions in the system, *validators* that participate in the consensus, *auditors* that can passively see a selected number of transactions in the system, and *regulators* that can enforce policies (e.g., ban nodes) without necessarily participating in the consensus. Notice that nodes can take more than one role in the system.

We assume that nodes are interested in joining different committees, so called *satellite chains*, in the network. Satellite chains consist of an arbitrary number of stakeholders that share a given business logic or commonly interact with each other to fulfill a desired goal. Conforming with existing industry standards, we assume that stakeholders are not interested in sharing their transactions with parties with whom they did not establish any relationship.

3.2 Satellite Chains

We define a satellite chain to be a distributed private ledger maintained by a subset of stakeholders in the network. These stakeholders also act as *validators* in their satellite chain, participate in the consensus, and maintain the ledger state (cf. Fig. 1). Unlike Sidechains [1], our model makes no restriction on the underlying consensus layer used in each satellite chain. As we will show later, each satellite chain can decide to adopt any consensus protocol, such as PBFT [2], MinBFT [9], FastBFT [7], that does not violate the policies mandated by the regulator. However, similar to Sidechains, our solutions supports asset transfer among different satellite chains. Access control to the private ledger is maintained by each satellite chain, and is defined by a policy determined by the *validators* of the chain and the regulator. Notice that, in our solution, a single node is not bound to a single satellite chain and could join different chains simultaneously [5].

To form a satellite chain, a group of nodes first agrees on the validators of the chain, the consensus protocol, and the access policies. This agreement can be

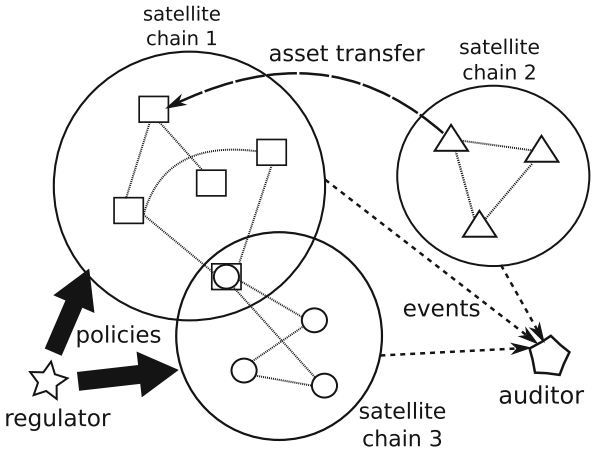

Fig. 1 Our approach featuring multiple interconnected satellite chains. Validator nodes maintain the private ledger within the satellite chains while the assets can be transferred across chains. The regulators push policies into chains and the auditors subscribe to events generated by chains

reached offline (i.e., using an external channel) or could be realized within the blockchain system itself [5].

Notice that auditors can subscribe to any given satellite chain in order to receive notifications about selected transactions in that chain. This subscription request needs to be authorized by the chain [5].

3.3 Regulators

Regulators are entities which ensure that all transactions in the network are validated and comply with some high level policy. Unlike previous proposals, regulators do not participate in the consensus protocol, and have the sole role of pushing the regulation policies to the selected satellite chains.

This is achieved by deploying the regulation policies using smart contracts. To apply these policy contracts with full flexibility, we also introduce a *policy directory contract* which is designed to manage all the *policy contracts* by providing functionalities such as registration, search by transaction type, etc. The directory contract is mandated by the regulators, and is deployed in each satellite chain. The policy directory contract listens to all publish/update events about policy contracts released by the regulator—thus ensuring that new policy contracts will be automatically deployed in their respective satellite chains and registered in the directory contract.

Moreover, we require *all* smart contracts deployed in each satellite chain to contain a hook to this policy directory contract. Namely, during transactions validation, transactions will be forwarded to the policy directory contract, which will apply appropriate policy checks before allowing the satellite chain's smart contracts to execute them. This proposal ensures that, as long as there are enough honest

validators in each satellite chain, the regulation policies are enforced correctly in each chain without the need for active intervention from the regulators [5].

3.4 Cross-Chain Asset Transfer

As mentioned earlier, each satellite chain processes transactions therein and maintains the ledger independently among the member stakeholders. However, in some use cases, assets need to flow between stakeholders across multiple satellite chains. This would be beneficial, for example, in cross-border payments between financial institutions that belong to different administrative domains (i.e., different satellite chains).

To address this problem, our proposal supports transferring assets between independent satellite chains. We refer the reader to [5] for more details on the asset transfer protocol. Notice that the assert transfer operation is atomic at all times: the sender's and recipient's accounts are either both updated in their respective satellite chains or both unchanged. We do not allow implicit roll-backs based on timeout since the process is asynchronous. Only explicit roll-backs with reject token from the recipient chain are allowed. More specifically, the sender expects either a receipt token or a reject token from the recipient chain to conclude the asset transfer. Since the consensus layer of the satellite chains guarantees availability and consistency, we argue that the sender will eventually get a response from the recipient's chain. If the transfer operation is successful, only one consensus round is required within each chain; if the operation fails in the recipient chain, the sender chain is required to execute an additional round of consensus to roll back the sender's account [5].

3.5 FastBFT

As mentioned earlier, each satellite chain executes a specific BFT protocol, dubbed FastBFT, to reach consensus within each chain.

FastBFT is an optimistic BFT protocol that guarantees safety in asynchronous networks but requires weak synchrony for liveness.

At the heart of FastBFT is a novel message aggregation technique that combines hardware-based trusted execution environments (e.g., Intel SGX) with lightweight secret sharing. Here, we assume that each replica holds a hardware-based Trusted Execution Environment (TEE) that maintains a monotonic counter and a rollback-resistant memory. We assume that faulty replicas may be Byzantine but TEEs may only crash [7].

Aggregation reduces message complexity from $O(n^2)$ to $O(n)$. Unlike previous schemes, message aggregation in FastBFT does not require any public-key operations (e.g., multi-signatures), thus incurring considerably lower computation/communication overhead [7].

FastBFT further balances load by arranging nodes in a tree topology, so that inter-server communication and message aggregation take place along edges of the tree. FastBFT adopts the optimistic BFT paradigm that separates agreement from execution, allowing it to only require a subset of nodes to actively run the protocol. Namely, in FastBFT, only $f + 1$ active replicas need to agree and execute the requests and the other f passive replicas just update their states. Such an optimistic design achieves a strong tradeoff between efficiency and resilience (see [7] for more details).

Finally, FastBFT uses a simple failure detection mechanism to deal with non-primary faults efficiently [7].

3.5.1 Performance Evaluation

In Fig. 2, we compare the throughput achieved by FastBFT to XPaxos [6] (one of the most popular BFT protocols) as the numbers of nodes that execute consensus increases in the system. Here, we deployed our BFT implementations on a private network consisting of five 8 vCore Intel Xeon E3-1240 equipped with 32 GB RAM and Intel SGX. All BFT replicas were running in separate processes. At all times, we load balance the number of BFT replicas running on each machine; by varying the server failure threshold f from 1 to 99, we spawned a maximum of 298 processes across 5 machines. The clients were running on an 8 vCore Intel Xeon E3-1230 equipped with 16 GB RAM as multiple threads. Each machine has 1 Gbps of bandwidth and the communication between various machines was bridged using a 1 Gbps switch. This setup emulates a realistic enterprise deployment; for example IBM plans the deployment of their blockchain platform within a large internal

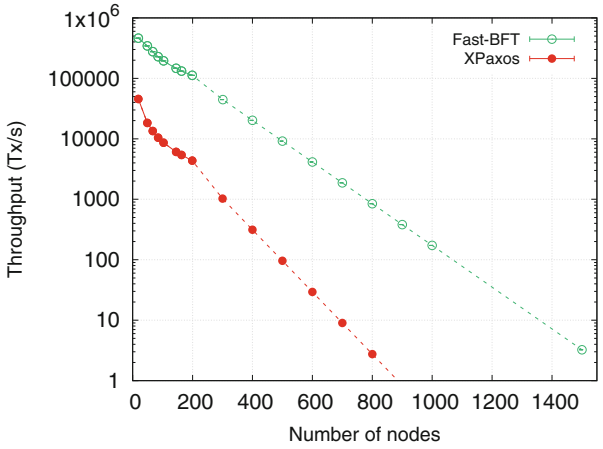

Fig. 2 Performance evaluation of FastBFT when compared with XPaxos [6] as the number of nodes in a satellite chain increases

cluster, serving mutually distrustful parties (e.g., a consortium of banks using a cloud service for running a permissioned blockchain).

We assume a block size of 1 MB and transactions of 250 Bytes each. Our results show that FastBFT considerable outperforms XPaxos. For instance, FastBFT can achieve almost 100,000 transactions per second (tps), when the network comprises 200 nodes, almost 12 times faster than XPaxos. Even as the network scales to, e.g., 800 nodes, FastBFT achieves more than 1000 transactions per second—two orders of magnitude faster than XPaxos.

Notice that the combination between the use of the satellite chains architecture and FastBFT further promotes the scalability of our system. For instance, consider a blockchain network comprising 800 nodes. If the blockchain network were to be equipped with XPaxos in a standalone chain, the resulting throughput would be around 5 transactions per second. On the other hand, organizing the network into four satellite chains running FastBFT for consensus, each comprising of 200 nodes, allows each chain to reach 100,000 tps and the overall network to hit the bounds of 400,000 tps.

4 Concluding Remarks

In this paper, we discussed a blockchain architecture devised specifically to meet industrial standards. Our proposal leverages the notion of *satellite chains* that form interconnected but independent subchains of a single blockchain system, and supports an unbounded number of active chains that can run in parallel at any point in time. Moreover, our proposal allows different satellite chains to transfer assets among themselves without compromising the security and soundness guarantees in the system, and accounts for the role of a passive regulator that can at any point in time enforce specific network-wide policies.

Within each satellite chain, a scalable consensus protocol is executed. Our protocol, called FastBFT, achieves unprecedented performance and scalability. Notice that our proposal is agnostic of the underlying blockchain platform, and as such can be easily integrated within existing blockchain platforms such as Hyperledger Fabric and Corda. Moreover, our proposal supports heterogenous consensus protocols by allowing different satellite chains to execute different consensus protocol as long as such consensus is in line with the policies set by the regulator.

Notice that by effectively organizing nodes within interconnected satellite chains, our proposal supports business privacy within each satellite chain; transactions exchanged within each satellite chain are only visible to those nodes that populate the satellite chain and cannot be seen/received by other nodes that are part of other satellite chains. We refer the readers to [5] and [7] for further details on our architecture and FastBFT, respectively.

Moreover, we believe that our proposal enables the realization of blockchain sharding based on functional requirements such as node relationships. Blockchain

sharding has received considerable attention in the literature; while there are a number of security challenges that effectively hinder practical sharding (for load balancing), our solution groups relevant stakeholders in a single shard. We believe that our solution finds direct applicability in a number of emerging industrial blockchain applications, such as trade finance, asset management, supply chain management, and retail services. We therefore hope that our findings motivate further research in this area.

Acknowledgments This talk at ICIAM19 is partly based on the following scientific publications:

- [7] in collaboration with Jian Liu, Wenting Li, and N. Asokan.
- [5] in collaboration with Wenting Li, Sebastien Andreina, Sergey Fedorov, and Alessandro Sforzin.

References

1. Back, A., Corallo, M., Dashjr, L., Friedenbach, M., Maxwell, G., Miller, A., Poelstra, A., Timón, J., Wuille, P.: Enabling Blockchain Innovations with Pegged Sidechains (2014)
2. Castro, M., Liskov, B., et al.: Practical Byzantine Fault Tolerance. In: OSDI, vol. 99, pp. 173–186 (1999)
3. Gervais, A., Karame, G.O., Wüst, K., Glykantzis, V., Ritzdorf, H., Capkun, S.: On the security and performance of proof of work blockchains. In: Proceedings of the 2016 ACM SIGSAC Conference on Computer and Communications Security, pp. 3–16. ACM, New York (2016)
4. Hyperledger Fabric. https://hyperledger-fabric.readthedocs.io/en/v0.6/
5. Li, W., Sforzin, A., Fedorov, S., Karame, G.O.: Towards scalable and private industrial blockchains. In: Proceedings of the ACM Workshop on Blockchain, Cryptocurrencies and Contracts, BCC '17, pp. 9–14. ACM, New York (2017). http://doi.acm.org/10.1145/3055518.3055531
6. Liu, S., Viotti, P., Cachin, C., Quema, V., Vukolic, M.: XFT: practical fault tolerance beyond crashes. In: 12th USENIX Symposium on Operating Systems Design and Implementation (2016). https://www.usenix.org/conference/osdi16/technical-sessions/presentation/liu
7. Liu, J., Li, W., Karame, G.O., Asokan, N.: Scalable byzantine consensus via hardware-assisted secret sharing. IEEE Trans. Comput. **68**(1), 139–151 (2019). https://doi.org/10.1109/TC.2018.2860009
8. Nakamoto, S.: Bitcoin: A Peer-to-Peer Electronic Cash System (2008)
9. Veronese, G.S., Correia, M., Bessani, A.N., Lung, L.C., Verissimo, P.: Efficient byzantine fault-tolerance. IEEE Trans. Comput. **62**(1), 16–30 (2013)
10. Wood, G.: Ethereum: A Secure Decentralised Generalised Transaction Ledger. Ethereum Project Yellow Paper (2014)

Industrial Mathematics: Driving a New Management Approach

M. Pina

Abstract The current challenge of managing businesses and companies is enormously complex, due to the ever-changing markets, the speed of mass communication, the power of the highly informed customers, the disruptive nature of some sectors and the difficulty in quickly incorporating everything simultaneously. The critical and intuitive vision, extremely valuable and necessary nowadays, demands a higher level of accurate data to assess the diverse business factors and more precise forecasts. Today, we are facing numerous of those changes in the automotive industry, as well as the associated uncertainty of the impact on our existing business model. Nevertheless, it is certain that it will be huge and require a detailed preparation. Industrial Mathematics (IM) provides extremely valuable methods and tools to manage these challenges, while demanding open, creative and critical thinking to reach novel solutions. Based on an integrated approach to know-how, IM acts as a mobilizing agent which drives organizations to higher levels of performance. At NORS we strongly believe in the cooperative interactions between academy, research centres and industry, which provide unique conditions for fostering people and in essence the bottom-line—the business profitability. This paper aims to share our industrial mathematics journey and somehow highlight the potential of changing an organizational mindset. In the first section, a brief company overview will be present followed, in the second section, by an explanation of how and why a mathematical approach was selected. In the following sections, the lessons learned and the achievements obtained during this process will be presented—the results speak for themselves.

1 The NORS Group, Company Profile

The NORS Group is a Portuguese group whose vision is to be a world leader in transport solutions, construction equipment and agriculture equipment. In its

M. Pina (✉)
NORS Group, Porto, Portugal

M. Cruz et al. (eds.), *Progress in Industrial Mathematics: Success Stories*,
SEMA SIMAI Springer Series 5, https://doi.org/10.1007/978-3-030-61844-5_3

genesis are 86 years of history and activity in Portugal, which started with the representation of the Volvo brand in 1933. Today, fully assuming its multinational vocation, the NORS Group governs itself by a strategy of cross-cutting principles and policies and a global Group culture, aimed at a sustained growth, supported by excellent products, services and Human Resources. Currently, the NORS Group is present in 17 countries across 4 continents: Portugal, Spain, Brazil, Angola, Botswana, Namibia, Mozambique, Cuba, Mexico, USA, Turkey, Austria, Czech Republic, Slovakia, Romania, Hungary and Croatia with more than 3700 employees and sales exceeding 1.6 billion Euros. Historically associated with its leadership in the automotive sector, NORS Group today is a multinational with a wide scope of action, conducting its activities in four major business areas: Original Equipment Solutions, Integrated Aftermarket Solutions, Recycling Solutions and Safekeeping Solutions (Fig. 1).

The Original Equipment Solutions embodies the Group's historical activity, thanks to their relationship with Volvo since 1933, and includes the sale and after-sale of trucks, buses, construction machines, agriculture equipment, cars, marine and industrial engines, generators and original components. In the business area of Integrated Aftermarket Solutions, the Group gathers all the companies of its after-sale structure, which includes the importation and distribution of OEM (Original Equipment Manufacturer) multi-brand parts for trucks, cars, building and decorative glass. The environmental sector has been a strong focus of the Group. The Recycling Solutions area works in the production of urban waste's collecting and treatment equipment and solutions for temporary deposition of solid waste. In order to provide safekeeping Solutions, Amplitude Seguros is an insurance and risk consultant of total service, which operates in various segments and sectors of the economy.

Fig. 1 NORS Group

The genesis of the NORS Group dates to 1933, when Luiz Óscar Jervell became the representative for the Volvo brand in Portugal. In 1949, April 1st, the name Auto Sueco appears for the first time, when, together with Yngvar Poppe Jensen, the decision is made to empower the business.

2 The Industrial Mathematics Journey @NORS

This paper mainly strives to present our success story and highlight some of the milestones and challenges tackled during the journey of implementing industrial mathematics in this group. Our story began six years ago, when we started a partnership with a Portuguese research center—LEMA Laboratory of Mathematical Engineering from Instituto Superior de Engenharia do Porto—and began to apply a mathematical approach to some of our challenges, step by step, or more precisely, company by company.

2.1 @The Starting Line

The first challenge started with a complex issue in our aftermarket spare parts stocks, which was managed with a basic model, supported on a weak IT system without any scientific methodology to forecast our most important performance indicator—the sales. Thus, we carefully reflected on how to address this issue, since the spare parts distribution business was very traditional, and any out-of-the-box idea would be misunderstood. We needed to accurately define a strategy that should be simultaneously, economical and discrete. This led us to our pilot project, which began in one of the group's companies—a multi-brand spare parts company for passenger cars in Portugal. Some background information regarding the situation is important to fully comprehend our challenge. At that time, we had an 8-million-euro spare parts stock, in which there were more than two hundred thousand parts number, supplied by one hundred and twelve suppliers (parts manufacturers). This volume represented approximately 4 months of sales coverage, which was an excessively elevated figure and vastly impacting our profitability. Additionally, a lean project implementation was ongoing in our warehouses, which was supported by a weak and inaccurate information management system. As so, improving our operation model in order to reduce our logistic costs was on the top of our priorities. Generally speaking, we may state that we wanted and needed to sell more, while reducing our spare parts stocks and logistic costs, in order to be more profitable. We decided to challenge ourselves by trying to solve this problem with a different approach and using a different subject matter. But we knew that we weren't able to do it alone. Nobody in NORS Group had ever worked with industrial mathematicians and we didn't have an academic partnership culture. It was really

the first time. And because of that we tried to be wizards and to work as discretely as possible!

2.2 Pilot Project with the Academia

Six years ago, we developed a partnership with the LEMA, Laboratory for Mathematical Engineering, and started working with an Industrial Mathematics approach. The first project lasted 9 months where we modelled, developed, and implemented a new methodology for the spare parts forecasting, improving the accuracy in predictions. One year after, a specific algorithm to manage the NORS stock was developed. This tailor-made model based on updated forecasting techniques was implemented, taking into account the company limitations in terms of expertise and computing capacity. One year after the model being fully implemented on several families of products, the level of service raised 1%, the mean stock value decreased about 18%, in a period where sales increased more than 9%. Besides that, the time needed to conclude the suppliers orders had a significant reduction (>50%). Additionally, the months of stock KPI, was decreased by around 25%, from 5.7 to 4.2 months (Fig. 2).

A software tool that implemented automatically all the features that NORS asked in the beginning of the project was also developed, as well as some upgrades made during the development phase. An easy to use graphical user interface was developed to operate the software Fig. 3, reducing the order processing times in more than 70%, when compared with NORS native system.

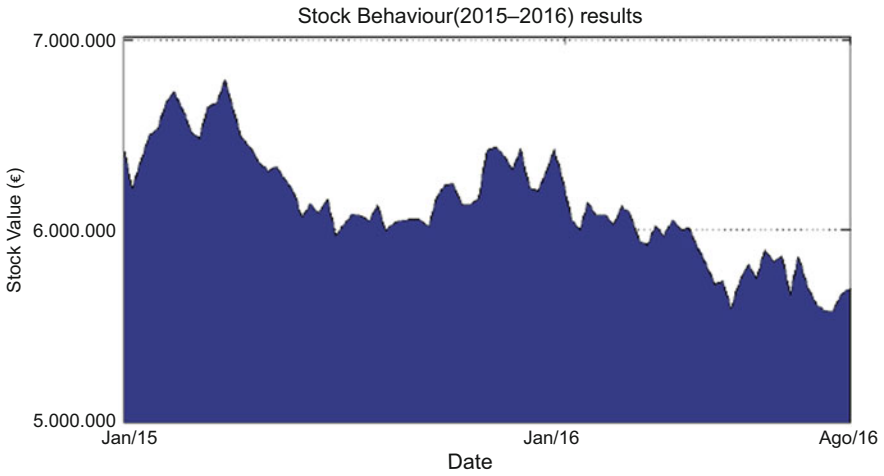

Fig. 2 Stock behaviour

Fig. 3 Suppliers orders purchase interface

As achievement, a new mathematical model for stock management of spare parts was developed in-house. From that day we not only manage our stock better, but also have the ability to manage our cash flow and risk level—results from the second phase of the project. We had used MSO (Modeling, Simulation and Optimization) methodology and Matlab language to build that graphical interface. After 5 years we are still upgrading the model. It's a nonstop work. To recap:

- A mathematical model for minimizing cost according to management strategies was developed using the MSO framework;
- The model was fully developed, programmed and implemented by mathematicians according to management strategies;
- The implementation was made in such a way that it is independent of the Company CRM (e.g. the migration to SAP went smoothly);
- The project highlighted the Industrial Mathematics importance within the company;
- Today, we are working in the rappel optimization model and introducing other factors that may impact the sales (promotions, sales effects, etc.). The next step will be to add some data about the Portuguese car park.

2.3 Our Mathematical Footprint

We can proudly reveal that one and half years after that pilot project began, the company and part of the NORS Group have opened their minds to this new way of working. That moment, during 2015, was a turning point for our plans of introducing a new way to support the business decisions. Our results highlighted

Fig. 4 NORS Innovation Prize

the role of industrial mathematics in modern management, within the NORS Group. In addition, NORS awarded this project in 2015 with the Innovation prize, fostering awareness in other areas of the group to the goals achieved by industrial mathematics (Fig. 4).

Since then, new proposals and requests for exploratory studies have been addressed to this team on a regular basis. As consequence a new laboratory, the LAB MI (acronym for Industrial Mathematics Laboratory) was created within the NORS aftermarket development section. The initial internship had become into a permanent workplace.

As mentioned before, the first project and its results drove the company to another stage. Our company's reluctance had shifted and now it demanded more and pushed further. So, we started to work on a tool to manage our cash flow and risk level. We decided to add mathematics to one of our core process, the purchase tool. In the new IT platform based on SAP, that we are implementing, we decided to base one of our core business processes in a Matlab add-on tool. The stock management tool will be processed inhouse with our mathematicians, out of the system but in the new IT platform. We are presently working on the final interfaces. The path that lead to have some permanent positions for Mathematicians in NORS began slowly, first with an academic internship, followed by a professional internship and finally we, NORS, decided to create a new position in the business development department. The way this new approach was managed revealed to us two key success factors: our slow and discrete implementation of maths into NORS's daily life and our first mathematician as well as those LEMA/ISEP mentors who accurately made the match based on our needs. Our first intern merits recognition for his extensive knowledge and keen soft skills which were vital for the success of this project. Nowadays it's different. Internally we have, what we call, a mathematical footprint in the company. People want to add maths to their jobs. Six years ago, we said, it would be a waste of time, we would never have a "pure" mathematical approach into the heart of our business. A new management paradigm was born, supported by data analyses and less people's intuition. Which is, nowadays, used and improved every day by our team.

2.4 The LAB MI

Backed up by the success of this collaboration, LAB MI, the Laboratory of Industrial Mathematics of NORS Group, was created. Based on the MSO paradigm (Mathematical Modelling, Simulation and Optimization) the procedure, applied in several challenges, is based on the creation of a mathematical model tailored for the needs of each specific company. This process is the foundation of the methodology used by some of the main European industries.

LAB MI is a business development area at NORS Group, formed by a team of full-time collaborators and a recurrent curricular internship. From 2014 until now, seven master's degree thesis and one bachelor's degree dissertation were concluded by LAB MI members. During this period, the retention rate of interns was over 80%. The coding and software are developed in Matlab, R and Python, always focusing on process automation and integration with the group's ERP. It has been, and it will be a long haul. Since the beginning we have had nine mathematicians helping us to solve our issues. Nowadays we have a team of four mathematicians and one internship working with us.

3 The Side Effects and the Work in Progress

And suddenly we had several opportunities to provide more efficiency and accuracy in other activities and processes within the group. Likewise, some additional effects of having a math insider appeared.

It starts with a pilot project but now is part of the NORS aftermarket business architecture. It aims to ensure excellent service levels in the aftermarket business, to reduce logistics costs and optimize the investment return. It was possible to implement the developed mathematical models within the existing ERP. Moreover,

a Matlab application was developed to evaluate and analyse the purchases, resulting that the model was extended with the Purchase Control Toolbox—a tool that gathers data from all Aftermarket suppliers of the group, returning purchasing projections and fulfilment levels (Figs. 5 and 6).

Fig. 5 Suppliers orders purchase interface

Fig. 6 Suppliers orders purchase interface

Fig. 7 Data analysis tools

In this context, besides developing several tools that support the warehouse and store operation management, we started to extract other levels of information due to data analysis tools. New approach to the sales predictions of vehicles based on (till now, e-garbage) stored data. The challenge was to gather all key sales indicators in an intuitive application and custom-made to NORS' own needs and deploy a model adjusted to the specificities of each market in which NORS operates (e.g. light vehicles vs heavy duty, original manufacturers vs Aftermarket). And also, the needs to create additional mechanisms to control sales activities, with a macro and dynamic perspective.

To transfer the knowledge and supply tools for the company's managers, we developed, and implemented, applications created with Matlab and Python, custom-made to the needs of each company and Power BI application to analyse, among others, the distribution of clients and sales income per store, client segment or sales personnel. Based on this, a new approach to the profitability analysis was developed. We are still trying to find a way to put all the pieces together: the information that we have inside the company, the information from the market, the information that we can obtain "looking" at our customers and the information we can collect from each vehicle. Our conviction is that this will result in more on-demand studies and management support decision information (Figs. 7 and 8).

Fig. 8 Geographic distribution analysis tools

This challenge was about optimizing shipping routes and calculate distances in a dynamic way, reduce logistics costs and maintain the existing service level to our clients. As a result, we developed a tool integrated with geolocation API, for real time route calculation, whose main goal is the optimization of sales personnel portfolios and, as a consequence, improve customer service level. As a result, in one of the companies, we reduced 20% on the logistical costs (Fig. 9).

To focus on the customer needs, we need to define which of the several dimensions regarding the interaction of NORS with its customers are key to their satisfaction. By doing so, we are able to standardize and build transversal indicators based on different surveys conducted by each NORS Group company. The main purpose of this development is the ultimate definition of key factors to customer satisfaction, try to find and keep updated the drivers of excellence. So, we supported the implementation process of the Net Promoter Score, NPS application, in all the companies within NORS Group and created a standard customer satisfaction survey platform for the whole group (Fig. 10).

Fig. 9 Vehicle routing

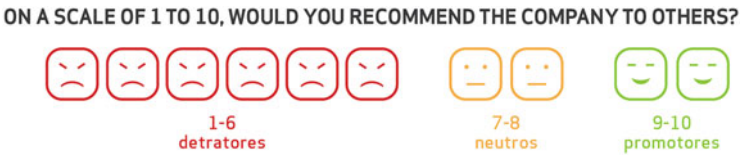

Fig. 10 NPS application

Analysing the data of all customer contact channels (in site and via contact centre) allowed us to understand the seasonality of customer's demand regarding those channels. With that data, we developed a tool to simulate our client's interactions with the shops and use it to optimize the amount of work addressed to each collaborator. This model allows us to have different shift loads throughout the day, in order to increase the model adherence to reality. The model simulations allowed us to understand the impact of applying different number of resources, in order to manage the attendant's allocation and showed us a way to ensure a minimum of 95% service level (Fig. 11).

Fig. 11 Customer's interactions simulation

Fig. 12 Assistance contracts' interface

The first goal of this project was to analyse the costs of maintenance contracts in heavy duty and determine a fair value per contract, parametrized by the different risk levels to be defined by the product manager. But, working together with the team in charged for the Assistant Contracts, we've made more than that. We created a support tool for control and management of maintenance contracts (Fig. 12).

This approach presents a costs global view and models the distribution of the historical data in order to estimate the costs for forthcoming contracts, based on several variables. Additionally, we are getting closer to model the "life" of the main parts of each truck model, making it possible to improve workshop trips with preventive maintenance and even cost anticipation.

This project was based on the construction of safety bands, based on forecasting models, to identify significant deviations in values predicted by the busi-

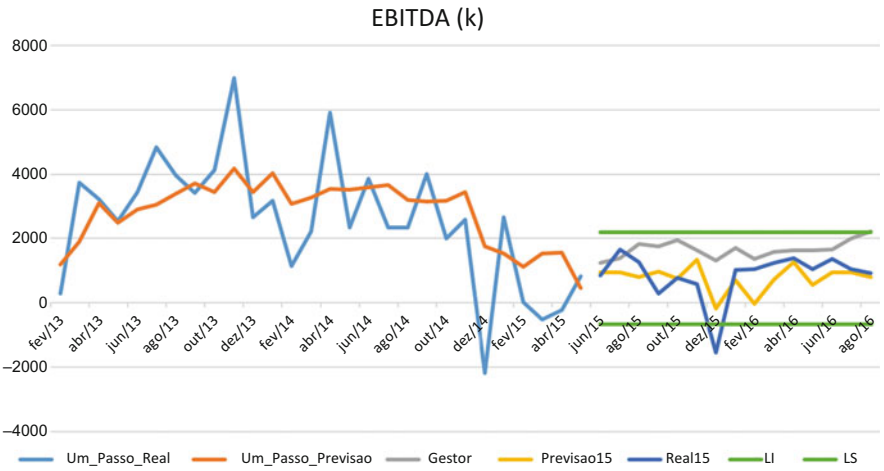

Fig. 13 Budget forecast tool

ness manager in relation to the trends forecasted by NORS Group management. This upgraded the existing methodology, decreasing the high user-dependency in parametrization, such as number of time periods to be considered, forecasting methods to be used or which amplitude of safety bands should be defined.

At the end, we developed a tool for the NORS Group strategic management that periodically updates the budget forecast with the updated data, automating the choice of best forecasting mode, parameterizations and definition of safety band amplitudes. Those forecasts, which provide forecasts up to a 15-month period, are based on several theoretical forecasting models (Fig. 13).

4 Conclusions

Industrial Mathematics was a foreign concept @NORS until about 6 years ago when our journey began. Today we have a team of four mathematicians working with us, several core business processes supported by applied maths developments and an awareness of how important thinking in a different way to address our challenges, really is. Currently we are working with study areas using several approaches of Industrial Mathematics such as MSO, Statistics, Discrete Mathematics, Time Series, Numerical Analysis, Data and Web Mining, Vehicle Routing or Big Data. In fact, we are now starting to use other available information and new artificial intelligence techniques, to obtain better supply and demands forecasts.

It has been a long journey but it's only the beginning...

Acknowledgments I would like to express my sincere gratitude to all the LAB MI Team, those that still work with us and those who are spreading industrial mathematics in other companies. A special thanks to the LEMA Professors: Manuel Cruz e Sandra Ramos, without their commitment this success story would not have happened.

Pattern Similarity Measures Applied to Mass Spectra

Arun S. Moorthy and Anthony J. Kearsley

Abstract Mass spectrometry is a core analytical chemistry technique for elucidating the structure and identity of compounds. Broadly, the technique involves the ionization of an analyte and analysis of the resulting *mass spectrum*, a representation of ion intensity as a function of mass to charge ratios. In this article, the notion of *similarity* as it applies to mass spectra is explored. In particular, several modes of approximating distances and similarities in patterns are touched upon: ℓ_1 and ℓ_2 distances, the Wasserstein metric (earth mover's distance) and cosine similarity derived measures. Concluding the manuscript is a report on the performance of the similarity measures on a small test set of data, followed by a discussion of mass spectral library searching and prospects for quantifying uncertainty in compound identifications leveraging mass spectral similarity.

1 Background and Motivation

When discussing industrial mathematics, it is natural for one to think of the modeling, simulation, and optimization of industrial processes (operations research), a field in which some of the great mathematicians of the twentieth century made their mark. More recently, industrial mathematicians have been tasked with making sense of the abundance of data that exists on public and private servers (data science) which has spawned beautiful algorithms in statistical and machine learning. From the operations research specialist to the data scientist, all industrial mathematicians leverage mathematical thinking with application-specific knowledge to solve problems of industrial importance.

One task of significant industrial importance is the characterization of complex material composition. These materials may include natural products, foods and drugs, fuels, biological fluids, plastics, etc. As examples of the importance of

A. S. Moorthy (✉) · A. J. Kearsley
National Institute of Standards and Technology, Gaithersburg, MD, USA
e-mail: arun.moorthy@nist.gov; anthony.kearsley@nist.gov

M. Cruz et al. (eds.), *Progress in Industrial Mathematics: Success Stories*,
SEMA SIMAI Springer Series 5, https://doi.org/10.1007/978-3-030-61844-5_4

material composition characterization, consider the implications of a fuel containing impurities causing inefficient performance, or of a food containing contaminants negatively affecting the health of consumers. It is of utmost importance that the composition of materials is accurately characterized and, to this end, one of the most commonly employed tools to approach this task is mass spectrometry.

The objective of this manuscript is to introduce the notion of estimating similarity between measurements obtained through mass spectrometry. In particular, the similarity of mass spectra, the resulting measurements from analysis using mass spectrometry, for pure compounds is explored. There are two primary reasons why estimating the similarity of mass spectra is of great importance. (1) Measures of spectral similarity are leveraged in mass spectral library searching, the process of sorting through curated libraries of mass spectra of known compounds to aid in the identification of an analyte from its mass spectrum. (2) Accurate measures of mass spectral similarity are necessary for quantifying the uncertainty of compound identification using mass spectrometry.

The manuscript is organized as follows. In Sect. 2, a brief overview of mass spectrometry and mass spectral library searching is provided, followed by details of several pattern similarity measures in Sect. 3. Concluding the manuscript is a report on the efficacy of each similarity measure for an illustrative test set of mass spectra, and a larger discussion about the implications of similarity measures to mass spectral library searching and uncertainty quantification in Sect. 4.

2 Mass Spectrometry and Mass Spectral Library Searching

Mass spectrometry has been a prominent tool in the analysis of matter for over one hundred years. Broadly, the technique involves the ionization of an analyte, through one of a variety of methods, followed by detecting the intensity of ions across a mass-to-charge (m/z) range. After processing, the output of a mass spectrometry analysis is a mass spectrum. A comprehensive discussion of the technology is outside the experience of the authors and thus the scope of this manuscript, however, good introductory texts [22] and historical review articles [7] can be readily found in the literature. The discussion in this manuscript will focus exclusively on *unit-mass resolution* mass spectra of pure compounds (molecules) obtained through electron ionization (EI) mass spectrometry.[1]

A mass spectrum of the molecule caffeine is shown in Fig. 1. The measure along the x-axis is mass-to-charge (m/z) and the y-axis indicates the relative abundance at each m/z. For reference, a standard 2-dimensional representation of the structure of caffeine is overlaid on the mass spectrum. Note that in EI mass spectrometry,

[1]The specification of "unit-mass resolution" indicates that the mass-to-charge ratio of ions will always be positive integer values. This resolution of electron ionization mass spectra are commonly used in many industrial applications.

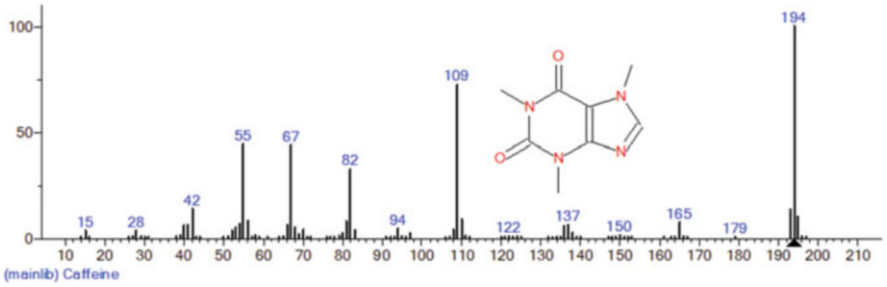

Fig. 1 A representative electron ionization mass spectrum of caffeine from the NIST17 Demo Library [15] with the structure of caffeine overlaid on the spectrum

the charge of an ion is most often 1, and so m/z is often interpreted and referred to as mass. Ideally, every peak in a mass spectrum can be explained exclusively as a *molecular ion* or a *fragment ion*.

A molecular ion, as its name implies, is an ion of the intact molecule being analyzed. In the example of caffeine with nominal molecular mass 194 Da, the molecular ion peak appears at m/z 194 (see Fig. 1). The peaks occurring with m/z values greater than 194 are molecular ions where the molecule is constructed with heavier isotopes (e.g. Carbon-13 instead of Carbon-12). For some molecules, molecular ions will contain weak bonds that cause it to fragment prior to reaching the detector, resulting in the molecular ion being unobserved in the mass spectrum.

Under normal conditions, an ionized molecule will almost always fragment. The portion of the molecule that remains charged after fragmentation is referred to as a fragment ion and the portion(s) that are neutral charged are referred to as neutral losses. Fragment ions are recorded in mass spectra, neutral losses are not. Most ionized molecules can fragment in several ways. Accordingly, mass spectra will typically contain a number of fragment ion peaks; however, there are some cases where a very stable ion—either the molecular ion or a fragment ion—will lead to mass spectra of very few peaks (see Fig. 2).

Since a mass spectrum summarizes the mass of a molecule and its fragments, it is possible for an analytical chemist to identify a molecule directly through interpretation of its mass spectrum. This is particularly true for simple molecules with limited mechanisms for fragmentation. For more complex molecules, identification through interpretation is impractical if not impossible. An important resource used by many analysts to aid in identifying molecules are *mass spectral libraries*. These carefully curated databases of mass spectra of known molecules can be sorted through by comparing to the mass spectrum of the analyte, a process referred to as mass spectral library searching, potentially finding a match to the analyte spectrum or providing information that supports further investigation. For interested readers, a seminal report on the topic of mass spectral library searching was provided by Stein and Scott [21].

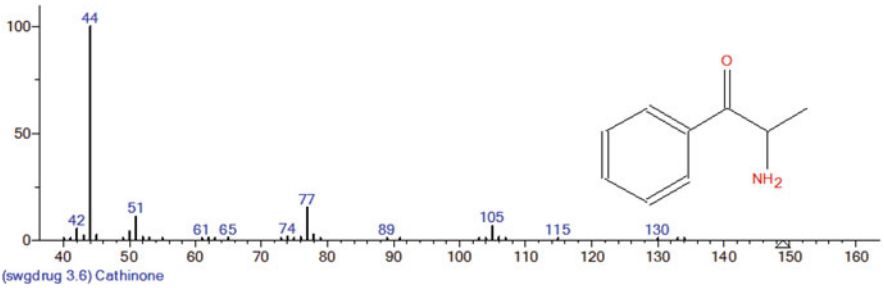

Fig. 2 A representative electron ionization mass spectrum of cathinone from the Scientific Working Group for the Analysis of Seized Drugs (SWGDRUG) mass spectral library [19] with the structure of cathinone overlaid on the spectrum

3 Pattern Similarity Measures

All unit-mass resolution EI mass spectra can be easily represented as vectors of equivalent length, where the index of each element in the vector is representative of the mass-to-charge of an ion and the value of each element being the corresponding relative abundance from the spectrum. It is between these vectors that a similarity estimate is computed. This section first describes similarity measures that are traditionally used in mass spectral library searching, followed by similarity measures used in general pattern recognition tasks and a final measure motivated by the study of histograms.

Using the standard dot-product formula we can define the cosine similarity between two non-zero vectors, $\mathbf{x}$ and $\mathbf{y}$ as ξ_1,

$$\xi_1 = \frac{\sum_{i=1}^{n} \mathbf{x}[i]\,\mathbf{y}[i]}{\sqrt{\sum_{i=1}^{n} (\mathbf{x}[i])^2}\,\sqrt{\sum_{i=1}^{n} (\mathbf{y}[i])^2}}\,, \tag{1}$$

where n is the length of the vectors, and the $\mathbf{x}[i]$ notation indicates the ith element of the vector $\mathbf{x}$. A commonly employed variant of cosine similarity is the *simple match factor*. It differs from standard cosine similarity by three modifications: (i) the values of the elements of the input vectors are replaced with their square roots, (ii) the resulting cosine similarity measure is squared, and (iii) the resulting value is scaled by a constant. This sequence of modifications result in a simple match factor, ξ_2,

$$\xi_2 = C\,\frac{\left(\sum_{i=1}^{n} (\mathbf{x}[i])^{1/2}\,(\mathbf{y}[i])^{1/2}\right)^2}{\sum_{i=1}^{n} \mathbf{x}[i]\;\sum_{i=1}^{n} \mathbf{y}[i]}\,, \tag{2}$$

where C is, for historical reasons, 999. In mass spectral library search programs that use simple similarity, the value is further rounded to the nearest integer, also for

historical reasons. A further modified measure of similarity commonly employed in mass spectral library searching is the *identity match factor*. It was first introduced in [21] and is referred to as the "composite score". This measure differs from the simple similarity match factor in that it is modified by a ratio based on relative abundances at adjacent m/z values. An alternate identity match factor is computed in this manuscript. A vector, $\mathbf{r}$ is computed with each element defined

$$\mathbf{r}[i] = \begin{cases} \boldsymbol{\gamma}[i] & \text{if } \mathbf{x}[i]\mathbf{x}[i-1]\mathbf{y}[i]\mathbf{y}[i-1] > 0, \\ 0 & \text{if } \mathbf{x}[i]\mathbf{x}[i-1]\mathbf{y}[i]\mathbf{y}[i-1] = 0, \end{cases}$$

where

$$\boldsymbol{\gamma}[i] = \frac{\mathbf{x}[i]}{\mathbf{x}[i-1]} \frac{\mathbf{y}[i-1]}{\mathbf{y}[i]}.$$

The set of indices marking non-zero values of $\mathbf{r}$ is denoted α. A modification term, F, is computed

$$F = \frac{\sum_i^{m_1} \alpha[i] \cdot \min\left(\mathbf{r}[\alpha[i]], 1/\mathbf{r}[\alpha[i]]\right)}{\sum_i^{m_1} \alpha[i]}$$

where m_1 is the number of elements in the set α. The modified identity match factor, ξ_3, is then computed as

$$\xi_3 = C \frac{m_1 F + m_2 \frac{\xi_2}{C}}{m_1 + m_2}, \tag{3}$$

where m_2 is the number of indices where elements of both $\mathbf{x}$ and $\mathbf{y}$ have non-zero values, and C is 999 as in (2).

For general pattern recognition tasks, the set of ℓ_p distances are often employed. For consistency and completeness, we present the ℓ_1 distance, ξ_4, and ℓ_2 distance, ξ_5, between non-zero vectors,

$$\xi_4 = \sum_{i=1}^{n} |\, \mathbf{x}[i] - \mathbf{y}[i] \,|\,, \tag{4}$$

$$\xi_5 = \left(\sum_{i=1}^{n} (\mathbf{x}[i] - \mathbf{y}[i])^2 \right)^{1/2}. \tag{5}$$

An intriguing measure of similarity comes from viewing the mass spectra as discrete probability distributions with finite support on a metric space. The Wasserstien metric, a commonly employed method in computer vision and often called the earth mover's distance [18], can be viewed as a distance that represents

the minimum cost associated with transforming a reference mass spectrum into a second to which it is being compared. We denote this distance as ξ_6,

$$\xi_6 = \mathrm{EMD}\,(\mathbf{x}, \mathbf{y}) \ , \tag{6}$$

and note that it is a far more complicated computation than ξ_i, where $1 \leq i \leq 5$. The numerical results presented in this paper result from (6) being evaluated using a transportation simplex algorithm with a ground distance computed using an ℓ_1 metric. It is worth noting that the larger cost associated with evaluating (6) has resulted in significant research on reducing the computational costs including approximations to the metric [20] and the development of parallel programming algorithms [12].

4 Results and Discussion

To demonstrate the performance of the similarity measures outlined in Sect. 3, pairs of replicate spectra[2], and non-replicate spectra[3] were chosen at random from two highly regarded commercial libraries. The distribution of similarity measures generated with each method are shown in Fig. 3 as box and whisker plots, generated using the default *boxplot* function as implemented in base-R [16]. Each box and whisker object describes the distribution of similarity measures computed on a set of mass spectra. The set of non-replicate spectra is labeled on the x-axis of each plot as "other", and the set of replicate spectra is labeled "replicate". For each distribution, the outlined box is the computed Inter Quartile Range (IQR) with the 2nd quartile (median) marked as a darkened line within the box, and the bottom and top edges of the box indicating the 1st and 3rd quartile measurements, respectively. The upper whisker indicates either the maximum measured value in the distribution or the maximum similarity measure within 1.5 IQR of the 3rd quartile value. Similarly, the lower whisker is minimum similarity measure or the minimum measure within 1.5 IQR of the first quartile value. Outlier scores greater than 1.5 IQR of the 1st or 3rd quartile are shown as open circles.

The three cosine similarity derived measures traditionally employed in mass spectral library searching are summarized in panels a-c of Fig. 3. It is clear that the distribution of these measures differ notably between the sets of replicate and non-replicate spectra. That is to say, the cosine similarity derived measures are performing as desired. There is, however, still overlap between computed measures

[2]The term "replicate spectra" is used here to indicate spectra of one compound sourced from two different commercial libraries, differing from the usual convention of a repeated measurement by a single individual/source.

[3]The term "non-replicate spectra" is used here to indicate a pair of spectra from two different compounds, each spectrum from a different library.

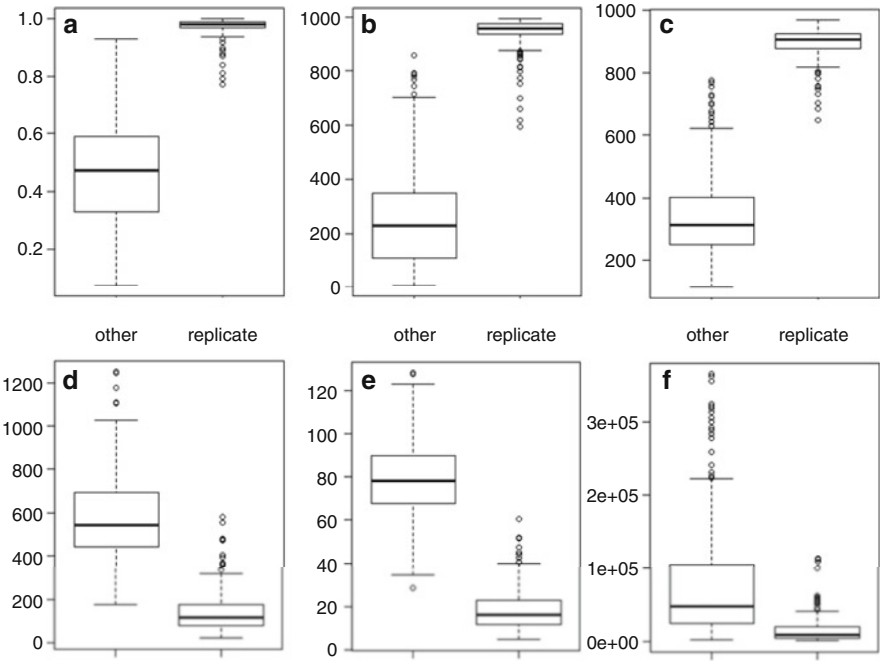

Fig. 3 Distribution of similarity and distance measures when considering spectra of the same molecules (replicate) and of different molecules (other). Note that the scale of the ordinate axis varies for each similarity measure. (**a**) Similarity as approximated by a cosine similarity. (**b**) Similarity as approximated by a simple match factor. (**c**) Similarity as approximated by an identity match factor. (**d**) Distance as approximated by an ℓ_1 norm. (**e**) Distance as approximated by the ℓ_2 norm. (**f**) Distance as approximated by the earth mover's distance

between the two sets. The maximum similarity measure computed between a pair of non-replicate spectra is greater than the minimum similarity measure computed between a pair of replicate spectra. We do see that the modifications from cosine similarity (Fig. 3a) to simple match factor (Fig. 3b), and then identity match factor (Fig. 3c) do improve the separation between similarity scores computed on replicate and non-replicate spectra, with only outlier measures overlapping using identity match factors.

The results of measuring similarity by the ℓ_1 and ℓ_2 distance are shown in Fig. 3d–e. In general, both distance measures do perform as desired, with replicate spectra having smaller computed distances than non-replicate spectra. The separation, however, is not as pronounced as was the case in the cosine similarity derived measures. Using earth mover's distance to measure similarity (Fig. 3f), replicate spectra have smaller computed distances than non-replicate spectra across the total distribution of similarity measures. However, a substantial number of non-replicate spectra are similar according to this metric.

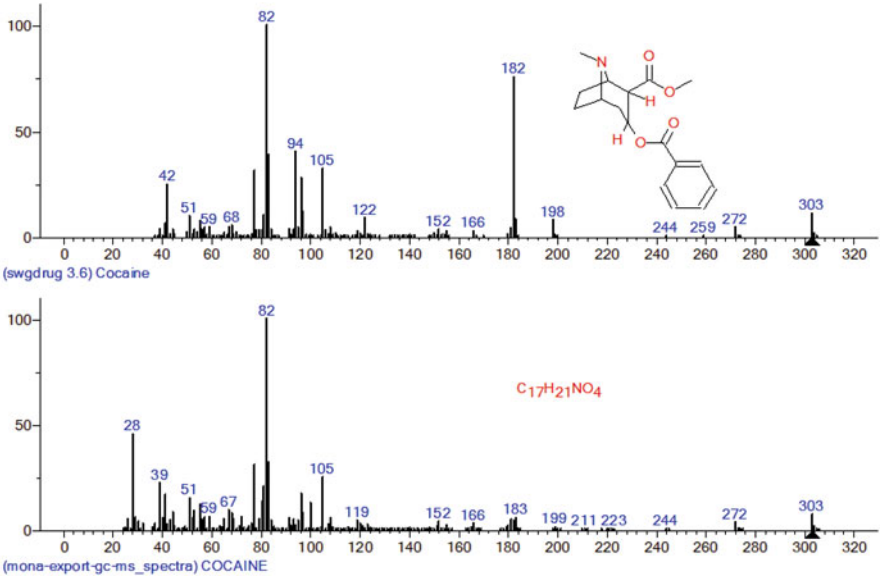

Fig. 4 Representative electron ionization mass spectra of cocaine from (top) the Scientific Working Group for the Analysis of Seized Drugs (SWGDRUG) mass spectral library [19] with structure overlaid and (bottom) the Mass Bank of North America [13] with chemical formula overlaid

In general, the superior efficacy of the identity match factor as compared to the distance measures is due to the nature of variability in mass spectra and the modifications built-in to the identity match factor. Consider the replicate spectra of *cocaine*, taken from two publicly available mass spectral libraries, presented in Fig. 4. Both spectra are valid measurements of cocaine, yet vary substantially in the relative abundance of certain fragment ions (see m/z 182). The processes of taking the square root of relative abundances as in simple match factors (2) and accounting for the ratio of relative abundances for adjacent peaks are able to mitigate some of the natural variability observed in mass spectra. The use of similar modifications to improve the separation of similarity measures between replicate and non-replicate spectra using the ℓ_p and earth mover's distances is on-going work.

It is also worth discussing the limitations of the numerical assessments described in this manuscript. The random selection of non-replicate mass spectra for assessment limits the interpretation of the results. Some of the non-replicate mass spectra may have come from vastly different molecules, and others may have come from molecules of very similar nature, such as positional isomers or chemical analogs. Creating subsets of mass spectra for testing, based on either properties of chemicals (e.g. molecule size, molecule type, etc.) or the mass spectra themselves (e.g. small numbers of peaks, large numbers of peaks, etc.), may illuminate insights about what similarity means in different situations. For example, we may find that similarity of

mass spectra with few peaks is better captured by one similarity measure than the others.

Implications for Mass Spectral Library Searching

A mass spectral library search algorithm sifts through a reference library of mass spectra and produces a list, commonly referred to as a "hits list" or "hitlist", of mass spectra that are presumably similar to a query spectrum. From this hitlist, a chemist will either propose an identity for the analyte or will conclude that further investigation is needed. A thorough numerical evaluation of how each described dissimilarity measure would affect mass spectral library searching requires defining several specific and involved identification tasks. This and the subsequent selection of search parameters is outside the scope of this manuscript. General evaluations of similarity measures in library searches where the objective is to return a hitlist where the top entry is the correct identification of the analyte can be found in the literature [9–11, 21].

In general, for the purpose of sifting through the library, any of the similarity measures outlined in Sect. 3 can be used and one of the top few library mass spectra appraised to be most similar to the queried spectrum will be measurements of the same compound. One concern with using any similarity measure, especially the Earth Mover's distance, is that some of the reference spectra that appear in the hitlist may not be measurements of the same compound producing the query spectrum, thus challenging the identification of the analyte. However, it is possible that a hitlist containing non-replicate spectra can also aid the identification process. In 2017, a measure of spectral similarity referred to as "Hybrid Similarity" was introduced [4, 6, 14], as a means of searching through libraries when it was suspected that a reference spectrum of the analyte was not contained in the library (e.g. a novel designer drug with no representative mass spectrum contained in the library). This measure is able to capture the similarity between mass spectra of molecules that differ by a single modification, that does not significantly alter the fragmentation mechanism of common fragment ions, resulting in spectra differing by predictable shifts in ion m/z values—these types of molecules are now referred to as *cognates*. A hitlist containing several cognates of the query can provide a chemist adequate information to propose additional investigations or, potentially, even propose a possible identity of the compound generating the query spectrum. There have been several recent publications describing applications of hybrid similarity [1–3, 5, 8, 17].

The popularity of hybrid similarity in mass spectral library searching is evidence supporting the continued exploration of novel similarity measures for mass spectra. Though it is not immediately clear whether the similarity measures outlined in this manuscript will be beneficial, it is possible that one or more of these measures will be useful in identifying particular types of molecules or in very specific situations (e.g. identifying a molecule based on a spectrum with poor signal-to-noise as is often the case when samples are collected in less-than-ideal circumstances). Further investigation of these similarity measures with specific test cases is an on-going course of work.

Towards Uncertainty Quantification

The last section of this manuscript is a discussion of leveraging similarity measures for quantifying uncertainty with compound identifications using mass spectrometry. As was noted in Sect. 1, the accurate identification of pure compounds, that may be contained within complex materials, is of incredible industrial importance. At present, using only the numerical value of any mass spectral similarity measure to identify a molecule from its spectrum should be avoided—there is adequate overlap in similarity measures that incorrect identifications are possible. It is worth noting that using mass spectrometry alone for identifying compounds is generally not recommended. Rather, using a series of complimentary measurements is prudent, such as gas chromatography retention times [23] to simultaneously identify compounds.

As noted previously, conducting strict systematic investigations with subsets of mass spectra may provide useful insights about the types of mass spectra that generate high similarity measures. For example, if we find that good similarity scores using the ℓ_2 distance only occur between molecules that are isomers, this suggests the uncertainty of an identification using only an ℓ_2 measure of similarity will be a function of the number of possible isomers of the proposed molecular identity. Another approach that may support uncertainty quantification is the simultaneous analysis of multiple similarity measures. If two spectra are completely identical, then all computed similarity measures should return their optimal value. If two mass spectra are deemed similar using the ℓ_2 distance, but the two spectra appear significantly dissimilar when measured by cosine similarity, this casts significant doubt upon the identification of the compound that generated the mass spectra. Developing composite measures or schemes for evaluating mass spectra may be fruitful endeavors that greatly reduce uncertainty and enhance the efficacy of mass spectrometry based compound identification procedures.

Acknowledgments The first author would like to thank Prof. Peregrina Quintella Estevez (Universidade de Santiago de Compostella) for coordinating Industry Day at the International Congress of Industrial and Applied Mathematics 2019 meeting. The meeting has generated meaningful relationships and discussion that will greatly benefit future work in this field. The authors also acknowledge Christopher Schanzle (National Institute of Standards and Technology) for an implementation of the earth mover's distance, and Dr. Gary Mallard (National Institute of Standards and Technology) for his guidance in preparing this manuscript.

References

1. Barupal, D.K., Fan, S., Fiehn, O.: Integrating bioinformatics approaches for a comprehensive interpretation of metabolomics datasets. Curr. Opin. Biotechnol. **54**, 1–9 (2018)
2. Blaženović, I., Kind, T., Ji, J., Fiehn, O.: Software tools and approaches for compound identification of LC-MS/MS data in metabolomics. Metabolites **8**(2), 31 (2018)
3. Blaženović, I., Oh, Y.T., Li, F., Ji, J., Nguyen, A.K., Wancewicz, B., Bender, J.M., Fiehn, O., Youn, J.H.: Effects of gut bacteria depletion and high-Na+ and low-K+ intake on circulating levels of biogenic amines. Mol. Nutr. Food Res. **63**(4), 1801184 (2019)

4. Burke, M.C., Mirokhin, Y.A., Tchekhovskoi, D.V., Markey, S.P., Heidbrink Thompson, J., Larkin, C., Stein, S.E.: The hybrid search: a mass spectral library search method for discovery of modifications in proteomics. J. Proteome Res. **16**(5), 1924–1935 (2017)
5. Burke, M.C., Zhang, Z., Mirokhin, Y.A., Tchekovskoi, D.V., Liang, Y., Stein, S.E.: False discovery rate estimation for hybrid mass spectral library search identifications in bottom-up proteomics. J. Proteome Res. **18**(9), 3223–3234 (2019)
6. Cooper, B., Yan, X., Simón-Manso, Y., Tchekhovskoi, D., Mirokhin, Y., Stein, S.: Hybrid search: a method for identifying metabolites absent from tandem mass spectrometry libraries. Anal. Chem. **91**(21), 13924–13932 (2019)
7. Griffiths, J.: A brief history of mass spectrometry. Anal. Chem. **80**(15), 5678–5683 (2008)
8. Jang, I., Lee, J.u., Lee, J.m., Kim, B.H., Moon, B., Hong, J., Oh, H.B.: LC–MS/MS software for screening unknown erectile dysfunction drugs and analogs: artificial neural network classification, peak-count scoring, simple similarity search, and hybrid similarity search algorithms. Anal. Chem. **91**(14), 9119–9128 (2019)
9. Kim, S., Zhang, X.: Comparative analysis of mass spectral similarity measures on peak alignment for comprehensive two-dimensional gas chromatography mass spectrometry. Computat. Math. Methods Med. **2013** (2013). Article ID 509761
10. Kim, S., Koo, I., Wei, X., Zhang, X.: A method of finding optimal weight factors for compound identification in gas chromatography–mass spectrometry. Bioinformatics **28**(8), 1158–1163 (2012)
11. Koo, I., Kim, S., Zhang, X.: Comparative analysis of mass spectral matching-based compound identification in gas chromatography–mass spectrometry. J. Chromatogr. A **1298**, 132–138 (2013)
12. Li, W., Ryu, E.K., Osher, S., Yin, W., Gangbo, W.: A parallel method for earth mover's distance. J. Sci. Comput. **75**(1), 182–197 (2018)
13. Mass Bank of North America (MoNA). https://mona.fiehnlab.ucdavis.edu/. Accessed 26 Nov 2019
14. Moorthy, A.S., Wallace, W.E., Kearsley, A.J., Tchekhovskoi, D.V., Stein, S.E.: Combining fragment-ion and neutral-loss matching during mass spectral library searching: a new general purpose algorithm applicable to illicit drug identification. Anal. Chem. **89**(24), 13261–13268 (2017)
15. NIST 2017 Mass Spectral Library (demo). https://chemdata.nist.gov. Accessed 26 Nov 2019
16. R Core Team: R: a Language and Environment for Statistical Computing. R Foundation for Statistical Computing, Vienna, Austria (2019). https://www.R-project.org/
17. Remoroza, C.A., Mak, T.D., De Leoz, M.L.A., Mirokhin, Y.A., Stein, S.E.: Creating a mass spectral reference library for oligosaccharides in human milk. Anal. Chem. **90**(15), 8977–8988 (2018)
18. Rubner, Y., Tomasi, C., Guibas, L.J.: The earth mover's distance as a metric for image retrieval. Int. J. Comput. Vis. **40**(2), 99–121 (2000)
19. Scientific Working Group for the Analysis of Seized Drugs (SWGDRUG) Mass Spectral Library v.3.6. https://swgdrug.org. Accessed 26 Nov 2019
20. Shirdhonkar, S., Jacobs, D.W.: Approximate earth mover's distance in linear time. In: 2008 IEEE Conference on Computer Vision and Pattern Recognition, pp. 1–8. IEEE, New York (2008)
21. Stein, S.E., Scott, D.R.: Optimization and testing of mass spectral library search algorithms for compound identification. J. Am. Soc. Mass Spectrom. **5**(9), 859–866 (1994)
22. Watson, J.T., Sparkman, O.D.: Introduction to Mass Spectrometry: Instrumentation, Applications, and Strategies for Data Interpretation. Wiley, Chichester (2007)
23. Wei, X., Koo, I., Kim, S., Zhang, X.: Compound identification in GC-MS by simultaneously evaluating the mass spectrum and retention index. Analyst **139**(10), 2507–2514 (2014)

Numerical Study of In-Situ Acoustic Impedance and Reflection Coefficient Estimation of Locally Reacting Surfaces with Pressure-Velocity Probes

G. Carrillo, D. Fernández, D. Cabo, and A. Prieto

Abstract The characterization of the acoustic sound pressure and velocity field on the surface of absorbing materials plays a key role for the computation of their surface impedance and absorption coefficients. In this work, a technique based on the equivalent source method (ESM) is used to estimate the pressure and velocity field in order to compute the surface impedance and reflection coefficient of a locally reacting surface. The assessed in-situ technique only requires measuring on a single layer with an array of pressure-velocity (p-u) probes. A numerical simulation study is performed to compare the estimated values with those obtained using a double layer of pressure sensors. Results show a significant improvement in the lower frequency range in terms of both reconstruction accuracy and robustness against noise.

1 Introduction

The in-situ characterization of acoustic impedance and reflection coefficient of materials is of considerable interest for a wide range of applications. There has been an increasing amount of literature on novel in-situ methods which can be categorized in two major groups. On the one hand, several methods rely upon assumptions about the excitation sound source and the reflected sound field [1–3], such as planar, mirror model with planar reflection or spherical wave model. Such techniques often suffer from limitations when the assumptions are not satisfied in a real environment. On the other hand, sound field reconstruction techniques can also be applied without prior information about the sound field. One of the most commons methods was introduced by Tamura [4] based on the spatial Fourier

G. Carrillo (✉) · D. Fernández · D. Cabo
Microflown Technologies, Arnhem, Netherlands
e-mail: carrillo@microflown.com

A. Prieto
CITIC, Department of Mathematics, Universidade da Coruña, Coruña, Spain
e-mail: andres.prieto@udc.es

M. Cruz et al. (eds.), *Progress in Industrial Mathematics: Success Stories*,
SEMA SIMAI Springer Series 5, https://doi.org/10.1007/978-3-030-61844-5_5

Transform of sound pressure measurements at two parallel planes. With a similar configuration, an in-situ technique based on the Equivalent Source Method (ESM) was presented by Zhang et al. [5]. The ESM method has significant advantages over Tamura technique, such as a smaller measurement aperture and more accurate results. In contrast, it is currently limited to locally reactive materials because the ESM-based method is not able to account for the changes of the reflection coefficient with the angle of incidence [5]. In addition, a novel technique has recently been proposed for oblique incidence based on statistically optimized near-field acoustic holography (SONAH) also using several layers of sound pressure microphones [6].

Along with the introduction of particle velocity transducers for sound field characterization, reconstruction techniques have also been developed using a single-layer of *p-u* probes [7, 8]. Although ESM-based methods have already been used in combination with sound pressure microphones and particle velocity sensors, a comparison of the performance achieved when determining surface impedance and reflection coefficient has not yet been undertaken.

In this chapter, ESM-based methods are studied for the determination of the surface impedance and the reflection coefficient of locally reactive surfaces. Results obtained with a single layer of sound pressure microphones and particle velocity sensors (*p-u*) are compared with a double layer configuration of sound pressure microphones. In the following sections the theory of the ESM-based methods is described for both single layer and two layers case. A numerical study is presented, including results and a discussion about the performance of both methods.

2 Measurement Technique Based on Equivalent Source Method

ESM relies on modeling the sound field as the superposition of waves generated by a set of point sources. This key concept allows for splitting the contributions of different sources and it can be used for separating the incoming and reflected sound field. Accordingly, the idea is also suitable for the characterization of the surface impedance and the reflection coefficient of multiple materials.

The evaluated techniques use sound pressure or/and particle-velocity measured in one or two planes in the near-field of the tested sample, while the sound field is excited by a sound source at normal incidence. Inverse methods are applied to estimate the strength of the sound source and its image source, in such a way that the sound field on the surface can be recovered. As a result, the surface impedance and reflection coefficient can then be computed. In the following sections a general formulation of ESM for single layer of pressure-velocity probes and a double layer of pressure microphones is described. A sketch of both approaches is shown in Fig. 1.

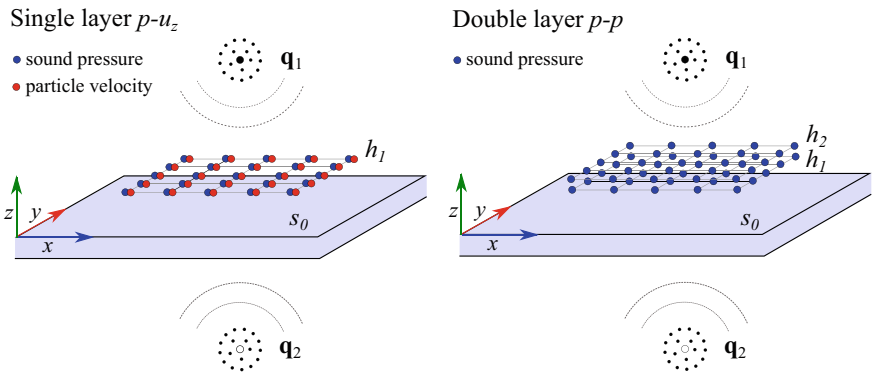

Fig. 1 Sketch of the Equivalent Source Method configuration for single layer p-u (*left*) and double layer p-p (*right*)

2.1 Theory

In the following sections the theory for the ESM is presented for both measurement configurations.

2.2 Single Layer Pressure-Velocity (p-u)

2.2.1 Forward Problem

Sound pressure and particle velocity can be expressed as the result of the superposition of the sound field created by multiple point sources. Considering the special case of having a sound source over a certain surface, the resulting sound field at the plane $z = h_1$ can be modeled as the combination of a set of equivalent sound sources $\mathbf{q}_1$ and its mirror set of image sources $\mathbf{q}_2$ as shown in Fig. 1. Hence,

$$\begin{bmatrix} \mathbf{p}_{h_1} \\ \mathbf{u}_{h_1} \end{bmatrix} = \begin{bmatrix} j\omega\rho\mathbf{G}_{q_1h_1} & j\omega\rho\mathbf{G}_{q_2h_1} \\ -\mathbf{G}^{u}_{q_1h_1} & -\mathbf{G}^{u}_{q_2h_1} \end{bmatrix} \begin{bmatrix} \mathbf{q}_1 \\ \mathbf{q}_2 \end{bmatrix}, \tag{1}$$

where the column vectors $\mathbf{p}_{h1}$ and $\mathbf{u}_{h1}$ are the pressure and the z-component of particle velocity located at the plane $z = h_1$, the vectors $\mathbf{q}_1$ and $\mathbf{q}_2$ are the equivalent source strengths that model the sound source and its image source, $\mathbf{G}_{q_ih_j}$ and $\mathbf{G}^{u}_{q_ih_j}$ are transfer functions that relates the propagation from the sources $\mathbf{q}_i$ to the plane $z = h_j$, ω is the angular frequency and ρ is the air density. These transfer functions are defined as the Green's function in free-space and its derivative in the normal

direction (to the measurement plane $z = h_1$), thus

$$\mathbf{G}(\mathbf{r}, \mathbf{r_0}) = \frac{e^{-jk|\mathbf{r}-\mathbf{r_0}|}}{4\pi\,|\mathbf{r}-\mathbf{r_0}|}\,, \tag{2}$$

$$\mathbf{G}^{u}(\mathbf{r}, \mathbf{r_0}) = \frac{\partial}{\partial z}\mathbf{G}(\mathbf{r}, \mathbf{r_0})\,, \tag{3}$$

where k is the wavenumber, $\mathbf{r}_0$ denotes the source position and $\mathbf{r}$ is the location where the sound field is computed.

2.2.2 Inverse Problem

Once the forward problem is formulated in closed form, the next step is to estimate the strength of the equivalent sources, i.e. vectors $\mathbf{q}_1$ and $\mathbf{q}_2$. Thus, an inverse problem must be solved on Eq. (1) using a weighted least squares solution as proposed in [9, 10],

$$\mathbf{q} = (\mathbf{WG})^{\dagger}\mathbf{Wb}\,, \tag{4}$$

$$\mathbf{W} = \begin{pmatrix} ||\mathbf{p}_h|| & 0 \\ 0 & ||\mathbf{u}_h|| \end{pmatrix}^{-1}\,, \tag{5}$$

where $\mathbf{q}$ is composed by the vectors of sources $\mathbf{q}_1$ and $\mathbf{q}_2$ in Eq. (1), $\mathbf{G}$ is the transfer matrix, $\mathbf{b}$ is a vector that contains the measured sound pressure $\mathbf{p}_h$ and particle velocity $\mathbf{u}_h$, and $\mathbf{W}$ is a weighting diagonal matrix. The superscript † refers to the Tikhonov regularized pseudo-inverse:

$$(\mathbf{WG})^{\dagger} = (\left[\mathbf{WG}^{H}\right]\mathbf{WG} + \lambda\mathbf{I})^{-1}\left[\mathbf{WG}^{H}\right], \tag{6}$$

where $\boldsymbol{\lambda}$ is the regularization parameter and $\mathbf{G}^{H}$ is the Hermitian transpose of matrix. The need of a weighting matrix $\mathbf{W}$ arises from the differences in magnitude between the sound pressure and the particle velocity by a factor which is approximately the characteristic acoustic impedance value. The application of a weighting factor avoids the residual of the minimization process to be dominated by the pressure misfit error.

2.2.3 Surface Impedance Reconstruction

The sound pressure and the particle velocity on the material surface $z = s_0$ can now be reconstructed from the estimated equivalent sources $\mathbf{q}_1$ and $\mathbf{q}_2$ and applying the

propagation Green's functions Eqs. (2) and (3). In this manner, the surface pressure and the z-component of the particle velocity are given by

$$\mathbf{p}_{s_0} = j\omega\rho(\mathbf{G}_{q_1 s_0}\mathbf{q}_1 + \mathbf{G}_{q_2 s_0}\mathbf{q}_2)\,, \tag{7}$$

$$\mathbf{u}_{s_0} = -(\mathbf{G}^u_{q_1 s_0}\mathbf{q}_1 + \mathbf{G}^u_{q_2 s_0}\mathbf{q}_2)\,. \tag{8}$$

It is possible to compute the surface impedance Z_{s_0} and reflection coefficient $R_{s_0}(\theta)$ by using the estimation of the pressure and velocity fields at N points on the surface $z = s_0$, given in Eqs. (7) and (8). Consequently, given the point values of pressure and velocity fields, $\mathbf{p}^{(n)}_{s_0}$ and $\mathbf{u}^{(n)}_{s_0}$, averaged estimates can be obtained by applying the following relationships:

$$Z_{s_0} = \frac{1}{N}\sum_{n=1}^{N}\frac{p^{(n)}_{s_0}}{u^{(n)}_{s_0}}\,, \tag{9}$$

$$R_{s_0}(\theta) = \frac{Z_{s_0}\cos\theta - Z_0}{Z_{s_0}\cos\theta + Z_0}\,, \tag{10}$$

where Z_0 is the characteristic acoustic impedance (ρc). Note that the expression of the reflection coefficient for different angles Eq. (10) is valid under the assumption of locally reactive surfaces, which holds for the present work.

2.3 Double Layer Pressure-Pressure (p-p)

As shown in [5, 11], the equivalent sources method can also be applied for sound pressure only measurements, by the use of two measurement planes $z = h_1$ and $z = h_2$,

$$\begin{bmatrix}\mathbf{p}_{h_1}\\ \mathbf{p}_{h_2}\end{bmatrix} = j\omega\rho\begin{bmatrix}\mathbf{G}_{q_1 h_1} & \mathbf{G}_{q_2 h_1}\\ \mathbf{G}_{q_1 h_2} & \mathbf{G}_{q_2 h_2}\end{bmatrix}\begin{bmatrix}\mathbf{q}_1\\ \mathbf{q}_2\end{bmatrix}\,, \tag{11}$$

where the vectors $\mathbf{p}_{h1}$ and $\mathbf{p}_{h2}$ correspond to measurements of the sound pressure on the planes $z = h_1$ and $z = h_2$; the transfer functions $\mathbf{G}_{q_i h_j}$ are given by Eq. (2) which models the sound propagation from the sources $\mathbf{q}_i$ to the plane h_j.

To solve the inversion problem, a regularized inversion approach analogous to the one presented in Sect. 2.2 is used. In this case there is no need to apply any weighting procedure. Based on the estimated equivalent source strength vectors $\mathbf{q}_1$ and $\mathbf{q}_2$, the sound pressure and the particle velocity on the surface $z = s_0$ are obtained by using Eqs. (7) and (8). The surface impedance and the reflection coefficient can then be estimated by employing Eqs. (9) and (10).

3 Numerical Study

A numerical investigation has been conducted to study the performance of the ESM-based methods described in the previous sections. Firstly, a model for the sound propagation over an impedance half-space is chosen. Next, the impedance model of a porous material is characterized. At the end, the simulation setup and the performance metric is described.

3.1 Sound Field over an Impedance Half-Space

The sound field produced by a sound source over a locally reactive surface was represented following the model proposed by Di and Gilbert [12]. The sound pressure above an infinite half-space with a given impedance is derived assuming a locally reactive surface. Thus, the sound pressure and particle velocity generated by a time-harmonic sound source of volume velocity Q at a position $\mathbf{r}$ are defined as

$$p(\mathbf{r}) = \frac{j\omega\rho Q}{4\pi}\left(\frac{e^{-jk|\mathbf{r}-\mathbf{r}_1|}}{|\mathbf{r}-\mathbf{r}_1|} + \frac{e^{-jk|\mathbf{r}-\mathbf{r}_2|}}{|\mathbf{r}-\mathbf{r}_2|} - 2k_0\beta\int_0^\infty e^{k\beta q}\frac{e^{-jk\sqrt{d_1^2+(r_{1z}+r_z-jq)^2}}}{\sqrt{d_1^2+(r_{1z}+r_z-jq)^2}}dq\right), \tag{12a}$$

$$u_z(\mathbf{r}) = \frac{-1}{j\omega\rho}\frac{\partial}{\partial z}p(\mathbf{r}), \tag{12b}$$

where $\mathbf{r}_1$ and $\mathbf{r}_2$ are the locations of the sound source and its image source, r_z and r_{1z} are the heights of the measurement point and the sound source with respect to the material surface, d_1 is the horizontal distance between the sound source and $\mathbf{r}$, and $\beta = Z_0/Z_{s_0}$ is the normalized surface acoustic admittance at normal incidence.

3.2 Locally Reacting Surface and Porous Impedance Model

The absorbing surface material under test is supposed to be locally reacting. Thus, the input impedance related to the acoustic behavior of a porous layer is assumed independent of the angle of incidence of the sound waves. Under this assumption, the ESM method could be applied and the reflection coefficient could also be computed for several angles of incidence. Without loss of generality, the model for the porous material is assumed to be of the type Delany and Bazley [13]. The surface impedance with a given flow resistivity σ (N m s^{-4}) at a frequency f is given by

$$Z_s(f) = Z_0\left[1 + 9.08(10^3 f/\sigma)^{-0.75} - j11.9(10^3 f/\sigma)^{-0.73}\right]. \tag{13}$$

3.3 Simulation Setup and Error Estimation

A sound source was placed 0.1 m above the material while a uniform line array was located at certain distance above the surface along the x-axis. For the single layer p-u configuration the array was located at $z = 0.01$ m, while the double layer p-p sensor array was at $z = 0.01$ m] and $z = 0.03$ m. The sound field was measured at 21 equally spaced points in the interval $[-0.1, 0.1]$ at the x-axis. Despite the axial symmetry of the problem, sensors were placed at both sides of the x-axis in order to account for uncorrelated noise between transducers. The equivalent sources were located in two circles with a radius of 0.01 m around the sound source and its image source, consisting of 12 elements at each location. A sketch of the problem addressed is illustrated in Fig. 2.

The noise added to the simulated data was assumed white isotropic Gaussian noise of equal variance for all transducers with a fixed signal-to-noise ratio (SNR) of 30 dB. The SNR is defined as the signal power to noise ratio: $10 \log_{10}(P_{signal}/P_{noise})$. All results presented were obtained using a Monte Carlo simulation over 100 runs.

Results are assessed by evaluating the reconstruction error with respect to the reference values. The relative error $E\{\gamma_{\text{ref}}\}$ of an arbitrary estimation γ_{est} is calculated with respect to the reference γ_{ref} as follows,

$$E\{\gamma_{\text{ref}}\} = 20 \log_{10} \left(\frac{\|\gamma_{\text{est}} - \gamma_{\text{ref}}\|_2}{\|\gamma_{\text{ref}}\|_2} \right) \tag{14}$$

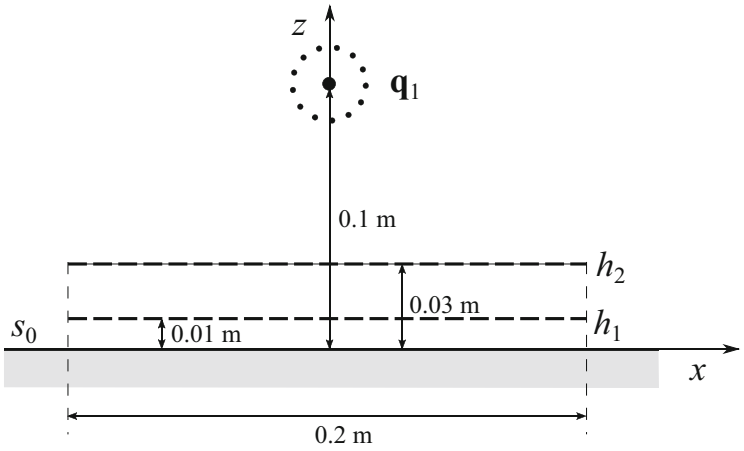

Fig. 2 Sketch of the numerical simulation configuration

4 Results and Discussion

In the following sections a numerical investigation has been performed with two main objectives:

1. To study the performance of ESM-based methods with two different configurations: single layer *p-u* and double layer *p-p* methods.
2. To assess the impact of different SNR conditions on the reconstruction error across frequency.

4.1 Surface Impedance and Reflection Coefficient

Results of normalized surface impedance estimations are shown in Fig. 3. The reconstruction error indicates that the double layer *p-p* configuration achieves a good

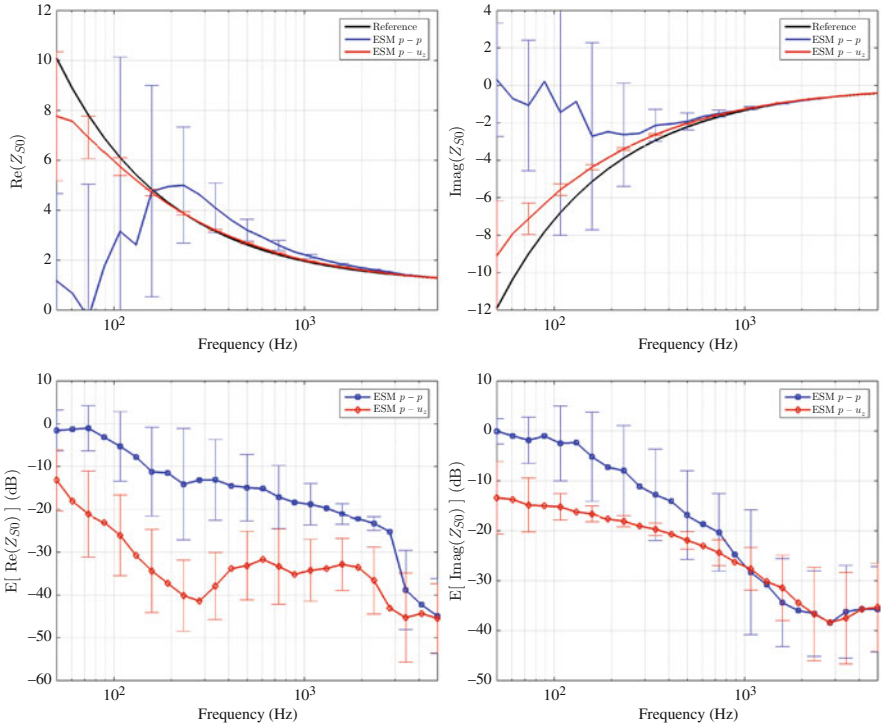

Fig. 3 Normalized complex surface impedance: real part (*top left*), imaginary part (*top right*), relative error of real part estimation (*bottom left*) and relative error of the imaginary part estimation (*bottom right*). A confident interval of 95% is displayed with the same colors as the corresponding method

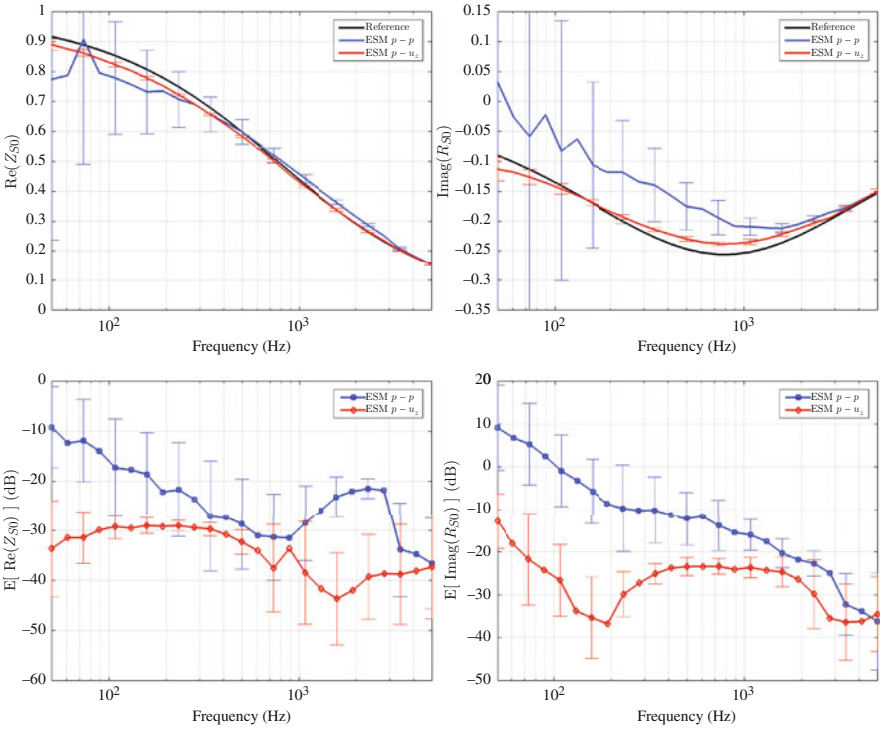

Fig. 4 Normalized complex reflection coefficient: real part (*top left*), imaginary part (*top right*), relative error of real part estimation (*bottom left*) and relative error of the imaginary part estimation (*bottom right*). A confident interval of 95% is displayed with the same colors as the corresponding method

performance for frequencies above 800–1000 Hz, where the relative reconstruction error is below −20 dB (i.e. 10% error). In contrast, the *p-u* single layer shows a good performance also for lower frequencies, even at 300 Hz.

Results obtained for the reflection coefficient R_{s_0} are presented in Fig. 4. As shown, the *p-p* double layer configuration has significant performance differences in the reconstruction of the real and the imaginary part. The reconstruction error of the imaginary part is acceptable above 1500 Hz, while the real part is valid from 200 Hz. On the other hand, the single layer *p-u* array yields accurate results from 50 Hz for both real and imaginary part of the reflection coefficient.

Interestingly, reconstruction results of the reflection coefficient using the *p-u* configuration are more consistent and less sensitive to noise than the ones obtained for the surface impedance. Furthermore, results achieved with the *p-p* configuration have a greater variance across the Monte Carlo runs. In conclusion, the reconstruction error and the variance of the results suggest that the single layer *p-u* configuration is generally more robust and accurate than the double layer *p-p* array, especially in the low frequency range.

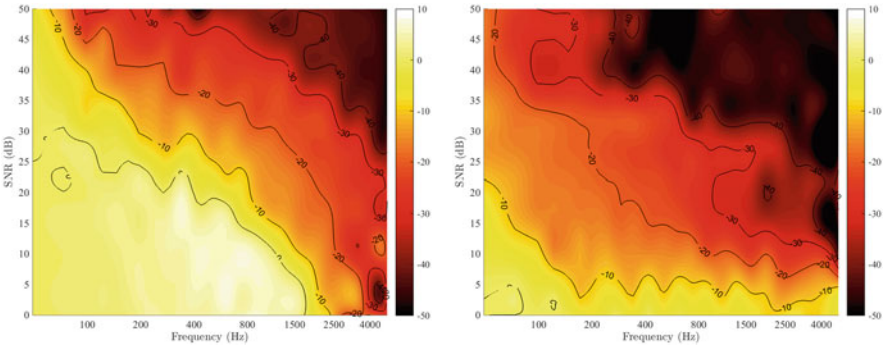

Fig. 5 Reconstruction error of the surface impedance for variable SNR and frequencies with two different sensor configurations: single layer p-u (*left*) and double layer p-p (*right*)

4.2 Surface Impedance Reconstruction Error for Variable SNR

The SNR plays a key role in the performance and robustness of ESM methods. Previous results suggest that both tested configurations are affected by noise in a different manner. In order to gain a better understanding about the influence of noise on the reconstructions, an additional Monte Carlo simulation has been undertaken. Relative reconstruction errors obtained with both configurations are presented in Fig. 5 for different levels of SNR, where brighter colors to indicate large errors.

As shown in Fig. 5, the *p-u* method significantly outperforms the *p-p* configuration, especially in the low frequency range (<1000 Hz).

4.3 Discussion and Future Research

The *p-u* method seems to outperform the alternate *p-p* method for large wavelengths (low frequency). A possible explanation for this effect could be the differences capturing the information on both methods that grant incident and mirror sound field reconstruction. As *p-p* method relies on the differences between two measurements planes, at large wavelengths, the interference patterns and the noise dominate over the differences in the sound field. The ability to acquire the two quantities at the same plane seems to be key for avoiding large estimation errors when the wavelength is large.

Nevertheless both methods seem to present a bias at very low frequency. To certain extent, it looks like that the location of the equivalent sources present difficulties to represent the scattered sound field. A future extension of this work could include the addition of equivalent sources along the impedance half-space to better capture the scattered sound field.

In addition, future research should examine the use of more elaborated impedance porous models and determine until which extend the locally reaction assumption is hold.

5 Conclusion

The acoustic properties of a locally reactive surface have been calculated using both a single-layer of *p-u* probes and a double layer of sound pressure microphones in combination with ESM. A numerical comparison of these configurations has been conducted assessing the impact of SNR on the results at different frequencies. It has been shown that both configurations yield good results (reconstruction error lower than 10%) at high frequencies, above 800 Hz for the surface impedance and 1500 Hz for the reflection coefficient. However, single layer *p-u* has a significantly better performance in the low frequency range, for wavelengths that are much larger than the distance to the surface or spacing between layers of the *p-p* configuration. In addition, the single layer *p-u* is also most robust against noise, achieving accurate results with relatively low levels of SNR.

References

1. Brandão, E., Lenzi, A., Paul, S.: Acta Acustica United Acustica **101**(3), 443 (2015)
2. Alvarez, B., Jacobsen, F.: INTER-NOISE and NOISE-CON Congress and Conference Proceedings, vol. 5, pp. 4055–4065. Institute of Noise Control Engineering (2008)
3. Nocke, C., Mellert, V., Waters-Fuller, T. Attenborough, K., Li, K.: Acta Acustica United Acustica **83**(6), 1085 (1997)
4. Tamura, M.: J. Acoust. Soc. Am. **88**(5), 2259 (1990)
5. Zhang, Y.B., Lin, W.L., Bi, C.X.: INTER-NOISE and NOISE-CON Congress and Conference Proceedings, vol. 249, pp. 3220–3227. Institute of Noise Control Engineering (2014)
6. Ottink, M., Brunskog, J., Jeong, C.H., Fernandez-Grande, E., Trojgaard, P., Tiana-Roig, E.: J. Acoust. Soc. Am. **139**(1), 41 (2016)
7. Jacobsen, F., Jaud, V.: J. Acoust. Soc. Am. **121**(3), 1550 (2007)
8. Fernandez Grande, E.: Near-field acoustic holography with sound pressure and particle velocity measurements. Ph.D. thesis, Acoustic Technology, Technical University of Denmark, Kgs. Lyngby (2012)
9. Hansen, P.C.: SIAM Rev. **34**(4), 561 (1992)
10. Fernandez-Grande, E., Jacobsen, F., Leclere, Q.: J. Acoust. Soc. Am. **132**(6), 3818 (2012)
11. Zhang, Y.B., Jacobsen, F., Bi, C.X., Chen, X.Z.: J. Acoust. Soc. Am. **126**(3), 1257 (2009)
12. Di, X., Gilbert, K.E.: J. Acoust. Soc. Am. **93**(2), 714 (1993)
13. Delany, M., Bazley, E.: Appl. Acoust. **3**(2), 105 (1970)

Part II
The Academia Point of View

Multiscale Modelling and Simulation of Advanced Battery Materials

Mauricio R. Bonilla, Fabián A. García Daza, Mario Fernández-Pendás, Javier Carrasco, and Elena Akhmatskaya

Abstract Development of efficient strategies for the rational design of materials involved in the production and storage of renewable energy is essential for accelerating the transition to a low-carbon economy. To contribute to this goal, we propose a novel workflow for the assessment and optimization of battery materials. The approach effectively combines quantum and atomistic modelling/simulations, enhanced by efficient sampling, Bayesian parameterization, and experimental information. It is implemented to study prospective materials for lithium and sodium batteries.

1 Introduction

Nearly 30 years ago Sony Co. launched the first commercial lithium-ion battery (LIB) and changed the world [25]. LIBs powered the revolution in portable

M. R. Bonilla
Basque Center for Applied Mathematics, Bilbao, Spain

F. A. García Daza
Department of Chemical Engineering and Analytical Science, The University of Manchester, Manchester, UK

M. Fernández-Pendás
Basque Center for Applied Mathematics, Bilbao, Spain

Kimika Fakultatea, Euskal Herriko Unibertsitatea (UPV/EHU) and Donostia International Physics Center (DIPC), Donostia, Spain

J. Carrasco
Centre for Cooperative Research on Alternative Energies (CIC energiGUNE), Basque Research and Technology Alliance (BRTA), Alava Technology Park, Vitoria-Gasteiz, Spain

E. Akhmatskaya (✉)
Basque Center for Applied Mathematics, Bilbao, Spain

IKERBASQUE, Basque Foundation for Science, Bilbao, Spain
e-mail: akhmatskaya@bcamath.org

M. Cruz et al. (eds.), *Progress in Industrial Mathematics: Success Stories*,
SEMA SIMAI Springer Series 5, https://doi.org/10.1007/978-3-030-61844-5_6

electronics, allowing the transformation of mobile phones into general purpose computers within a decade. Moreover, governments around the globe have gained awareness of the role greenhouse gases play in climate change, leading to incentives for the development of renewable energy technologies (solar, wind, etc.) and electric vehicles (EVs). For all of these technologies to be effectively implemented, energy storage systems are key enablers. As an example, the European Commission has set the target of achieving emission-free urban passenger transportation by 2050 (i.e. abandoning the use of conventionally fuelled cars in cities) and emission-free urban freight transportation by 2030 [15]. Consequently, research and development on LIBs have exploded (in the span of 7 years, researchers around the globe have added at least 119188 new publications on batteries from 2010 to 2017 [54]). A recognition of the current importance of the field comes from the 2019 Nobel Prize in Chemistry, awarded to John Goodenough, M. Stanley Whittingham and Akira Yoshino for the invention of the rechargeable LIB.

While the bulk of battery research is directed towards LIBs, it is important to consider that lithium is not regarded as an abundant element (the relative abundance of lithium in the Earth's crust is only 20 parts per million). Moreover, lithium resources are greatly concentrated in South America, which means that regional politics can have an outsized effect on its price. The second-smallest alkali metal, sodium, constitutes 1% of the earth's crust and is a strong candidate to substitute lithium in rechargeable batteries [78]. For this reason, sodium-ion batteries (NIBs) are one of the most widely investigated alternatives to LIBs, and commercial units are being produced already for systems with low energy density (e.g. e-bikes, e-scooters) [11]. For most applications, though, LIBs are yet to find a credible contender.

While advances in materials and battery design have been impressive, the fundamental purpose of battery research has remained unchanged over the years: to decrease the weight and volume of the battery, increase its durability (i.e. the number of charge/discharge cycles of the battery) and minimize its cost while maintaining safety. Achieving these objectives requires an interdisciplinary approach involving material scientists, chemists, physicists, and a growing army of applied mathematicians and computer scientists. Indeed, increasing computing power, and improving the algorithms for quantum, atomistic and continuous simulations are making the feedback loop between the chemistry lab and the laptop screen a practical reality. Still, the complex multiscale nature of LIBs and NIBs, involving solid state ionics, interface science, polymer physics and engineering, means that plenty of open problems remain to be satisfactorily tackled.

From a mathematical and computational perspective, the goals stated above often translate into answering the following questions: (i) is it possible to accurately and efficiently estimate the electronic and/or ionic conductivities of the materials involved, based on prior knowledge of their atomistic structure?; (ii) can the chemical composition be optimized to enhance desirable features such as conductivity, cyclability or energy density?; (iii) can the structure and transport properties of the interface between different components be predicted from models of the individual phases?; and (iv) how can all this information be integrated into the macroscopic

model of a realistic battery? Our research program in the recent years has attempted to contribute to answering these questions.

One of the critical challenges involving the atomistic simulation of battery materials is the slow diffusion of charge carriers at room temperature. To tackle this issue, we have developed enhanced sampling methods and multi-stage integration schemes that are suitable for solid-state systems including polarizable atoms, allowing us to simulate the ionic transport in materials for LIBs and NIBs at realistic operating conditions [2, 6, 30, 32, 61]. In order to produce experimentally meaningful results, an accurate model of the interatomic interactions (a *force field*) must be first developed or adapted. For the specific case of polarizable systems, the development of a force field can be quite challenging and the resulting model might not be accurate or lead to instability at certain chemical compositions of interest. We have overcome this shortcomings by introducing composition dependant force fields, adjusted with respect to accurate quantum mechanical simulations and/or experimental data [18, 19, 34]. Also, we provided a simple solution to deal with the additional degrees of freedom posed by the core-shell polarizability model [18].

One promising way to reduce the costs associated with experimental synthesis and characterization of new materials is in-silico material discovery and optimization. Despite considerable progress and the seemingly unstoppable growth of computing power, novel techniques to perform this task that can efficiently incorporate experimental information are still needed [38, 57]. On this front, we have designed Bayesian inference algorithms coupled with multi-stage integrators that will combine incoming data from atomistic simulations and information from experiments to produce the distribution of compositions that is most likely to maximize the expectation of a desired set of macroscopic properties [6, 60].

The article summarizes these contributions and demonstrates some key examples involving state-of-the-art LIB and NIB components. In Sect. 2, we offer a short but necessary summary of the key fundamental aspects of rechargeable batteries. In Sect. 3, we provide a brief introduction to traditional atomistic simulation methods and present our enhanced sampling techniques for molecular simulation and computational statistics [60], along with the in-house advanced adaptive integration schemes for Hamiltonian dynamics [6]. In Sect. 4, we discuss the development of force fields for polarizable and non-polarizable materials. Sect. 5 presents our published applications of the discussed algorithms for modelling of sodium intercalation cathodes for NIBs and solid electrolyte garnets for LIBs [18, 19, 32, 41]. Finally, Sect. 6 provides concluding remarks and some future research directions. Specifically, we discuss the incorporation of the in-house Bayesian parameterization technique Mix & Match Hamiltonian Monte Carlo (MMHMC) [60] into the proposed framework for Bayesian materials screening and comment on the multiscale simulation of composite materials using the novel version of our Generalized Shadow Hamiltonian Monte Carlo (GSHMC) [2] that is specially adapted for sampling of coarse-grained systems (meso-GSHMC) [3].

2 Fundamental Aspects of LIBs and NIBs

We provide a summary of the key fundamental properties of the rechargeable batteries essential for this study.

2.1 Structure and Chemistry of Electrochemical Cells

The basic building blocks of any battery are the electrochemical cells (Fig. 1), in which charge carriers move from the anode (negative electrode) to the cathode (positive electrode) during the discharge. In LIBs, the carrier consists of positively charged lithium ions (Li^+) and the process is reversible: when an external voltage above the cell potential is applied, Li^+ is transferred from the cathode to the anode, charging the cell once again. The cathode and the anode are separated by the electrolyte containing dissociated lithium salts. In most commercial LIBs, electrolytes are comprised of organic liquid salts confined within a porous separator membrane, which avoids direct contact between the electrodes. When a lithium atom leaves the anode during the discharge, an electron is released to the outer circuit and performs electrical work. During the charge, electrons are injected into the anode from the external source, driving the release of Li^+ from the

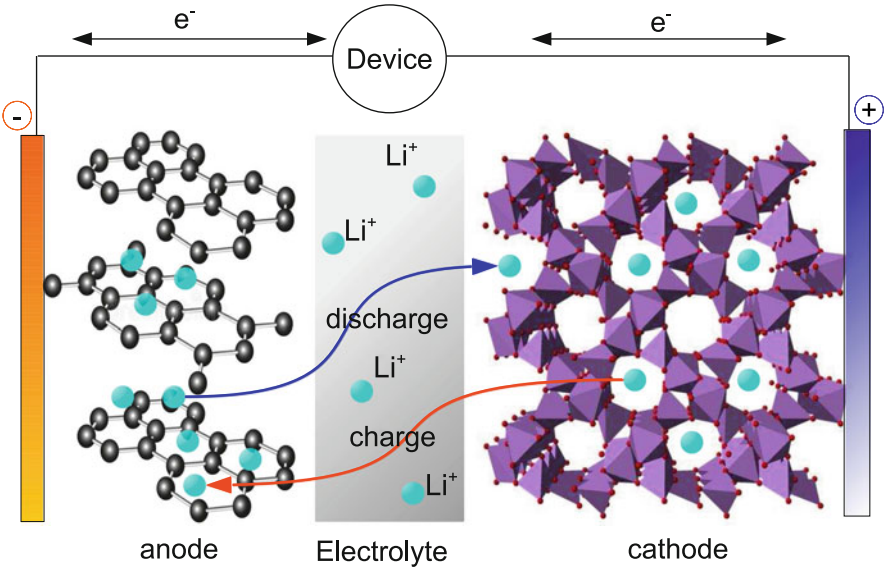

Fig. 1 Simplified structure of the electrochemical cell in a LIB. Each LIB consists of the anode (negative electrode) and the cathode (positive electrode) separated by the electrolyte containing dissociated lithium salts, which enables transfer of lithium ions between the two electrodes

cathode. Hence, it is clear that the electrolyte must be electronically insulating while constituting a good medium for the diffusion of Li^+. In NIBs, the charge carriers are sodium ions (Na^+).

Currently, cathode materials are made of electrochemically active metal oxide particles (such as $XCoO_2$ and $XFePO_4$, with X = Li for LIBs or X = Na for NIBs), an inert binder "gluing" them together and some electronically conductive coating (typically carbon). The key feature of the active particles is their ability to accept and release Li^+ ions (lithiation/delithiation) with minimal changes to their crystal structure, through a process which Whittingham called the *intercalation* mechanism [76]. Anodes are most commonly made of graphite, because the lithiation/delithiation reaction is quite reversible without altering the mechanical and electrical properties of the material. On the first charge of the battery, a *passivation* layer, the so-called *solid electrolyte interphase* (SEI), forms from the decomposition of the electrolyte on the anode surface. This layer is of crucial importance for the battery operation in terms of safety, as it prevents the carbon from reacting with the electrolyte and helps avoiding graphite exfoliation [37, 54].

Important efforts have been made to replace liquid electrolytes with solids, due to the safety problems associated with the flammability of the organic salts that comprise them. Another driver is the impossibility to use metallic lithium (Li^0) as the anode along with liquid electrolytes, because the fast and disorder electrodeposition of Li^+ leads to the formation of Li^0 filaments (dendrites) that can penetrate the separator and connect both electrodes, producing a short-circuit. Since Li^0 anodes have a much higher energy density, their safe and efficient incorporation could greatly reduce battery volume/weight. Several solid and semi-solid electrolytes have been developed in recent years, including crystalline materials, polymers, gels, and composites mixing these three families [80]. Still, none has yet achieved the combination of ionic conductivity, thermal, mechanical and chemical stability and low cost necessary for widespread adoption.

While there are many factors influencing battery performance, we will focus on the one of particular importance: ionic conductivity.

2.2 Ionic Conduction in Battery Materials

The rate of X^+ ion transfer between the electrodes is a multiscale variable depending on (i) the ionic diffusivity within the active electrode particle; (ii) the grain boundary resistance between adjacent electrode particles; (iii) the rate of interfacial exchange between electrode and electrolyte; (iv) the ionic diffusivity within the electrolyte and, for solid electrolytes, the grain boundary resistance between adjacent electrolyte particles; and (iv) the ionic diffusivity within the SEI (Fig. 2). It is still possible to subdivide these resistances further, as electrode particles may be agglomerated through a binder and contain some coating particles to enhance the electronic properties (see Fig. 2).

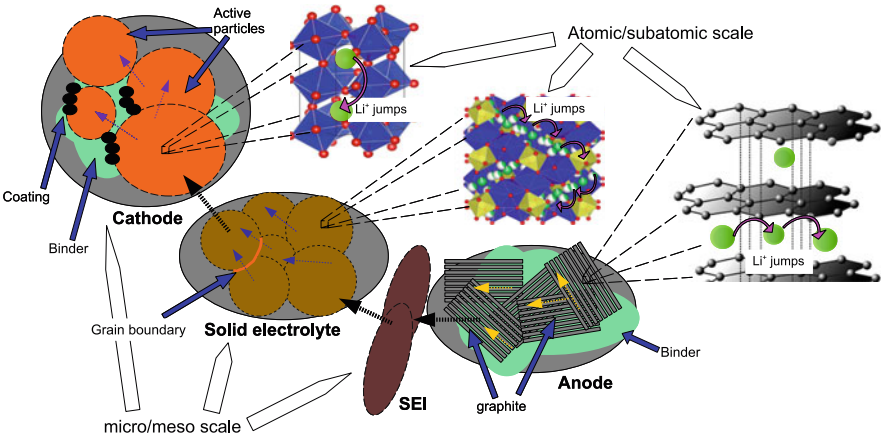

Fig. 2 The several scales of ionic conduction in an electrochemical cell for LIBs. Cathode, anode and electrolyte (a solid one in the sketch) are composed of active particle agglomerates, presenting grain boundary resistances at the particle/particle interfaces. Often, these particles are glued by a polymeric binder and may be coated to enhance electronic conduction. These micro/meso structures ($\sim 10^{-6}$–10^{-5} m) are generally isotropic. Within single active particle crystals, structural anisotropy can create preferential diffusion paths for Li^+. In addition, only particular sites are capable of accepting Li^+ ions, which means that intracrystalline Li^+ motion occurs in discrete jumps between those sites. Individual jumps occur at the atomistic scale ($\sim 10^{-10}$–10^{-9} m) and long range conduction happens over many such jumps ($\sim 10^{-8}$–10^{-7} m). However, subatomic scale phenomena such as oxygen polarization ($\sim 10^{-12}$ m) can strongly influence the energy barriers associated with the jumps

2.2.1 Ionic Conduction in Cathodes

Within the active particles of the cathode, insertion of an X^+ leads to the reduction (acceptance of an electron) by the transition metal (M) (e.g. in $LiFePO_4$, iron is reduced from Fe^{3+} to Fe^{2+}). Clearly, the ease with which electrons can reach and reduce M and the ease with which X^+ can travel from the surface to the bulk of the particle are of paramount importance. The latter is captured by the ionic conductivity tensor ($\boldsymbol{\sigma}_X$), which is defined as

$$\mathbf{J} = \boldsymbol{\sigma}_X \mathbf{E},$$

where $\mathbf{J}$ is the electric current density transported by the charge carrier and $\mathbf{E}$ the electric field. Most active cathode particles, however, are orthotropic at the nanoscale ($\sim 10^{-9}$ m) and only the diagonal components of $\boldsymbol{\sigma}_X$ are needed. In addition, because cathodes are made of randomly oriented collections of active particles, mesoscopic ionic conduction is isotropic and the conductivity tensor at this scale reduces to a simple scalar $\sigma_{X,meso}$.

Most experimental measurements are microscopic ($\sim 10^{-6}$ m). Moreover, electron movement and reduction of M is comparatively fast compared to ionic diffu-

sion, which means that the cathode conductivity reported in the literature normally corresponds to $\sigma_{\mathrm{X,meso}}$ [10]. There are, nonetheless, single crystal measurement methods capable of capturing conductivity anisotropy [7]. In most atomistic studies (ours included), it is assumed that intraparticle diffusion dominates over interparticle diffusion, and $\sigma_{\mathrm{X,meso}}$ is simply estimated as $\sigma^*_{\mathrm{X,meso}} = \frac{1}{3}\mathrm{tr}(\boldsymbol{\sigma}_{\mathrm{X}})$ [18, 19, 30, 70, 75]. This is not entirely correct, as grain boundary and other interfacial resistances can be quite significant and neglecting them leads to overestimated conductivities. In general terms, if the atomistically estimated conductivity is within an order of magnitude above the experimental values, the estimation is considered good enough. Extending atomistic methods to the mesoscale simulation of cathodes (coarse-graining) will provide powerful means for examining the impact of large-scale interfacial effects.

The self-diffusion coefficient for X^+ in an orthotropic crystal is a diagonal tensor $\boldsymbol{D}_{\mathrm{X}}$ whose i-th entry is given by

$$\langle \Delta^2 r_i(t) \rangle = 2D_{\mathrm{X},i}t, \qquad t >> t_c, \tag{1}$$

where $\langle \Delta^2 r_i(t) \rangle$ is the mean square displacement of the ions in the i-th direction after time t, and t_c is a characteristic diffusion time (for the cathode, it corresponds to the average interval between consecutive ionic jumps). $D_{\mathrm{X},i}$ is related to $\sigma_{\mathrm{X},i}$ through the corrected Nernst-Einstein equation:

$$\sigma_{\mathrm{X},i} = c_{\mathrm{X}}(Q_{\mathrm{X}}F)^2 \frac{D_{\mathrm{X},i}}{H_r k_B T}, \tag{2}$$

where c_{X} is the charge carrier concentration, Q_{X} is its ionic charge, F is the Faraday's constant, k_B is the Boltzmann's constant, T is the temperature and $H_r \leq 1$ is the Haven's ratio. H_r corresponds to the ratio of the charge carrier collective diffusivity to the self-diffusivity; it is unity in the small concentration limit. Above that, ionic displacements are correlated due to long-range Coulomb interactions and this correction is required [56].

2.2.2 Ionic Conduction in Electrolytes

In most electrolytes, positive ions (cations) move isotropically in all directions. However, in liquid and polymer electrolytes, X^+ usually originates from the dissociation of a salt, which means that negative counterions (anions) are also present (e.g. standard Li salt $\mathrm{LiPF_6}$ dissociates into Li^+ and $\mathrm{PF_6^-}$). Since the mobility of anions and cations is different (the anion is always much heavier), the diffusivity of both species must be considered in the calculation of the conductivity:

$$\sigma_i = c_{\mathrm{tot}}F^2 \frac{Q_+^2 D_{+,i} + Q_-^2 D_{-,i}}{H_r k_B T}, \tag{3}$$

where c_{tot} is the total ionic concentration, Q_v is the ionic charge of species v and $D_{v,i}$ its self-diffusivity in the i-th direction. $v = +$ for the cation and $v = -$ for the anion. Using atomistic simulations, it is straightforward to estimate the terms in equations (2) and (3) [20]. While for single ionic carriers it is often a reasonable approximation to take $H_r = 1$, this almost always leads to large errors for dissolved salts, because of the strong tendency cations and anions have to cluster and behave in a collective fashion. Finally, in crystalline solid electrolytes such as $Li_7La_3Zr_2O_{12}$, X^+ moves through a partially unoccupied lattice embedded within a crystalline framework [19, 41]. In these systems, ionic conduction occurs through discrete jumps between X sites. However, because the lattice contains vacancies, diffusion is somewhat more *fluid* than it is in typical cathode particles (there, diffusion requires the prior formation of a *defect* in order to produce a vacant site to which X^+ can jump to). Since no counterions are present in crystalline solid electrolytes, Eq. (2) can be used to obtain the ionic conductivity.

2.2.3 Ionic Conduction in Anodes

Since we have not tackled yet the study of conduction in graphite anodes, we will not discuss it in detail. Suffice it to say that ion intercalation in graphitic anodes involves ion absorption and diffusion through the SEI, and the occurrence of phase transitions within the ordered graphite structure. As a consequence, it is rather complex and multiscale in nature. A recent review on advances in the modelling of anodes can be found in [58].

3 Sampling in Atomistic Simulation

Molecular dynamics (MD) and Metropolis Monte Carlo (MC) are traditional sampling techniques broadly used for solid-state atomistic simulation [39]. Recently, we have proposed the class of enhanced sampling methods [4] which combine the advantages of both MD and MC offering improved sampling efficiency and accuracy vital for the success of a molecular simulation. The methods utilize the modified Hamiltonians for sampling enhancement and hence the name of the class—Modified Hamiltonian Monte Carlo (MHMC). In this section, we briefly review the molecular dynamics and Monte Carlo approaches and discuss the main features of MHMC as well as the benefits of employing them in the study of battery materials.

3.1 Molecular Dynamics

Molecular Dynamics (MD) is a computer simulation approach in which the evolution in time of a group of interacting atoms is followed by integrating the

Newtonian equations of motion. In general, MD is not trying to generate physically accurate trajectories: this is often an impossible task. Instead, quantities of interest are statistical averages computed during the sampling of phase space.

Let us denote the positions of a system of n particles as $\mathbf{r} \in \mathbb{R}^d$, where $d = 3n$, and the velocities as $\mathbf{v} \in \mathbb{R}^d$ and assume that the system is conservative, i.e. a potential energy function U exists such that

$$F(\mathbf{r}) = -\nabla_{\mathbf{r}} U(\mathbf{r}), \tag{4}$$

where F are the forces. The function U is also called a *force field* and it contains the contribution to the potential energy from all interatomic interactions. Then, for the classical n-body problem in MD-simulations, Newton's second law can be expressed as

$$\frac{\mathrm{d}\mathbf{r}}{\mathrm{d}t} = \mathbf{v}, \quad M\frac{\mathrm{d}\mathbf{v}}{\mathrm{d}t} = F(\mathbf{r}), \tag{5}$$

where $M \in \mathbb{R}^{d\times d}$ is the (symmetric positive definite) mass matrix.

The Hamiltonian formulation of Newtonian mechanics (5) reads

$$\frac{\mathrm{d}\mathbf{r}}{\mathrm{d}t} = \frac{\partial H}{\partial \mathbf{p}} = M^{-1}\mathbf{p}, \quad \frac{\mathrm{d}\mathbf{p}}{\mathrm{d}t} = -\frac{\partial H}{\partial \mathbf{r}} = -\nabla_{\mathbf{r}} U(\mathbf{r}). \tag{6}$$

Here $\mathbf{p} = M\dot{\mathbf{r}}$,[1] $\mathbf{p} \in \mathbb{R}^d$ is the linear momenta and the *Hamiltonian* or energy functional is defined as

$$H(\mathbf{r}, \mathbf{p}) = \frac{1}{2}\mathbf{p}^T M^{-1}\mathbf{p} + U(\mathbf{r}), \tag{7}$$

where the super index T denotes the transpose vector. The equations in (6) are the *Hamilton equations of motion*. By introducing the $2d \times 2d$ matrix $J = \begin{bmatrix} 0_{d\times d} & -I_{d\times d} \\ I_{d\times d} & 0_{d\times d} \end{bmatrix}$, (6) can be rewritten as (cf. [65])

$$\frac{\mathrm{d}}{\mathrm{d}t}\begin{bmatrix}\mathbf{r}\\ \mathbf{p}\end{bmatrix} = J^{-1}\nabla H(\mathbf{r}, \mathbf{p}), \tag{8}$$

where

$$\nabla H(\mathbf{r}, \mathbf{p}) = \left[\frac{\partial H}{\partial \mathbf{r}}, \frac{\partial H}{\partial \mathbf{p}}\right]^T.$$

[1] For simplicity, we use here the dot-notation for the derivatives in time.

The space defined by the vectors $(\mathbf{r}, \mathbf{p})$ satisfying Eq. (8) is called the *phase space*. Under suitable conditions, there is a unique exact solution at a time t for every initial point $(\mathbf{r}(0), \mathbf{p}(0))$, and, for any time t, a *flow map* ϕ_t can be defined as

$$(\mathbf{r}(t), \mathbf{p}(t)) = \phi_t(\mathbf{r}(0), \mathbf{p}(0)). \tag{9}$$

Hamiltonian flows have a number of important properties, including (cf. [65]):

1. **Symplecticity**: For all t, a flow map ϕ_t is symplectic if, at each point $(\mathbf{r}, \mathbf{p})$ in phase space,

$$\phi_t'(\mathbf{r}, \mathbf{p})^T J \phi_t'(\mathbf{r}, \mathbf{p}) = J,$$

where $\phi_t'(\mathbf{r}, \mathbf{p})$ is the $2d \times 2d$ Jacobian matrix of ϕ_t. An important consequence of symplecticity is phase volume preservation (oriented volume): If A represents a region in phase space, then the volume of $\phi_t(A)$ is invariant in t.
2. **Time reversibility**: The Hamiltonian system described by Eqs. (7)–(9) is time reversible; i.e., for all t, $\phi_t^{-1} = \phi_{-t}$.

There are another two characteristics that do not apply generically to all Hamiltonian flows. However, they have been empirically observed in the flows arising from many systems in MD simulations (cf. [52]):

3. **Ergodicity**: In statistical physics, ergodicity is defined to be the property that for any observable Ω, the time averages of Ω eventually converge to the average of Ω over the phase space. More precisely, for a probability measure π preserved under the Hamiltonian flow, ergodicity implies that

$$\lim_{T\to\infty} \frac{1}{T} \sum_{t=0}^{T} \Omega(\phi_t(\mathbf{r}, \mathbf{p})) = \lim_{T\to\infty} \frac{1}{T} \int_0^T \Omega(\mathbf{r}, \mathbf{p}) \mathrm{d}\pi(\mathbf{r}, \mathbf{p}). \tag{10}$$

This is very useful for simulations, as it allows approximating the spatial averages by means of time-averages available through MD.
4. **Sensitive dependence on initial conditions (SDIC)**: In high-dimensional Hamiltonian systems, there are arbitrarily close points $(\mathbf{r}', \mathbf{p}')$ to $(\mathbf{r}(0), \mathbf{p}(0))$, such that the positive orbit starting at $(\mathbf{r}', \mathbf{p}')$ eventually diverges from the one starting at $(\mathbf{r}(0), \mathbf{p}(0))$. As a consequence, MD trajectories cannot be computed for long periods of time in a classical sense (that is, point-to-point matching between exact value and computed value), because even the unavoidable round-off error will naturally be magnified, thus potentially rendering computed values that are far from the actual values.

SDIC and ergodicity are two phenomena playing complementary roles in computing long-term trajectories of MD flow-maps: while SDIC prevents the computation of accurate trajectories, ergodicity allows the extraction of statistical information from the same computations. From a numerical standpoint, if a discretization $\phi_{L\Delta t}$ of the flow map ϕ_t (where $L\Delta t$ is a trajectory length and

Δt is a time step) is symplectic, then averages of an observable Ω calculated along orbits of $\phi_{L\Delta t}$ will converge to the desired spatial average as the time step Δt tends to 0. Efficient and simple integrators providing symplecticity and time reversibility are available, the most popular of which are the Störmer-Verlet method and its extensions (leapfrog, velocity Verlet, etc.). Nonetheless, MD still suffers from several drawbacks:

(i) As stated in Eq. (10), making use of ergodicity (if it exists) requires sufficiently long trajectories. In systems with large energy barriers such as the ones between adjacent sites in cathode materials, meaningful trajectories may need to be hundreds of nanoseconds long ($\sim 10^{-7}$ s) to sample atomic jumps. Because time steps need to be small (typically $\sim 10^{-15}$ s), the number of steps required can be as high as $L \sim 10^8$. For a tens-of-thousands atoms system this can be very demanding, even with robust computing architectures.

(ii) Because MD only allows for slow exploration of configurational space through a sequence of many small steps, systematic discretization errors can be significant.

(iii) In the absence of external forces, the flow defined by (9) is energy preserving: the dynamics occurs on a surface in $\mathbb{R}^{2d}$ for which H is constant. The probability density arising from this condition is the so-called *microcanonical ensemble*. However, most practical applications occur either at constant number of particles, N, temperature, T, and volume V (the *canonical* or NVT ensemble) or at given N, T and pressure, P (the *isothermal-isobaric* or NPT ensemble). In the latter two ensembles, the Hamiltonian must be modified by adding additional degrees of freedom, which are coupled to the particle velocities (thermostatting) and simulation domain dimensions (barostatting), increasing computational cost and introducing additional sources of error.

One significant advantage of MD is the ability to capture dynamical properties, such as the diffusion coefficients in Eqs. (2) and (3). In addition, even though the *true* evolution of the system may not be captured, qualitative information regarding the underlying mechanisms of the physical processes can still be extracted.

3.2 Monte Carlo Simulations

While MD tries to estimate the value of the integral on the r.h.s. of Eq. (10) using a deterministic scheme, Monte Carlo (MC) simulations attempt to approximate the value of such integral using a stochastic approach. For simplicity, we will refer only to the canonical ensemble, for which the probability density distribution is

$$\pi(\mathbf{r}, \mathbf{p}) \propto \exp(-\beta H(\mathbf{r}, \mathbf{p})), \tag{11}$$

where $\beta = (k_B T)^{-1}$ is the thermodynamic beta. The position and momenta contributions to the Hamiltonian in Eq. (7) are separable. Moreover, the momenta

part can be analytically integrated, which means that only the target distribution

$$\pi(\mathbf{r}) \propto \exp(-\beta U(\mathbf{r})), \tag{12}$$

needs to be sampled using the Metropolis-Hastings Markov chain MC algorithm [42]:

- The current configuration in the chain $\mathbf{r}$ is randomly perturbed to generate a trial atomic configuration $\mathbf{r}'$. A typical perturbation might be a single-particle displacement: randomly pick an atom and displace its position by a small amount.
- Accept the proposal configuration to become $\mathbf{r}^{\text{new}}$ with probability

$$\alpha = \min\left\{1, \frac{\pi(\mathbf{r}')}{\pi(\mathbf{r})}\right\} = \min\left\{1, \exp[-\beta(U(\mathbf{r}') - U(\mathbf{r}))]\right\}.$$

  Otherwise, dismiss $\mathbf{r}'$ and set $\mathbf{r}^{\text{new}}$ to $\mathbf{r}$.
- Repeat the two steps until the number of configurations reaches N.

Following this procedure, due to the law of the large numbers, the average of an observable Ω can be estimated as

$$\langle\Omega\rangle = \lim_{N\to\infty} \frac{1}{N} \sum_{i=1}^{N} \Omega(\mathbf{r}^i),$$

where $\{\mathbf{r}^i\}$ is the set of accepted configurations.

Metropolis MC has a number of advantages with respect to MD. Thus, MC does not have an equivalent of a time step error, its sampling is exact with only statistical errors involved. The method is flexible in the choice of sequences of steps which potentially can lead to rapid exploration of configurational space. However, it also has a number of important drawbacks: for systems with large numbers of degrees of freedom, such as biomolecules, it may become impractical due to the difficulties in specifying a physically meaningful move leading to high acceptance rates. In addition, the method does not provide dynamical information, which means that quantities such as diffusivities or conductivities (Eqs. (1)–(3)) cannot be estimated.

3.3 Modified Hamiltonian Monte Carlo Methods

Our choice of simulation techniques for the effective study of ion transport in bulk and nanostructured materials is based on four requirements critical for the success of the project. Such methods should (i) sample efficiently multidimensional space; (ii) reproduce dynamical properties of a simulated system; (iii) be able to detect rare events; and (iv) be easily extended to simulations on meso-scales.

The Modified Hamiltonian Monte Carlo (MHMC) methods were originally developed for atomistic simulations of complex systems [1, 2, 45, 68] and then adapted for multiscale [31] and mesoscale simulations [3]. They proved to be successful in the study of rare events in complex biological processes [3, 4, 31, 74] though never have been applied to solid-state chemistry until recently when we proposed using them for the simulation of battery materials [18, 19, 32, 41].

MHMC are importance sampling Hybrid Monte Carlo (HMC) methods [28] that achieve higher efficiency than MC, HMC or MD by sampling with respect to a modified Hamiltonian. Such methods are especially appropriate when exploring high-dimensional configurational spaces, helping in finding energy global minima and simulating rare events such as slow chemical reactions or phase transitions. Furthermore, the MHMC methods originated from the generalized hybrid Monte Carlo (GHMC) [44, 49] can keep the dynamic information throughout the sampling process similar to stochastic Langevin and Brownian dynamics simulations.

In general, to simulate the properties of physical systems, one collects samples with respect to a target distribution such as $\pi(\mathbf{r})$ in (12). For that purpose, HMC methods are a suitable choice as a sampling technique. Given a separable Hamiltonian (7), HMC generates samples of configurations from the augmented canonical distribution (11). Then, marginalizing momenta variables out, one can obtain the samples with respect to the target distribution $\pi(\mathbf{r})$ in (12).

Instead of sampling from the canonical distribution (11), MHMC methods sample from an importance canonical density

$$\tilde{\pi}(\mathbf{r}, \mathbf{p}) \propto \exp\left(-\beta \tilde{H}^{[k]}(\mathbf{r}, \mathbf{p})\right), \tag{13}$$

where $\tilde{H}^{[k]}$ is the kth order truncation of the modified Hamiltonian which is preserved exactly by a symplectic integrator [65]. For certain $H_2, H_3, \ldots$, a modified Hamiltonian reads as

$$\tilde{H} = H + \Delta t H_2 + \Delta t^2 H_3 + \ldots,$$

where Δt is an integration time step. For an integrator of order m, $\tilde{H} = H + \mathcal{O}(\Delta t^m)$, so that $H_2, \ldots, H_m$ vanish. Thus, for $k > m$,

$$\tilde{H}^{[k]} = H + \Delta t^m H_{m+1} + \cdots + \Delta t^{k-1} H_k. \tag{14}$$

According to [6, 14], for a system of D particles, the expectation of the increments of H and $\tilde{H}^{[k]}$ in an integration leg satisfy

$$\mathbb{E}[\Delta H] = \mathcal{O}\left(D \Delta t^{2m}\right), \tag{15}$$

and

$$\mathbb{E}\left[\Delta\tilde{H}^{[k]}\right] = \mathcal{O}\left(D\Delta t^{2k}\right) \tag{16}$$

respectively.

Let us now describe the algorithm of a generic MHMC method. Given a sample $(\mathbf{r}, \mathbf{p})$ from the distribution $\tilde{\pi}$, the next configuration $(\mathbf{r}^{\text{new}}, \mathbf{p}^{\text{new}})$ is obtained as follows:

- Set up the new momentum $\mathbf{p}^*$ by applying a momentum refreshment procedure that preserves the importance density $\tilde{\pi}$ (13).
- Generate a proposal configuration $(\mathbf{r}', \mathbf{p}')$ by simulating the Hamiltonian dynamics (6) with the Hamiltonian H in (7) and the initial condition $(\mathbf{r}, \mathbf{p}^*)$ using a symplectic and time-reversible numerical integrator Ψ (cf. [65]).
- Accept the proposal configuration $(\mathbf{r}', \mathbf{p}')$ to become $(\mathbf{r}^{\text{new}}, \mathbf{p}^{\text{new}})$ with probability

$$\alpha = \min\left\{1, \frac{\tilde{\pi}(\mathbf{r}', \mathbf{p}')}{\tilde{\pi}(\mathbf{r}, \mathbf{p}^*)}\right\}.$$

  Otherwise, reject the proposal and perform a momentum flip, i.e. $(\mathbf{r}^{\text{new}}, \mathbf{p}^{\text{new}}) = (\mathbf{r}, -\mathbf{p}^*)$.

The reader should notice that

$$\frac{\tilde{\pi}(\mathbf{r}', \mathbf{p}')}{\tilde{\pi}(\mathbf{r}, \mathbf{p}^*)} = \exp\left(-\beta\left(\tilde{H}^{[k]}(\mathbf{r}', \mathbf{p}') - \tilde{H}^{[k]}(\mathbf{r}, \mathbf{p}^*)\right)\right) = \exp\left(-\beta\Delta\tilde{H}^{[k]}\right). \tag{17}$$

For comparison, in the Hybrid Monte Carlo algorithm, the corresponding ratio is given by

$$\frac{\pi(\mathbf{r}', \mathbf{p}')}{\pi(\mathbf{r}, \mathbf{p})} = \exp\left(-\beta\Delta H\right). \tag{18}$$

Therefore, since $k > m$, one can see from (15)–(18) that MHMC methods may provide higher acceptance rates than regular HMC methods. The fewer rejections has a positive impact not only on the sampling efficiency but also on the accuracy of dynamics since less momentum flips occur [2, 5]. Moreover, for very big systems, where performance of HMC degrades dramatically, MHMC algorithms may counterbalance the error introduced by the size D and maintain a high acceptance rate by choosing a bigger truncation order k without increasing the order of the integrator m [6].

Since in MHMC methods the samples are generated with respect to the importance density (13), the computation of averages of any observable Ω with respect to the canonical distribution (11) requires a *reweighting*. Given N samples of the observable Ω_i, $i = 1, 2, \ldots, N$ along a trajectory $(\mathbf{r}^i, \mathbf{p}^i)$ drawn from (13), the

average of Ω with respect to (11) is calculated as

$$\langle \Omega \rangle_\pi = \frac{\sum_{i=1}^N \omega_i \Omega_i}{\sum_{i=1}^N \omega_i}, \tag{19}$$

where the importance weights are computed as

$$\omega_i = \exp\left(-\beta \left(H(\mathbf{r}^i, \mathbf{p}^i) - \tilde{H}^{[k]}(\mathbf{r}^i, \mathbf{p}^i)\right)\right) \quad \forall i = 1, 2, \ldots, N.$$

A big variability among weights would mean that the canonical density π in (11) and the importance density $\tilde{\pi}$ in (13) are not close. This would lead to errors in the averages, as many samples would not contribute significantly to the computation in (19). Such a situation is well controlled, however, in the MHMC methods through the appropriate choice of an integration step and an order of a modified Hamiltonian (cf. (14)). This makes samples of (13) an efficient means towards computing expectations with respect to (11).

The various algorithms in the MHMC class of methods may differ in the elements described above: refreshing the momenta, simulating the Hamiltonian dynamics or computing the modified Hamiltonians.

For our purposes here, the Generalized Shadow Hybrid Monte Carlo (GSHMC) method [2] is of special interest. As its predecessor the Targeted Shadowing Hybrid Monte Carlo (TSHMC) method [1], GSHMC takes advantage of a partial momentum update based on the ideas of Horowitz [44], which helps preserving partially dynamics and enhancing sampling efficiency:

$$\begin{aligned} \mathbf{p}^r &= \cos\varphi\ \mathbf{p} + \sin\varphi\ \mathbf{u}, \\ \mathbf{u}^r &= -\sin\varphi\ \mathbf{p} + \cos\varphi\ \mathbf{u}, \end{aligned} \tag{20}$$

where $\varphi \in (0, \pi/2]$ is a parameter and $\mathbf{u}$ a random noise drawn from $\mathcal{N}(0, \beta^{-1}M)$. The proposed refreshed momentum $\mathbf{p}^r$ is accepted, i.e. $\mathbf{p}^* = \mathbf{p}^r$, with the probability

$$\alpha_p = \min\left\{1, \frac{\hat{H}(\mathbf{r}, \mathbf{p}^r, \mathbf{u}^r)}{\hat{H}(\mathbf{r}, \mathbf{p}, \mathbf{u})}\right\}, \tag{21}$$

where

$$\hat{H}(\mathbf{r}, \mathbf{p}, \mathbf{u}) = \tilde{H}^{[k]}(\mathbf{r}, \mathbf{p}) + \frac{1}{2}\mathbf{u}^T M^{-1}\mathbf{u}.$$

In the case of rejection, we set $\mathbf{p}^* = \mathbf{p}$.

GSHMC was originally introduced for atomistic simulations in canonical ensembles [2, 30, 74] and then adapted to simulations in isobaric-isothermal ensembles [35].

Different extensions of GSHMC aiming at specific applications appeared recently. For meso-scale simulations, the meso-GSHMC method [3] was proposed. In coarse-grained mesoscopic models, the fluctuation-dissipation contributions should mimic the impact of non-resolved finer details of an atomistic model on the coarse grained length and time scales while maintaining the system at a desired temperature. For this purpose, the stochastic thermostat called Dissipative Particle Dynamics (DPD) [33] is used. The meso-GSHMC puts DPD in the GSHMC framework by introducing a DPD-type momentum update step which conserves total linear and angular momenta. Unlike original DPD, meso-GSHMC samples exactly from the canonical distribution (11) while dealing with the fluctuation-dissipation terms.

For multiscale simulations, a naturally possessed weak stochasticity of GSHMC can be combined with the modified impulse multi-time-stepping (MTS) molecular dynamics and the modified Hamiltonians specially derived for modified MTS integrators. The resulting MTS-GSHMC method [31] demonstrates the improved stability of the MTS integrators and superior sampling performance over multi-time-stepping molecular and Langevin dynamics.

More recently, the MHMC method for solid-state atomistic simulations called Randomized Shell Mass GSHMC (RSM-GSHMC) has been proposed [32]. In this algorithm, a mass randomization is implemented as part of the momentum update step in order to reduce the negative effect of a shell mass within a dynamical shell model on the kinetics of a simulated system. Before updating the momenta, a fraction of the atomic mass is redistributed between the core and the shell, maintaining the total mass constant. Apart from the study where the methodology was introduced [32], it has been also used in [18].

All variants of GSHMC described above posses the strongest features of GSHMC such as the enhanced sampling, ability to reproduce dynamical properties of simulated systems and rigorous temperature control. As demonstrated in the studies cited above (see also [6] and references therein) for different problems, the use of GSHMC methods resulted in a systematic improvement of the sampling efficiency and accuracy with respect to those observed with conventional sampling techniques, such as MD, MC, HMC or Langevin dynamics.

While GSHMC methods were designed for applications in the field of molecular simulation, the Mix & Match Hamiltonian Monte Carlo (MMHMC) [60] method has been recently proposed for Bayesian inference problems. In simple terms, MMHMC is an adaptation of GSHMC to computational statistics. It proved to be successful in the simulation of popular statistical models such as multivariate Gaussian, Bayesian Logistic Regression and Stochastic volatility [60].

Two possible strategies for enhancing performance of MHMC methods are (i) a suitable choice of the method-specific parameters; and (ii) an optimization of conservation properties of numerical integrators used for simulating the Hamiltonian dynamics. The latter is explored in the following section.

3.4 Modified Adaptive Integration Approach

In this study, we limit ourselves to *separable* Hamiltonians, such as the one in (7), meaning that the Hamiltonian can be written as a sum $H \equiv A + B$ of two partial functions

$$A(\mathbf{r}, \mathbf{p}) = \frac{1}{2}\mathbf{p}^T M^{-1}\mathbf{p}, \quad B(\mathbf{r}, \mathbf{p}) = U(\mathbf{r}),$$

which correspond to the kinetic and potential energies, respectively. Thus, the Hamilton equations of motion (6) can be rewritten as

$$\frac{\mathrm{d}\mathbf{r}}{\mathrm{d}t} = \nabla_{\mathbf{p}} A(\mathbf{r}, \mathbf{p}) = M^{-1}\mathbf{p}, \quad \frac{\mathrm{d}\mathbf{p}}{\mathrm{d}t} = -\nabla_{\mathbf{r}} B(\mathbf{r}, \mathbf{p}) = -\nabla_{\mathbf{r}} U(\mathbf{r}).$$

These equations can be integrated analytically and their solution flows at a time t are given by (cf. (9))

$$(\mathbf{r}(t), \mathbf{p}(t)) = \phi_t^A(\mathbf{r}(0), \mathbf{p}(0)) = (\mathbf{r}(0) + tM^{-1}\mathbf{p}(0), \mathbf{p}(0)), \tag{22}$$

and

$$(\mathbf{r}(t), \mathbf{p}(t)) = \phi_t^B(\mathbf{r}(0), \mathbf{p}(0)) = (\mathbf{r}(0), \mathbf{p}(0) - t\nabla_{\mathbf{r}} U(\mathbf{r}(0)). \tag{23}$$

These solution flows of the partial systems, for a time t, associate the exact solution value $(\mathbf{r}(t), \mathbf{p}(t))$ with each initial condition $(\mathbf{r}(0), \mathbf{p}(0))$.

A splitting integrator can be constructed as a palindromic composition of the solutions flows (22) and (23) of the partial systems (cf. [16]). Here, we limit our attention to the one-parameter family of two-stage[2] splitting integrators studied in detail in previous works [6, 17, 36]. The map that advances the solution over one step Δt is

$$\psi_{\Delta t} = \phi^B_{b\Delta t} \circ \phi^A_{\Delta t/2} \circ \phi^B_{(1-2b)\Delta t} \circ \phi^A_{\Delta t/2} \circ \phi^B_{b\Delta t}, \tag{24}$$

where $b \in (0, 1/4]$ is the parameter that fully characterizes a two-stage integrator. Then, for a time $\tau = L\Delta t$ with $L \in \mathbb{N}$, one can also define the transformation Ψ_τ as the composition

$$\Psi_\tau = \underbrace{\psi_{\Delta t} \circ \cdots \circ \psi_{\Delta t}}_{L \text{ times}}.$$

[2]The *stage* notation first suggested by Blanes et al. [17] indicates the number of force evaluations performed per step.

The integrators in (24) are symplectic because they are a composition of Hamiltonian flows [65]. Moreover, they are also time-reversible due to the palindromic structure of (24) [17].

The optimal choice of a parameter b in (24) has been thoroughly investigated for the HMC [36] and MHMC methods [6, 61]. The suggested criteria for such "optimality" is the maximization of acceptance rates in HMC or MHMC due to the conservation properties of a chosen integrator.

For MHMC, the focus is on those two-stage integration schemes ψ that provide the lowest expected error $\Delta\tilde{H}^{[k]}$ in modified Hamiltonians with respect to a modified density (13). Here,

$$\Delta\tilde{H}^{[k]} = \tilde{H}^{[k]}(\Psi_\tau(\mathbf{r}, \mathbf{p}^*)) - \tilde{H}^{[k]}(\mathbf{r}, \mathbf{p}^*), \tag{25}$$

for a given time $\tau = L\Delta t$. Thus, the acceptance criterion in (17) is integrator-dependent.

In contrast to the well established practice in molecular simulation to use the same integrator, usually Verlet/leapfrog, for a broad range of the simulated systems, in [6], it has been proposed to construct *a system specific* two-stage integrator prior to an MHMC simulation. The Modified Adaptive Integration Approach (MAIA), which realises this idea, adapts the parameter b to a given simulated system and a chosen by a user value of step size Δt in such a way that the expected value of (25), $\mathbb{E}\left[\Delta\tilde{H}^{[k]}\right]$, is minimal. Based on the detailed analysis of the one-dimensional harmonic oscillator, the MAIA approach provides the upper bound $\rho(h, b)$ of $\mathbb{E}\left[\Delta\tilde{H}^{[k]}\right]$,[3] where h is a dimensionless step size related to Δt by

$$h = \sqrt{3}\tilde{\omega}\Delta t.$$

Here, $\sqrt{3}$ is a safety factor used to avoid nonlinear resonances (cf. [6, 36, 67]) and $\tilde{\omega}$ is the fastest angular frequency of the two-body interactions. Then, the value of b is found as the one that minimizes

$$\max_{0<h<\tilde{h}} \rho(h, b),$$

where $\tilde{h}$ is the dimensionless time step associated to a user defined Δt.

One should note that, for a realistic physical model consisting of D harmonic oscillators, $(0, \tilde{h})$ is the shortest interval that contains all $h_i = \sqrt{3}\omega_i\Delta t$, where ω_i are the D frequencies in the problem.

It has to be stated that MAIA is a never-fail strategy, meaning that it guarantees, by construction, that the numerical stability is not lost. For the biggest allowed integration step sizes, the parameter b in (24) becomes 1/4, which means that the

[3]The expression for $\rho(h, b)$ as well as the details of its derivation can be found in [6].

integrator of choice is the two-stage version of the classic velocity Verlet. This integration scheme is known as the integrator with the largest stability interval among two-stage integrators, namely (0, 4).

The extended MAIA (e-MAIA) [6] is capable of keeping the momenta acceptance rate (21) at the user-desired level for any given problem through the intelligent choice of the parameter φ in the momentum update (20).

Both MAIA and e-MAIA proved their efficiency in simulations of complex molecular systems in Materials Science, Biology and Chemistry [6, 18, 19, 32, 41].

3.5 Software Implementation

The GSHMC methods for molecular simulation, i.e. GSHMC, meso-GSHMC, RSM-GSHMC, described in Sect. 3.3 have been implemented in the in-house software package MultiHMC-GROMACS [30, 35, 36] which is built on top of the popular suite of programs for molecular dynamics simulations GROMACS [12, 43]. GROMACS supports state-of-the-art molecular simulation algorithms and is well known for its computational efficiency and parallel scaling properties. These features are carefully maintained in MultiHMC-GROMACS.

Two-stage integrators (24) are implemented in MultiHMC-GROMACS as a concatenation of velocity Verlet steps[4] [36]. The implementation is general enough to allow the use of all members of the family (24), including the adaptive integration schemes MAIA and e-MAIA (Sect. 3.4). The analysis required for the MAIA and e-MAIA methods is done within the GROMACS preprocessing module [6]. Thus, no computational overheads are introduced. Once the integrator parameter b and the angle φ (in the e-MAIA case) are obtained, they are passed to the running module prior to a simulation.

The package offers the efficient implementation of various formulations of modified Hamiltonians derived for the range of GSHMC methods and numerical integrators. In addition to the GSHMC methods, the HMC samplers have been included in MultiHMC-GROMACS as particular cases of GSHMC [36]. The user can select any GSHMC or HMC method from the code simply by predetermining appropriate parameters in the modified GROMACS input file. The same applies to numerical integrators.

A detailed description of the MultiHMC-GROMACS package may be found in [6, 30, 32, 35, 36].

The Mix & Match Hamiltonian Monte Carlo (Sect. 3.3), proposed for applications in computational statistics, is implemented in the in-house software package HaiCS [60]. The package is designed for statistical sampling of high dimensional, complex distributions and parameter estimation in different models by means of

[4]The main idea is that, for every b, an integration step $\psi_{\Delta t}$ can be rewritten as $\psi_{\Delta t} = \left(\phi^B_{b\Delta t} \circ \phi^A_{\Delta t/2} \circ \phi^B_{(1-2b)\Delta t/2}\right) \circ \left(\phi^B_{(1-2b)\Delta t/2} \circ \phi^A_{\Delta t/2} \circ \phi^B_{b\Delta t}\right)$.

Bayesian inference using HMC-based methods. The code benefits from the efficient implementation of modified Hamiltonians, multi-stage splitting integrators [61], performance analysis tools compatible with CODA toolkit [59] and provides a user-friendly interface for implementing alternative HMC-type samplers, splitting integrators and statistical models.

Both MultiHMC-GROMACS and HaiCS are written in C and targeted to computers running UNIX certified operating systems.

4 Force Fields

As briefly introduced in Sect. 3.1, a force field is a mathematical expression describing the dependence of the energy of a system on the positions of its particles. It is fully defined by a functional form of the interatomic potential energy, $U(\mathbf{r})$, and a set of parameters. There are several force fields in use addressed to particular families of materials (e.g. AMBER, for proteins and DNA [27] or CHARMM for polymers [24]). However, it is clear that for many specific materials and applications, custom force fields must be developed. Force field development has three fundamental requirements:

- an appropriate functional form for the interaction potentials,
- a training data set of structural, mechanical and/or thermodynamic properties (e.g. experimental, computed, etc.) to fit the model, and
- an optimization strategy to perform the fitting.

Ideally, a force field must be simple enough to be evaluated quickly, but sufficiently detailed to reproduce the properties of interest. Below, we elaborate on each of these requirements, with particular focus on those interactions that are typical to intercalation in cathodes and solid electrolyte materials. Hence, metallic systems are not included in this discussion.

4.1 Functional Form of the Interaction Potentials

Let us denote a position of atom i in an n-particle system as $\mathbf{r}_i$, and the Euclidean distance between atoms i and j as r_{ij}. The general expression for most force fields has the form:

$$U(\mathbf{r}_1, \ldots, \mathbf{r}_n) = U_{\text{non-bonded}}(\mathbf{r}_1, \ldots, \mathbf{r}_n) + U_{\text{bonded}}(\mathbf{r}_1, \ldots, \mathbf{r}_n).$$

Contributions to $U_{\text{bonded}}(\mathbf{r}_1, \ldots, \mathbf{r}_n)$ come from groups of chemically linked atoms (sharing electrons), and are typically divided into two-body bond-stretching potentials, three-body angular-bending potentials, and four-body dihedral potentials (Fig. 3a). For instance, the form of U_{bonded} in the popular OPLS [48] and AMBER

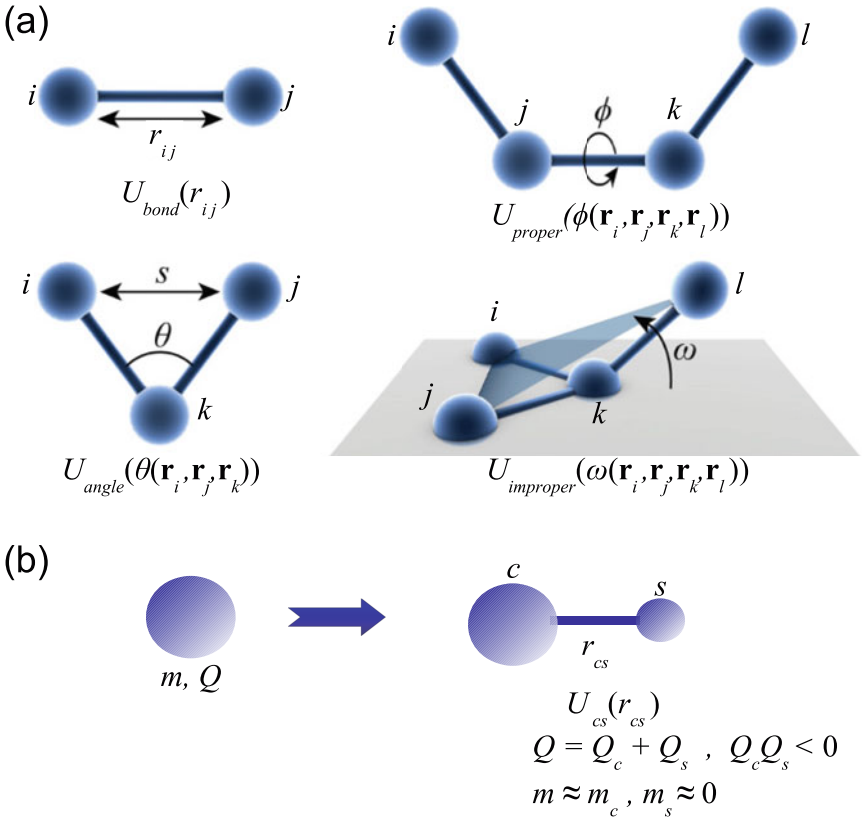

Fig. 3 (**a**) Typical bonded interactions: bonding (U_{bond}), angular (U_{angle}), proper dihedral (U_{proper}) and improper dihedral (U_{improper}) interactions. $U_{\text{bonded}} = U_{\text{bond}} + U_{\text{angle}} + U_{\text{proper}} + U_{\text{improper}}$. (**b**) Core-shell model of polarizability: the polarizable ion of mass m and charge Q is represented as a core (c) and a shell (s) with opposite charges Q_c and Q_s, respectively, interacting through a bond potential U_{cs} (usually harmonic, $U_{cs} = k_{cs} r_{cs}$). The mass of the ion is concentrated in the core ($m = m_c$), to allow for instantaneous thermalization of the shell. In practice, however, it is better to choose a small shell mass ($m_s > 0, m_s << m_c$) to boost computational efficiency

[27] force fields is:

$$U_{\text{bonded}}(\mathbf{r}_1, \ldots, \mathbf{r}_n) = \sum_{b=1}^{n_{\text{bonds}}} k_b (r_{ij} - r_{0,b})^2_{i,j \in b} + \sum_{a=1}^{n_{\text{angles}}} k_a (\theta_{ijk} - \theta_{0,a})^2_{i,j,k \in a}$$

$$+ \sum_{d=1}^{n_{\text{dihedrals}}} \sum_{m=1}^{3} \frac{k_{d,m}}{2} (1 + \cos m\phi_{ijkl})_{i,j,k,l \in d},$$

where angle $\theta_{ijk} = \theta(\mathbf{r}_i, \mathbf{r}_j, \mathbf{r}_k)$ (analogously for proper dihedral ϕ_{ijkl}), and $\{r_{0,b}\}$, $\{\theta_{0,a}\}$, $\{k_a\}$, $\{k_b\}$ and $\{k_{d,m}\}$ are positive force field parameters. There are no improper dihedrals in the original version of these force fields, but later updates have included them.

Polarizability is the ability for some atoms to form instantaneous dipoles. In many cases, its effect can be strong enough to significantly influence thermodynamic and transport properties [75, 79]. One of the simplest way to incorporate polarizability into the force field is the core–shell model suggested by Dick and Overhauser [26], in which a central core of a charge Q_c and a shell of a charge Q_s, with $Q_s Q_c < 0$, are introduced in such a way that the sum of these charges $Q_c + Q_s$ equals the ion charge Q (Fig. 3b). The core and shell are coupled together in a unit via a bond potential (usually harmonic), which allows the shell to move with respect to the core, thus simulating a dielectric polarization. In the original proposal by Dick and Overhauser, the core mass m_c was equal to the mass of the ion, m (i.e. the shell mass m_s was zero), in order to enable instant thermalization of the shell. Mitchell [55] showed that taking a sufficiently small value for m_s allowed simulating the core-shell system using conventional MD, as the thermal contribution from the shell was insignificant. This is called the cs-adiabatic scheme (cs-adi), which we have employed in our previous work [18]. The force field parameters for the harmonic cs-adi model, $U_{cs} = k_{cs} r_{cs}^2$, are the spring constant k_{cs}, Q_s and m_s.

The non-bonded interactions present in a typical force field are pairwise Coulomb, U_{Coul}, and van der Waals, U_{vdW}, interactions

$$U_{\text{non-bonded}} = U_{\text{Coul}} + U_{\text{vdW}},$$

acting over all atom pairs (i, j). In general, however, contributions from pairs already interacting through bonded potentials are totally or partially excluded. U_{Coul} is given by

$$U_{\text{Coul}} = \frac{1}{4\pi\epsilon} \sum_{i,j=1}^{n} \frac{Q_i Q_j}{r_{ij}}, \tag{26}$$

where ϵ is the vacuum permittivity and Q_i the charge of atom i. Q_i is a force field parameter, but in solid state systems its value is often taken as eZ_i, where e is the electron charge and Z_i the oxidation state of atom i. U_{vdW} can take many possible forms, the simplest non-trivial of which is the hard-sphere potential. For battery materials, two types of vdW potentials are particularly common: the Lennard-Jones (LJ)-type potentials, U_{LJ} (for liquid and polymeric electrolytes) and the softer Born potential U_{Born} (for crystalline materials) [40]. The LJ potentials between i and j atoms is given by

$$U_{\text{LJ},ij} = \frac{A_{ij}}{r_{ij}^n} - \frac{B_{ij}}{r_{ij}^m},$$

where $A_{ij} > 0$ and $B_{ij} > 0$ are force field parameters. Powers (n, m) typically assume the values (9,6) or (12,6), but can also be taken as adjustable parameters. $U_{\mathrm{Born},ij}$, on the other hand, is a softer potential, allowing for greater interatomic overlap:

$$U_{\mathrm{Born},ij} = A_{ij} \exp\left(- \frac{r_{ij}}{\rho_{ij}} \right) - \frac{C_{ij}}{r_{ij}^6} + \frac{D_{ij}}{r_{ij}^8}, \tag{27}$$

where A_{ij}, ρ_{ij}, C_{ij} and D_{ij} are positive force field parameters. U_{vdW} can, of course, be written as a combination of several types of potentials: e.g. when modelling polymer/garnet composite solid electrolytes, the LJ potentials can be employed to model the interactions in the polymer phase, while the Born potential can be used to model interactions within the garnet. In any scenario, $U_{\mathrm{vdW}} = \frac{1}{2} \sum_{i,j=1}^{n} U_{\mathrm{vdW},ij}$.

4.2 Training Dataset

It is important to note that force fields partition the total electronic energy into well defined atom-atom contributions, such as Coulomb, polarization, dispersion, etc. However, it is impossible to fully separate the intricate electronic effects this way. The proper choice of a functional form of a force field and a set of data used to parameterize it (the training dataset, TD) usually makes it possible to generate a force field that is valid at least for specific problems and within the chemical and environmental constraints from the TD.

The TD typically comprises data obtained either from *ab initio* or semi-empirical quantum mechanical (QM) calculations, or from experimental measurements such as neutron, X-ray and electron diffraction, NMR, Raman spectroscopy, etc. Naturally, experiments can only probe a limited set of properties and their reliability depends on the quality of the experimental setup and the examined sample. The synthesis of many battery materials is by no means an exact science, and structural defects and impurities can be significant. That is why, it is expected that TDs from extensive QM calculations lead to more generally applicable force fields compared to those from experimental data. However, QM calculations still contain plenty of approximations, and a QM-based force field is of little or no use if it cannot reproduce experimental values or trends. In many cases, force fields trained through QM-based TDs are further fine-tuned with respect to experimental measurements.

4.3 Optimization Strategy to Perform the Fitting

The optimization strategy refers to the technique through which the set of optimal parameters is determined. When using an experimental TD, the general idea is to

find the set of force field parameters $\gamma_1, \ldots, \gamma_M$ that minimizes the scoring function

$$f(\gamma_1, \ldots, \gamma_M) = \sum_{i=1}^{L} \parallel \omega_i(\langle\Omega\rangle_{\mathrm{sim},i} - \Omega_i^0) \parallel, \tag{28}$$

where Ω_i^0 is the ith reference observation in the TD, $\langle\Omega\rangle_{\mathrm{sim},i}$ its atomistically simulated value with the trial force field, L the total number of observations, ω_i is the weight given to observation i and $\|\cdot\|$ a suitable norm.

In exploiting a QM-based TD, the scoring function has a rather different form. While experimental TD's are invariably composed of average properties (e.g. unit cell sizes, Young's moduli, etc.) that result from a configurational average in a particular ensemble (even the fastest neutron scattering measurement results from averaging over an infinite number of configurations), QM-based TDs are normally composed of instantaneous snapshots of the equilibrated system. Hence, one can set up the particles in the exact positions provided by the snapshots, and then find the values of $\gamma_1, \ldots, \gamma_M$ that achieve, for example, the total energy closest to the QM energy for each snapshot. This in fact is what most studies have done. A much more effective strategy is to additionally adjust $\{\gamma_k\}$ to multidimensional variables such as forces and stresses, which are also available from QM calculations. This is precisely what the so-called *force-matching algorithm* (FMA) does and what we employ in our study. For a training dataset consisting of L configurations, a suitable FMA scoring function is given by [22]

$$f(\gamma_1, \ldots, \gamma_M) = \sum_{l=1}^{L} \left[3\omega_e(e_l - e_l^0)^2 + \frac{1}{2}\omega_s \sum_{p=1}^{6}(s_{p,l} - s_{p,l}^0)^2 + \sum_{i=1}^{3n_l}(f_{i,l} - f_{i,l}^0)^2 \right], \tag{29}$$

where n_l is the number of particles in configuration l. $\{e_l\}$, $\{s_{p,l},\ p = 1, \ldots, 6\}$ and $\{f_{i,l}, i = 1, \ldots, 3n_l\}$ are the energies, stresses and forces obtained with the trial force field, respectively. The superindex 0 denotes the reference values from the TD. ω_e and ω_s are user-defined weights to balance the amount of available information for each quantity. Such a scoring function has been proposed and implemented in the open software *potfit*, developed by Brommer et al. [22, 23]. We have adjusted this function to parametrization of a broader range of models by incorporating in it core-shell polarizable potentials and angular terms [18, 32].

The scoring functions (28) and (29) can be highly multidimensional and non convex. Occasionally, some of the force field parameters can be reliably set to known values from similar force fields, simplifying the problem and allowing the use of local optimization strategies [19]. In most cases, however, stochastic global optimization techniques, such as simulated annealing, are necessary to avoid local minima. This, of course, comes with the hurdle of finding suitable adjustable parameters for the algorithm itself.

5 Applications

Below, we summarize the highlights of recent work performed in our group on the atomistic simulation of battery materials for LIBS and NIBS, using the numerical schemes described above. Specifically, we focus on cathode material olivine $NaFePO_4$ for NIBs, and solid electrolyte material $Li_7La_3Zr_2O_{12}$ for LIBs.

5.1 Na Diffusion in Cathode Material Olivine $NaFePO_4$ for NIBS

Olivine $LiFePO_4$ is likely the most studied commercial cathode for LIBs [73]. It provides high stability, rate capability, and sustained high voltage throughout the discharge cycle. In principle, one could expect $NaFePO_4$ to inherit these properties from its isostructural lithium counterpart, making it a suitable cathode for NIBs. The first fundamental studies revealed that the *intercalation mechanisms* (see Sect. 2.1) of Li^+ and Na^+ in $FePO_4$ are, however, significantly different [81]. While Li_xFePO_4 ($0 \leq x \leq 1$) is stable at all values of x, Na_xFePO_4 is only stable at discrete Na^+ contents: $x \in \{0.0, 0.66, 0.83, 1.0\}$ [66]. This means that during the discharge, the structure of Na_xFePO_4 evolves through combinations of these stable, highly organized phases (Fig. 4), adding another level of complexity to the study of Na^+ intercalation as compared to that of Li^+. This issue is particularly relevant when studying dynamic properties such as Na^+ mobility using simulations, requiring large supercells and long simulation times to account for possible sodium orderings. These requirements make the use of first-principles methods, such as density functional theory (DFT), prohibitive in terms of computational cost. We addressed this computational challenge using atomistic simulations. Two key elements are required for this task: an accurate force field and an efficient sampling technique.

Whiteside et al. [75] developed a force field for the structural simulation of $NaFePO_4$, incorporating the polarizability of the oxygen atoms through the core-shell model. We will denote such force field as **Whiteside-ff** from here on. However, removal of one Na^+ ion leads to the oxidation of one iron (i.e. iron goes from Fe^{2+} to Fe^{3+}), which means that Na_xFePO_4, with $x < 1$, contains a combination of both Fe^{2+} and Fe^{3+} (Fig. 4b). Whiteside-ff does not consider the presence of Fe^{3+} and, as a consequence, is not suitable for a general study of charge transport in Na_xFePO_4. To overcome this issue, we developed a new force field for this system, the **Na_xFePO_4-ff**, using accurate DFT calculations at the stable Na^+ contents. The force field employs the cs-adi model described in Sect. 4.1 to incorporate polarizability in oxygen and iron atoms.

For configurational sampling of the system, conventional MD (see Sect. 3.1) has two key disadvantages. On the one hand, it requires many simulation steps for the estimation of the room temperature diffusivities. On the other hand, the cs-adi version of the core-shell polarizability model allows only for small time steps,

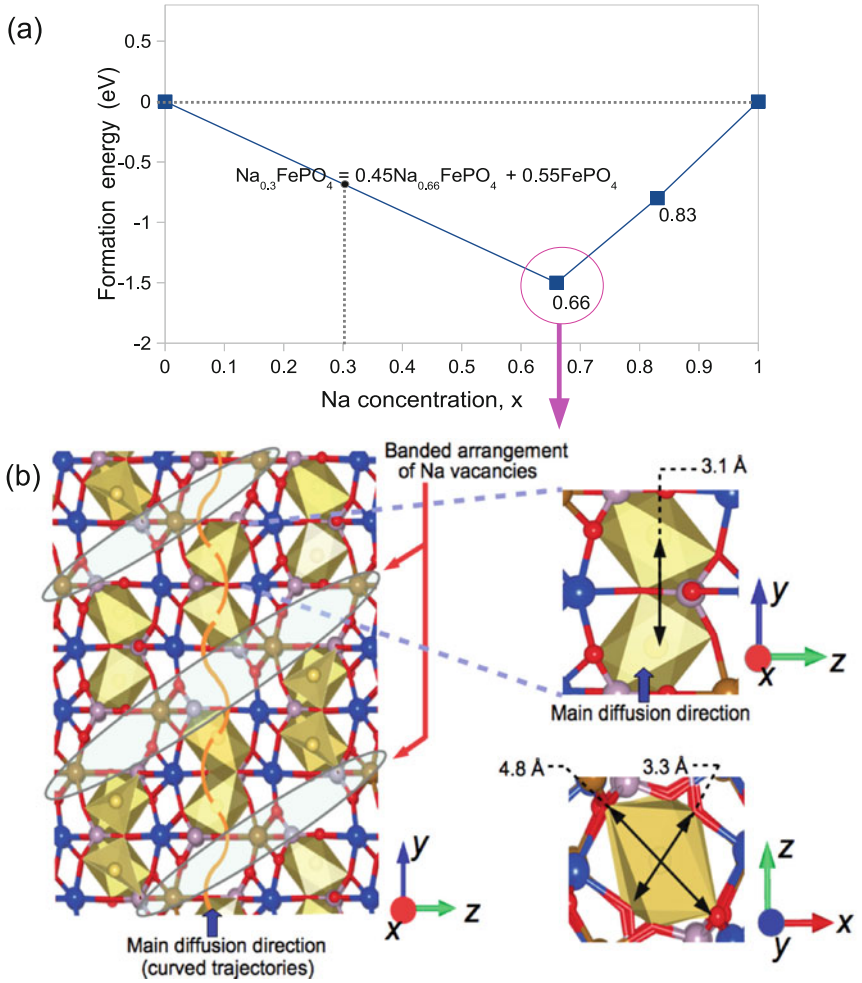

Fig. 4 (**a**) The convex-hull (blue line) of Na_xFePO_4. At any x, all possible system structures will have an energy of formation above the convex hull. As a consequence, the most stable structure for a given x will be a segregated mixture of the structures corresponding to the closest vertices in the convex-hull. These vertices are located at $x = 0.0, 0.66, 0.83$, and 1.0 [66]. For instance, a mol of $Na_{0.3}FePO_4$ will comprise 0.45 moles of $Na_{0.66}FePO_4$ and 0.55 moles of $FePO_4$. **b** *Left*: Structure of $Na_{0.66}FePO_4$: O^{2-} in green, P^{5+} in purple, Fe^{2+} in blue and Fe^{3+} in red. Na^+ is coordinated by six O^{2-} atoms (yellow octahedra). The curved trajectory followed by Na^+ along one of the channels in the main diffusion direction, **y**, is depicted as the solid orange line. Na^+ vacancies and Fe^{3+} ions follow a highly organized banded arrangement (similarly for $x = 0.83$). *Right-top*: close up showing the characteristic Na^+ jumping distance. *Right-bottom*: Cross section of a diffusion channel along **y**. The channels along **x** and **z** are much narrower, which means that jumps in these directions are rare. (Adapted with permission from [18]. Copyright (2018) American Chemical Society)

increasing the computation time even further. In sight of this, we selected instead the in-house RSM-GSHMC technique as our simulation tool [32] (see Sect. 3.3), which simultaneously provides enhanced sampling while incorporating a scheme to minimize the computational impact of the small shell mass.

5.1.1 Force Field Development

Derivation

Ionic polarizability plays an important role in the dynamics of Na_xFePO_4. Similarly to Whiteside-ff [75], we divided the Fe^{2+} and O^{2-} ions into polarizable core-shell units. Hereafter, O_{sh} and Fe_{sh} will refer to the O^{2-} and Fe^{2+} shells, respectively. For the bonded interactions, we considered only the angular potential between the covalently linked O-P-O ions in PO_4 tetrahedra, following

$$U_{\text{bonded}} = U_{\text{angle}} = k_a \sum_{i=1}^{n_a} \frac{1}{2}(\theta_k - \theta_0)^2,$$

where n_a is the number of angles, and k_a and θ_0 are force field parameters. Non-bonded interactions were represented by a sum of the Coulomb (26) and Born (27) potentials. Only interactions between X - O^{2-}_{sh} pairs were considered in the Born contribution (X = Fe^{2+}_{sh}, Fe^{3+}, Na^{+}, P^{5+}, O^{2-}_{sh}). The cores of Fe^{2+} and O^{2-} only interacted electrostatically. The TD (see Sect. 4.2) comprised 58 olivine Na_xFePO_4 configurations consisting of (a) 11 quantum mechanically optimized structures at 0 K, ranging from 72 to 84 atoms, and (b) 58 equilibrated snapshots taken out of *ab initio* MD trajectories of an ideal $NaFePO_4$ crystal at 500 and 1000 K. All TD configurations were computed with the plane wave DFT code VASP [50]. As an optimization strategy, we used the force-matching algorithm described in Sect. 4.3 with the scoring function (29) and the adaptive simulated annealing scheme implemented in the in-house extended version of the open source software *potfit* [18, 22, 23].

Since the core-shell unit is simply a construct to introduce polarizability within an empirical force field, the *ab initio* dataset does not provide information on how to specify the core and shell coordinates. For the core, a sensible solution consists in setting its position to that of the actual ion, because the core carries most of the core-shell unit mass. For the shell, its position should be selected in such a way that the total force on it is zero. We proposed a consistent approach to treat the shells positions, which have usually been randomly chosen in previous works [18]. We fix the spring constant and charge distribution for all core-shell units prior to starting the parameter estimation. Then, given that dispersion interactions in a core-shell unit l are assigned to a shell only, the total force on a core l, $\mathbf{F}_{l,\text{core}}$, becomes

$$\mathbf{F}_{l,\text{core}} = \mathbf{F}^{\text{elect}}_{l,\text{core}} + k_l(\mathbf{r}_{l,\text{shell}} - \mathbf{r}_{l,\text{core}}),$$

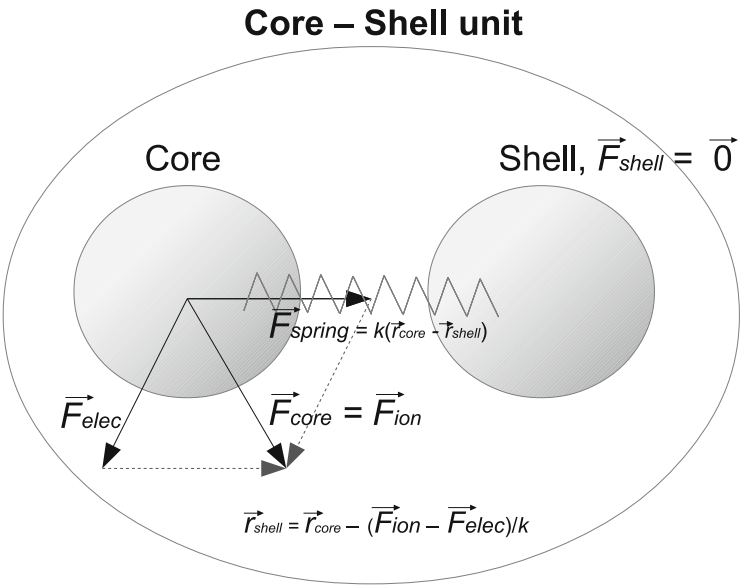

Fig. 5 Correct positioning of the shell within a core-shell unit. If the charges and the spring constant k are set, the fact that dispersive forces do not act on the core uniquely determines the exact position of the shell

where $\mathbf{F}^{\text{elect}}_{l,\text{core}}$ is the electrostatic force on a core l, and $\mathbf{r}_{l,\text{core}}$ and $\mathbf{r}_{l,\text{shell}}$ are the respective core and shell positions. Since the force on a shell must in principle be zero, $\mathbf{F}_{l,\text{core}}$ should correspond to the force on the lth ion $\mathbf{F}_{l,\text{ion}}$, estimated from DFT. Thus, the shells must be allocated such that

$$\mathbf{r}_{l,\text{shell}} - \mathbf{r}_{l,\text{core}} + (\mathbf{F}_{l,\text{ion}} - \mathbf{F}^{\text{elec}}_{l,\text{core}})/k_l = 0, \quad \text{for } l = 1, \ldots, L. \tag{30}$$

$\mathbf{F}^{\text{elec}}_{l,\text{core}}$ depends only on the charge distribution and atom positions. Hence, expression (30) represents a system of $3L$ force field-independent equations and $3L$ unknown variables for the shells coordinates. In this work, the charge distribution and spring constants were taken from [75]. The equations in (30) were solved by a simple fixed-point iteration scheme. The schematic of the method is presented in Fig. 5.

Validation

The validation involved a comparison of experimental data *outside* the TD with the results obtained through atomistic simulations incorporating the proposed force field. To simulate the present system we chose the RSM-GSHMC simulation method, which helped to reduce potential negative effects on the kinetic properties

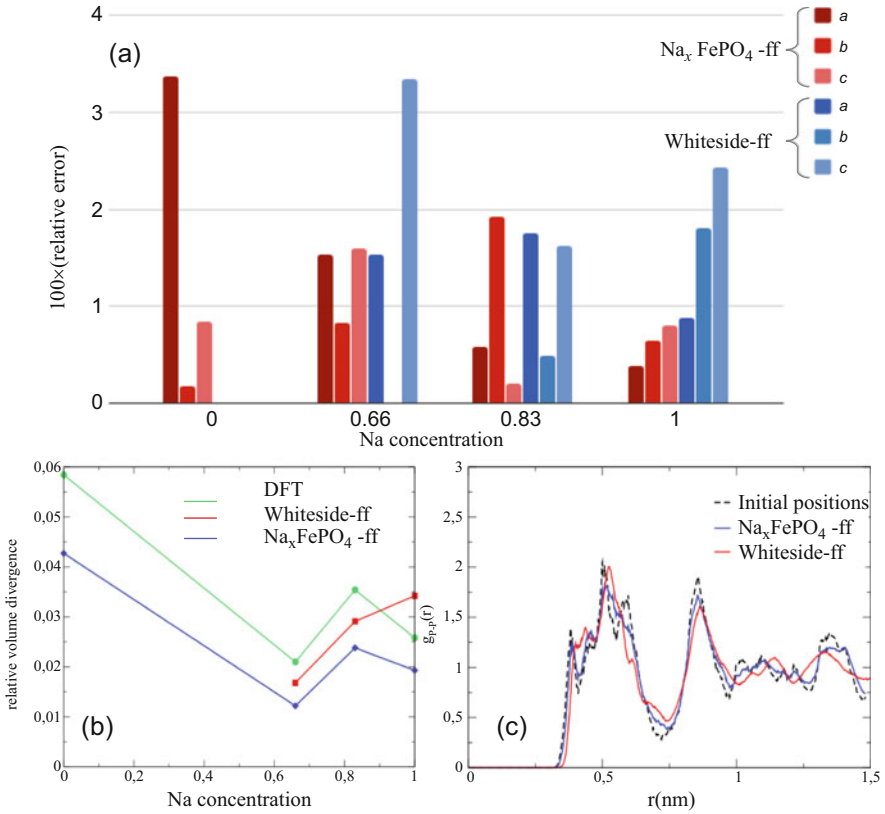

Fig. 6 Force field validation. All simulated values in this figure were obtained by combining Na_xFePO_4-ff or Whiteside-ff with the RSM-GSHMC technique. In Whiteside-ff, the parameters involving Fe^{3+} were taken to be the same as those for Fe^{2+}. (**a**) Relative error $\times 100$ for the unit cell parameters (a, b, c) with respect to experimental measurements at room temperature [66]. (**b**) Relative volume divergence with respect to experimental results at room temperature. (**c**) Radial distribution functions for phosphorous atoms in a $Na_{0.58}FePO_4$ system after 10 ps at 300 K. The dashed line corresponds to the initial positions, which is the same for both force fields

of the system caused by the use of the cs-adi model. We further combined RSM-GSHMC with the MAIA integrator (Sect. 3.4) to achieve the highest possible integration accuracy when using two-stage splitting methods, including Verlet.

The final set of parameters of Na_xFePO_4-ff can be found in [18]. Figure 6 compares the accuracy of Na_xFePO_4-ff and Whiteside-ff. Figure 6a depicts the relative error $\times 100$ for the unit cell parameters (a, b, c) with respect to experimental measurements at room temperature [66]. In the absence of Na^+ ($x = 0$), Whiteside-ff leads to numerical instability and values cannot be extracted. For $x = 0.66$ and $x = 0.83$ both force fields display comparable levels of accuracy, and at $x = 1.0$, Na_xFePO_4-ff is clearly better. When comparing the volume divergence at room temperature, Fig. 6b shows that Na_xFePO_4-ff is clearly superior. The

DFT data are calculated at 0 K and thus, its divergence is high. However, it is clear that Na_xFePO_4-ff follows the same trend as the DFT values. Finally, Fig. 6c presents the radial distribution functions between phosphorous atoms, $g_{P-P}(r)$, in the $Na_{0.58}FePO_4$ system after 10 ps at 300 K. The dashed line corresponds to the initial configurations, which are the same for both force fields. After 10 ps of simulation, there is a distortion in the position of the peaks for Whiteside-ff with respect to the initial $g_{P-P}(r)$, evidencing the additional repulsion between oxygens of adjacent tetrahedrals when a Na^+ ion is removed. This is an anomalous effect not observed with Na_xFePO_4-ff due to the reoptimized parameters. Such an anomaly leads to errors in the diffusivities when using Whiteside-ff.

5.1.2 MD vs. RSM-GSHMC

Figure 7a presents the MSD for Na^+ at 700 K in the main diffusion direction, y, obtained from both traditional MD and RSM-GSHMC. Convergence to the equilibrium slope that provides the diffusion coefficient through Eq. (1) is reached nearly 2 ns quicker through RSM-GSHMC, demonstrating its ability to sample the configurational space more efficiently than MD. The noise in the MSD curves in Fig. 7 is at least partially due to the fact that a fraction of the Na^+ atoms do not perform any jump or jumps only once. While the situation could be improved by extending the simulations, the cs-adi model severely limits the simulation time-step, and further increasing the simulation time comes with a significant increase in the computation time.

Figure 7b shows the three-dimensional diffusion coefficients of Na^+, $D = \frac{1}{3}(D_x + D_y + D_z)$, for a range of temperatures using RSM-GSHMC with both force fields. We also plot results for similar simulations using standard MD with Na_xFePO_4-ff. Comparison of the three curves suggests that not only does the force field affects the diffusion coefficients but the sampling efficiency of the chosen sampler also does. Indeed, at higher temperatures the computed diffusions using MD and RSM-GSHMC combined with the same force field (for equal simulation times) diverge visibly. This is a consequence of the higher sampling efficiency of GSHMC methods [2]. For longer simulation times, both methods are expected to converge [32].

5.1.3 Mechanism of Na^+ Diffusion

Because RSM-GSHMC does a good job in preserving dynamical information, it allows an atom-eye perspective of the physics behind the diffusion dynamics of Na^+ in Na_xFePO_4. We confirmed that the main transport mechanism involves single Na-ion hops through the one-dimensional channels along the y axis (the [010] crystallographic direction). Furthermore, we identified the novel Na-ion diffusion dynamics involving the formation and annihilation of Na^+/Fe^{2+} antisite defects (the exchange of positions between Na^+ and Fe^{2+} ions), which effectively facilitate the migration of Na-ions between adjacent y-oriented channels (see Fig. 8 for a

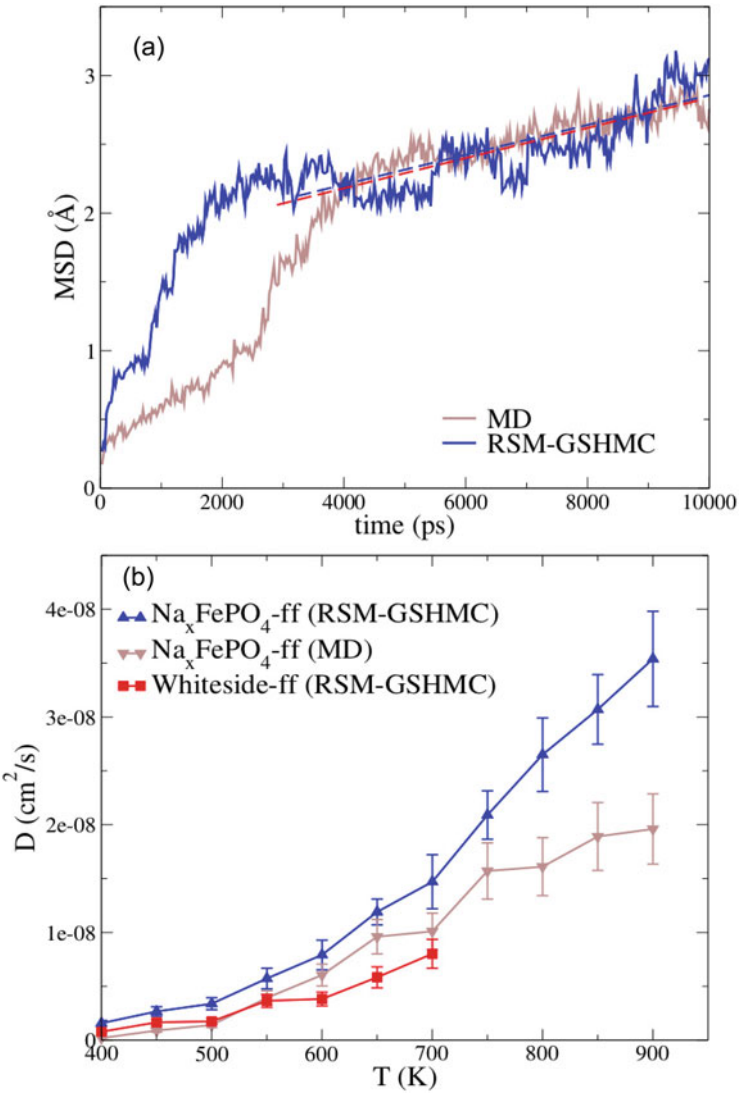

Fig. 7 (**a**) MSD at 700 K in the main diffusion direction, y, using both traditional MD and RSM-GSHMC combined with Na_xFePO_4-ff. Convergence to the equilibrium slope is reached faster through RSM-GSHMC. (**b**) Three-dimensional diffusion coefficient as a function of temperature (legends indicate force field and sampler combinations) (Adapted with permission from [18]. Copyright (2018) American Chemical Society)

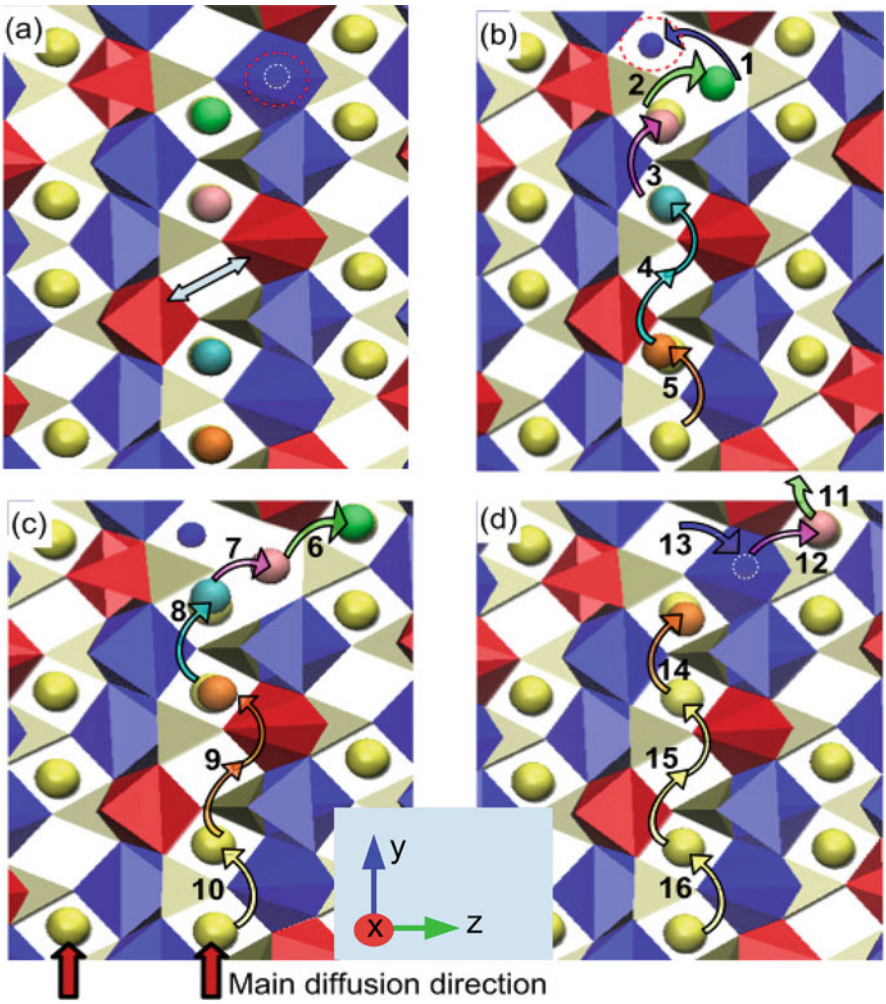

Fig. 8 Two-dimensional trajectory at 700 K. At this temperature, the coordination polyhedra are slightly distorted. The red octahedra are $Fe^{3+}O_6$ units, the blue octahedra are $Fe^{2+}O_6$ units, and the tetrahedrals correspond to $(PO_4)^{-3}$ units. The green, pink, cyan and orange atoms are tagged Na^+ ions; the remaining Na^+ ions are colored in yellow. The numbers in the figure specify the order in which atomic jumps occurred. (**a**) Initial, defect-free configuration. The double arrow shows the diametrically opposed Fe^{3+} ions around an extrinsic vacancy. (**b**) Antisite-like defect. A Fe^{2+} atom (encircled in red in (**a**) and (**b**) moves to the adjacent extrinsic vacancy (jump 1), allowing the green Na^+ to jump to the empty Fe^{2+} site (jump 2). (**c**) Since the central diffusion channel is blocked, the green Na^+ transfers to an adjacent channel (jump 6), leading to the cascade of jumps 7–10. (**d**) After the defect in the Fe^{2+} site is removed (jump 13), one-dimensional diffusion is reestablished. Notice that Na^+ diffuses through the extrinsic vacancies in single, long curvilinear jumps (4, 9, and 15) (Adapted with permission from [18]. Copyright (2018) American Chemical Society)

detailed explanation). Na^{+}/Fe^{2+} antisite defects were expected to block y channels and, therefore, hinder Na-ion mobility in the bulk material. In contrast, our results revealed that such defects can indeed favor Na-ion exchange between parallel y channels. This result is in general agreement with simulations of two-dimensional diffusion in $LiFePO_4$ [69]: occasional jumps of charge carriers in the y axis can overcome (at a cost of reduced diffusivity) the damaging effect of antisite defects.

5.2 *Li^{+} Diffusion in Cubic Ga/Al Substituted $Li_7La_3Zr_2O_{12}$ (LLZO) Solid Electrolyte*

LLZO garnet is a strong solid electrolyte contender for all-solid-state LIBs, which can in principle eliminate the safety problems associated with current liquid electrolyte-based batteries [9, 62]. LLZO garnets can crystallize in at least two different crystal structures, a poorly Li-ion conductive tetragonal structure (t-phase) and a significantly more conductive cubic one (c-phase) (Fig. 9). The c-phase structure contains partially occupied Li-sites (at any given instant they may or may not contain a Li^{+}) and is unstable at room temperature, but can be stabilized by substitution of, for instance, Li^{+} by Al^{3+} and Ga^{3+} ions [64]. Despite having the same formal charge, gallium substitution is found to lead to higher room temperature conductivities ($\sim 10^{-3}$ S/cm) than aluminium substitution [13, 62, 63] ($\sim 10^{-4}$ S/cm). However, the origin and degree of this phenomenon is yet to be fully understood.

We tackled this question using atomistic simulations, performed with traditional MD and our in-house GSHMC simulation method (Sect. 3.3). For this study, the

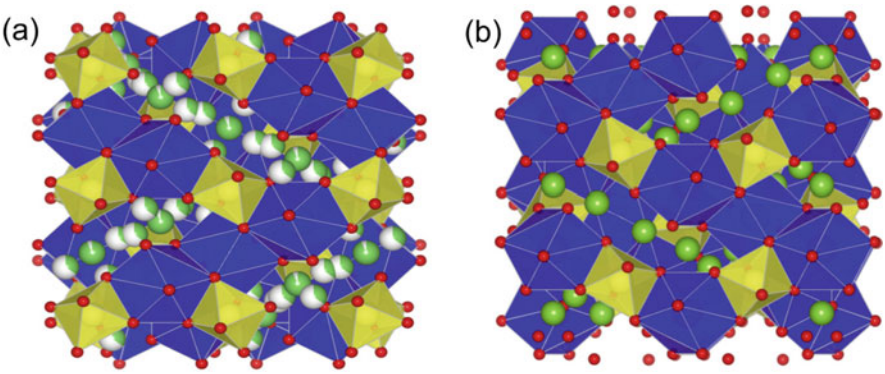

Fig. 9 Crystal structures of garnet-type LLZO. (**a**) c-phase. Li atoms are represented by partially filled spheres, indicating partial occupancy. (**b**) t-phase, containing an ordered distribution of fully occupied Li-sites (Li^{+} ions are shown in green). La dodecahedra and Zr octahedra are shown in blue and yellow, respectively. The red spheres correspond to oxygen atoms. (Reproduced with permission from [19]. Copyright (2019) Elsevier)

chosen force field was based on that from Jalem et al. [47], but further adjusted with respect to experimental structural data reported in [63]. Details on the fitting procedure can be found in [41]. Below, we will use the notation Ga_yAl_x-LLZO to denote $Li_{7-3(x+y)}Ga_yAl_xLa_3Zr_2O_{12}$.

5.2.1 MD vs. GSHMC

To compare the sampling efficiency of MD and GSHMC methods for the simulation of the substituted LLZO systems, we calculated the integrated autocorrelation functions ($IACF$) of the potential energy U

$$IACF^U = \sum_{l=0}^{K'} ACF(l), \tag{31}$$

where $ACF(l), l = 0, \ldots, K \leq K'$ is the standard autocorrelation function for the time series U_k of K samples, $k = 1, \ldots, K$. Lower values of $IACF$ indicate a more efficient sampling, since it estimates the time required, on average, to generate an uncorrelated sample. In Fig. 10, we present the values of $IACF^U_{\text{MD}}/IACF^U_{\text{GSHMC}}$ for $Ga_0Al_{0.10}$-LLZO and $Ga_0Al_{0.12}$-LLZO in the t-phase and $Ga_0Al_{0.20}$-LLZO and $Ga_0Al_{0.25}$-LLZO in the c-phase at room temperature in the NVT ensemble. GSHMC simulations exhibit a sampling performance up to 25 times better than MD for the tested systems in the t-phase. In contrast, for the c-phase the performance of both methods are comparable, because the intersite energy barriers are relatively low. Based on this analysis, we have used GSHMC for simulations of the t-phase [41], as well as for simulations of the c-phase below room temperature, where the intersite

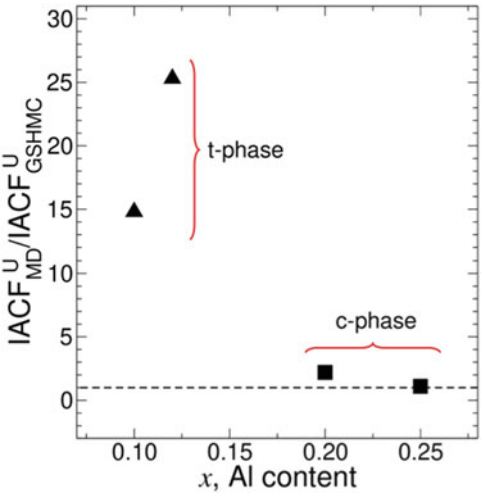

Fig. 10 Relative $IACF^U$ with respect to GSHMC at T = 298 K achieved when calculating the potential energy during the equilibration stage with the MD method. (Reproduced with permission from [19]. Copyright (2019) Elsevier)

barriers are much more significant [19]. Otherwise, we chose to use the conventional MD approach in order to minimize the efforts required for tuning of the GSHMC parameters.

5.2.2 Simulation Results

Length and Time Scales of Li^+ Diffusion in Cubic LLZO

A simple way to understand the Li^+ lattice in the c-phase is to consider it as a three-dimensional diffusion network, in which each node is connected to its closest four neighboring nodes through one intermediate site. Those intermediate sites are coordinated by six oxygen atoms, and thus are called Octahedral Li-sites, O_h. The nodes, in turn, are coordinated by four oxygen atoms, and thus are called tetrahedral sites, T_d. Hence, a typical Li^+ diffusion path involves a succession of jumps of the form $O_h \rightarrow T_d \rightarrow O_h \rightarrow T_d \rightarrow \ldots$. In Fig. 11, we provide an atom's eye view of Li-ion transport by considering a complete trajectory of a selected Li^+ ion across simulations at different temperatures and total time lengths.

Li-ion transport is isotropic. At 313 K, the selected Li^+ crosses frequently different T_d and O_h sites in a relatively short lapse of time (80 ns). In addition, we notice that a Li^+ ion can visit the same T_d site several times. This is revealed by the presence of branches centered in the nodal T_d sites along the diffusive path as shown in the inset of Fig. 11. When the temperature is decreased to 253 K, the distance covered by the Li^+ ion in 80 ns decreases. In fact, even after 200 ns the number of T_d and O_h sites visited has decreased considerably in comparison with the simulation at 313 K, resulting as well in a lower number of branches along the diffusive path. Finally, at 193 K we see that diffusion is severely hindered, with the Li^+ ion barely visiting more than one T_d site in less than 80 ns.

Variation of Li^+ Conductivity with Ga/Al in Cubic LLZO

Figure 12 depicts the variation of the ionic conductivity σ_{Li} (calculated through (2)) with the inverse of temperature for $Ga_{0.2-x}Al_x$-LLZO and $x = 0.0$, 0.1 and 0.2. It is clear that for a constant concentration of substituents, increasing the ratio of Ga^{3+} to Al^{3+} has a positive effect on the conductivity. However, as temperature increases, the difference between Ga^{3+} and Al^{3+} vanishes, in agreement with recent experimental work [63]. This observation was explained on the grounds that a Ga^{3+} content above 0.15 leads to a phase change, in which shortcuts to the typical $O_h \rightarrow T_d \rightarrow O_h \rightarrow \ldots$ diffusion path appear. However, if this was the only explanation, the curves would not display the observed temperature dependance.

Through a detailed analysis of the radial distribution functions (see [41] for details) we were able to determine that the local environment around Ga^{3+} and Al^{3+} cations disrupts active diffusion paths. Hence, regions within the crystal volume that do not contribute to Li-ion conduction arise. Figure 13 depicts volume density maps

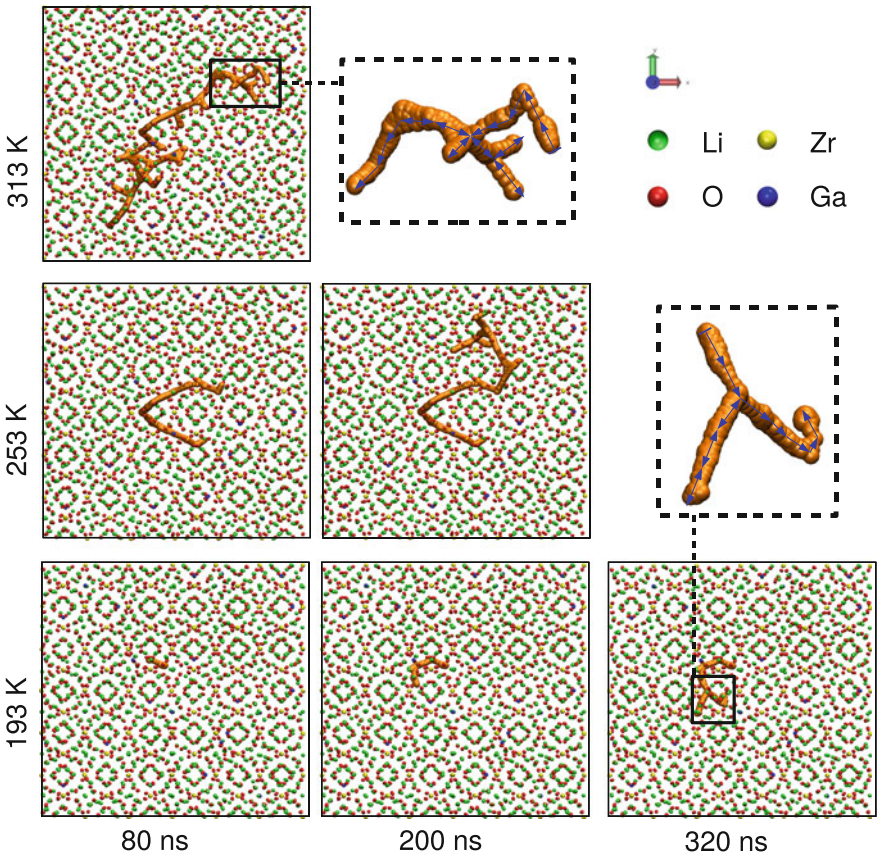

Fig. 11 Simulated trajectories of an individual Li^+ ion (orange) in the $Ga_{0.2}Al_{0.0}$-LLZO system at different temperatures. From *top* to *bottom* the temperature decreases, whereas from *left* to *right* the simulation time increases. Li, Zr, O and Ga ions are depicted in green, yellow, red and blue, respectively (La ions are not shown for simplicity) (Reproduced with permission from [41]. Copyright (2019) American Chemical Society)

of mobile Li^+ ions at 233 K in $Ga_{0.2}Al_{0.0}$-LLZO and $Ga_{0.0}Al_{0.2}$-LLZO, showing a depletion of active diffusion paths around Ga^{3+} and Al^{3+}. However, because of the particular parameters of the Al^{3+}–O^{2-} interaction potential, the disruptive effect of Al^{3+} is more pronounced. As temperature increases, Li^+ ions acquire enough thermal energy to overcome the barriers surrounding Ga^{3+} and Al^{3+} ions, eliminating the difference in performance between both cations.

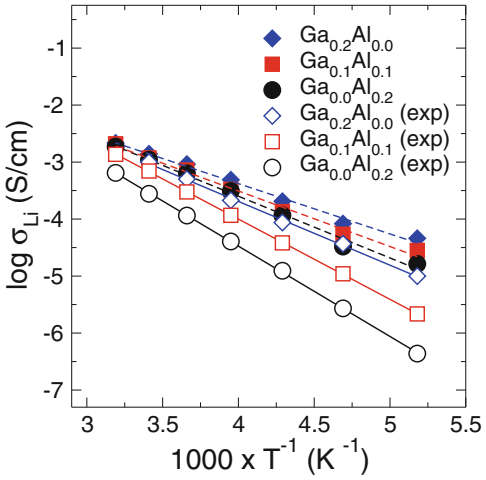

Fig. 12 Calculated Li-ion conductivity as a function of inverse temperature for $Ga_{0.2-x}Al_x$ ($x = 0.0,\ 0.1,\ 0.2$). Filled data points refer to simulation data. Experimental values, represented by empty symbols, were taken from Ref. [63]. Notice that the simulated data overestimate the experimental values, because the boundary resistances discussed in Sect. 2.2.1 cannot be easily incorporated. Those resistances are particularly high in $Ga_{0.0}Al_{0.2}$-LLZO, which has a powdery macrostructure. However, the trends in the simulated and experimental curves are clearly consistent

Variation of Conductivity in the Experimental Data for $Ga_{0.0}Al_x$-LLZO

There is significant variability in the literature regarding the conductivity of Gal_0Al_x-LLZO. Given the recently reported gradients in Al content within a single sample [72], one potential scenario is that Al-rich regions crystallize in the c-phase, while the Al-poor regions form the t-phase. The second potential scenario is that thermodynamic equilibrium can be established between the two phases at the same x. To the best of our knowledge, neither scenario can be categorically dismissed. Presuming that thermodynamic equilibrium exists between the c- and t-phases at some Al contents, we can estimate the proportion of each phase through an adequate mixing model. Assuming that both phases mix randomly and homogeneously at the microscopic scale ($\sim 10^{-6}$ m), Bruggeman's effective medium model [51] predicts that

$$v_c \frac{\sigma_c - \sigma_m}{\sigma_c + 2\sigma_m} + v_t \frac{\sigma_t - \sigma_m}{\sigma_t + 2\sigma_m} = 0, \tag{32}$$

where v_i is phase volume fraction, σ_i is conductivity and $i = \{c, t, m\}$ denotes the cubic, tetragonal, and mixed phases, respectively. By equating the c-phase volume fraction v_c to the experimental values, it is possible to determine the theoretical conductivity of the mixed c- and t-phases using (32). Considering the experimental works by Botros et al. [21] and Tsai et al. [71], who report weight percentages

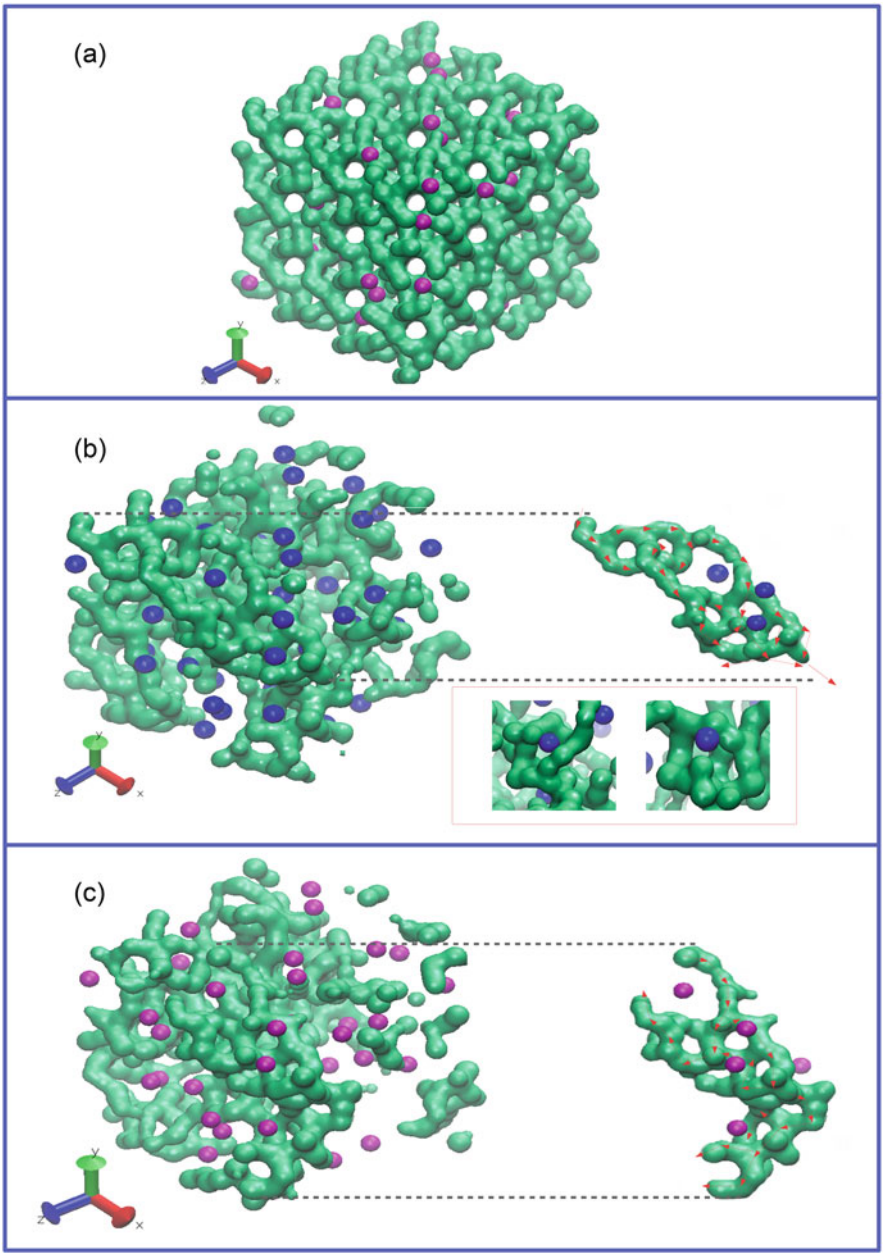

Fig. 13 Density volume maps at 233 K for all Li^+ ions in $Ga_{0.0}Al_{0.2}$-LLZO (**a**), and only those Li^+ ions jumping at least one T_d site-T_d site length after 190 ns (>4 Å) in $Ga_{0.2}Al_{0.0}$-LLZO (**b**) and $Ga_{0.0}Al_{0.2}$-LLZO (**c**). Al^{3+} and Ga^{3+} ions are represented by magenta and blue spheres, respectively. (**a**) Can be interpreted as the total available volume for Li-ion diffusion, while (**b**) and (**c**) correspond to the active volume where diffusion is actually occurring. Clearly, active diffusion paths avoid the vicinity of Al^{3+} and Ga^{3+} (see insets to the *right* of (**b**) and (**c**) but the disruption of diffusion paths in $Ga_{0.0}Al_{0.2}$-LLZO is much more severe (Reproduced with permission from [41]. Copyright (2019) American Chemical Society)

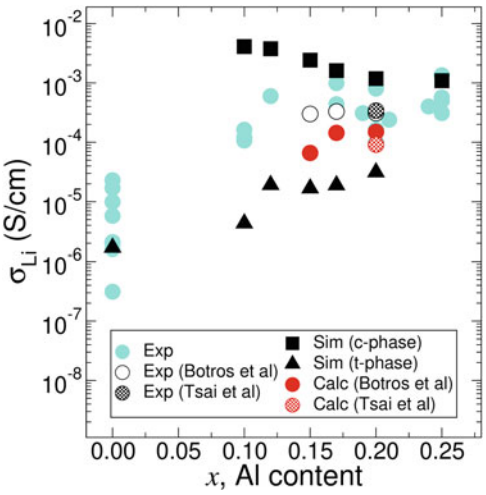

Fig. 14 Experimental and simulated Li-ion conductivities, σ_{Li}, of Al_x-LLZO for $x = [0.0, 0.10, 0.12, 0.15, 0.17, 0.20, 0.25]$ at room temperature. Cyan circles correspond to experimental data taken from several experimental studies (the complete list of references can be found in the caption of Fig. 8 in [19]). Empty and dotted circles correspond to the experimental conductivities from Botros et al. [21] and Tsai et al. [71], respectively, who provide the percentages of c- and t-phases present in their samples. Filled squares (triangles) correspond to σ_{Li} for c-phase (t-phase) obtained in this work. Red filled and dotted circles correspond to the conductivities obtained by combining Bruggeman's model in (32) with the simulated σ_{Li} to represent the coexistence of t- and c-phases at the proportions reported in Botros et al. [21] and Tsai et al. [71] (Reproduced with permission from [19]. Copyright (2019) Elsevier)

for mixed cubic/tetragonal samples, we estimated the corresponding mixed phase conductivities by using conductivities simulated over the range of Al content. The predictions are shown in Fig. 14 as red circles, while the measurements from [21] and [71] are highlighted through the empty circles. Our predictions are in good agreement with the conductivities provided by [21] and [71], reproducing the experimental results better than either of the pure phases at all Al contents. Thus, we provide a sound basis for the analysis of phase coexistence in substituted LLZO and similar polycrystalline solid electrolyte materials.

6 Conclusions

In this work, we present a brief review of the work performed in our team towards multiscale modelling and simulation of advanced battery materials. We have attempted to make the current material self-contained, and thus we have included sections on the basic science and engineering aspects of LIBs and NIBs (Sect. 2), as well as a short discussion of conventional simulation methods (Sects. 3.1 and 3.2)

and force field development (Sect. 4). These sections can be selectively avoided by experienced practitioners.

We focus on the family of Modified Hamiltonian Monte Carlo (MHMC) methods recently introduced for atomistic simulations of complex systems [1, 2, 4, 32, 45, 68] and later adapted to multiscale [31] and mesoscale simulations [3]. In particular, we have found members of this family, the Generalized Shadow Hybrid Monte Carlo (GSHMC) method [2] and its latest extension Randomized Shell Mass GSHMC (RSM-GSHMC) [32], to be powerful tools for unveiling the structural, thermodynamic and transport properties of solid state battery materials. As application examples, we present our recent results in the modelling of ionic conduction in $NaFePO_4$ cathode material for NIBs and LLZO solid electrolyte material for LIBs [18, 19, 32, 41]. Future work will focus on two key areas: probabilistic screening of advanced energy materials and multiscale simulation of composite materials.

Probabilistic Screening of Advanced Energy Materials

There is a considerable activity in the field of materials discovery using high-throughput computing combined with statistical screening approaches. However, incorporating macroscopic materials properties of practical importance, such as ionic conductivity, tensile moduli or phase transition temperatures into a materials design scheme in an efficient way remains a standing challenge.

Bayesian parameterization provides a principled way of combining prior information with data, within a solid decision theoretical framework. Past information and experimental data can readily be accounted for and form a prior distribution for future analysis. Moreover, when new observations become available, the previous posterior distribution can be used as a prior. More importantly, it provides interpretable answers from an experimental standpoint, such as "the optimal compound has a probability of 0.95 of falling in a 95% credible interval".

Our in-house Bayesian parameterization technique, the Mix & Match Hybrid Monte Carlo (MMHMC) method [60], will be at the core of a novel framework that will combine incoming data from atomistic simulations and information from experiments, in order to provide the distribution of compositions that is most likely to maximize the expectation of a desired set of macroscopic properties (Fig. 15).

Multiscale Simulation of Composite Materials

In Sect. 2, we have briefly mentioned that one strategy to develop novel battery components with properties that no individual material has, is through the combination of several types of materials into segregated multiphase components called composites. Often, one of the phases is organic (e.g. a polymer) that provides mechanical flexibility, while the other is composed by inorganic particles (e.g. ionic crystals) providing good conductivity. The atomistic simulation of diffusional exchange between the various phases in composite materials is a relatively new subject. Despite the difficulty to experimentally examine the interface (and hence validate computational studies), simulations can provide very useful insights regarding the main barriers to particle exchange, and how the chemistry and environmental conditions affect them. Moreover, with advanced sampling methods

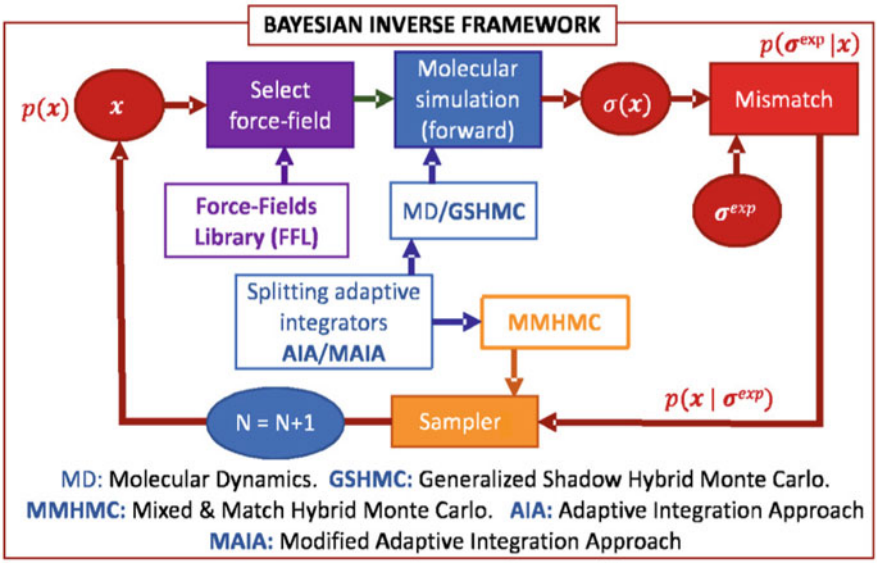

Fig. 15 One cycle in the proposed probabilistic materials screening approach. The number of iterations, *N*, the cycle is repeated, is set *a priori* by the user. The algorithms highlighted in bold were developed in our group and are discussed in the body of this manuscript

such as GSHMC combined with splitting integrators, it is feasible to test many realizations of the polymer/crystal interface and systematically study the impact of contact defects. However, simulating an entire inorganic particle surrounded by polymer remains a great computational challenge that has been attempted only with very small nanoparticles. We are working on the coarse-grained simulation of such a system using our in-house simulation technique meso-GSHMC [3]. The transport coefficients and selectivities obtained this way can be incorporated in continuous or effective medium approaches, providing a multiscale modelling framework for the modelling of composite materials.

Acknowledgments We acknowledge the financial support by the Ministerio de Economia y Competitividad (MINECO) of the Spanish Government through grants PID2019-104927GB-C22 and BCAM Severo Ochoa accreditation SEV-2017-0718. This work was supported by the BERC 2018e2021 Program and by ELKARTEK Program, grants KK-2020/00049 and KK-2020/00008, funded by the Basque Government. The research is partially supported by the Basque Government under the grant "Artificial Intelligence in BCAM number EXP. 2019/00432". This work has been possible thanks to the support of the computing infrastructure of the i2BASQUE academic network, DIPC Computer Center and the technical and human support provided by IZO-SGI SGIker of UPV/EHU and European funding (ERDF and ESF).

References

1. Akhmatskaya, E., Reich, S.: The targeted shadowing hybrid Monte Carlo (TSHMC) method. In: Leimkuhler, B., Chipot, C., Elber, R., Laaksonen, A., Mark, A., Schlick, T., Schütte, C., Skeel, R. (eds.) New Algorithms for Macromolecular Simulation, pp. 141–153. Springer, Heidelberg (2006)
2. Akhmatskaya, E., Reich, S.: GSHMC: an efficient method for molecular simulation. J. Comp. Phys. **227**, 4934–4954 (2008)
3. Akhmatskaya, E., Reich, S.: Meso-GSHMC: a stochastic algorithm for meso-scale constant temperature simulations. Proc. Comp. Sci. **4**, 1353–1362 (2011)
4. Akhmatskaya, E., Reich, S.: New Hybrid Monte Carlo methods for efficient sampling: from physics to biology and statistics. Prog. Nucl. Sci. Technol. **2**, 447–462 (2012)
5. Akhmatskaya, E., Bou-Rabee, N., Reich, S.: A comparison of generalized hybrid Monte Carlo methods with and without momentum flip. J. Comp. Phys. **228**, 2256–2265 (2009)
6. Akhmatskaya, E., Fernández-Pendás, M., Radivojević, T., Sanz-Serna, J.M.: Adaptive splitting integrators for enhancing sampling efficiency of modified Hamiltonian Monte Carlo methods in molecular simulation. Langmuir **33**, 11530–11542 (2017)
7. Amin, R., Balaya, P., Maier, J.: Anisotropy of electronic and ionic transport in LiFePO4 single crystals. J. Power Sources **10**, A13–A16 (2007)
8. Amores, M., Ashton, T.E., Baker, P.J.,Cussen, E.J., Corr, S.A.: Fast microwave-assisted synthesis of Li-stuffed garnets and insights into Li diffusion from Muon spin spectroscopy. J. Mater. Chem. A **4**, 1729–1736 (2016)
9. Awaka, J., Kijima, N., Hayakawa, H., Akimoto, J.: Synthesis and structure analysis of tetragonal Li $_7$La $_3$Zr $_2$O $_{12}$ with the garnet-related type structure. J. Solid State Chem. France **182**, 2046–2052 (2009)
10. Barsoukov, E., Macdonald, J.R.: Impedance Spectroscopy: Theory, Experiment, and Applications. Kluwer, Boston (2005)
11. Bauer, A., Song, J., Vail, S., Pan, W., Barker, J., Lu, Y.: The scale-up and commercialization of nonaqueous Na-Ion battery technologies. Adv. Ener. Mat. **8**, 1702869 (2018)
12. Berendsen, H., van der Spoel, D., van Drunen, R.: GROMACS: a message-passing parallel molecular dynamics implementation. Comp. Phys. Commun. **91**, 43–56 (1995)
13. Bernuy-Lopez, C., Manalastas, W., Lopez del Amo, J.M., Aguadero, A., Aguesse, F., Kilner, J.A.: Atmosphere controlled processing of Ga-substituted garnets for high Li-ion conductivity ceramics. Chem. Mater. **26**, 3610–3617 (2014)
14. Beskos, A., Pillai, N., Roberts, G., Sanz-Serna, J.M., Stuart, A.: Optimal tuning of the hybrid Monte Carlo algorithm. Bernoulli **19**, 1501–1534 (2013)
15. Biresselioglu, M.E., Kaplan, M.D., Yilmaz, B.K.: Electric mobility in Europe: a comprehensive review of motivators and barriers in decision making processes. Transp. Res. A: Policy Pract. **109**, 1–13 (2018)
16. Blanes, S., Casas, F.: A Concise Introduction to Geometric Numerical Integration. Chapman and Hall, London (2016)
17. Blanes, S., Casas, F., Sanz-Serna, J.M.: Numerical integrators for the hybrid Monte Carlo method. SIAM J. Sci. Comput. **36**, A1556–A1580 (2014)
18. Bonilla, M. R., Lozano, A., Escribano, B., Carrasco, J., Akhmatskaya, E.: Revealing the mechanism of sodium diffusion in Na_xFePO_4 using an improved force field. J. Phys. Chem. C. **122**, 8065–8075 (2018)
19. Bonilla, M. R., García Daza, F. A., Carrasco, J., Akhmatskaya, E.: Exploring Li-ion conductivity in cubic, tetragonal and mixed-phase Al-substituted $Li_7La_3Zr_2O_{12}$ using atomistic simulations and effective medium theory. Acta Mater. **175**, 426–435 (2019)
20. Borodin, O., Smith, G.D.: Na-ion mobility in layered Na2FePO4F and olivine Na[Fe,Mn]PO4. Macromolecules **39**, 1620–1629 (2006)

21. Botros, M., Djenadic, R., Clemens, O., Möller, M., Hahn, H.: Assisted sintering of fine-grained $Li_{7-3x}La_3Zr_2Al_xO_{12}$ solid electrolyte and the influence of the microstructure on the electrochemical performance. J. Power Sources **309**, 108–115 (2016)
22. Brommer, P., Gähler, F.: Potfit: effective potentials from ab initio data. Model. Simul. Mater. Sci. Eng. **15**, 295 (2007)
23. Brommer, P., Kiselev, A., Schopf, D., Beck, P.: Classical interaction potentials for diverse materials from ab initio data: a review of potfit. Model. Simul. Mater. Sci. Eng. **23**, 074002 (2015)
24. Brooks, B.R., Bruccoleri, R.E., Olafson, B.D., States, D.J., Swaminathan, S., Karplus, M.: CHARMM: a program for macromolecular energy, minimization, and dynamics calculations. J. Comput. Chem. **4**, 187–217 (1983)
25. Crabtree, G., Kocs, E., Trahey, L.: The energy-storage frontier: Lithium-ion batteries and beyond. MRS Bull. **40**,1067–1076 (2015)
26. Dick, B.G., Overhauser, A.W.: Theory of the dielectric constants of alkali halide crystals. Phys. Rev. **112**, 90–103 (1958)
27. Duan, Y., Wu, C., Chowdhury, S., Lee, M.C., Xiong, G., Zhang, W., Yang, R., Cieplak, P.: A point-charge force field for molecular mechanics simulations of proteins based on condensed-phase quantum mechanical calculations. J. Comput. Chem. **24**, 1999–2012 (2003)
28. Duane, S., Kennedy, A.D., Pendleton, B. J., Roweth, D.: Hybrid Monte Carlo. Phys. Lett. B **195**, 216–222 (1987)
29. Duin, A. C.T., Dasgupta, S., Lorant, F., Goddard, W.A.: ReaxFF: a reactive force field for hydrocarbons. J. Phys. Chem. A **41**, 9396–9409 (2001)
30. Escribano, B., Akhmatskaya, E., Mujika, J. I.: Combining stochastic and deterministic approaches within high efficiency molecular simulations. Centr. Eur. J. Math. **11**, 787–799 (2013)
31. Escribano, B., Akhmatskaya, E., Reich, S., Azpiroz, J. M.: Multiple-time-stepping generalized hybrid Monte Carlo methods. J. Comp. Phys. **280**, 1–20 (2015)
32. Escribano, B., Lozano, A., Radivojević, T., Fernández-Pendás, M., Carrasco, J., Akhmatskaya, E.: Enhancing sampling in atomistic simulations of solid-state materials for batteries: a focus on olivine $NaFePO_4$. Theo. Chem. Acc. **136** (2017). Article number: 43
33. Español, P., Warren, P.: Statistical mechanics of dissipative particle dynamics. Europhys. Lett. **30**, 191–196 (1995)
34. Famprikis, T., Canepa, P., Dawson, J.A., Islam, M.S.: Fundamentals of inorganic solid-state electrolytes for batteries Nat. Mater. **18**, 1278–1291 (2019)
35. Fernández-Pendás, M., Escribano, B., Radivojević, T., Akhmatskaya, E.: Constant pressure hybrid Monte Carlo simulations in GROMACS. J. Mol. Mod. **20**, 2487 (2014)
36. Fernández-Pendás, M., Akhmatskaya, E., Sanz-Serna, J.M.: Adaptive multi-stage integrators for optimal energy conservation in molecular simulations. J. Comp. Phys. **327**, 434–449 (2016)
37. Franco A.: Multiscale modelling and numerical simulation of rechargeable lithium ion batteries: concepts, methods and challenges. RSC Adv. **3**, 13027–13058 (2013)
38. Franco, A. A., Rucci, A., Brandell, D., Frayret, C., Gaberscek, M., Jankowski, P., Johansson, P.: Boosting rechargeable batteries R&D by multiscale modelling: Myth or reality?. Chem. Rev. **119**, 4569 (2019)
39. Frenkel, D., Smit, B.: Understanding Molecular Simulation: From Algorithms to Applications. 2nd edn. Academic, San Diego (2002)
40. Fumi, F.G., Tosi, M.P.: Ionic sizes and born repulsive parameters in the NaCl-type alkali halides I. J. Phys. Chem. Solids **25**, 31–43 (1964)
41. García Daza, F. A., Bonilla, M. R., Llordés, A., Carrasco, J., Akhmatskaya, E.: Atomistic insight into ion transport and conductivity in Ga/Al-substituted $Li_7La_3Zr_2O_{12}$ solid electrolytes. ACS Appl. Mater. Interfaces **11** (2019)
42. Hastings, W.K.: Monte Carlo sampling methods using Markov chains and their applications. Biometrika **57**, 97–109 (1970)

43. Hess, B., Kutzner, C., van der Spoel, D., Lindahl, E.: GROMACS 4: algorithms for highly efficient, load-balanced, and scalable molecular simulation. J. Chem. Theo.Comp. **4**, 435–447 (2008)
44. Horowitz, A. M.: A generalized guided Monte Carlo algorithm. Phys. Lett. B **268**, 247–252 (1991)
45. Izaguirre, J. A., Hampton, S. S.: Shadow hybrid Monte Carlo: an efficient propagator in phase space of macromolecules. J. Comp. Phys. **200**, 581–604 (2004)
46. Izaguirre, J. A., Reich, S., Skeel, R. D.: Longer time steps for molecular dynamics. J. Chem. Phys. **110**, 9853–9864 (1999)
47. Jalem, R., Rushton, M.J.D., Manalastas, W., Nakayama, M., Kasuga, T., Kilner, J.A., Grimes, R.W.: Effects of gallium doping in Garnet-type $Li_7La_3Zr_2O_{12}$ solid electrolyte. Chem. Mater. **27**, 2821–2831 (2015)
48. Jorgensen, W.L., Maxwell, D.S., Tirado-Rives, J.: Development and testing of the OPLS all-atom force field on conformational energetics and properties of organic liquids. J. Am. Chem. Soc. **118**, 11225–11236 (1996)
49. Kennedy, A.D., Pendleton, B.: Cost of the generalised hybrid Monte Carlo algorithm for free field theory. Nucl. Phys. B **607**, 456–510 (2001)
50. Kresse, G., Hafner, J.: Ab initio molecular dynamics for liquid metals. Phys. Rev. B **47**, 558 (1993)
51. Landauer, R.: Electrical conductivity in inhomogeneous media. J. AIP Conf. Proc. **40**, 2–45 (1978)
52. Leimkuhler, B., Matthews, C.: Molecular dynamics with deterministic and stochastic numerical methods. In: Interdisciplinary Applied Mathematics, vol. 39. Springer, New York (2015)
53. Leimkuhler, B., Reich, S.: Simulating Hamiltonian dynamics. In: Cambridge Monographs on Applied and Computational Mathematics, vol. 14. University Press, Cambridge (2004)
54. Li, M., Lu, J., Chen, C., Amine, K.: 30 years of lithium-ion batteries. Adv. Mater. **30**, 1800561 (2018)
55. Mitchell, P.J., Fincham, D.: Shell model simulations by adiabatic dynamics. J. Phys.: Condens. Matter **5**, 1031 (1993)
56. Murch, G.: The haven ratio in fast ionic conductors. Solid State Ion. **7**, 177–198 (1982)
57. Oganov, A.R., Kvashnin, A.G., Saleh, G.: Computational materials discovery: dream or reality? In: Oganov, A.R., Saleh, G., Kvashnin, A.G. (eds) Computational Materials Discovery, pp. 1–14. The Royal Society of Chemistry, London (2019)
58. Park, M., Zhang, X., Chung, M., Less, G.B., Sastry, A.M.: A review of conduction phenomena in Li-ion batteries. J. Power Sources **195**, 794–7929 (2010)
59. Plummer, M., Best, N., Cowles, K., Vines, K.: CODA: Convergence diagnosis and output analysis for MCMC. R News **6**, 7–1 (2006)
60. Radivojević, T., Akhmatskaya, E.: Modified Hamiltonian Monte Carlo for Bayesian inference. Stat. Comp. **30**, 377–404 (2020)
61. Radivojević, T., Fernández-Pendás, M., Sanz-Serna, J.M., Akhmatskaya, E.: Multi-stage splitting integrators for sampling with modified Hamiltonian Monte Carlo methods. J. Comp. Phys. **373**, 900–916 (2018)
62. Ramaswamy. M., Venkataraman, T., Werner, W.: Fast lithium ion conduction in Garnet-type $Li_7La_3Zr_2O_{12}$. Angew. Chem. Edn.: Int. **46**, 7778—7781 (2007)
63. Rettenwander, D., Redhammer, G., Preishuber-Pflugl, F., Cheng, L., Miara, L., Wagner, R., Welzl, A., Suard, E., Doeff, M.M., Wilkening, M., Fleig, J., Amthauer, G.: Structural and electrochemical consequences of Al and Ga cosubstitution in $Li_7La_3Zr_2O_{12}$ solid electrolytes. Chem. Mater. **28**, 2384–2392 (1998)
64. Rettenwander, D., Geiger, C.A., Tribus, M., Tropper, P., Amthauer, G.: A synthesis and crystal chemical study of the fast ion conductor $Li_7La_3Zr_2O_{12}$ with $x = 0.08$ to 0.84 in $Li_7La_3Zr_2O_{12}$ solid electrolytes. Chem. Mater. **53**, 6264–6269 (2014)
65. Sanz-Serna, J.M., Calvo, M.P.: Numerical Hamiltonian Problems. Chapman and Hall, London (1994)

66. Saracibar, A., Carrasco, J., Saurel, D., Galceran, M., Acebedo, B., Anne, H., Lepoitevin, M., Rojo, T., Cabanas, M.C.: Investigation of sodium insertion-extraction in olivine Na_xFePO_4 ($0 \leq x \leq 1$) using first-principles calculations. Phys. Chem. Chem. Phys. **18**, 13045–13051 (2016)
67. Schlick, T., Mandziuk, M., Skeel, R. D., Srinivas, K.: Nonlinear resonance artifacts in molecular dynamics simulations. J. Comp. Phys. **140**, 1–29 (1998)
68. Sweet, C. R., Hampton, S. S., Skeel, R. D., Izaguirre, J. A.: A separable shadow Hamiltonian hybrid Monte Carlo method. J. Chem. Phys. **131**, 174106 (2009)
69. Tealdi, C., Spreafico, C., Mustarelli, P.: Lithium diffusion in $Li_{1-x}FePO_4$: the effect of cationic disorder. J. Mater. Chem. **22**, 24870–24876 (2012)
70. Tripathi, R. Wood, S. M., Islam, M. S. Nazar, L. F.: Na-ion mobility in layered Na_2FePO_4F and olivine Na[Fe,Mn]PO4. Energ. Environ. Sci. **6**, 2257–2264 (2013)
71. Tsai, C.L., Dashjav, E., Hammer, E.M., Finsterbusch, M., Tietz, F., Uhlenbruck, S., Buchkremer, H.P.: High conductivity of mixed phase Al-substituted $Li_7La_3Zr_2O_{12}$. Nanoscale **35**, 25–32 (2015)
72. Wachter-Welzl, A., Kirowitz, J., Wagner, R., Smetaczek, S., Brunauer, G.C., Bonta, M., Rettenwander, D., Taibl, S., Limbeck, A., Amthauer, G., Fleig, J.: The origin of conductivity variations in Al-stabilized $Li_7La_3Zr_2O_{12}$ ceramics. Solid State Ionics **319**, 203–208 (1978)
73. Wang, J., Xueliang, S.: Olivine $LiFePO_4$: the remaining challenges for future energy storage. Energy Environ. Sci. **8**, 1110–1138 (2015)
74. Wee, C.L., Sansom, M.S.P., Reich, S., Akhmatskaya, E.: Improved sampling for simulations of interfacial membrane proteins: application of generalized shadow hybrid Monte Carlo to a peptide toxin/bilayer system. J. Phys. Chem. B **112**, 5710–5717 (2008)
75. Whiteside, A., Fisher, C.A.J., Parker, S.C., Islam, M.S.: Particle shapes and surface structures of olivine $NaFePO_4$ in comparison to $LiFePO_4$. Phys. Chem. Chem. Phys. **39**, 21788–21794 (2014)
76. Whittingham M.S.: Electrical energy storage and intercalation chemistry. Science **192**, 1126–1127 (1976)
77. Wu, J.F., Chen, E.Y., Yu, Y., Liu, L., Wu, Y., Pang, W.K., Peterson, V.K., Guo,: X. Gallium-doped $Li_7La_3Zr_2O_{12}$ Garnet-type electrolytes with high lithium-ion conductivity. ACS Appl. Mater. Interfaces **9**, 1542–1552 (2017)
78. Yabuuchi, N., Kubota, K., Dahbi, M., Komaba, S.: Research development on sodium-ion batteries. Chem. Rev. **114**, 11636–11682 (2014)
79. Yan, T., Burnham, C.J., Del Pópolo, M.G., Voth, G.A.: Molecular dynamics simulation of ionic liquids: the effect of electronic polarizability. J. Phys. Chem. B. **108**, 11877–11881 (2004)
80. Zheng, F., Kotobuki, M., Song, S., Lai, Man, O., Lu, L.: Review on solid electrolytes for all-solid-state lithium-ion batteries. J. Power Sources **389**, 198–213 (2018)
81. Zhu, Y., Xu, Y., Liu, Y., Luo, C., Wang, C.: Comparison of electrochemical performances of olivine $NaFePO_4$ in sodium-ion batteries and olivine $LiFePO_4$ in lithium-ion batteries. Nanoscale **5**, 780–787 (2013)

Optimization of the Scheduling of the Compound Production Machines in a Tires Factory

Carlos Gorria and Mikel Lezaun

Abstract The target of the investigation is to efficiently organize the scheduling of the rubber components manufacturing of a vehicle tire production plant. A mathematical formulation followed by a computational code have to be found in order to optimize the assignment of the tasks to the machines. The complexity of the problem lies in the large number of different components to be considered together with the limitations in the compatibility between some machines and components. In addition, the production flow depends on several sequentially ordered sets of products, that comprise from grinding the raw material until manufacturing the final product ready to be assembled. Occasionally, urgent incoming demand of products can cause a sudden change in the factory environment that needs a fast answer. In this scenario, operations research tools and optimization models become crucial for calculating at any given moment a feasible solution that reaches the new constraints. A linear discrete formulation is suitable to deal with the problem. The results of the simulations clearly improving manufacturing productivity and competitiveness.

1 Introduction

A tire factory is an infrastructure where complex processes take place. In this environment, the optimization techniques can be very useful when efficiently planning of sequences of jobs or task chains has to be planned. Many examples of investigations about process optimization in companies in the sector of tire manufacturing can be found, for example in references [10, 12] and [21].

A car tire is built of several different rubber layers. Each layer will provide different property to the tire, indeed, resistance, flexibility or adhesion. Each one of these layers is the product of the processing of a sequence of tasks. Each task consists in the mixture of a rubber compound with a particular pigment in big

C. Gorria (✉) · M. Lezaun
Department of Applied Mathematics, Statistics and Operations Research, University of the Basque Country (UPV/EHU), Leioa, Spain
e-mail: carlos.gorria@ehu.eus; mikel.lezaun@ehu.eus

M. Cruz et al. (eds.), *Progress in Industrial Mathematics: Success Stories*,
SEMA SIMAI Springer Series 5, https://doi.org/10.1007/978-3-030-61844-5_7

rubber mixing machine to become a new compound. It means that before starting the processing of a compound, certain quantity of the preceding one has to be available in stock. The last compound of a sequence is called "final stage compound". Strips of determinate size of each of the final compounds are cut in order to assemble progressively the tire.

In the processing of a sequence of tasks each compound is associated with a different stage that requires a particular manufacturing process. Depending on the design of a machine in the factory, it may be multi-functional having the capability for processing a variety of compounds. The problem of the optimal assignment of tasks to machines was analyzed in references [6, 20] and [26], where conditions imposed by the skills were considered. The work-flow process considering the interactions between compounds and compatible machines can be represented by a directed graph. There the compounds are the nodes and the machines available to process a compound represent the directed edges or arcs of the graph. Several examples of the use of graphs to schematize the flow of an industrial process can be found in the literature [1, 22] and [3].

The sequences of products or task chains considered for the scheduling can be complete, or incomplete as a result of inventory replenishment operations or due to rearranging previously aborted productions. The graph of Fig. 1 shows several product chains, one complete, $\{R_1, O_{12}, \ldots, O_{15}\}$, another incomplete, $\{O_{43}, \ldots, O_{45}\}$, and two chains sharing the same raw material, $\{R_2, O_{22}, \ldots, O_{24}\}$, and, $\{R_2, O_{32}, \ldots, O_{35}\}$.

Eventually, one or more compounds can compete for a common raw material, but we will consider this option here only in the second stage. It means that different chains could share the same original raw material obtained from the initial grind process. This situation has been illustrated in Fig. 1, where the original compound R_2 is the common raw material for compounds O_{22} and O_{32}. For example, before

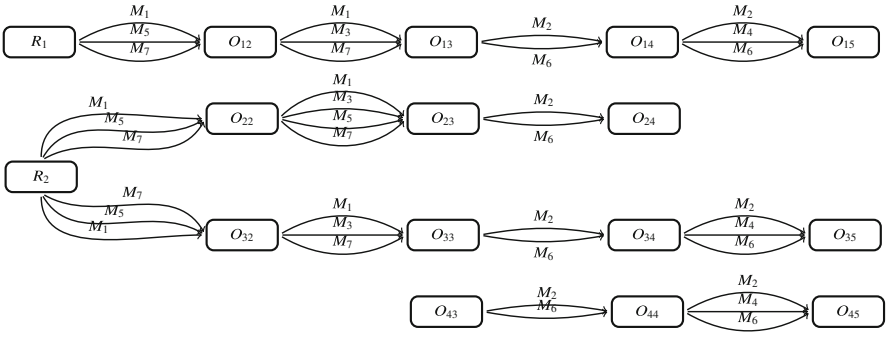

Fig. 1 The graph represents an example of the process flow for some sequences of rubber compounds, represented by nodes, ranging from the initial raw material R_i to the rest of intermediate stages O_{ij} as far as the final compound O_{il_i}. Several machines M_k, represented by arcs, are available to process a compound O_{ij} by mixing the previous one O_{ij-1} with the corresponding pigments

allowing the production of compound O_{22} at determinate moment the scheduling has to take into account the stock of compound R_2, the previous production of the this compound and consumption made by the competitors.

The aim of this work is to build a model suitable to obtain efficient scheduling for the job processing in the mixing machines, minimizing in some sense the idle time of the machines. This challenge can be categorized in the classical *job shop problem*, introduced initially in Ref. [19] and widely analyzed in the literature, [5, 8, 9, 14, 24] and [28]. In general, the problem of finding optimal scheduling for manufacturing in different industrial sectors has been studied in detail in the last decades by several authors, see [15, 16] and [13]. The analysis of the computational performance of the different formulations and algorithms designed to deal with the job shop problem has been a source for several papers as [2] and [11].

In the problems about optimal scheduling different criteria for optimization can be established. One of the most common is to minimize the makespan, that measures the time interval between starting and ending the whole set of jobs. This measurement can be calculated by each machine or on a global scale. In the first case, the optimization is equivalent to the minimization of the sum of gaps or the idle time of the machines. Other criteria can make us of a penalty weights proportional to the tardiness related to the deadline compliance, see, for example Ref. [31].

In this work we use an linear integer programming formulation together with a branch and bound algorithm. This formulation have been used previously in several papers as [7] and [25].

Traditionally it has been observed a computational impracticability of finding global optima or even feasible solutions of many job shop scheduling for large scale problems. Unfortunately, in practice, this case is very usual. With the aim of going beyond this obstacle, recently, heuristic techniques based on genetic algorithms and tabu search have been developed to find computationally efficient feasible solutions in this field. Some hints in this direction can be found in the papers [4, 18, 27–29] and [26].

This investigation has been developed in the frame of a collaboration with a large tire manufacturing company. The aim of the project was to design an automatic and fast method to calculate feasible scheduling for the machines repeatedly. In practice a scheduling will cover one working day, but because of frequent incidents, maintenance service or incoming urgent orders, during the day successive run of the method have to be made. In that circumstances a quick response proposing feasible scheduling that considers the previous incomplete manufacturing is of fundamental importance.

In Sect. 2 we will describe the manufacturing circumstances that determine the parameters of the model. In Sect. 3 we will present the mathematical formulation related to this particular job shop problem, the variables, the constraints and the objective function. In Sect. 4 a simulation will be shown. Some possible applications and conclusions are discussed in the last section.

2 The Job Shop Problem Conditioned by the Environment

Here we present a job shop environment with a catalog of $i = 1, \ldots, I$ jobs. Each job is and ordered set of tasks, $O_i = \{O_{ij}\}_{j=1}^{l_i}$, where l_i is the length of the ith job or task chain. A task consists on processing a compound O_{ij} together with certain pigment giving rise to the next compound of the job, O_{ij+1}. Usually the job i has a deadline p_i which would not have to be exceeded.

We consider $\{M_k\}_{k=1}^{K}$ machines available to process the jobs. The time interval when the machine k is active is $[S_k, E_k]$, which is included in the global time frame $[1, T]$ of the simulation. Each machine k is only compatible with a set of compounds, defined as $\boldsymbol{\Phi_k}$. Equivalently, the compound O_{ij} can be processed only by set of machines $\boldsymbol{\Lambda_{ij}}$. When $O_{ij} \in \boldsymbol{\Phi_k}$ we shall say that the machine M_k and the compound O_{ij} are compatible. An example about the compatibility between machines and compounds is shown in Table 1. There, the suitability of a machine k for processing a compound O_{ij} is expressed by 1 and the unsuitability by 0. The information expressed in this table is equivalent to the graph of Fig. 1.

The basic ideas of the scheme is that a machine cannot process more than one task at the same time and the flow conditions have to be guaranteed every time. The second condition means that a task O_{ij} cannot start until enough quantity of previous compound O_{ij-1} is available in the system. The inventory of the compound O_{ij-1} at any time depends on the initial stock plus the quantity produced earlier than the order for processing O_{ij} minus the quantity consumed by the competitors of O_{ij} by the same raw material O_{ij-1}.

In the model we will consider the possibility of overlapping in time the manufacturing of two consecutive compounds belonging to the same job, O_{ij-1} and O_{ij}, when different machines are assigned to each of them. The processing of

Table 1 Matrix of suitability (1) or unsuitability (0) for a machine M_k to produce compound O_{ij}

	M_1	M_2	M_3	M_4	M_5	M_6	M_7
O_{12}	1	0	0	0	1	0	1
O_{13}	1	0	1	0	0	0	1
O_{14}	0	1	0	0	0	1	0
O_{15}	0	1	0	1	0	1	0
O_{22}	1	0	0	0	1	0	1
O_{23}	1	0	1	0	1	0	1
O_{24}	0	1	0	0	0	1	0
O_{32}	1	0	0	0	1	0	1
O_{32}	1	0	0	0	1	0	1
O_{33}	1	0	1	0	0	0	1
O_{34}	0	1	0	0	0	1	0
O_{35}	0	1	0	1	0	1	0
O_{44}	0	1	0	0	0	1	0
O_{45}	0	1	0	1	0	1	0

O_{ij} may start as soon as the 30% of the previous compound O_{ij-1} has been already made.

The time length taken by the machine M_k to process the task O_{ij} is measured by an integer number of time units $d_{ijk} \in \mathbb{N}$, according with the discretization of the time frame. The components d_{ijk} are stored in the array D.

The manufacturing of certain compounds O_{ij} in a machine M_k may produce some impurity which could cause damages in certain compounds $O_{i'j'}$ processed immediately after in the same machine M_k. In those cases it would be convenient to proceed with a brief cleaning process of $h_{iji'j'}$ time length, in between both manufacturing, in order to avoid eventually damages.

The use of products in stock and the possibility of ordering jobs for inventory replenishment purposes are considered in the mathematical model. The stock of compound O_{ij} is denoted as S_{ij}. The compounds eventually available in stock can be introduced in the task flow. In the same way, when the inventory of a very demanded compound O_{ij} is below a security level, then the incomplete task chain $\{O_{i1}, \ldots, O_{ij}\}$ which leads to this critical compound can be ordered. This type of sequences dedicated to inventory replenishment often are scheduled in order to fill the idle time of the machines. When an interruption of the machines causes the stop of the processing of some jobs, the compounds manufactured up to that moment become part of the stock.

Let define FJ_{ij} the end time of the O_{ij}. Therefore, the end time of the job i will be $FJ_i = FJ_{il_i}$. At the same time, let define FM_k the end time of the last task in the scheduling assigned to machine M_k. Then, since the time is discretized in this mathematical model, M_k machine will be free to process new tasks from $FM_k + 1$ moment. It means that a new scheduling could be developed for a new set of jobs taking $S_k = FM_k + 1$ as he new activation time of any M_k machine. The new scheduling may join the previous one in order to have a long scheduling. We can't guarantee the global optimality of this long scheduling, but it might be very practical in order to evaluate the possibility of manufacturing the jobs in time.

3 Mathematical Formulation of the Problem

In the last decades several algorithms have been developed for attacking a wide variety of problems encompassed under the frame of the job shop scheduling. Big scale problems demand heuristic algorithms for searching feasible solutions under an optimization criterion. In the case under examination all the constraints and criterion for optimization can be represented by linear equations. At the same time the number of tasks and machines and the time frame are not too large. In this framework the time frame $[0, L]$ is discretized into $t = 1, \ldots, T$ disjoint sub-intervals which have the same length Δt, thus the sub-interval $t = 1$ covers the time frame $[0, \Delta t]$, the sub-interval $t = 2$ covers the time frame $[\Delta, 2\Delta t]$ and so on as far as $t = T$.

Under this considerations, the problem can be dealt by a linear integer formulation based on binary variables related to decision-making process. This formulation is suitable for using a modular integer programming techniques [30].

Nevertheless, in case a long time scheduling calculation is necessary, the problem can split out into separate time intervals, proceeding independently with the calculation of each optima and finally joining chronologically the collection of sub-scheduling. Although the joining together of all the partial sub-scheduling doesn't give the global optimum, it can give a useful feasible solution.

3.1 Variables Model

First we define the integer binary variables used to make the decisions about choosing a machine for processing a task in a particular time interval. Particularly we choose the variables $X_{ijkt} \in \{0, 1\}$, where $X_{ijkt} = 1$ if O_{ij} compound starts being processed by machine M_k at time t and $X_{ijkt} = 0$ otherwise. The ranges of the sub-indexes of variables X_{ijkt} are $i = 1, \ldots, I$, $j = 1, \ldots, l_i$, $k = 1, \ldots, K$ and $t = 1, \ldots, T$.

3.2 Constraints

A set of linear constraints have been designed in order to guarantee the fulfillment of the conditions imposed by the particular industrial environment considered here.

(1) *Each compound of final stage type has to be processed once and only once by any one of the machines available to do it.*

This set of constraint together with the conditions imposed by the flow of supply chain, Eq. (2), will guarantee the manufacturing of all the necessary products for fulfilling the demand. Thereby, the products out of stock, which belong to any demanded task chain has to be processed. For each one of these final tasks, O_{il_i}, $i = 1, \ldots, I$, all the possible starting point have to be explored along the time frame, $1 \leq t \leq T - d_{ijk} + 1$.

$$\sum_{k \in \Lambda_{il_i}} \sum_{t=S_k}^{r_{ik}} X_{il_ikt} = 1, \quad \forall i = 1, \ldots, I. \tag{1}$$

where $\{r_{ik} = \min p_i, E_k - d_{ijk} + 1\}$ is the last moment for starting the compound O_{il_i} and fulfilling the deadline of the sequence as well as timetable availability of the machine k.

The number of this type of constraints is not more than I.

(2) *Each machine only can process one task at the same time.*

This set of constraint is repeated for each task $O_{ij} \in \Phi_{\mathbf{k}}$ compatible with the machine k while this is in service and available to deal with the task, $S_k \leq t \leq E_k - d_{ijk} + 1$. If the task O_{ij} starts being processed by the machine k at time t, then none of the other task compatible, $O_{i'j'} \in \mathbf{\Phi_k}$, could be processed by machine M_k until O_{ij} ends at $t' = t + d_{ijk}$. In this set of constraint only tasks compatible with machine M_k are involved.

$$\sum_{\substack{O_{i'j'} \in \mathbf{\Phi_k}, \\ O_{i'j'} \neq O_{ij}}} \sum_{t'=t}^{t+d_{ijk}+h_{iji'j'}-1} X_{i'j'kt'} + \sum_{t'=t+1}^{t+d_{ijk}-1} X_{ijkt'} \leq L(1 - X_{ijkt}),$$

$$\forall k = 1, \ldots, K,\ \forall O_{ij} \in \mathbf{\Phi_k},\ \forall S_k \leq t \leq E_k - d_{ijk} + 1. \quad (2)$$

where L is a constant large enough, $L > \max_k |\mathbf{\Phi_k}| \cdot \max_{i,j,k} |d_{ijk}|$. Here $|\cdot|$ represents the cardinal of a set. This set of constraint is repeated for each time step while the machine M_k is in service, $S_k \leq t \leq E_k$, therefore the number of constraints of this type is around $(E_k - S_k) \times \sum_k |\mathbf{\Phi_k}|$.

(3) *The jobs have to be finished within a set time or deadline.*

Once a deadline p_i has defined for some jobs, each of them will be finished not later than this time,

$$\sum_{k \in \mathbf{\Lambda_{il_i}}} \sum_{t=S_k}^{E_k} t X_{il_ikt} \leq p_i, \quad \forall i = 1, \ldots, I. \quad (3)$$

This constraint may induce the infeasibility of the problem in case of wrong estimation of the number of jobs the deadlines and the power of the machines. However, sometimes these constraints are substitute by a penalty on the objective function according to the tardiness or delay in jobs finishing.

The number of this type of constraints is not more than I.

(4) *The management of the supply chain has to be guaranteed.*

Because of the discretization in time and the binary variables suggested, the formulation of this job shop problem can be significantly simplified. The most complex constraint corresponds to the supply flow. Before accomplishing a task the existence in stock of certain quantity of the previous compound has to be guaranteed. At this point the compound to be processed O_{ij}, the previous one O_{ij-1} and occasionally the competitors will be involved. The competitors of the compound O_{ij} are other compounds of second stage which also use O_{ij-1} as raw material. The set of competitors associated to compound O_{ij} will be

identified as $\mathbf{C_{ij}}$.

$$\sum_{k\in\mathbf{\Lambda_{ij}}} X_{ijkt} \le S_{ij-1} + \sum_{k'\in\mathbf{\Lambda_{ij-1}}} \sum_{t'=1}^{t-d_{ij-1k}} X_{ij-1k'} - \sum_{O_{i'j'}\in\mathbf{C_{ij}}} \sum_{k''\in\mathbf{\Lambda_{i'j'}}} \sum_{t''=1}^{t} X_{i'j'k''},$$

$$\forall i = 1,\ldots,I,\ j = 1,\ldots,l_i,\ \forall t = 1,\ldots,T - \min_{k\in\mathbf{\Lambda_{ij}}} d_{ijk} + 1. \tag{4}$$

In summary, the sum of the raw material stored at the beginning of the simulation S_{ij-1} plus the raw material produced along the simulation, but earlier than the starting of O_{ij} minus the raw material consumed by the competitors $O_{i'j'} \in \mathbf{C_{ij}}$ will not be less than the quantity of O_{ij} which will start being processed.

The number of this type of constraints is around $I \times ml \times T$, where ml is the average of the number of compounds included in one job.

3.3 Objective Function

The simulations implemented here have been oriented to schedule an efficient sequential assignment of jobs to machines. The efficiency of the performance can be defined and measure in different ways. In our first option we have given priority to minimize the global idle time of the set of machines. Thereby, to find the minimum of the sum of idle time or gaps in the machines is equivalent to find the minimum of the sum of starting time of each of the jobs. It is straightforward to set out a linear objective function representing this measurement,

$$f_1(X) = \sum_{i=1}^{I}\sum_{j=1}^{l_i}\sum_{k\in\mathbf{\Lambda_{ij}}}\sum_{t=1}^{r_{ik}} t X_{ijkt}. \tag{5}$$

where $r_{ik} = \min\{p_i, E_k - d_{ijk} + 1\}$ as in Eq. (1). However, in case of choosing the global ending time of the group of jobs as minimization criterion, then, an integer variable E has to be defined by an additional group of constraints. E cannot be less than each of the ending times of the jobs assigned to any machine,

$$E \ge \sum_{k\in\mathbf{\Lambda_{il_i}}} \sum_{t=S_k}^{E_k - d_{il_ik}+1} (t + d_{il_ik} - 1) X_{il_ikt}, \quad i = 1,\ldots,I. \tag{6}$$

In this case, the objective function to be minimized can be represented by the following brief expression,

$$f_2(X) = E. \tag{7}$$

In the literature a wide variety of suggestions for the objective function can be found, depending on the magnitudes to be under control. For example an objective function could be addressed to the tardiness accumulated by the jobs. The tardiness N_i of the job i is defined as the positive part of the time exceeding the deadline, $N_i = |FJ_{il_i} - p_i|^+$. It means that N_i is greater than 0 only when $FJ_{il_i} - p_i > 0$ and 0 otherwise $N_i = 0$. This quantity is nonlinear but anyway it can be introduce in the linear scheme by a simple set of constraints. Other works as [31] have explored multiobjective formulations for the job shop scheduling problem. But in practice the balance between the different contributions on the objective function is very subjective and increases significantly the computation cost.

4 A Sample Case for Scheduling

Several simulations for making a schedule with the assignments of machines to jobs have been implemented. The objective is to verify and measure the efficiency of the mathematical model. The approach has been developed using C++ programming language and two different optimization tools or solvers. On the one hand, the very well known CPLEX [17] commercial software has been used. On the other hand, COIN libraries [23], one of the most powerful open codes for optimization, has been used. The implementation of these computing tools has the advantage of grouping the variables in one dimensional array Z, vanishing the unused variables. The definition of the variables is correlative from X_{111S_1} to $X_{Il_lKE1_K}$, but only for the compatible compounds O_{ij} and Machines M_k. It means that we do not consider all the variables associated to the pairs (O_{ij}, M_k) with a 0 value in a matrix similar to the one shown in Table 1 in the particular problem to be solved.

One could think on considering all the possible variables, including the corresponding to incompatible pairs (O_{ij}, M_k), and the complete time frame $[1, T]$ in order to write the constraints (1)–(4) in an straight forward manner. The code would have to incorporate a new constraint which would force the sum of all the unused variables to be zero. The disadvantage of this formulation lies with the unnecessary growth of the dimension of the problem. It may result in the eventually collapse of the solver due to the size of the problem and the dimensions of the arrays involved. In order to fit the dimension of the model to the real indispensable set of variables and constraints, it is preferable to use only the variables associate to compatible states. The strategy of setting a one dimension array of correlative list of variables is computationally efficient but makes difficult the reading of the constraints. A strategy to make the formulation more comprehensive involve creating a translation function that links each index set (i, j, k, t) corresponding to (O_{ij}, M_k, t) to a

particular index of the array Z. This procedure makes much more comprehensive the implementation of the constraints in a recursive way taking advantage of the symmetry of the problem. However, modern interfaces implemented in languages as Python incorporates the possibility of working with sets of elements, which makes the code very similar to the classical mathematical formulation of the constraints.

In this work several simulations managing different number of jobs, from 4 to 6, have been performed. Each job is made of 3–5 compounds. The performance obtained by the commercial CPLEX solver is always leading the one obtained by COIN solver. The latter one has the limit of 80×10^6 on the number of elements of the matrix, indeed variables multiplied by constraints. It means that orders larger that six jobs considered to be scheduled in 15 h will not be feasible for COIN, while CPLEX can tackle larger problems.

The schedule obtained by COIN solver for each machine on a group of 7, which are installed in a tire factory, is shown in Table 2. Six jobs have been considered, each one made of 5, 4, 5, 3, 4 and 5 rubber compounds respectively. In total, there are 26 tasks to be assigned to 7 multipurpose machines, M_1, M_2,. . .,M_7. The average number of machines compatible with each compound are 2.5 and the reciprocal average number of compounds compatible to be processed by each machine is 9.3. The scheduling obtained by CPLEX commercially licensed solver under the same environment is shown in Table 3. A time limit of 300 s has been applied to the computation in both cases. We are well aware that the scheduling obtained doesn't reach the absolute optimum, but the branch and bound algorithm here takes

Table 2 A scheduling for 7 machines and 6 product chains over 90 time intervals performed by COIN solver after 2 min of running branch and bound algorithm. Each column indicates the sequence of compounds and starting times assigned to a machine, including gaps or idle time and technical stops

	M_1	M_2	M_3	M_4	M_5	M_6	M_7
	gap = 10	gap = 42	gap = 14	gap = 30	gap = 18	gap = 5	O_{31} $t = 1$
	O_{33} $t = 11$	stop = 12	O_{34} $t = 15$	O_{22} $t = 31$	O_{35} $t = 19$	O_{32} $t = 6$	O_{61} $t = 14$
	O_{62} $t = 20$	O_{43} $t = 55$	gap = 5	gap = 32	gap = 12	gap = 8	O_{21} $t = 26$
	O_{41} $t = 31$	gap = 4	O_{64} $t = 29$	O_{53} $t = 76$	O_{24} $t = 45$	O_{63} $t = 26$	O_{51} $t = 39$
	gap = 18	O_{15} $t = 69$	O_{23} $t = 40$		O_{65} $t = 58$	O_{42} $t = 38$	O_{11} $t = 52$
	O_{13} $t = 60$	gap = 1	gap = 15			gap = 8	
	O_{52} $t = 71$	O_{54} $t = 81$	O_{14} $t = 65$			O_{12} $t = 56$	
End time	$t_1 = 83$	$t_2 = 92$	$t_3 = 75$	$t_4 = 88$	$t_5 = 71$	$t_6 = 67$	$t_7 = 63$
Sum of gaps	$g_1 = 28$	$g_2 = 47$	$g_3 = 34$	$g_4 = 62$	$g_5 = 30$	$g_6 = 21$	$g_7 = 0$

Table 3 A scheduling for 7 machines and 6 product chains over 90 time intervals performed by CPLEX solver after 2 min of running branch and bound algorithm. Each column indicates the sequence of compounds and starting times assigned to a machine, including gaps or idle time and technical stops

	M_1	M_2	M_3	M_4	M_5	M_6	M_7
	O_{41} $t = 0$	gap = 8	gap = 4	gap = 63	gap = 19	gap = 5	O_{61} $t = 1$
	O_{63} $t = 11$	O_{43} $t = 9$	O_{42} $t = 5$	O_{34} $t = 64$	O_{65} $t = 20$	O_{62} $t = 6$	O_{11} $t = 14$
	O_{13} $t = 22$	gap = 11	gap = 1	gap = 28	gap = 6	gap = 2	O_{21} $t = 26$
	gap = 2	O_{15} $t = 32$	O_{64} $t = 16$		O_{24} $t = 40$	O_{12} $t = 19$	O_{51} $t = 39$
	O_{23} $t = 35$	stop = 12	gap = 2		O_{54} $t = 54$	gap = 2	O_{31} $t = 52$
	gap = 10	gap = 16	O_{14} $t = 27$			O_{22} $t = 31$	
	O_{32} $t = 56$	O_{35} $t = 71$	gap = 11			gap = 1	
			O_{53} $t = 48$			O_{52} $t = 44$	
			gap = 2				
			O_{33} $t = 60$				
End time	$t_1 = 66$	$t_2 = 80$	$t_3 = 69$	$t_4 = 76$	$t_5 = 67$	$t_6 = 54$	$t_7 = 63$
Accumulated gaps	$g_1 = 12$	$g_2 = 35$	$g_3 = 18$	$g_4 = 63$	$g_5 = 25$	$g_6 = 10$	$g_7 = 0$

unacceptable long time to converge. In such conditions an acceptable as well as fast solution is better than a slow solution, even though it is close from the global optimum. Only in simulations developed for two jobs by COIN and for four jobs by CPLEX the global optimum was found before 500 s of computing time.

Within the industrial context analyzed in this study case, a reasonable measure to compare the output given by COIN and by CPLEX is the gaps or idle time accumulated by the seven machines and the latest of the end times of the schedules. In one hand, the idle time accumulated by seven machines in the scheduling calculated by COIN solver is $\sum_{i=1}^{7} g_i = 222$ and the last of the end times $t_2 = 92$. On the other hand, the idle time accumulated by seven machines in the scheduling calculated by CPLEX solver is $\sum_{i=1}^{7} g_i = 163$ and the last of the end times $t_2 = 80$. The greater performance of the results given by CPLEX solver can be very clearly observed.

In many simulations we have observed that CPLEX solver takes advantage of the possibility of overlapping consecutive compounds of the same job very efficiently when early feasible solutions are calculated. This phenomenon can be observed in

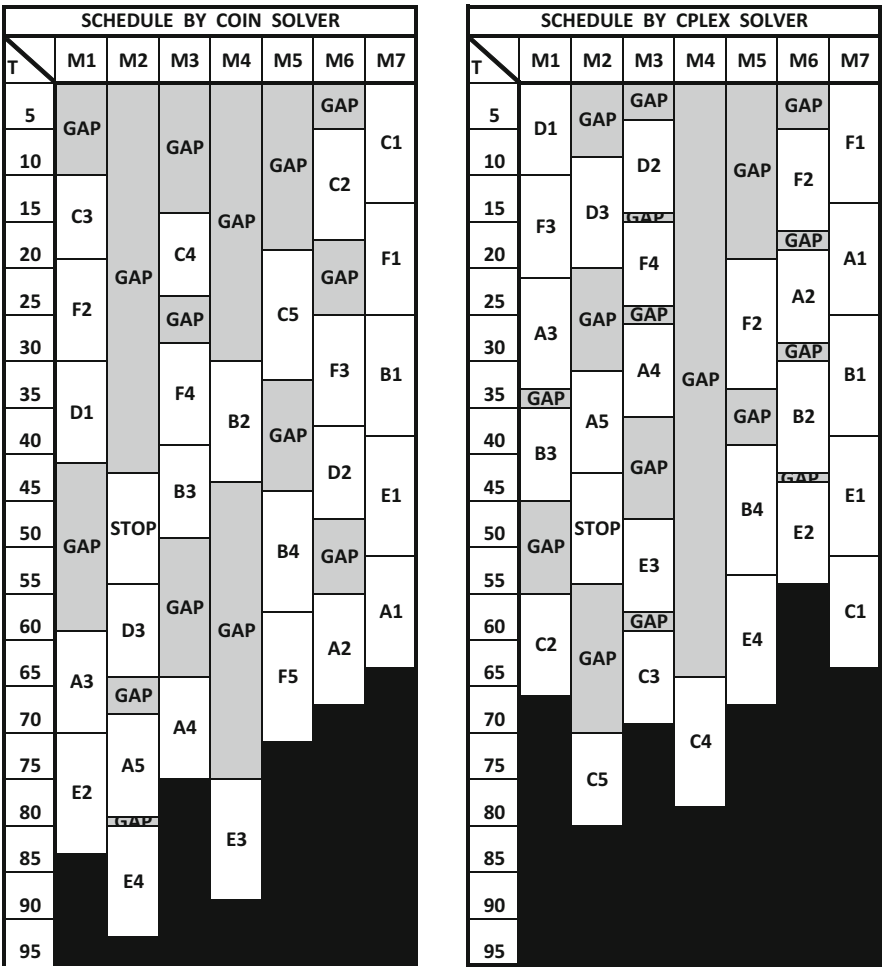

Fig. 2 A comparison of a scheduling of six sequences of jobs, A, B, C, D, E and F, assigned to seven machines, M1,. . ., M7, and computed independently by COIN solver and by CPLEX solver. The jth job of each sequence is labeled by "j" digit. The range of the discretized time frame is $t = 1, 2, \ldots, 95$. Grey cells correspond to idle time periods of the machines

the staggered manner of the manufacturing of some jobs in the graphical scheduling shown in Fig. 2.

Comparison between CPLEX solver performance and COIN solver performance have been made for sets of 4, 6 and 8 jobs and different time limits applied to computation, indeed, from 50 to 600 s. Repeatedly the performance shown by CPLEX commercially licensed solver is significantly better than the one given by COIN free software. Anyway the difference in the performance between two solvers is bigger as shorter is the time limit of the simulation. However, when the time

limit applied to the simulation increases, then the performance of the scheduling calculated by two solvers approach. It means that the algorithms to find a the initial feasible solution and the strategies to apply branch and bound cutting plane is more efficient in the case of CPLEX, but in so far as simulation is prolonged, solutions given by COIN improve significantly and also can be considered as a good option for practical scheduling.

5 Conclusions

A tire manufacturer manages a long catalog of rubber layers because each type of vehicle needs tires conforming to particular specifications. A rubber compound ready for assembling is made of an ordered sequence of compounds. The manufacturing of those compounds is a very suitable process to be optimized by operations research techniques, because of the flow conditions and the multipurpose character of the machines. Companies dedicated to producing tires very often need to update the scheduling that determinate the tasks to be accomplished by the machines. The incidents arising in the machines and the management of new urgent incoming orders are frequently the reason for this. In the case of recalculation of the scheduling, the promptness for giving an optimal solution for a small set of sequences of compounds, for example 4, is more useful than a large scheduling that needs a long computing time. In this scenario the use of discrete integer linear programming formulation for modeling the requirements of the scheduling in terms of constraints and objective function is simple and efficient.

Several types of simulations characteristic of each one of the case studies have been performed in this work. In our experiments, commercial solvers running on a personal computer can deal with groups of 4 jobs integrated by around 25 compounds, while free solvers can deal with groups of 3 jobs integrated by around 15 compounds. In both cases the computing time doesn't exceeds 4 min and the outputs give rise to the scheduling fitting the global minimum of the idle time of the machines. Long-scale production scheduling can be elaborated by joining consecutive partial scheduling made for subgroups of jobs. A strategy consisting of dividing the problem and joining partial schedules doesn't guarantee the global optimum, but anyway it lead to practical and fast feasible solution. The partner company has recognized that the response time for recalculating the schedule when the conditions suddenly change, has been reduced around four times. The results of this work show the successfully contribution of the operations research tools in the improvement of the profits quality of existing industrial processes.

As future research, other real elements concerning the manufacturing dynamics of the company can be considered. For example the case of machines blocked for performing pre-programmed tasks or the case of programmed maintenance stop of some machine into the time frame of the simulation. Those new considerations as well as the possibility of planning simulations for larger groups of around 10 jobs makes the problem more complex. In that scenario integer programming

formulation is insufficient for giving rise to successful solutions and mixed integer programming could be more suitable for dealing with the problem.

Acknowledgments Mikel Lezaun and Carlos Gorria has received funding from the European Union's Horizon 2020 research and innovation programme under the Marie Sklodowska-Curie grant agreement No 777778 (MATHROCKS), the Project of the Spanish Ministry of Economy and Competitiveness with reference MTM2016-76329-R (AEI/FEDER, EU) and the Basque Government through the two Elkartek projects ArgIA (KK-2019-00068) and MATHEO (KK-2019-00085), and the Consolidated Research Group MATHMODE (IT1294-19), given by the Department of Education.

References

1. Akers, S.B.: A graphical approach to production scheduling problems. Oper. Res. **4**(2), 244–245 (1956). https://doi.org/10.1287/opre.4.2.244
2. Applegate, D., Cook, W.: A computational study of the job-shop scheduling problem. Informs J. Comput. **3**(2), 149–156 (1991). https://doi.org/10.1287/ijoc.3.2.149
3. Bazaraa, M.S., Jarvis, J.J., Sherali, H.D.: Linear Programming and Network Flows. Wiley, Hoboken (2010). https://doi.org/10.1016/0377-2217(91)90043-U
4. Bierwirth, C., Mattfeld D.C.: Production scheduling and rescheduling with genetic algorithms. Evol. Comput. **7**(1), 1–17 (1999). https://doi.org/10.1162/evco.1999.7.1.1
5. Blazewicz, J., Domschke, W., Pesch, E.: The job shop scheduling problem: conventional and new solution techniques. Eur. J. Oper. Res. **93**(1), 1–33 (1996). https://doi.org/10.1016/0377-2217(95)00362-2
6. Brucker, P., Schlie, R.: Job-shop scheduling with multi-purpose machines. Computing **45**(4), 369–375 (1990). https://doi.org/10.1007/BF02238804
7. Brucker, P., Jurisch, B., Sievers, B.: A branch and bound algorithm for the job-shop scheduling problem. Discrete. Appl. Math. **49**(1), 107–127 (1994). https://doi.org/10.1016/0166-218X(94)90204-6
8. Carlier, J., Pinson, E.: An algorithm for solving the job shop problem. Manage. Sci. **35**(29), 164–176 (1989). https://doi.org/10.1287/mnsc.35.2.164
9. Carlier, J., Pinson, E.: A practical use of Jackson's preemptive schedule for solving the job-shop problem. Ann. Oper. Res. **26**, 269–287 (1990). https://doi.org/10.1007/BF03543071
10. Darayi, M., Eskandari, H., Geiger, C.D.: Using simulation-based optimization to improve performance at a tire manufacturing company. QScience Connect **2013**(1), 1–12 (2013). https://doi.org/10.5339/connect.2013.13
11. Dauzère-Pérès, S., Paulli, J.: An integrated approach for modeling and solving the general multiprocessor job-shop scheduling problem using tabu search. Ann. Oper. Res. **70**, 281–306 (1997). https://doi.org/10.1023/A:1018930406487
12. Degraeve, Z., Schrage, L.: A tire production scheduling system for Bridgestone/Firestone off-the-road. Oper. Res. **45**(6), 789–796 (1997). https://doi.org/10.1287/opre.45.6.789
13. Framinan, J.M., Leisten, R., Ruiz, R.: Manufacturing Scheduling Systems. Springer, London (2014). https://doi.org/10.1007/978-1-4471-6272-8
14. French, S.: Sequencing and scheduling. An introduction to the mathematics of the job-shop. Wiley, New York (1982). https://doi.org/10.1002/net.3230130218
15. Giffler, B., Thompson, G.L.: Algorithms for solving production scheduling problems. Oper. Res. **8**(4), 487–503 (1960). https://doi.org/10.1287/opre.8.4.487
16. Graves, S.C.: A review of production scheduling. Oper. Res. **29**(4), 646–675 (1981). https://doi.org/10.1287/opre.29.4.646

17. High-performance mathematical programming commercial solver for linear programming, mixed-integer programming and quadratic programming. https://www.ibm.com/analytics/cplex-optimizer
18. Hurink, J, Jurish, B, Thole, M.: Tabu search for the job shop scheduling problem with multi-purpose machines. OR-Spektrum **15**(4), 205–215 (1994). https://doi.org/10.1007/BF01719451
19. Jackson J.R.: Simulation research on job shop production. Nav. Res. Logist. Q. **4**(4), 287–295 (1957). https://doi.org/10.1002/nav.3800040404
20. Jurisch, B.: Lower bounds for the job-shop scheduling problem on multi-purpose machines. Discrete. Appl. Math. **58**(2), 145–156 (1995). https://doi.org/10.1016/0166-218X(93)E0124-H
21. Kim, H.H., Kim, D.G., Choi, J.Y., Park, S.C.: Tire mixing process scheduling using particle swarm optimization. Comput. Ind. Eng. **110**, 333–343 (2017). https://doi.org/10.1016/j.cie.2017.06.012
22. Lageweg, B.J., Lenstra, J.K., Rinnooy Kan, A.H.G.: Job shop scheduling by implicit enumeration. Manag. Sci. **24**(4), 441–450 (1977). https://doi.org/10.1287/mnsc.24.4.441
23. Open source interface and libraries for the operations research community. https://www.coin-or.org/
24. Ovacik, I. M., Uzsoy, R.: Decomposition methods for complex factory scheduling problems. Springer Science & Business Media, New York (1997). https://doi.org/10.1007/978-1-4615-6329-7
25. Özgüven, C., Yavuz, Y., Özbakir, L.: Mixed integer goal programming models for the flexible job-shop scheduling problems with separable and non-separable sequence dependent setup times. Appl. Math. Model. **36**, 846–858 (2012). https://doi.org/10.1016/j.apm.2011.07.037
26. Peng, C., Wu, G., Liao, T.W., Wang, H.: Research on multi-agent genetic algorithm based on tabu search for the job shop scheduling problem. PLoS One **14**(9), e0223182 (2019). https://doi.org/10.1371/journal.pone.0223182
27. Pezzella, F., Morganti, G.: A genetic algorithm for the flexible job-shop scheduling problem. Comput. Oper. Res. **35**(10), 3202-3212 (2008). https://doi.org/10.1016/j.cor.2007.02.014
28. Pinedo, M.L.: Scheduling. Springer, Heidelberg (2016). https://doi.org/10.1007/978-3-319-26580-3
29. Tamssaoueta, K., Dauzère-Pérès, S., Yugmaa, C.: Metaheuristics for the job-shop scheduling problem with machine availability constraints. Comput. Ind. Eng. **125**, 1–8 (2018). https://doi.org/10.1016/j.cie.2018.08.008
30. Wolsey, L.A., Nemhauser, G.L.: Integer and combinatorial optimization. Wiley-Interscience, New York (1999). https://doi.org/10.1057/jors.1990.26
31. Xia, W., Wu, Z.: An effective hybrid optimization approach for multi-objective flexible job-shop scheduling problems. Comput. Ind. Eng. **48**(2), 409–425 (2005). https://doi.org/10.1016/j.cie.2005.01.018

Traveling Salesman Problem in a Geographic Information Management System

José Luis Santos and André Oliveira

Abstract This work results from the consortium formed by the company Smartgeo, in the role of leading developer, and by the University of Coimbra. The main goal was the development of a totally innovative Geographic Information System application, which operates on a Web platform, allowing to integrate, manage and manipulate geographic information at a lower cost and simpler utilisation than other solutions on the market. In addition, the developed application incorporates two new functionalities—the capacity to manipulate and display large volumes of information ("Big Data") and the ability to optimise, according to multiple criteria, the routes of mobile agents in a network. This work focuses on the routes optimisation (second functionality) and not in the first one (Big Data). Two versions were analysed depending if a single or multiple agents were considered. The first case was modelled using the multi-objective travelling salesman problem and the proposed algorithm depends on a parameter which allows controlling the number of Pareto optimal solutions and, consequently, its performance. The second case is dedicated to the route optimisation for several mobile agents using a multiple travelling salesman model. Several heuristics were considered to find balanced routes for all the agents with the minimum cost.

1 Introduction

Geographic Information Systems (GIS) are tools for visualising, analysing and managing georeferenced data. Due to the simplicity with which these systems present the information, they can easily be integrated into the framework of the information system of any company. The GIS can be also provided with other

J. Luis Santos (✉)
University of Coimbra, CMUC, Department of Mathematics, Apartado, Coimbra, Portugal
e-mail: zeluis@mat.uc.pt

A. Oliveira
Bitsight, Lisboa, Portugal

M. Cruz et al. (eds.), *Progress in Industrial Mathematics: Success Stories*,
SEMA SIMAI Springer Series 5, https://doi.org/10.1007/978-3-030-61844-5_8

functionalities, according to the specific needs of each company. In the case of customers with the need to monitor mobile elements within a network, there is a clear market priority in providing them with decision support mechanisms in the form of optimized routes. For example, suppose a customer has the need to provide its services in several locations and has one or more mobile agents to do so. Therefore, this customer needs to be provided with the functionality to find the "best" route that passes through all the locations. This is the problem that will be considered throughout the present paper. Given the difficulty of the addressed problem, the instances solved in this paper are necessarily small.

In general, existing solutions on the market currently provide the user with an ideal route for each mobile agent, which must then follow. However, these solutions, particularly in the GIS market, allow us to define the optimal path based on only one criterion and for each agent separately. The company has analyzed the existing commercial software and concluded that none of them enables the optimization of routes in several objectives simultaneously. Nevertheless, optimising the route for each of the agents separately may not provide the best overall solution to the problem. Additionally, in most real cases, the cost/benefit ratio that is associated with a particular route is characterised by a significantly higher number of criteria. Depending on the parametrisation capability, it is possible to find several variables, independent or not, which should be part of the decision process. For example, variables such as distance, cost, time, effort, etc., should enter simultaneously into the optimisation process in order to obtain an optimal result that is closer to a real scenario.

The SGP-GIMS platform was designed and developed to become one of the main products of the Smartgeo offering. Once the implementation phase of the prototype is completed, it is intended to develop the application to carry out a commercial implementation that allows the integration of new functionalities: the ability to manipulate and display large volumes of information ("Big Data") and the ability to perform multi-objective optimisation of routing of mobile assets in a network. The paper focuses on the optimization of the routes (second functionality) and not in the first one (Big Data).

2 Consortium Smartgeo-UC

The main goal of the SGP-GIMS was the development of a totally innovative Geographic Information System (GIS) application, which operates on a Web platform, allowing to integrate, manage and manipulate geographic information at a lower cost and simpler utilisation than other solutions on the market. In addition, the developed application incorporates two new and significant functionalities—the capacity to manipulate and display large volumes of information ("Big Data") and the ability to optimise the routes of mobile agents in a network.

The project was developed by a consortium formed by the company Smartgeo Solutions, Lda. (Smartgeo), in the role of leading developer, and by the University

of Coimbra (UC). Smartgeo is a company created in November 2012 with the aim of being a benchmark in the development of GIS applications and the supply of products and services associated with it. In this way, SmartGeo's strategy is to move away from more traditional areas of collection and manipulation of basic information, pointing to the development of tailor-made products as a means of approaching the real needs of its target market. The University of Coimbra was founded in 1290 and is dedicated to teaching and research. Teachers and researchers develop R&D activities in research units that are regularly evaluated by international panels. In the particular case of this consortium, the researcher responsible for the optimisation problem belongs to the Department of Mathematics of the Faculty of Science and Technology. His research is carried out in the Centre for Mathematics of the University of Coimbra, which has awarded the highest classification ("Excellent") in the last four evaluations.

3 The Mathematical Models

The topics proposed within the consortium were modelled as variants of the travelling salesman problem (TSP) depending if a single or multiple agents are considered [41]. In the first case, it is used the multi-objective version of the TSP in order to provide the customer with a tool that allows selecting the best route taking into account several criteria. When several agents are considered, the problem was modelled as a multiple TSP (mTSP) to supply a global solution to all the agents. In this case, only one criterion was considered, but it is intended in a future to consider the multi-objective version of the mTSP.

In the next sections, it is described a brief overview of the classical TSP, the mTSP and the multi-objective TSP.

3.1 The Travelling Salesman Problem: A Brief Review

The Hamiltonian path problem is a decision problem that has an easy description: given a finite graph, decide if there is a path that passes through each node exactly once. Although its simple description, it can be proved that it is NP-complete [20, 32]. The problem is known since the early 1800s [16] and W.R. Hamilton was one of the first mathematicians dealing with this subject proposing several related problems like the Icosian Game [54, 55].

The TSP is a classical combinatorial topic related to the previous one and consists of finding the cheapest Hamiltonian path in a network. The first mathematical formulation of the general form of the TSP seems to be done by Karl Menger in 1932, [39]. After that, several advances were made on this subject where we emphasise the integer linear programming formulation proposed by Dantzig, Fulkerson and Johnson with $O(2^n)$ subtour elimination constraints [15] and the one

proposed by Miller, Tucker and Zemlin with $O(n^2)$ subtour elimination constraints [40]. To obtain more details about the TSP, the interested reader is referred to [8, 9, 11, 43, 52]. Like the Hamiltonian path problem, it is hard to solve and can be proved that the TSP is NP-hard [21, 33].

There are several variants of the TSP in the literature [28]. A few examples are the TSP with [34] or without return [44], depending if the path is a cycle or not. The cost arcs have a strong influence in the performance of the algorithms and define the symmetric and the asymmetric TSP depending if the arcs (i, j) and (j, i) have always the same cost. There is a special case for the symmetric TSP (the Euclidian TSP) where the cost of the arc (i, j) is the Euclidian distance from i to j.

The TSP has many applications in several fields: crystallography [10], automatic warehouse [3], DNA sequence [1], logistic [17], psychology [27], biology [29], radiotherapy [30], radio astronomy [4]. Many other interesting TSP applications can be found in [34, 38].

3.2 The Multiple Travelling Salesman Problem

It was proposed by Miler, Tucker and Zemlin [40] considering m (fixed) paths to visit all the nodes exactly once, minimising the total distance travelled (*minSum* version). The paths obtained by this way are sometimes unbalanced much shorter/longer than the others. To avoid that, Frederickson [18] considerer a version of the mTSP where it is intended to minimise the maximum distance among all the m paths (*minMax* version).

The mTSP can be defined considering a single depot [40] where all the paths start and end in the same node (the depot node) or considering multiple depots [46] where the paths can return [36] or not [24] to the same depot. The *minSum* mTSP can be transformed into an asymmetric TSP making copies of the depots [7, 24], allowing to use TSP approaches to solve the mTSP. The number of paths, m, can also be a variable of the problem [35] and it could be added lower/upper bounds to the number of nodes for each individual path [31].

The mTSP has many applications in the industry, for example, School Bus Scheduling [2], interview scheduling [22], global navigation satellite system [51], overnight security service [12], routing of unmanned aerial vehicles [49]. The interested reader can find more examples of applications associated with the mTSP on [5].

3.3 The Multi-Objective Travelling Salesman Problem

The topic of multi-objective (MO) optimisation was introduced by Vilfredo Pareto and has gained increasing interest from researchers. Here, we are interested to

minimise several objective functions under a set of admissible solutions. In the general case, the objective functions are conflicting and there is no solution that minimise all the criteria at the same time. Consequently, the optimal solutions are those for which it is not possible to get better in one criterion without worsening another one. These solutions are called efficient or Pareto optimal solutions and the corresponding values of the objective function are called non-dominated points. Even for the bi-objective case, the number of efficient solutions can increase exponentially with the dimension of the problem [25] making it much harder to solve than the mono-objective counterpart.

The problem is usually solved with one of the following methods: the Pareto and the scalarisation method [23]. The first one works like a labelling algorithm, removing at each iteration the labels corresponding to dominated points and expanding the other ones. In the scalarisation method, all the criteria are aggregate into a utility (mono-objective) function that needs to be minimised. This process allows to obtain an efficient solution for the original problem. The weighted sum is a classical utility function used in this context and varying the (positive) weights of each criterion permit to obtain different efficient solutions. Despite being easier to use, only a portion of the entire set of Pareto optimal solutions is obtained (called the supported efficient solutions).

In what concerns to the TSP, MO optimisation has attracted attention within the researchers. As an example, Lust and Teghem [37] summarise the existing methods with a special focus on evolutive algorithms and local search techniques for the MO TSP.

The MO mTSP was studied by Chang and Yen [13] considering also time windows constraints to improve city couriers services. MO optimisation can be performed even when a single cost is associated with the edges of the networks. This is the case presented by Shim, Tan and Tan [53] where they intend to find the Pareto optimal solutions when the total cost of the m paths is minimised as well as the highest cost of any single path.

4 Computational Study

The computational study considers symmetric and asymmetric instances of the TSPLIB online library [47]. Given the difficulty of the addressed problem, the instances solved in this paper are necessarily small. Altogether they were considered 89 instances: 70 for the symmetric TSP (up to 1002 nodes) and all the 19 available instances (up to 443 nodes) for the asymmetric TSP. For each one of the TSP variants analysed in this work, we focus only on constructive heuristics.

4.1 Computational Results for the TSP

There are several surveys making a good description of methods used to solve the classical TSP, including exact and heuristic approaches [34, 45, 50]. These algorithms are usually evaluated by the ratio between the cost of the heuristic solution and the cost of the optimal one. Thus, it is said that an algorithm is $\mathcal{R}(p)$ to indicate that p is an upper bound for this ratio in the worst-case scenario. In this paper, we focus only on the following constructive heuristics:

- **NN**: the *Nearest Neighbour* algorithm is an easy and intuitive technique to implement, either for the symmetric and asymmetric case. Given an initial node, the solution is constructed iteratively by adding the nearest available neighbour of the last node included in the path. On completed networks, it always produces an admissible solution and it has a run-time of $O(n^2)$, where n is the number of nodes. For the complete Euclidian symmetric TSP, it can be proved [48] that this algorithm is $\mathcal{R}(0.5\lceil \ln(n) \rceil + 0.5)$.
- **CN**: the *Cheapest Node* algorithm is an insertion heuristic which starts with a solution formed by two nodes initially selected. At each iteration, it expands the solution by introducing a new node between two consecutive nodes in the cheapest way. On completed networks, it always produces a solution and it runs on $O(n^2 \ln(n))$. For the complete Euclidian symmetric TSP, it can be proved [48] it is $\mathcal{R}(2)$ which means the value of the heuristic solution is at most twice the optimal one.
- **CL**: the *Cheapest Link* heuristic works in a similar way than Kruskal algorithm for the Minimum Spanning Tree problem. Thus the arcs are searched by nondecreasing order and included in the solution if they allow to obtain an admissible solution. This algorithm has an order of complexity of $O(n^2 \ln(n)))$ and for the complete Euclidian symmetric TSP, it can be proved [19] that it is $\mathcal{R}(\lceil \ln(n) \rceil)$.
- **PL**: the *Priority Link* algorithm works in a similar way than the *Cheapest Link* method, but it assigns a "priority" value to each link [41, 42]. This procedure allows to obtain, in general, better solutions than **CL** because it prevents introducing arcs with the highest cost.
- **CA**: the *Christofides Algorithm* [14] is the constructive heuristic with the best worst-case performance for the ratio between the heuristic value and the optimal one ($\mathcal{R}(3/2)$) on complete Euclidian symmetric instances. Initially, it determines the minimum spanning tree and after that it does a perfect matching of minimum cost on the nodes with odd degree for the spanning tree. This allows to obtain an Eulerian circuit from which is extracted the solution of the TSP. On complete symmetric instances, the algorithm runs in $O(n^3)$.

Table 1 contains the distribution of the gap to the best solution reported on [47] on symmetric and asymmetric instances. For the symmetric case, we conclude that the **CN** heuristic obtains the best performance in our computational study, closely followed by the **CA**. We also observe that the **CL** heuristic has the worst

Table 1 Distribution of the gap to the best solution reported on [47] for symmetric instances up to 1002 nodes (70 instances) and asymmetric instances up to 443 nodes (19 instances)

	Symmetric instances					Asymmetric instances			
Gap	NN	CN	CL	PL	CA	NN	CN	CL	PL
]0.0, 0.1]	0.07	0.13	0.04	0.16	0.06	0.05	0.21	0.26	0.53
]0.1, 0.2]	0.19	0.69	0.09	0.36	0.59	0.16	0.42	0.11	0.37
]0.2, 0.3]	0.61	0.17	0.40	0.29	0.30	0.16	0.26	0.42	0.11
]0.3, 0.4]	0.07	0.01	0.33	0.20	0.06	0.32	0.05	0.11	–
]0.4, 0.5]	0.04	–	0.10	–	–	0.21	0.05	–	–
]0.5, 0.6]	0.01	–	0.03	–	–	0.05	–	–	–
]0.6, 0.7]	–	–	0.01	–	–	–	–	–	–
]0.7, 0.8]	–	–	–	–	–	–	–	0.05	–
]1.3, 1.4]	–	–	–	–	–	0.05	–	–	–
]1.4, 1.5]	–	–	–	–	–	–	–	0.05	–
Average	0.234	0.158	0.299	0.203	0.187	0.358	0.174	0.288	0.111

performance, but the introduction of the "priority" brings a big improvement in the results. In what concerns to the results in asymmetric instances, it is observed that the **NN** and the **CN** algorithms worsened its performance while the **CL** method keeps the same value to the average gap. However, the **PL** procedure has halved the average gap comparing to the symmetric instances, making it the algorithm with the best performance.

4.2 Computational Results for the mTSP

The TSPLIB does not have the optimal solutions for the mTSP and therefore, it is not possible to evaluate in this section the algorithm's performance in terms of the optimal gap. Instead, the gap was measured relatively to the best heuristic solution achieved on this study in each instance and to the TSPLIB solution (which corresponds to the optimal value for $m = 1$).

Two approaches were analysed to solve the mTSP. The first one consists of transforming the mTSP in a non-complete asymmetric TSP [7] and therefore applying the TSP algorithms. Table 2 reports the average results using this approach, where the **CN** and the **CA** algorithms were excluded because they did not solve any instances. From this table, it is observed that the percentage of instances solved by the **NN** heuristic decreases with m. Additionally, the gap between the heuristic solution and the TSPLIB solution increases for all the algorithms when compared with the TSP case because, in the mTSP, the paths must return m times to the depot. However, it does not vary significantly with m for the **PL** and the **CL** algorithms.

The **PL** method seems to have the best performance because, on this study, its solutions are on average the closest to the best ones for the mTSP, being this gap less than 3.1%. Furthermore, the gap to the TSPLIB solution increases only from 0.203

Table 2 Average gap to the best heuristic solution after transforming the mTSP to a TSP and average gap to the TSPLIB solution ($m = 1$)

Gap to:	Best mTSP solution			TSPLIB solution		
Heuristic	NN	CL	PL	NN	CL	PL
$m = 2$	0.075	0.197	0.031	0.345	0.758	0.260
$m = 3$	0.080[a]	0.174	0.022	0.379[a]	0.693	0.260
$m = 4$	0.126[b]	0.166	0.014	0.460[b]	0.693	0.260
$m = 5$	0.178[c]	0.222	0.012	0.486[c]	0.693	0.235

[a] Only 70.42% of the instances were solved
[b] Only 53.52% of the instances were solved
[c] Only 38.03% of the instances were solved

(in TSP) to 0.260 (in mTSP) meaning that the solutions obtained for the mTSP and the TSP ($m = 1$) have similar cost. Finally, the heuristic **CL** produces solutions which are, on average, around 20% worse than the best solutions achieved for the mTSP and the gap relative to the TSPLIB solution has more than doubled.

To better understand the kind of solutions obtained after the transformation of the mTSP into a TSP, it was computed the relative difference between the cost of the largest and shortest tour on each solution, that is, $\frac{c_M - c_m}{c_s}$, where c_M and c_m are the cost of the longest and shortest tour and c_s the cost of the entire solution. This ratio varies from 0 to 1, where 0 means that all the tours have the same cost (balanced solution) and 1 means that the solution resumes to a single tour. Table 3 gives the average results for this ratio, where it is observed that the solutions produced by the heuristics **PL** and **CL** are formed essentially by a single tour. In the opposite way, the solutions obtained from the **NN** algorithm become more balanced when m increases, but fewer instances were solved.

To overcome this situation, a second approach using specific heuristics for mTSP was considered. These heuristics are based in the insertion algorithm which initially selects m nodes and starts the solution with the tours between the depot and these nodes. After that, at each iteration, it selects a tour accordingly a specific rule to introduce the new node between two consecutive nodes in the cheapest way. In this paper, three rules were analysed:

Table 3 Average of the relative difference between the cost of the largest and shortest tours on each solution after transforming the mTSP to a TSP

Heuristic	NN	CL	PL
$m = 2$	0.53	0.96	1.00
$m = 3$	0.66[a]	0.98	1.00
$m = 4$	0.40[b]	0.99	1.00
$m = 5$	0.33[c]	0.99	1.00

[a] Only 70.42% of the instances were solved
[b] Only 53.52% of the instances were solved
[c] Only 38.03% of the instances were solved

Table 4 Results obtained with heuristics designed specifically for the mTSP

	Gap to the TSPLIB solution			Relative difference among tours		
Heuristic	ST	MT	MS	ST	MT	MS
$m = 2$	0.061	0.015	−0.046	0.042	0.003	0.060
$m = 3$	0.411	0.314	0.196	0.031	0.002	0.166
$m = 4$	0.707	0.614	0.409	0.010	0.005	0.033
$m = 5$	1.018	0.888	0.627	0.005	0.007	0.055

- **ST**: the *sequence tour* heuristic, where the tour is selected accordingly a sequence initially established. This rule ensures that the number of nodes in the tours differs at most one.
- **MT**: the *minimum tour* heuristic, where the minimum tour is selected to insert the new node.
- **MS**: the *minimum solution* heuristic, where the new node is inserted into the tour that leads to the minimum overall cost.

Table 4 shows the results using this approach. Here, it is observed that the solution cost increases with m for all the heuristics considered. Moreover, the **MS** heuristic seems to be the most efficient (since it uses a rule that minimise the overall cost) while the **ST** algorithm originates the worst results (because it does not take into account the cost of the solution). This table also presents the average relative difference among tours to assess how balanced the solutions are. It is observed that the **MT** algorithm produces, in general, the most balanced solutions with less than 1% of difference among the tour's cost. It was also noticed that the solutions obtained with the **ST** heuristic are more balanced when m increases and the opposite situation occurs when the **MS** algorithm is used.

4.3 Computational Results for the MO TSP

The TSP can be solved using dynamic programming [6, 26] and so it can be transformed into the shortest path problem with $O(2^n n)$ nodes. Thus, the set of Pareto optimal solutions, P, can be found with a labelling algorithm. However, due to the exponential term, only small instances can be solved until optimality. Table 5 shows how the number of Pareto optimal solution ($|P|$) and the execution time increase with the network size (n) and the number of criteria (k). The difficulty of this problem is not only due to the TSP nature but also because the number of solutions increases very fast with n and k.

In this work, it is proposed the heuristic **MONN** for the MO TSP based in the **NN** heuristic for the TSP. It consists of choosing the Pareto nearest neighbour for the last node included in the solution. In this sense, it works similarly to the labelling algorithm but expands fewer branches. This heuristic allows to obtain feasible solutions quicker than the labelling method, but the size of its set of solutions, P_{NN},

Table 5 Evolution of the number of Pareto optimal solutions ($|P|$) and CPU time with network size (n) and number of criteria (k)

	$k = 2$			$k = 3$		
n	5	10	15	5	10	15
$\|P\|$	3.1	14.8	57.55	6.6	147.2	717.1
Time (s)	0.002	0.329	118.025	0.003	1.612	2589.906

Table 6 Evolution of the average number of solutions ($|P_{NN}|$) obtained with the heuristic **MONN**, the portion of solutions that are optimal ($|P_{NN} \cap P|/|P_{NN}|$) and the CPU time with the network size (n) and the number of criteria (k)

	$k = 2$				$k = 3$			
n	5	10	15	20	5	10	15	20
$\|P_{NN}\|$	1.75	7.4	26.9	857.1	4.05	98.45	512.00	d.n.r.
$\|P_{NN} \cap P\|/\|P_{NN}\|$	0.600	0.410	0.200	–	0.838	0.723	0.593	–
Time (s)	0.003	0.02	2.99	766.69	0.004	0.348	497.236	d.n.r.

d.n.r.: *did not run*

still increases exponentially with n and k. Table 6 shows the results for this heuristic, where it can be observed that the portion of solutions that are optimal decreases with the number of nodes and increases with the number of criteria.

The major drawback of this procedure is that only a portion of its solutions are Pareto optimal and there is no way of knowing what they are. In this sense, it is proposed a second algorithm, **MOCL**—the *MO clustering algorithm*, based on the labelling technique and that also allows us to control the number of solutions obtained. In the classical labelling method, a new label is stored if it is not dominated by the remainder labels on the same state. In the **MOCL** algorithm, we add the restriction that the new label has also to be far away, from a given distance d, from the remainder labels on the same state. If the new label is near an existing label of the same state, it replaces the latter if it has a lower value on the sum of its costs. The distance d should depend on the length, ℓ, of the subpath associated with the new label. Thus, d was defined as a portion $\alpha > 0$ of the average cost of the paths with length ℓ, that is, $d = \alpha\ell\mathbf{a}$, where $\mathbf{a}$ is a vector containing the average of all the cost arcs in the network on each component. Table 7 presents the computational results obtained with this procedure. It should be emphasised that all the solutions obtained with **MOCL** are Pareto optimal solutions and they are scattered, given a general picture of the entire Pareto front. Finally, Table 8 presents the performance of the

Table 7 Evolution of the number of solutions ($|P_{CL}|$) obtained with **MOCL** and CPU time with the network size (n) and the number of criteria (k)

	$k = 2, \alpha = 0.1$				$k = 3, \alpha = 0.2$			
n	5	10	15	20	5	10	15	20
$\|P_{CL}\|$	1.75	5	10.45	13.15	3.85	12.7	22.05	34.5
Time (s)	0.002	0.016	1.502	198.574	0.002	0.064	6.201	515.79

Table 8 Evolution of the number of solutions ($|P_{CL}|$) obtained with **MOCL** and CPU time with α

α	0.00	0.05	0.10	0.15	0.20	0.30	0.50
$\lvert P_{CL}\rvert$	705.45	117.45	53.65	32.55	23.65	14.9	7.5
Time (s)	2447.77	432.79	104.52	41.61	21.85	8.03	6.7

algorithm with α. As it was expected, when α increases, the number of solutions determined and the execution time decrease.

5 Conclusion

In this work, some variants of the TSP were studied. Despite being a difficult problem to deal, it has been shown that using appropriate heuristics it is possible to apply it in an industrial environment. The proposed heuristics allow exploring solutions that were not obtained by the classical heuristics.

In what concerns to the TSP, the introduction of a "priority" value in the arcs produces a significant improvement in its performance. Additionally, the heuristics described for the mTSP produced good balanced solutions. Finally, in the MO TSP, the proposed algorithm makes it possible to obtain a set of solutions that provide a general picture of the entire Pareto front. It can be parameterised allowing to control the number of solutions computed and, therefore, the computational effort required. However, in general, a better performance relative to memory space and execution time is associated with a weak representation of the entire Pareto front. This parameter can be tuned to reflect a good compromise between the efficiency of the algorithm and the quality of the solutions obtained.

The SGP-GIMS platform was designed and developed to become one of the main products of the Smartgeo offering. Once the implementation phase of the prototype is completed, it is intended to develop the application to carry out a commercial implementation that allows the integration of new functionalities: the ability to manipulate and display large volumes of information ("Big Data") and the ability to perform multi-criteria optimisation of routing of mobile assets in a network.

Acknowledgments This work was partially supported by the Centre for Mathematics of the University of Coimbra—UIDB/00324/2020, funded by the Portuguese Government through FCT/MCTES and by the QREN (under the Program More Centre and the European Union through the European Regional Development Fund under the QREN 34164 project—SGP-GIMS, with reference CENTRO 07-0202-FEDER-034164).

References

1. Agarwala, R., Applegate, D.L., Maglott, D., Schuler, G.D., Schäffer, A.A.: A fast and scalable radiation hybrid map construction and integration strategy. Genome Res. **10**, 350–364 (2000)
2. Angel, R., Caudle, W., Noonan, R., Whinston, A.: Computer-assisted school bus scheduling. Manag. Sci. **18**(6), B-279–B-288 (1972)
3. Ascheuer, N., Grötschel, M., Abdel-Hamid, A.A.A.: Order picking in an automatic warehouse: solving online asymmetric tsps. Math. Methods Oper. Res. **49**(3), 501–515 (1999)
4. Bailey, C.A., McLain, T.W., Beard, R.W.: Fuel saving strategies for separated spacecraft interferometry. In: AIAA Guidance, Navigation, and Control Conference (2000)
5. Bektas, T.: The multiple traveling salesman problem: an overview of formulations and solution procedures. Omega **34**(3), 209–219 (2006)
6. Bellman, R.: Dynamic programming treatment of the travelling salesman problem. J. ACM **9**(1), 61–63 (1962)
7. Bellmore, M., Hong, S.: Transformation of multisalesman problem to the standard traveling salesman problem. J. ACM **21**(3), 500–504 (1974)
8. Bellmore, M., Nemhauser, G.: The traveling salesman problem: A survey. Oper. Res. **16**(3), 538–558 (1968)
9. Bellmore, M., Nemhauser, G.: The traveling salesman problem: A survey. In: Mathematical Models in Marketing, volume 132 of Lecture Notes in Economics and Mathematical Systems (Operations Research), pp. 443–448. Springer, Berlin (1976)
10. Bland, R.G., Shallcross, D.F.: Large traveling salesman problems arising experiments in x-ray crystollography: a preliminary report on computation. Oper. Res. Lett. **8**(3), 125–128 (1989)
11. Burkard, R.E.: Travelling salesman and assignment problems: a survey. In: Hammer, P., Johnson, E., Korte, B. (eds.) Discrete Optimization I, volume 4 of Annals of Discrete Mathematics, pp. 193–215. Elsevier, New York (1979)
12. Calvo, R.W., Cordone, R.: A heuristic approach to the overnight security service problem. Comput. Oper. Res. **30**(9), 269–1287 (2003)
13. Chang, T.S., Yen, H.M.: City-courier routing and scheduling problems. Eur. J. Oper. Res. **223**(2), 489–498 (2012)
14. Christofides, N.: Worst-case analysis of a new heuristic for the travelling salesman problem. Technical Report 388, Graduate School of Industrial Administration, Carnegie Mellon University, (1976)
15. Dantzig, G., Fulkerson, R., Johnson., S.: Solution of a large-scale traveling-salesman problem. Oper. Res. **2**, 393–410 (1954)
16. Ein alter Commis-voyageur. Der Handlungsreisende wie er sein soll und was er zu thun hat, um Aufträge zu erhalten und eines glücklichen Erfolgs in seinen Geschäften gewiß zu sein von einem alten Commis-Voyageur. B.Fr. Voigt Ilmenau (1832) (Reprinted: Verlag Bernd Schramm, Kiel, 1981)
17. Exnar, F., Machač, O.: The travelling salesman problem and its application in logistic practice. WSEAS Trans. Bus. Econ. **8**(4), 163–173 (2011)
18. Frederickson, G.N., Hecht, M.S., Kim, C.E.: Approximation algorithms for some routing problems. SIAM J. Comput. **7**(2), 178–193 (1978)
19. Frieze, A.: Worst-case analysis of algorithms for travelling salesman problems. Methods Oper. Res. **32**, 92 (1979)
20. Garey, M.R., Johnson, D.S.: Computers and Intractability. In: A Guide to the Theory of NP-Completeness. W. H. Freeman & Co., New York (1990)
21. Garey, M., Graham, R., Johnson, D.S.: Some NP-complete geometric problems. In: Proceedings of the 8th Annual ACM Symposium on Theory of Computing (STOC), pp. 10–22. ACM, Hershey (1976)
22. Gilbert, K.C., Hofstra, R.B.: A new multiperiod multiple traveling salesman problem with heuristic and application to a scheduling problem. Decis. Sci. **23**(1), 250–259 (1992)

23. Gunantara, N.: A review of multi-objective optimization: methods and its applications. Cogent Eng. **5**(1), 1502242 (2018)
24. GuoXing, Y.: Transformation of multidepot multisalesmen problem to the standard travelling sales- man problem. Eur. J. Oper. Res. **81**(3), 557–560 (1995)
25. Hansen, P.: Bicriterion path problems. In: Fandel, G., Gal, T. (eds.) Multiple Criteria Decision Making Theory and Application, volume 177 of Lecture Notes in Economics and Mathematical Systems, pp. 109–127. Springer, Berlin (1980)
26. Held, M., Karp, R.M.: A dynamic programming approach to sequencing problems. J. Soc. Ind. Appl. Math. **10**, 196–210 (1962)
27. Hubert, L.J., Baker, F.B.: Applications of combinatorial programming to data analysis: the traveling salesman and related problems. Psychometrika **43**(1), 81–91 (1978)
28. Ilavarasi, K., Joseph, K.S.: Variants of travelling salesman problem: A survey. In: Proceedings of the International Conference on Information Communication and Embedded Systems (ICICES2014). IEEE, Piscataway (2015)
29. Johnson, O., Liu, J.: A traveling salesman approach for predicting protein functions. Source Code Biol. Med. **1**(3), 1–7 (2006)
30. Kang, J.H., Wilkens, J.J., Oelfke, U.: Demonstrationof scan path optimization in proton therapy. Med. Phys. **34**(9), 3457–3464 (2007)
31. Kara, I., Bektas, T.: Integer linear programming formulations of multiple salesman problems and its variations. Eur. J. Oper. Res. **174**(3), 1449–1458 (2006)
32. Karp, R.M.: Reducibility among combinatorial problems. In: Miller, R.E., Thatcher, J.W. (eds.) Complexity of Computer Computations, pp. 85–103. Plenum (1972)
33. Korte, B., Vygen, J.: The traveling salesman problem. In: Combinatorial Optimization. Theory and Algorithms, volume 21 of Algorithms and Combinatorics, pp. 473–505. Springer, Berlin (2000)
34. Laporte, G.: The traveling salesman problem: an overview of exact and approximate algorithms. Eur. J. Oper. Res. **59**(2), 231–247 (1992)
35. Laporte, G., Nobert, Y.: A cutting planes algorithm for the m-salesmen problem. J. Oper. Res. Soc. **31**(11), 1017–1023 (1980)
36. Laporte, G., Nobert, Y., Taillefer, S.: Solving a family of multi-depot vehicle routing and location – routing problems. Transp. Sci. **22**(3), 161–172 (1988)
37. Lust, T., Teghem, J.: The multiobjective traveling salesman problem: a survey and a new approach. In: Coello Coello, C.A., Dhaenens, C., Jourdan, L. (eds.) Advances in Multi-Objective Nature Inspired Computing, pp. 119–141. Springer, Berlin (2010)
38. Matai, R., Singh, S.P., Lal Mittal, M.: Traveling salesman problem: an overview of applications, formulations, and solution approaches. In: Davendra, D. (ed.) Traveling Salesman Problem, Theory and Applications, chapter 1, pp. 1–24. InTech, Rijeka (2010)
39. Menger, K.: Das botenproblem. Ergebnisse eines Mathematischen Kolloquiums **2**, 11–12 (1932)
40. Miller, C., Tucker, A., Zemlin, R.: Integer programming formulations and traveling salesman problems. J. Assoc. Comput. Mach. **7**, 326–329 (1960)
41. Oliveira, A.: Extensões do Problema do Caixeiro Viajante. Dissertation to obtain the Master Degree in Mathematics, specialization area: Statistics, Optimization and Financial Mathematics (in Portuguese). Master's thesis, University of Coimbra (2015)
42. Oliveira, A.: O Problema do Caixeiro Viajante. Seminário em Estatística, Otimização e Matemática Financeira (in Portuguese). University of Coimbra (2015)
43. Orman, A.J., Williams, H.P.: A survey of different integer programming formulations of the travelling salesman problem. In: Kontoghiorghes, E.J., Gatu, C. (eds.) Optimisation, Econometric and Financial Analysis, volume 9 of Advances in Computational Management Science, pp. 93–108. Springer, Berlin (2006)
44. Papadimitriou, C.H.: The euclidean travelling salesman problem is np-complete. Theor. Comput. Sci. **4**, 237–244 (1977)
45. Prabakaran, S., Kumar, T.S., Ramana, J., Reddy, K.C.: A survey on approaches to solve travelling salesman problem. Eurasian J. Anal. Chem. **13**(SP), 292–299 (2018)

46. Rao, M.R.: Technical note a note on the multiple traveling salesmen problem. Oper. Res. **28**(3-part-i), 628–632 (1980)
47. Reinelt, G.: Tsplib - library of sample instances for the tsp (and related problems). http://comopt.ifi.uni-heidelberg.de/software/TSPLIB95/ (2015)
48. Rosenkrantz, D.J., Stearns, R.E., Lewis II, P.M.: An analysis of several heuristics for the traveling salesman problem. SIAM J. Comput. **6**(3), 563–581 (1977)
49. Ryan, J.L., Bailey, T.G., Moore, W.B., Carlton, J.T.: Reactive tabu search in unmanned aerial reconnaissance simulations. In: 1998 Winter Simulation Conference. Proceedings (Cat. No. 98CH36274), vol. 1, pp. 873–879 (1998)
50. Saharidis, G.K.D.: Review of solution approaches for the symmetric traveling salesman problem. Int. J. Inf. Syst. Supply Chain Manag. **7**(1), 73–87 (2014)
51. Saleh, H.A., Chelouah, R.: The design of the global navigation satellite system surveying networks using genetic algorithms. Eng. Appl. Artif. Intell. **17**(1), 111–122 (2004)
52. Schrijver, A.: On the history of combinatorial optimization (till 1960). In: Aardal, K., Nemhauser, G., Weismantel, R. (eds.) Discrete Optimization, volume 12 of Handbooks in Operations Research and Management Science, pp. 1–68. Elsevier, New York (2005)
53. Shim, V.A., Tan, K.C., Tan, K.K.: A hybrid estimation of distribution algorithm for solving the multi-objective multiple traveling salesman problem. In: 2012 IEEE Congress on Evolutionary Computation, pp. 1–8 (2012)
54. The Puzzle Museum. The icosian game. https://www.puzzlemuseum.com/month/picm02/200207icosian.html. Accessed 08 Nov 2019
55. The Worlds of David Darling - Encyclopedia of Science. Icosian game. http://www.daviddarling.info/encyclopedia/I/IcosianGame.html. Accessed 08 Nov 2019

Order and Stock Costs Optimization in an Automotive Spare Parts Wholesaler

M. B. Cruz, S. F. Ramos, M. Pina, and R. Costa

Abstract We address a demand forecast problem posed by Nors, a Portuguese group working in the automotive sector and transport solutions. The aim is to define a procedure that efficiently forecasts the references demand and to obtain an optimized procedure for their ordering methodology. Nors works with several suppliers, resulting in a portfolio of hundreds of thousands of different parts number. Each supplier has its own lead-time and order periodicity. On an annual basis, and for each supplier, the yearly budget for purchases is agreed in order to define possible quantity discounts and the profitability of the business. Sales distribution is highly scattered, as there are high, medium and low rotation sales values for different references. Since the number of references and their total value is very high, the stock value and operational costs are non-negligible factors concerning the company costs. Nors goal is to reduce these costs while maintaining a high service level. In this paper, we implement a mixed methodology for the forecasting problem, present an alternative for the safety stock value, and discuss an optimization model to decide which and how many parts number should be ordered in each period. Finally, we present a set of computational and real implementation results, obtained with Nors data regarding two suppliers.

M. B. Cruz (✉)
LEMA - Engineering Mathematics Laboratory, School of Engineering, Polytechnic of Porto, Porto, Portugal
e-mail: mbc@isep.ipp.pt

S. F. Ramos
LEMA - Engineering Mathematics Laboratory, School of Engineering, Polytechnic of Porto and CEAUL - Faculty of Sciences, University of Lisbon, Lisbon, Portugal
e-mail: sfr@isep.ipp.pt

M. Pina · R. Costa
Nors Group, Porto, Portugal

M. Cruz et al. (eds.), *Progress in Industrial Mathematics: Success Stories*,
SEMA SIMAI Springer Series 5, https://doi.org/10.1007/978-3-030-61844-5_9

1 Introduction and Problem Characteristics

It is widely recognized that the spare parts area is often the most profitable part of a corporation [13], especially when working at the repair, maintenance and aftersales business. In aftersales, the usage of appropriate forecasting methods reduces safety stocks, decreases several costs related with the stock level without penalizing the level of service and is one of the management key challenges [12]. In the aftermarket automotive sector this is even more critical for the wholesalers, as several aspects add complexity layers to the demand forecast and subsequent inventory management. Namely, the huge number of spare parts with heterogeneous sales patterns, the risk of stock obsolescence for some parts of the portfolio as well as the importance given by the costumers to the vehicle which lead them to have very small comprehension with long waiting times [1, 2, 4]. Despite the published work about this matter by many authors, there is a considerable gap between research and practice, as stated in [4] or [1]. In [11] it is presented a survey about the application of spare parts management methods at a national level, based on the work done by Rodrigues and Sirova in the Czech Republic. In this paper we address the practical implementation, in a Portuguese company, of a stock management process designed to meet the company constrains w.r.t. hardware and data availability, as well as to deliver accurate outputs and reliable Key Performance Indicators (KPI).

During this work, it was possible to observe very distinct sales behaviour across the references that compose the company portfolio. There are references with sporadic demand, in the sense that they are consumed in certain moments, followed by long and variable intervals with no demand, as well as there are references that are sold in high quantities for a long continuous period of time. In Fig. 1, it is presented the sales history for a given sub-family of 460 references (y-axis), across

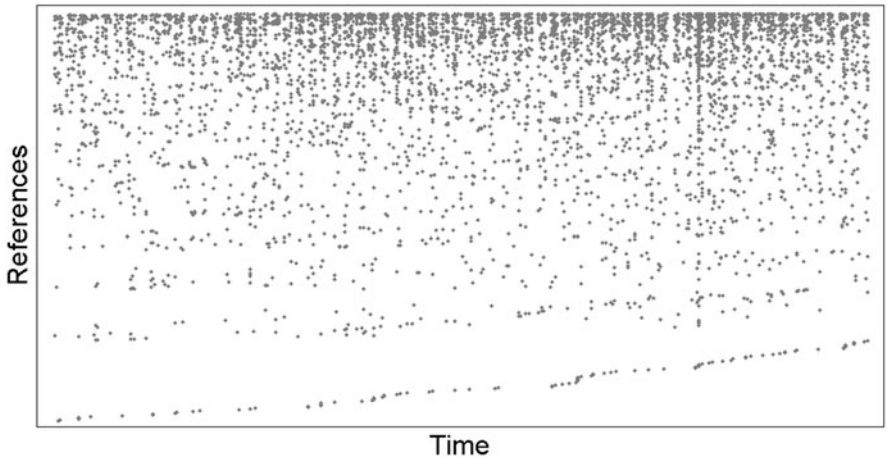

Fig. 1 Scatter of sales for a set of spare-parts references, during a 9-month period

a period of 9 months (x-axis). Each marker placed on (x, y) represents, at least, one sale of the y reference at time x.

Several facts may explain this behaviour. On the one hand, it is well known that the aftermarket spare parts sales for a given car model is, among other factors, correlated with its age. It is known that, some years after the model is launched there is an increase on the number of spare parts sold, followed by an equilibrium phase, and a subsequent decay on the end of the car's expected life [8, 9]. However, those trends depend also on many other factors as, for instance, the number of sold vehicles from that particular model, the number of years since the model was released, the expected life for each vehicle component. On the other hand, the same spare part may be applied in different car models, which may have distinct beginning and ending production periods, and a single car reference may have several different aftermarket suppliers. Finally, there are many additional factors that are related with the spare parts demands to a given company, as the mileage and the type of utilization of each car or the marketshare the company owns which is, in fact, time and reference dependent. All of these make very difficult for a wholesaler to accurately evaluate the parameters needed to deploy such a model.

Due to all the previous stated reasons, in the next section we present a model that uses several computationally cheap forecasting methods aiming at: being suitable for the different rotation type of references that compose the company portfolio; reacting quickly to market changes, and at maintaining the computational complexity at reasonable levels regarding its implementation on a company with regular hardware resources. Table 1 indicates the notation used in this paper, regarding the methods described in the next section, where, in its final subsections we present the results of their application to real databases and discuss these intermediate results. This will be the support to set the background regarding the

Table 1 Notation for the forecasting methods

Parameter	Notation	Method
d_t	Real demand for period t	All methods
$\hat{X}_t$	Demand forecast for period t	All methods
$\hat{S}_t$	Demand forecast for period t, given that the demand is positive	CR, SBA e TSB
$\hat{K}_t$	Forecast for period t, for the consecutive number of months with positive demand	CR e SBA
k_t	Number of months since the last positive demand, for period t	CR e SBA
$\hat{p}_t$	Probability forecast, for period t, of having positive demand	TSB
p_t	Binary variable, indicating positive demand for period t	TSB
a_t	Series level for period t	SAGA
b_t	Series trend for period t	SAGA
α, β	Smoothing constants ($0 \leq \alpha, \beta \leq 1$)	ES, CR, SBA, TSB, SAGA

optimization model that is presented on Sect. 3. Finally, we discuss the overall results on Sect. 4.

2 An Adjustable Model for Forecasting Spare Parts Demand

Several methods for the forecast of multi rotation references are presented in the literature [2, 6, 12]. Syntetos and Boylan [2] present a comprehensive review on forecasting spare parts demand, and the work of Romeijnders et al. in [12] is a very good survey on the subject this paper deals with, as it was based on the work done by the authors for Fokker Services, a company which deals with spare parts for aviation industry that has very similarities with the automotive business. Kennedy et al. [6] present also an overview on spare parts management that may be important for the second part of this paper.

2.1 Multirotation Reference Forecasting Methods

This section presents a brief review of methods for demand prediction, based on the description made by Romeijnders et al. in [12].

2.1.1 Zero Forecast

Zero Forecast method (ZF) forecasts the demand in the following period as 0 [12], that is:

$$\hat{X}_{t+1} = 0 \tag{1}$$

2.1.2 Moving Averages

The method of moving averages (MA) is one of the most famous methods for time series [7]. The demand on the next period is taken as the demand average of the previous N periods, eventually with respect to some weights $0 \leq \omega_i \leq 1$, where $\sum_{i=1}^{N} \omega_i = 1$. Unless stated otherwise, we use as default $\omega_i = \frac{1}{N}$:

$$\hat{X}_{t+1} = \sum_{i=1}^{N} \omega_i d_{t-N+i} \tag{2}$$

It is important to notice that Nors company already used MA to forecast the next period demand, with $N = 6$. We will denote this as MA(6) in further analysis.

Additionally, we used 12 months MA, with a combination for ω_i that gives more importance to the last three periods, a little less to the remaining of the last semester, and a small one to the first trimester. This will be stated hereafter as K-Method.

2.1.3 Naive Forecast

The so-called Naive Method (NF) is a particular case of the moving averages with N=1, as it sets the value of demand during the last period as the forecast for the following period [12].

$$\hat{X}_{t+1} = d_t \tag{3}$$

2.1.4 Exponential Smoothing

The Exponential Smoothing method (ES) is robust and is very well known as it fits itself rapidly to changes in the demand. Unlike MA, this method uses decreasing exponential combinations of past observations, to estimate future demands [3, 12]. In fact, it uses the forecast on the last period, adjusted by the prediction error $d_t - \hat{X}_t$, through the expression:

$$\hat{X}_{t+1} = (1-\alpha)\hat{X}_t + \alpha d_t \tag{4}$$

2.1.5 Croston Method

In the original paper [5], Croston showed that the ES and MA methods didn't fit to series with intermittent demands. He proposed to update the quantity $\hat{S}_{t+1}$ and the searching interval $\hat{K}_{t+1}$ separately. The ES model is used to estimate those components in the periods of positive demand. The Croston forecast (CR) for the search quantity in period t is

$$\hat{S}_{t+1} = \begin{cases} \hat{S}_t, & d_t = 0 \\ (1-\alpha)\hat{S}_t + \alpha d_t, & d_t > 0 \end{cases} \tag{5}$$

and the forecast for the number of periods with positive demand may be calculated through

$$\hat{K}_{t+1} = \begin{cases} \hat{K}_t, & d_t = 0 \\ (1-\beta)\hat{K}_t + \beta k_t, & d_t > 0 \end{cases} \tag{6}$$

The forecast suggested by Croston method is obtained through:

$$\hat{X}_{t+1} = \frac{\hat{S}_{t+1}}{\hat{K}_{t+1}} \tag{7}$$

2.1.6 SBA: Syntetos–Boylan Method

Syntetos and Boylan [14] presented in 2001 an update to the Croston method, the Syntetos–Boylan method (SBA). To avoid some bias, they proposed to include the factor $1 - \frac{\alpha}{2}$ in the Croston method, getting the following expression:

$$\hat{X}_{t+1} = \left(1 - \frac{\alpha}{2}\right) \frac{\hat{S}_{t+1}}{\hat{K}_{t+1}} \tag{8}$$

where $\hat{S}_{t+1}$ and $\hat{K}_{t+1}$ are evaluated using the expressions (5) and (6).

2.1.7 Teunter Method

Teunter method (TSB) [15] is an alternative to Croston method that updates the positive search probability, instead of updating the forecast for the periods with positive demand like the CR and TSB methods. The demand forecast for period t is achieved through:

$$\hat{S}_{t+1} = \begin{cases} \hat{S}_t, & d_t = 0 \\ (1-\alpha)\hat{S}_t + \alpha d_t, & d_t > 0 \end{cases} \tag{9}$$

and the probability to have positive search is given by:

$$\hat{p}_{t+1} = (1-\beta)\hat{p}_t + \beta p_t \tag{10}$$

As so, the forecast given by the Teunter method may be calculated by:

$$\hat{X}_{t+1} = \hat{p}_{t+1}\hat{S}_{t+1} \tag{11}$$

2.1.8 SAGA or Holt Method

The SAGA method, also known as Holt method, is suitable for series with linear trend. It uses the exponential smoothing technique to estimate the level a and the growing trend b [3]. This model uses the following update expressions:

$$a_t = \alpha d_t + (1-\alpha)(a_{t-1} + b_{t-1}), \tag{12}$$

and

$$b_t = \beta(a_t - a_{t-1}) + (1 - \beta)b_{t-1} \tag{13}$$

The forecast for the next period is obtained through:

$$\hat{X}_{t+1} = a_t + b_t \tag{14}$$

2.1.9 Poisson Method

Under certain well specified conditions, the Poisson distribution is used to count events that occur randomly in a given interval of time. This distribution can be used to get a forecast, as an alternative to methods based on time series [10]. This was adapted to this problem, using as rare event the quantity sold in a given period of time. As so, defining X_i as the random variable that represents the number of pieces sold for a given reference i on the time interval Δ, and supposing that $X_i \sim P_o(\lambda)$ with $\lambda = E(X_i) \approx \frac{1}{n}\sum_{j=1}^{n} d_{ij}$ where $\sum_{j=1}^{n} d_{ij}$ represents the total number of reference i articles sold in n periods Δ, the forecast, $\hat{X}_i$, for Poisson model (PO) is obtained solving the equation

$$P(X_i < \hat{X}_i) = 1 - \alpha \tag{15}$$

where α represents the desired confidence level.

Beside the methods described, many other could be inserted on this model. Indeed, several other methods were considered to be included in this work but, those failed to meet one of the requirements asked by the company: that its implementation should deliver results in reasonable time using the existing hardware. The Neural Networks approach and time series methods (like ARMA, ARIMA or SARIMA) didn't improve significantly our results in the several tests where this model was used and/or increased considerably the overall running-time to values that were not compatible with the company's available time to process the orders.

2.2 The Mixed Model: MM

The approach implemented in Nors was based on selecting, in each order period, the best method for each reference. With that purpose, we built a metric that uses recent periods to decide which method does fit better the present sales series and use it in the forthcoming forecasting period. More precisely, it receives the demand history for a given reference, and estimates which is the most suitable method for that series. This was done through the following error function (by default, the test

period uses $N = 18$ months)

$$\text{Error}_t = 0.6 \sum_{i=1}^{\lfloor N/2 \rfloor} (d_{t-i} - \hat{X}_{t-i})^2 + 0.4 \sum_{i=\lfloor N/2 \rfloor + 1}^{N} (d_{t-i} - \hat{X}_{t-i})^2 \tag{16}$$

where $\lfloor . \rfloor$ represents the floor function.

The methods MA, ES, CR, SBA, TSB e SAGA are parametric, implying that their use depends on the values assigned to each of their parameters. We made this using a brute-force parametrization test and selecting for the forecast of the next unknown period the combination that minimizes the Mean Squared Error (MSE) for the selected m test periods:

$$\text{MSE}_t = \frac{1}{m} \sum_{i=1}^{m} (d_{t-i} - \hat{X}_{t-i})^2 \tag{17}$$

2.2.1 The Dynamic Safety Stock Approach

The methods described in the last subsection deliver the forecasted demand for the next period. Apart from this, another important quantity to determinate is the Safety Stock (SS). As stated in [16] this quantity may be understood as an *extra stock*, important to prevent eventual consumptions above the predicted demand on the following period. In order to determine the real quantities to be ordered for the next period, Nors used a safety margin based on Economic Order Quantity (EOQ) expression

$$\text{EOQ}_t = OP_t - Q(0)_t + \hat{X}_{t+1} \times \epsilon \tag{18}$$

where OP_t is the order point, ϵ is a parameter given as function of both reference cost and next period forecast for each reference and $Q(0)_t$ represents the existing stock for the given reference at the time of placing the order (units). Those ϵ-values, that were pre-defined by the company commercial department, are presented in Table 2.

Table 2 Number of extra weeks to order, as function of reference's cost and demand forecast

		Next period demand forecast						
		A	B	C	D	E	F	G
Price		≥ 50	[10;50[	[5;10[	[2;5[	[1;2[	[0.5;1[	[0,0.5[
1	[0;1[	3	4	4	4	3	2	1
2	[1; 10[	2	2	3	4	3	2	1
3	[10; 50[	1	1	2	2	2	1	1
4	[50; 300[	1	1	1	2	2	1	1
5	≥ 300	1	1	1	1	1	1	1

Taking advantage of the data obtained from the tests made previously when selecting the best method, and given that the main reason for the safety stock is to cover the instances where the method underestimates the demand for the next period, we calculate the safety stock quantity in a different way. In fact, to evaluate the SS, we only use the periods in the past where the real demand was above the forecast

$$\text{Error}_{med_t} = \frac{1}{\#A_t} \sum_{i \in A_t} (d_{t-i} - \hat{X}_{t-i}),\ A_t = \left\{ i = 1, \cdots, n : d_{t-i} > \hat{X}_{t-i} \right\} \tag{19}$$

This value is upscaled by a risk factor,

$$\text{SS}_t = q_{1-\alpha'/2} \times \text{Error}_{med_t} \tag{20}$$

where q represents the $1 - \alpha'/2$ quantile of a suitable distribution for the errors series. The risk factor parametrization is intended to be settled using the company's technical knowledge (e.g., taking into account each reference critical importance).

As usual, the order point is defined as $OP_t = \hat{X}_t \times LT + SS_t \times LT$, where the Lead-Time (LT) is measured in the same temporal scale as the forecast $\hat{X}_t$.

2.3 Computational Results with Real Data

The previous model was implemented and applied with two real datasets, DS12016 and DS22016, consisting of 1172 and 4032 references, respectively, belonging to two suppliers for which this methodology has been tested and applied. The following results represent the comparison of the model within the year of 2016 (52 weeks) against the older model implemented in Nors that was based only in the MA(6). For this work, we also had access to the previous 30 months history of sales w.r.t. these references. The lead-time for this supplier is 28 days, and the orders were launched weekly, starting in January 4, and ending in December 26.

It should be noticed that although there are some references without sales (145 and 1010 for each dataset, respectively) for the whole year of 2016, we kept them in the datasets in order to reproduce real-world conditions in these tests, as it is impossible to know in advance if a reference will or not be sold in a given year. Those were only deleted when evaluating the relative errors. For the same reason, we also include the returned items in 2016, from 2015 sales. As so, the quantity sold per reference may be negative.

In Tables 3 and 4, the descriptive measures to characterize the datasets reinforces the idea of great amplitude of sales distribution per reference, introduced in the beginning of this paper, as high, medium and low rotation products coexist in the same family of products. This factor may be one of the main factors that leads to the values presented on the last line of this table, representing the number of different

Table 3 Descriptive statistics regarding the application of MM in DS12016

Parameter	Min	First Q	Median	Mean	Third Q	Max	Std	CV
Sold qty per ref.	−6	1	5	23.8	17	1071	71.0	3.0
Forecasted qty per ref.	0	1.2	4.9	22.8	17.1	997.6	67.4	3.0
Av. nr. of days between sales	1.5	20.4	61.2	96.9	122.3	≥365	104.8	1.1
Nr. of different methods/ref:	1	2	4	3.7	5	9	2	0.55

Table 4 Descriptive statistics regarding the application of MM in DS22016

Parameter	Min	First Q	Median	Mean	Third Q	Max	Std	CV
Sold qty per ref.	−23	0	2	20.4	5	12,092	287.3	14.1
Forecasted qty per ref.	0	0.27	1.4	19.8	5.2	11,231.6	276.9	14.0
Av. nr. of days between sales	1.3	52.4	122.3	164.4	≥365	≥365	129.2	0.8
Nr. of different methods/ref:	1	2	3	3.3	5	9	1.8	0.6

Table 5 Impact by method in DS12016 and DS22016

	DS12016			DS22016		
Parameter	Global impact (%)	Max. best method (wk)	Ref w/most usage (%)	Global impact (%)	Max. best method (wk)	Ref w/most usage (%)
ZF	40.7	52	42.7	51.5	52	58.1
NF	1.3	10	0	1.0	5	0
Poisson	0.0	2	0	0.0	5	0
MA(6)	0.7	15	0	0.5	13	0
ES	0.4	6	0	0.2	4	0
MA	21.1	42	20.9	16.7	35	16.6
SAGA	1.5	10	0	1.0	3	0
CR	0.8	9	0	0.7	8	0
SBO	1.1	13	0	0.8	12	0
TSB	0.2	5	0	0.2	8	0
K	31.7	45	36.4	27.5	31	25.3

methods per reference used to forecast at least one period in 2016, which seems to justify by itself, the idea presented in Sect. 2.2.

As so, proposing a single method for each reference is not a good choice. On average, each reference had its best prediction using between 3 and 4 different methods across the whole year. With respect to the performance of each method, Table 5 and Fig. 2 present the main idea although some comments should be made with that respect.

First, all the methods are used somewhere across the year and, as the computation time is acceptable for the company, there is no reason why any of them should be removed. Second, the K-method clearly overperforms the MA method which was the choice prior to this new implementation on Nors. Finally, the high frequency of ZF may be explained by its usage in references that have very scattered sales, as also

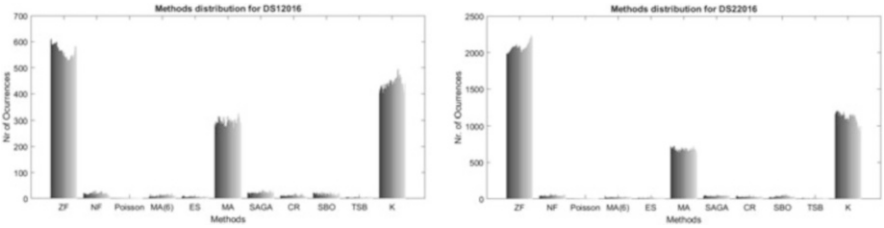

Fig. 2 Method's histogram regarding the number of times a method was selected as best, for each reference across the whole 52 weeks history

Table 6 Descriptive statistics for errors concerning the application of MM to both datasets

Dataset	Parameter	Min	First Q	Median	Mean	Third Q	Max	Std	CV
DS1	Real errors	−75	−1	0	−1.0	0	18	5.4	5.4
DS1	Relative errors (%)	−100	−13.0	0	−4.3	0	300	33.1	7.7
DS2	Real errors	−860	−1	0	−0.6	0	277	16.3	26.2
DS2	Relative errors (%)	−500	−8.0	0	−5.6	0	414	35.2	6.3

to references that have no sales at all. Nevertheless, it is impossible to know that in advance, and as such the decision to eliminate a given reference from the portfolio is a management decision, far beyond the scope of this work. We also highlight the fact that if a reference is predicted by means of ZF, that doesn't mean that the final ordered quantity will be 0, as the corresponding safety stock quantity may be positive.

For all these reasons, the MM mixed model is an upgrade to Nors prior state, as Table 6 clearly shows. The plots from Fig. 3 also allow to visualize the quality of predictions obtained by the model for both datasets.

2.4 Financial Results

As usual, the main quality indicators of the forecasting model in this industry are related with the service level and sales volume. In Table 7 we present those parameters obtained from simulating MM applied to both datasets against the simulation of old methodology, where we settled $q_{1-\frac{\alpha'}{2}} = 2$, in Eq. (20).

Table 7 Financial details for new (MM) and old (MA(6)) methodology for both datasets

Dataset	Method	Service level	Sales volume	Initial stock	Final stock
DS12016	MA(6)	94.0%	264,152 €	68,112€	35,471€
DS12016	MM	95.0%	267,240€	68,112€	38,999€
DS22016	MA(6)	93.6%	1,027,987€	556,806€	260,897€
DS22016	MM	95.1%	1,052,687€	556,806€	286,083€

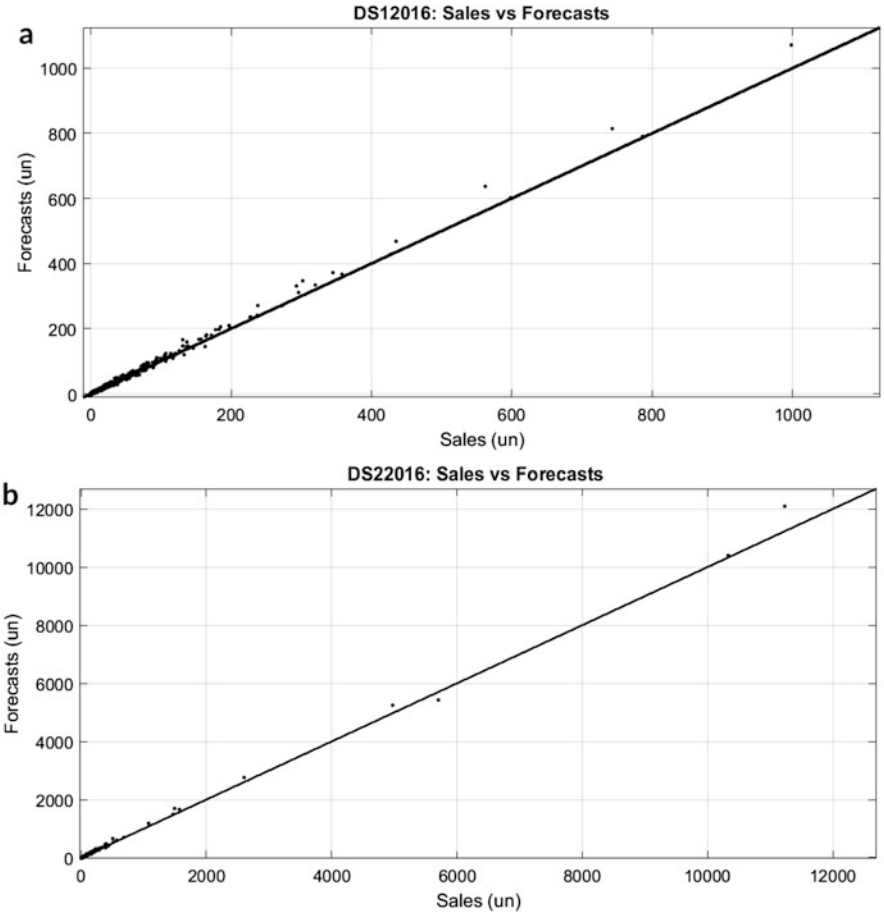

Fig. 3 Real errors applying MM to DS12016 (**a**) and DS22016 (**b**)

Given that it is common knowledge in this industry that increasing the service level towards values above 90% is very expensive, as well as that the presented sales volume is measured in cost price (in particular, the increase in sales has a higher return than the one stated in Table 7's third column) the previous results are good outputs of this model from a financial point of view. Is also important to notice that in the past, the reliability of the prediction model wasn't accurate enough, as they didn't used the SS notion, but only the safety margin given by the ABC procedure in Table 2. We made the simulations with the SS approach for all the methodology. If not, the service levels for MA(6) would drop to levels below 85%. In the past, to tackle that problem, the product managers increased the sales prediction by some factor related with their experience. Obviously, this had several negative aspects such as: depending on each manager experience and making the company's performance very vulnerable to changes in the staff. Also, the effect

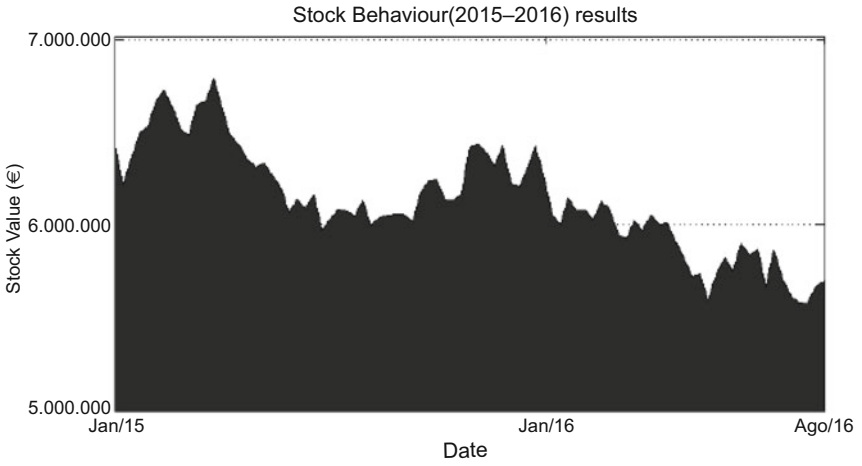

	2014	2015	Variation	
Mean Daily Stock (m€)	7.792	6.383	–1.409	–18%
Sales Volume (m€)	19.721	21.633	+1.712	+9%
Service Level (%)	91.9	92.8	+1%	
Cover rate (months)	5.7	4.2	–1.5 months	

Fig. 4 Evolution of stock value from Jan 2015 till Aug 2016 (top) and some important indicators from the previous year till the year after this model was implemented (bottom)

of trying to protect the company against out-of-stock episodes led it to reinforce manually the safety margins. In the end, the effects of applying this methodology to the whole set of the company's products in late 2014, led to the global results presented on Fig. 4.

3 MORS: A Lightweight Model for the Supplier Order Processing System

Due to the success of the MM approach explained in the previous section, it was decided to develop a new mathematical model to optimize the order processing system. One of the reasons to develop this optimization model—denoted as MORS in the forthcoming references—was related with the fact that often, product managers decide to place orders of considerable amount when the demand forecasts don't indicate so. Sometimes, this behaviour aims to accomplish contracts and to get some discounts agreed with the supplier when negotiating the rappel in the

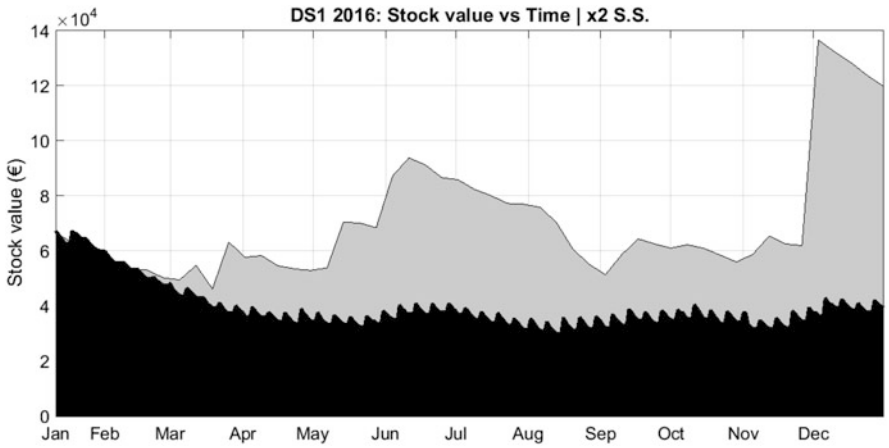

Fig. 5 Theoretical (black) vs Real Stock (grey) in DS12016 family

beginning of the year. This leads to several stock unbalances across the year, with low levels of stock during some parts of the year, that are compensated with big amounts of stock in the end of the year in order to reach the agreed amounts to accomplish the contracts or to reach some level of discount. An example may be seen in Fig. 5, where the daily stock value for the MM model (black) is plotted against the real stock (grey).

Table 8 presents the notation used for the optimization model regarding a supplier of a set comprising N references ($i = 1, \ldots, N$), supposed to be ordered in a periodic T-days scheme ($t = 1, \ldots, T$).

As those thresholds are known in the beginning of the year, our idea is to distribute the buying quantities all across the year, introducing the variable total budget (TB) and/or minimum budget to be spent (tb) as a parameter on the optimization model. This quantity is intended to be defined and evaluated across the year by the buyer manager, allowing him to decide the minimum (and/or maximum) amount to be spent in each order, as defined in constrains (30, 31). In our implementation, we distributed that value uniformly across the year, but this may be easily adapted to other types of requirements. It is also important to notice that, in grounds of a considerable loss in sales w.r.t. the goods supplied by a given supplier or some changes in the contract, the existence of this variable allows for a quick change/adaption to the buying strategy at any time of the process.

It is also natural for the manager to decide whether to restrain the number of days for which, in regular conditions, the system is allowed to maintain stock. Denoting this quantity by $Tmax_i$, the inequality (32) guarantees this possibility.

Obviously, non-feasibility of the model may be a strong indicator that the management decisions on TB and $Tmax$ may be incoherent. This may become an additional advantage of the model, as it may alert the managers to the existence of strategies that may be simultaneously unfeasible.

Table 8 Notation for the optimization model

Parameter	Description
Sets	
S	Set of all references from the given supplier
S_M	Set of the mandatory references to be ordered at the present time from the supplier
S_A	Set of the admissible references, that is, the ones that may optionally be included in the present time order to the supplier
$S' = \{S_M \bigcup S_A\}$	Set of the references allowed to be ordered in the present time from a given supplier
Decision variables	
x_{ij}	(binary decision variable) reference i is ordered for a period of $j \times P$ days
Quantities	
$Q_i(0)$	Existing stock for reference i at the time of placing the order (units)
$\hat{D}_i = \frac{\hat{X}_t}{t}$	Expected daily demand for reference i (units/day)
O_i	Reference i quantity already ordered but not delivered at the present time
R_i	The maximum inventory level for the i-th product (units)
SS_i	Reference i safety stock (units)
OP_i	Order point for reference i (units)
$I_i(t)$	The expected inventory level for the i-th product at day t (units)
Costs and incomes	
MC	Maximum inventory monetary value allowed for the existing stock w.r.t. the supplier (€)
TB	Total available budget for the supplier (€/year)
tb	Minimum budget to be spent with the supplier (€/year)
IR	Interest rate
pc_i	Reference i purchasing cost (€)
hc_i	Reference i holding cost per day (€/day)
fc_i	Reference i fixed ordering cost (€)
vc_i	Reference i variable ordering cost (€/piece)
Time quantities	
P	Supplier order periodicity (days)
LT	Supplier Lead-Time (days)
$Tmax_i$	Maximum number of days allowed to hold stock
Tf_i	Expected time-period needed to sold out all the reference i inventory (days)
Volumes	
wva	Maximum warehouse volume available for the whole stock from the supplier (m^3)
v_i	Reference i volume (m^3)
Other parameters	
SL_i	Reference i service level

Another side effect of this model, is the minimization of distinct buys per reference, as decreasing the number of different references purchased in each order pulls an additional positive effect at the warehouse level. Indeed, handling and put-away timings are important drawbacks within the warehouse management. The effect of a economy of scale, using deeper and narrower orders, may have an important impact on the global efficiency results. We noticed, prior to this model application, that there were a non-negligible number of occurrences where products, although at the warehouse, were not available to be sold as their status was "in conference" leading to worst performances at the level-of-service KPI.

Regarding the number of days in stock, we also added a constraint (33) to assure that, if the forecast model is accurate, the order will provide enough pieces of each reference to prevent that no stockout takes place before receiving the order placed in the next period.

From the implementation point of view, we ran a pre-processing analysis on the references list, splitting the references set in three different subsets. The mandatory subset, S_M, which comprises the references that must be ordered, as their stock is forecasted to end before the arrival of the next order. The admissible subset, S_A, comprehends all the references that don't belong to S_M, but whose stock is forecasted not to last more than a threshold $\tau \geq P + LT$ number of days, where P stands for the supplier order periodicity. These references, may or not be ordered within the current order (28, 29). All the references that don't belong to $S_M \cup S_A$, are discarded from the optimization model, and we will denote the resulting list as S'. In the scope of this real-world implementation, this fact may have important effects, as the number of different references by supplier may reach several thousands resulting in a significant reduction in the number of variables, which impacts the resources (memory/time) needed to run the model. We also restricted the maximum number of days for which the reference stock may be ordered to $Tmax$. We only allow our model to order the quantity of a given reference needed for multiples of the order periodicity. This option allow us to transform the integer decision variables for this type of problem $Q_i \in \mathbb{N}$, for $i \in S'$, that represent the reference i replenishment quantity, into the set of binary variables $x_{ij} \in \{0, 1\}$, $\forall i \in S'$, indicating the number of days $j \times P$, $j = 0, 1, \ldots, \lfloor \frac{Tmax}{P} \rfloor$ in which each reference i may be ordered. This transformation allow us to determine the replenishment quantity, using the identity

$$Q_i = \sum_{j=0}^{\lfloor \frac{Tmax}{P} \rfloor} j x_{ij} \hat{D}_i, \ \forall i \in S' \tag{21}$$

where $\hat{D}_i$ represents the expected daily demand for reference i. The warehouse space availability when receiving the order may also be added to the model through the inequality (34).

As our goal is to minimize the handling, storing and interest costs, the following components should be included in the objective function:

- The financial costs,[1] associated to purchase the references needed to fulfil the demand throughout a given period. Defining the reference i purchasing cost (pc_i) and the interest rate (IR), this may be represented as a function of the number of days (n) we decide to place the order,

$$\begin{aligned} f_1(n) &= \sum_{j=1}^{n} pc_i \, \hat{D}_i \, ((1 + IR/360)^j - 1) \\ &= pc_i \, \hat{D}_i \, (1 + IR/360) \frac{1 - (1 + IR/360)^n}{1 - (1 + IR/360)} - (pc_i \, \hat{D}_i) n \\ &= pc_i \, \hat{D}_i \, ((1 + IR/360) \frac{(1 + IR/360)^n - 1}{IR/360} - n) \end{aligned} \tag{22}$$

- The fixed cost fc_i associated with the administrative process of placing the order,

$$f_2(n) = fc_i \tag{23}$$

- The cost associated with the handling and put-way processes, when the goods arrive at the warehouse, where vc_i represents the variable cost per unit ordered,

$$f_3(n) = n \, vc_i \, \hat{D}_i \tag{24}$$

- Storage costs, which include warehouse rent and stock insurance, where hc_i represents the reference i unitary holding cost per day (€/day)

$$\begin{aligned} f_4(n) &= \sum_{j=1}^{n} hc_i \, \hat{D}_i \, (1 + IR/360)^j \\ &= hc_i \, \hat{D}_i \, (1 + IR/360) \frac{1 - (1 + IR/360)^n}{1 - (1 + IR/360)} \\ &= hc_i \, \hat{D}_i \, (1 + IR/360) \frac{(1 + IR/360)^n - 1}{IR/360} \end{aligned} \tag{25}$$

In order to make the comparison between different strategies simpler, a normalization is made with respect to the number of days for which a order is placed. As a consequence, the cost function with respect to a given reference i in the order placed

[1] We focused only on the interest value, as we don't consider the obsolescence rate.

to fulfil the needs for an n-days period, is defined by the following function:

$$C_i(n) = \frac{hc_i \hat{D}_i(1 + IR/360)((1 + IR/360)^n) - 1}{n\, IR/360} + \\ + pc_i\, \hat{D}_i\, ((1 + IR/360)\frac{(1 + IR/360)^n - 1}{n\, IR/360} - 1) + \\ + vc_i \hat{D}_i\, + \frac{fc_i}{n}\ (€/\text{day}) \tag{26}$$

where, w.r.t. the solution for the optimization model, the parcel $vc_i \hat{D}_i$ may be dropped.

The plot of $C_i(n)$ for a given set of references is presented in Fig. 6, showing that for each reference there are very distinct optimal order periods.

Given the previous considerations, the optimization model may be written as:

$$\min \sum_{i \in S'} \sum_{j=0}^{\lfloor \frac{Tmax_i}{P} \rfloor} C_i(jP) x_{ij} \tag{27}$$

s.t.

$$\sum_{j=0}^{\lfloor \frac{Tmax_i}{P} \rfloor} x_{ij} = 1,\ \forall i \in S_M \tag{28}$$

$$\sum_{j=0}^{\lfloor \frac{Tmax_i}{P} \rfloor} x_{ij} \leq 1,\ \forall i \in S_A \tag{29}$$

$$\sum_{i \in S'} pc_i\, Q_i \geq \frac{tb}{\frac{365}{P}} \tag{30}$$

$$\sum_{i \in S'} pc_i\, Q_i \leq \frac{TB}{\frac{365}{P}} \tag{31}$$

$$Q_i(0) + O_i + Q_i - LT * \hat{D}_i - SS_i \leq Tmax_i * \hat{D}_i,\ \forall i \in S' \tag{32}$$

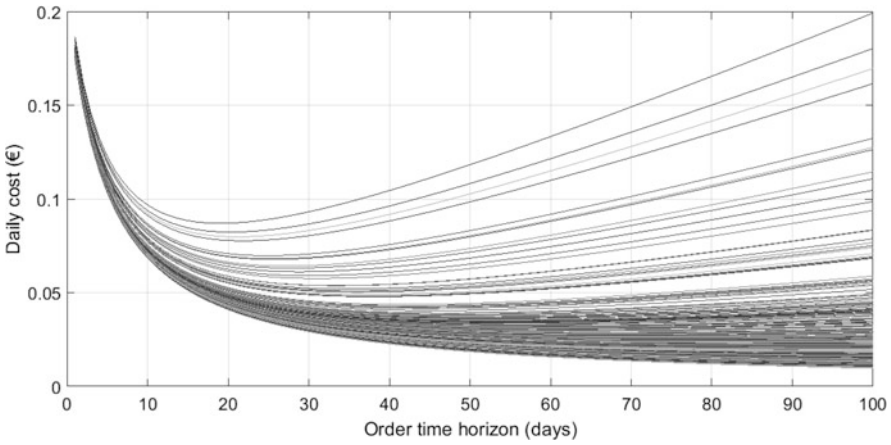

Fig. 6 Cost per day, for a given set of references, if the order is settled to cover the demand for the next x days

$$Q_i(0) + O_i + Q_i - LT * \hat{D}_i \geq (LT + P) * (\hat{D}_i + \frac{SS_i}{P}), \ \forall i \in S' \tag{33}$$

$$\sum_{i \in S'} v_i(Q_i + I_i(LT)) \leq wva \tag{34}$$

$$x_{ij} \in \{0, 1\} \tag{35}$$

4 Computational Study and Implementation Results

This optimization model was implemented using Matlab R2016b with the optimization toolbox. For both the DS12016 and DS22017 datasets, real sales and predictions given by the model described on Sect. 2.2 and respective results were compared with the existing rules for the Nors group (denoted as MM), as well as with the real order placed to the supplier. As in the previous section, we added the MA(6) method in order to be possible to check additional quality and financial indicators.

For the DS12016, we made 52 orders, resulting in a mean processing time of 20 s per order in a virtual machine with OS Windows 10, 8Gb RAM and a processor 2.8 GHz Intel Core i7. With the same hardware the solution for DS22016 dataset was exported, on average, after 46 s of computation time. Those times include the data importation and the solution exportation to an *Excel* worksheet, which is then imported by Nors native's ERP. We settled the total budget (TB) to the real amount bought by Nors in 2016 with each of the suppliers, and the order periodicity to 7

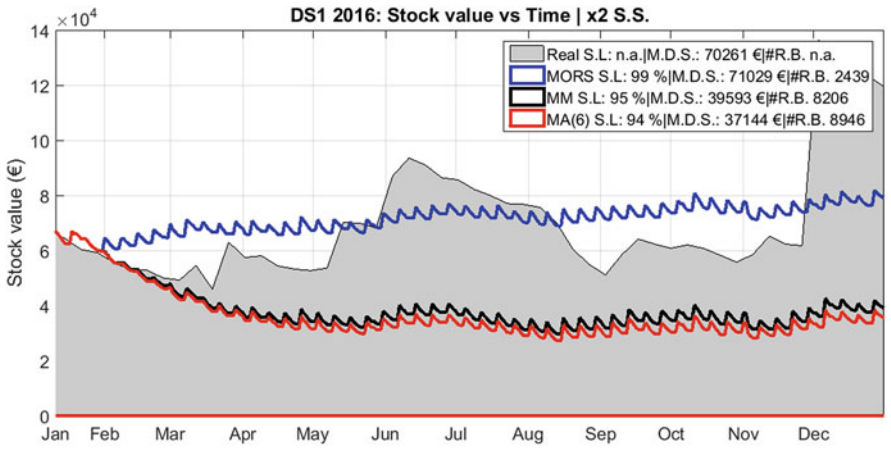

Fig. 7 DS12016: Comparative performance of three methods vs real data, using 2× Safety Stock and $T_{max} = 364$ days

days. We didn't set the tb parameter in (30), as was our purpose to demonstrate that the budget for DS12016 was clearly excessive even when $T_{max} = 364$, and that was not an issue regarding the other dataset. The maximum order value per week was defined as TB/52 although it may be settled in other ways (e.g. the remaining yearly budget divided by the number of remaining weeks till the end of the year). The maximum number of days to hold stock was defined in 364 days or 126 days (two different simulations) for DS12016, because the annual budget to this supplier was clearly excessive (Fig. 5). For DS22016 that value was settled to 94 days, as the yearly budget was much tighter w.r.t. the company needs. Both suppliers had an expected lead time of 28 days. For the MM and MA(6) the number of weeks for which the reference is ordered is one month plus the value indicated by EOQ (Table 2), and all the simulations used $Z_{1-\frac{\alpha'}{2}} = 2$ in (20).

In terms of daily stock, the overall behavior of the method is presented in Figs. 7, 8, and 9, with the following legend abbreviations:

- Real—Real stock on the company.
- MORS—Stock behaviour using MORS optimization process.
- MM—Stock behaviour using the MM model cf. Sect. 2.2.
- MA(6)—Stock behaviour using Nors original forecast model.
- S.L.—Service level (%).
- M.D.S.—Mean Daily Stock (€).
- #R.B.—Total of references unique buy's.

Analysing Table 9, where the main KPIs for the whole set of simulations are presented, some interesting facts are highlighted. The total amount really bought by Nors w.r.t. the DS12016 dataset is clearly excessive for the defined maximum period to hold stock. At the same time, the comparison between the MORS optimized

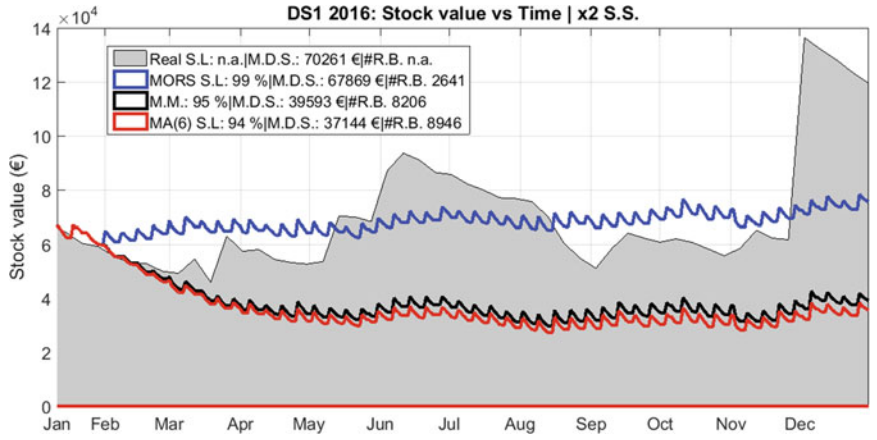

Fig. 8 DS12016: Comparative performance of three methods vs real data, using 2× Safety Stock and $T_{max} = 126$ days

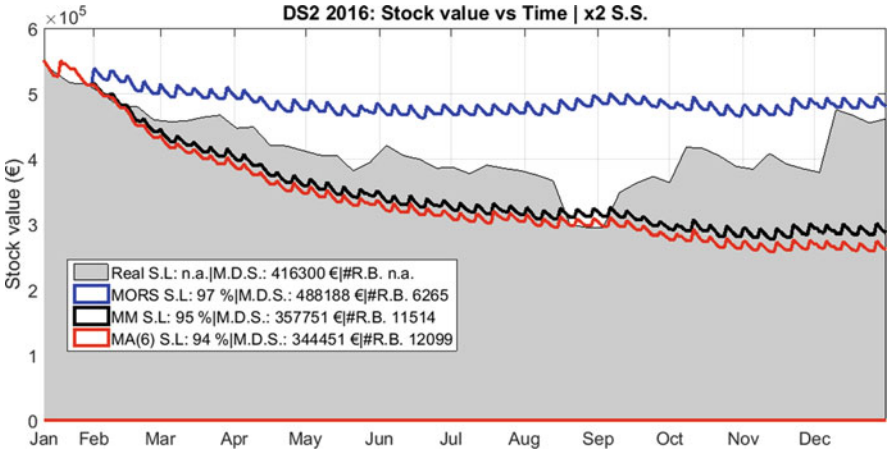

Fig. 9 DS22016: Comparative performance of three methods vs real data, using 2× Safety Stock and $T_{max} = 91$ days

model and the MM model, both based on the same forecasting model, clearly gives much better service-levels to our model. Also, the number of orders of different references made all over the year, reduces by a factor of 0.32 (0.54 for DS22016) when compared with the MM model. The purchase patterns of the models presented in Fig. 10, clearly emphasizes advantages at the warehouse level. The same pattern is found when looking at the mean percentage of times that the references are ordered in the whole year: 2.2 (per reference) for MORS versus 7.0 for the MM method, which emphasizes that impact, as it represents a very significant reduction on the number of different references that must be manipulated in the warehouse over the

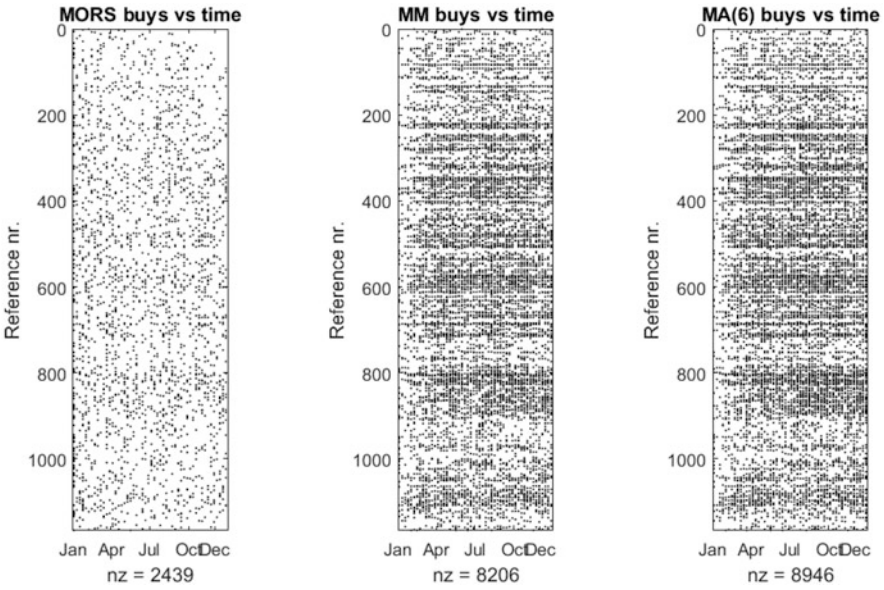

Fig. 10 DS12016: Purchases pattern for three methods with $T_{max} = 364$ days

year. These values are 1.6 and 2.9 for DS22016, resulting in 54% of reduction on the optimized model.

It is also important to notice that our model's Objective Function (27), had a global cost reduction factor between 0.5 (DS12016) and 0.71 (DS22016), which reflects very important savings within the logistics costs. The absolute values are not presented because of confidentiality related aspects. A final remark should be made w.r.t. the stock and/or purchases amounts as we just had access to the existing stock for those families in a weekly base (the day where the order was placed), as well as the orders placed in December 2015, that should had been delivered in January 2016. As so, some minor inconsistencies in this section may occur, regarding service levels in the first 28 (Lead-time) days of January or real stock levels. Nevertheless, independently of the goods being delivered in the beginning of 2017 due to lead time, we accounted for all the orders placed during 2016 in the financial results summary presented in Table 9. Concerning the lost sales KPI (Figs. 11 and 12), we evaluated these values based on the real sales recorded by the company. This happened because Nors didn't keep the record of lost sales in the system, and, as so it was impossible to evaluate that KPI accurately afterwards. The lost sales value is reduced in more than 50%, although based on different levels of purchases as the MM model doesn't take into account the available budget.

Figure 13 presents the order periodicity for the whole set of references, where a significant heterogeneity may be seen, resulting of minimizing order's cost according to the optimization model.

Table 9 Results main indicators for DS12016 and DS22016

Parameter	DS1 2016	DS2 2016
# References	1166	4032
Total budget (€)	333,283 €	1,051,848
Periodicity	7	7
Min. days stock	7	7
Max. days stock	126/364	91
Real M.D.S.(€)	70,261	416,299
MORS M.D.S. (€)	67,869/71,030	488,188
M.M. M.D.S (€)	39,594	357,751
MORS S.L. (%)	98.7/98.6	97.5
M.M. S.L. (%)	95.1/95.1	95.1
MORS # unique buys	2641/2439	6265
M.M. # unique buys	8206	11,514
Reduction in # buys (%)	32/30	54
Reduction in O.F. (%)	50/56	71
Initial stock (€)	68,112	556,806
Real final stock (€)	119,450	461,057
MORS final stock (€)	75,340/78,991	479,628
M.M. final stock (€)	38,999	286,084
MORS lost sales (€)	4028/4226	38,946
M.M. lost sales (€)	14,706	94,910
MORS purchase vol. (€)	293,308/297,131	1,040,644
M.M. purchase vol. (€)	243,061	776,754

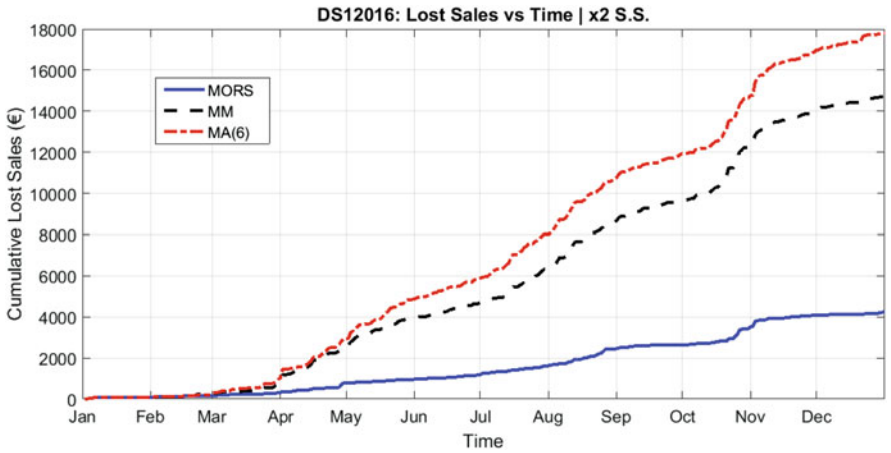

Fig. 11 DS12016: Lost Sales Monetary Value for three methods with $T_{max} = 364$ days

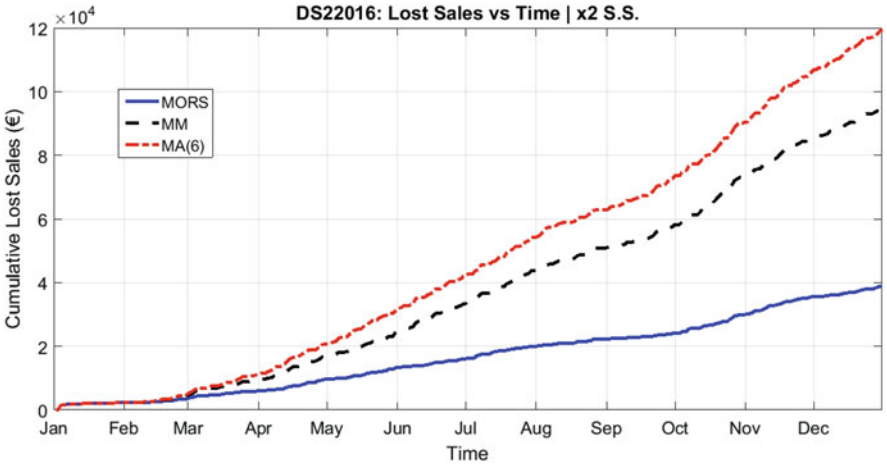

Fig. 12 DS22016: Lost Sales Monetary Value for three methods

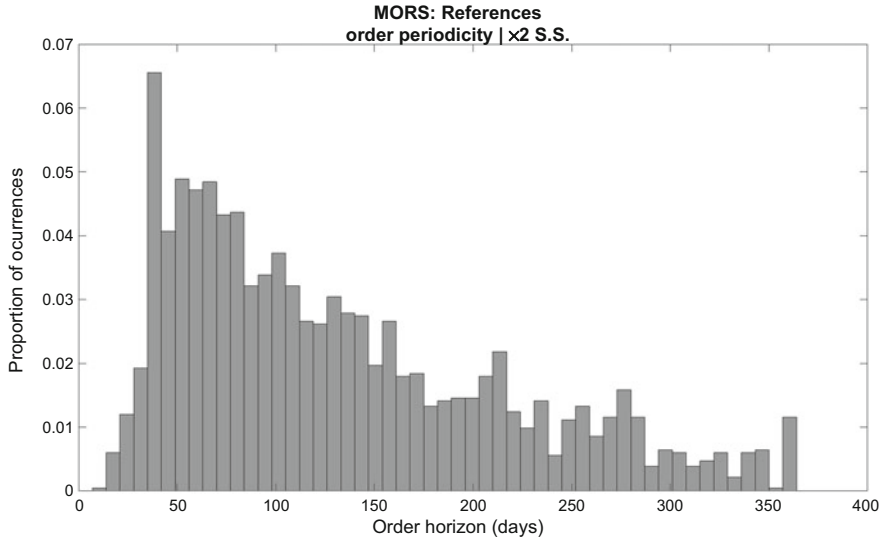

Fig. 13 DS12016: Histogram of relative frequencies vs orders periodicity. Only ordered references were considered

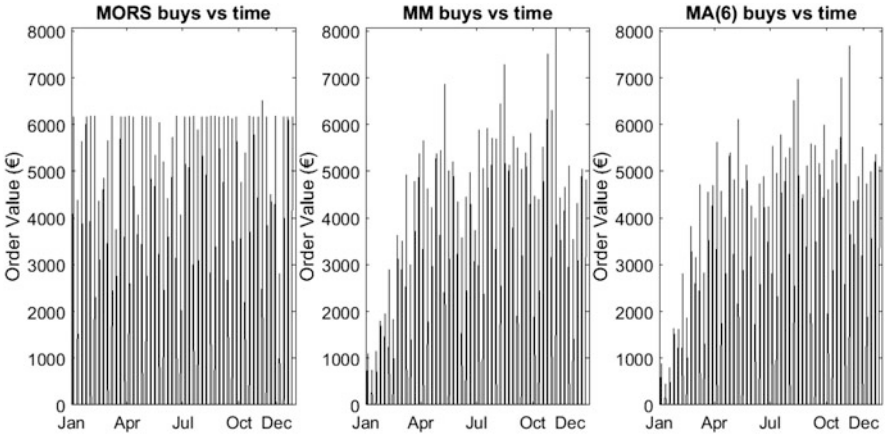

Fig. 14 DS12016: Buying amounts per order with $T_{max} = 364$ days

It is important to notice that although the MORS mean daily stock may increase as a direct consequence of the values used for T_{max}, the volume of buys is kept below the maximum allowed (that is, the real volume for 2016). Also, when compared with MM and with the original Nors model, the amount per order is made much more uniform across the year, as it may be seen in Fig. 14.

5 Conclusions

In this work we modelled, developed, and implemented a new methodology in Nors group for the spare parts forecasting, improving the accuracy in predictions. This was tested with two different suppliers with distinct orders of magnitude regarding their budget. Afterwards, those forecasts were used as input on a new optimization model to decrease the financial costs of the ongoing orders. The proposed methodology had two different outcomes when tested in those two distinct suppliers for the 2016 year. On the one hand, and regarding the forecasting accuracy, it increased the service level for more than 1% in both suppliers. On the other hand, applying the MORS optimization model with the same budget that the company used in 2016 for those suppliers, we found that: the service level increased in the range of 2.4–3.6%; the number of different reference purchases along the whole year was reduced between 30% and 54% which has a strong impact on the warehouse management and the stock level was kept smooth across the whole year. Finally, the objective function of the optimization model, that is, the indirect costs of the purchases (handling, interests, and warehouse renting) were reduced by a factor of between 0.5 and 0.71. As expected, the mean daily stock value was increased, but the costs of that raise were already contemplated in the objective function definition. All

of these were achieved in a model that is fully parametrizable by the management regarding factors like the maximum period to hold stock or the total budget amount, making it flexible to encompass any further changes in the management policy of the group. Despite the considerable gains achieved with this implementation, the model is being updated on the forecasting methods described on Sect. 2. In fact, the group is now using several other information available and new techniques of artificial intelligence, in order to obtain better forecasts for the references demands.

Acknowledgments The authors would like to thank the Nors Group management for all its support in the scientific release of this work. The authors would also like to thank the several LABMI members whose valuable comments helped to improve the results of this implementation.

References

1. Bacchetti, A., Saccani, N.: Spare parts classification and demand forecasting for stock control: Investigating the gap between research and practice. Omega **40**(6), 722–737 (2012)
2. Boylan, J.E., Syntetos, A.A.: Spare parts management: a review of forecasting research and extensions. IMA J. Manag. Math. **21**, 227–237 (2010)
3. Caiado, J.: Métodos de Previsão em Gestão. Edições Sílabo, Lisboa (2011)
4. Cohen, M.A., Agrawal, N., Agrawal, V.: Winning in the aftermarket. In: Harvard Business Review. https://hbr.org/2006/05/winning-in-the-aftermarket. Visited on 12 Feb 2017
5. Croston, J.D.: Forecasting and stock control for intermittent demands. Oper. Res. Q. **23**, 289–303 (1972)
6. Kennedy, W.J., Patterson, J.W., Fredendall, L.D.: An overview of recent literature on spare parts inventories. Int. J. Prod. Econ. **72**, 201–215 (2002)
7. Makridakis, S.G., Wheelwright S.C.: Forecasting Methods for Management. Wiley, London (1989)
8. Masoud, V., Manbir, S.: Application of game theory on inventory level decision making. Int. J. Bus. Econ. Res. **3(6)**, 211–219 (2014). https://doi.org/10.11648/j.ijber.20140306.12
9. Matsumoto, M., Ikeda, A.: Examination of demand forecasting by time series analysis for auto parts remanufacturing. J. Remanuf. **5**(1), 1–20 (2015)
10. Neves, G., Diallo, M., Lustosa, L.: Initial electronic spare parts sock and consumption forecasting. Investig. Oper. **28**, 45–58 (2008)
11. Rodrigues, M., Sirova, E.: Application of spare parts management methods in the companies in the Czech Republic. ACC J. **23**, 136–145 (2017)
12. Romeijnders, W., Teunter, R., Jaarsveld W.: A two-step method for forecasting spare parts demand using information on component repairs. Eur. J. Oper. Res., **220**, 386–393 (2012)
13. Suomala, P., Sievänen,M., Paranko, J.: The effects of customization on spare part business: a case study in the metal industry. Int. J. Prod. Econ. **79**(1), 57–66 (2002)
%bibitemSyntetosBoylan
14. Syntetos, A.A., Boylan, J.E.: On the bias of intermittent demand estimates. Int. J. Prod. Econ. **71**, 457–466 (2001)
15. Teunter, R.H., Syntetos, A.A., Zied Babai, M.: Intermitent demand: linking forecasting to inventory obsolescence. Eur. J. Oper. Res. **214**, 606–615 (2011)
16. Zermati, P.: A Gestão de Stocks. Editorial Presença, Lisboa (2000)

Topological Index Analysis and Its Application to Multi-Physical Systems in System Simulation Software

Michael Kolmbauer, Günter Offner, and Bernhard Pöchtrager

Abstract This work is devoted to the topological analysis of multi-physical networks stemming from automated modeling processes in system simulation software. A special focus is on the methodical treatment of multi-physical networks, which can be utilized to develop robust and user-friendly simulation tools. In the multi-physical case, the already available topological criteria of different physics have to be merged and reinterpreted. A general receipt for their analysis is described in terms of a representative example, a fluid-solid network which is thermally coupled. The theoretical results are put in context to a practical realization in a simulation software in terms of modeling and coupling concepts, which help to improve the useability of system simulation software for software application engineers.

1 Introduction and Industrial Background

The importance of system simulation in automotive industry has grown significantly during the past two decades and will grow further. Reasons are the improved power of computer systems and the applied software but also the increasing complexity of multi-physical systems to be modeled. Typical investigation topics related for instance to a hybrid vehicle incorporate mechanical, electrical, fluid dynamical and even chemical domains within one system. Therefore both, the simulation of each separated domain, but also of overall models combining a subset or even all domains

M. Kolmbauer (✉)
MathConsult GmbH, Linz, Austria
e-mail: michael.kolmbauer@mathconsult.co.at

G. Offner
AVL List GmbH, Graz, Austria
e-mail: guenter.offner@avl.com

B. Pöchtrager
Radon Institute for Computational and Applied Mathematics (RICAM), Austrian Academy of Sciences, Linz, Austria
e-mail: bernhard.poechtrager@ricam.oeaw.ac.at

M. Cruz et al. (eds.), *Progress in Industrial Mathematics: Success Stories*,
SEMA SIMAI Springer Series 5, https://doi.org/10.1007/978-3-030-61844-5_10

is of importance. As a consequence the applied software needs to be based on robust algorithms, which itself requires a structured mathematical and computer scientific basis framework. Based on this framework the according modeling equations and their implementation are build up on.

In this work we consider the analysis of multi-physical dynamical systems stemming from automated modeling processes in system simulation software. In this context, the term *multi-physical* is used to describe models which are a combination of different physical characteristic equations. For example for fluid and gas flows, those are *Navier-Stokes* or *Euler equations*, in electric those are *Maxwell's equations*, in translation or rotational mechanics those are *Newton's laws of motion* and for solid masses those are *heat equations*. The different equations are coupled by applying conservation laws on various levels. In system simulation the detailed analysis of the interaction between vehicle dynamics, transient combustion or electric engine performance and the corresponding thermal management systems is of special interest in order to calculate the complete energy and temperature distribution across the entire vehicle. In this work this kind of coupling is referred to as *thermal coupling*.

Today's system modeling software typically offers a wide range of basic physical components from several domains (e.g. fluid flow, electric networks, gas flow, heat flow), which can be assembled to customized physical networks simply by drag and drop. The governing equations are derived by representing the network as a linear graph whose edges and nodes correspond to the basic physical components (e.g. pipes, pumps, heat exchangers). Combining the connection structure of the graph with the physical equations of the components, the physical network is modeled as a differential algebraic equation (DAE). Typically those DAEs are of higher index. Hence in order to allow a stable numerical integration, the DAEs need to be reformulated to an index reduced (differential-index (d-index) 1 or strangeness-index (s-index) 0), representation, cf. [15]. Using algebraic graph and DAE theory, the solvability of the mathematical model as well as its index can be analyzed and translated as conditions on the network structure and properties of its elements. Hence *topology based* index analysis emerges as a suitable tool for the investigation of DAEs stemming from automatic generated system models in system simulations tools, since it combines the scientific disciplines of *Analysis for DAEs* [8] and *Graph Theory* [10]. Due to the seamless integration of the network structure in the simulation process, properties of the DAE can be directly reinterpreted on the network structure, allowing for an illustrative modeling paradigm. So far this methodology has been successfully used in various physical domains, including electric circuits [17], gas networks [13] and fluid networks [4–6]. The developed methodology focuses on the analysis of one specific physics. The challenges in the development of future *topology based* methods, do not lie in the analysis of the individual physical networks (electric, gas or fluid networks), but in the assessment of the multi-physical network as a whole (see e.g. [2]). Coupling different physics may lead to a change in the topological criteria of the individual subsystems.

The vice verse question arises, if an automated assembled multi-physical model has to be partitioned into several submodels. This use case is of importance if

multi-rate methods (see e.g. [3]) are applied to speed up numerical integration by taking advantage of different time constants of the individual physics. It is not straightforward to decompose a d-index 1 DAE into several DAEs of d-index 1 and guarantee existence and uniqueness of solutions at the same time. In terms of usability the decomposition has to conserve the model structure and consequently the solution. Especially in the constellation of automated generated DAEs the derivation of *topological criteria* for an appropriate decomposition seems to be promising. Since those decompositions typically cross multi-physical boarders, the *topological criteria* have to be multi-physical as well.

The structure of the work is the following. In Sect. 2 we formulate a multi-physical network model consisting of a fluid network and a solid network. Section 3 is devoted to the development of an automated partitioning algorithm of the coupled system. For this purpose the global network is divided into its individual physical parts, i.e. into a solid, cf. Sect. 3.1, and a fluid part, cf. Sect. 3.2. For each individual domain the corresponding DAE is stated in input-output form by introducing valid coupling variables (inputs and outputs). For both solvability and index results are provided. In Sect. 3.3 valid coupling conditions are formulated and the coupled system is analyzed with respect to solvability and index constraints. Sections 4 and 5 describe the possible application of the developed theory in commercial system simulation software. While Sect. 4 is devoted to the design of the simulation software in terms of the topological representation of a physical model and the transient solution of the model, Sect. 5 focuses on solver design in terms of transient multi-rate calculations. Section 6 provides an overview of the addressed issues. Therein another major focus is put on the description of open topics and further research requirements.

2 A Multi-Physical Model for Fluid Networks Coupled to Solid Networks

As an example we consider a simple thermal network model, which is an extension of the network model analyzed in [5]. After formulating the full coupled model, consisting of a fluid network and a solid network, we demonstrate, that the combined model obtains a domain specific topological criteria.

We consider a multi-physical network $\mathcal{N}$

$$\mathcal{N} = \{Pi, Pu, De, Vj, Lj, Re, Ht, Hs, Sw, Lw, Tb\}, \tag{1}$$

that is composed of pipes Pi, pumps Pu, demands De, volume junctions Vj, lumped junctions Lj and reservoirs Re, which are filled with an incompressible fluid and heat transfers Ht, heat sources Hs, solid walls Sw, lumped walls Lw and temperature boundaries Tb. The network is represented by a directed linear graph

$\mathcal{G} = \{\mathcal{V}, \mathcal{E}\}$, where the set of vertices $\mathcal{V}$ and edges $\mathcal{E}$ are defined as

$$\mathcal{V} = \{Vj, Lj, Re, Sw, Lw, Tb\},$$
$$\mathcal{E} = \{Pi, Pu, De, Ht, Hs\}.$$

The network $\mathcal{N}$ is assumed to satisfy the following assumptions on its connection structure.

Assumption 1 (Network Assumption) *Let $\mathcal{N}$ be a network as defined in* (1).

1. *The network is connected.*
2. *Two junctions are connected at most by one pipe or one pump.*
3. *Each pipe, pump and demand has an assigned direction.*
4. *Every junction is adjacent to at most one demand branch or heat source.*
5. *Every reservoir is connected at most to one pipe or pump.*
6. *Two walls are connected at most by one heat transfers.*
7. *Each heat transfer and heat source has an assigned direction.*
8. *Every wall is adjacent to at most one heat source.*
9. *Every temperature boundary is adjacent to at most one heat transfer.*
10. *A pair of a wall and a junction is connected at most by one heat transfer.*

Assumption 1 guarantees, that the network graph $\mathcal{G}$ is simple, oriented and connected. An example for $\mathcal{N}$ is displayed in Fig. 1.

The connection structure of the network $\mathcal{N}$ is described by the incidence matrix $A_{\mathcal{N}} = (a_{ij})$, which is defined as, cp. e.g. [7, 10, 16],

$$a_{ij} = \begin{cases} 1, & \text{if the edge } j \text{ leaves the vertex } i, \\ -1, & \text{if the edge } j \text{ enters the vertex } i, \\ 0, & \text{else.} \end{cases}$$

This incidence matrix can be further partitioned into blocks considering its involved types of edges $E \in \mathcal{E}$ as well its involved types of vertices $V \in \mathcal{V}$. The corresponding incidence matrices are given by $A_{V,E} \in \{-1, 0, 1\}^{n_V \times n_E}$, where n_V and n_E denote the number of elements of the relevant type. Using Assumption 1 and sorting the rows and columns of $A_{\mathcal{N}}$ according to the different element types,

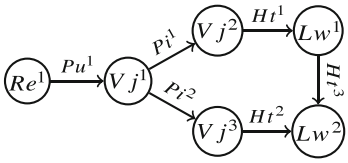

Fig. 1 Example of a graph $\mathcal{G}$ of a multi-physical network $\mathcal{N}$

the incidence matrix can be representation in the following form:

$$A_{\mathcal{N}} = \begin{bmatrix} A_{Vj,Pi} & A_{Vj,Pu} & A_{Vj,De} & A_{Vj,Ht} & A_{Vj,Hs} \\ A_{Lj,Pi} & A_{Lj,Pu} & A_{Lj,De} & A_{Lj,Ht} & A_{Lj,Hs} \\ A_{Re,Pi} & A_{Re,Pu} & 0 & 0 & 0 \\ 0 & 0 & 0 & A_{Sw,Ht} & A_{Sw,Hs} \\ 0 & 0 & 0 & A_{Lw,Ht} & A_{Lw,Hs} \\ 0 & 0 & 0 & A_{Tb,Ht} & 0 \end{bmatrix}. \tag{2}$$

Beside the connection structure, each network element is equipped with a characteristic equation, cf. [5, 6], describing the mass flow q_E and/or the enthalpy flow H_E on edge elements $E \in \mathcal{E}$ and the pressure p_V and/or the temperature T_V on vertex elements $V \in \mathcal{V}$. Applying mass and energy conservation laws, the dynamic of the coupled multi-physical network $\mathcal{N}$ is described by the DAE: Find $(q_{Pi}^T, q_{Pu}^T, p_{Vj}^T, p_{Lj}^T, H_{Pi}^T, H_{Pu}^T, T_{Vj}^T, T_{Lj}^T, H_{Ht}^T, T_{Sw}^T, T_{Lw}^T)^T$, such that

$$\begin{aligned}
\frac{dq_{Pi}}{dt} &= c_{1,Pi}\left(A_{Vj,Pi}^T p_{Vj} + A_{Lj,Pi}^T p_{Lj} + A_{Re,Pi}^T p_{Re}\right) \\
&\quad + c_{2,Pi}\,\mathrm{diag}\left(|q_{Pi}|\right) q_{Pi} + c_{3,Pi} \\
f_{Pu}(q_{Pu}) &= A_{Vj,Pu}^T p_{Vj} + A_{Lj,Pu}^T p_{Lj} + A_{Re,Pu}^T p_{Re} \\
0 &= A_{Vj,Pi} q_{Pi} + A_{Vj,Pu} q_{Pu} + A_{Vj,De} q_{De} \\
0 &= A_{Lj,Pi} q_{Pi} + A_{Lj,Pu} q_{Pu} + A_{Lj,De} q_{De} \\
m_{Vj} c_{p,Vj} \frac{dT_{Vj}}{dt} &= A_{Vj,Pi} H_{Pi} + A_{Vj,Pu} H_{Pu} + A_{Vj,De} H_{De} \\
&\quad + A_{Vj,Ht} H_{Ht} + A_{Vj,Hs} H_{Hs} \\
0 &= A_{Lj,Pi} H_{Pi} + A_{Lj,Pu} H_{Pu} + A_{Lj,De} H_{De} \\
&\quad + A_{Lj,Ht} H_{Ht} + A_{Lj,Hs} H_{Hs} \\
H_{Pi} &= B_{Vj}(q_{Pi}) T_{Vj} + B_{Lj}(q_{Pi}) T_{Lj} + B_{Re}(q_{Pi}) T_{Re} \\
H_{Pu} &= B_{Vj}(q_{Pu}) T_{Vj} + B_{Lj}(q_{Pu}) T_{Lj} + B_{Re}(q_{Pu}) T_{Re} \\
m_{Sw} c_{p,Sw} \frac{dT_{Sw}}{dt} &= A_{Sw,Ht} H_{Ht} + A_{Sw,Hs} H_{Hs} \\
0 &= A_{Lw,Ht} H_{Ht} + A_{Lw,Hs} H_{Hs} \\
H_{Ht} &= c_{Ht}\big(A_{Sw,Ht}^T T_{Sw} + A_{Lw,Ht}^T T_{Lw} \\
&\quad + A_{Vj,Ht}^T T_{Vj} + A_{Lj,Ht}^T T_{Lj} + A_{Tb,Ht}^T T_{Tb}\big)
\end{aligned} \tag{3}$$

for given boundary conditions $q_{De} = \bar{q}_{De}$, $H_{De} = \bar{H}_{De}$, $H_{Hs} = \bar{H}_{Hs}$ $p_{Re} = \bar{p}_{Re}$, $h_{Re} = \bar{h}_{Re}$, $T_{Tb} = \bar{T}_{Tb}$, positive definite diagonal coefficient matrices $c_{1,Pi}$, $c_{2,Pi}$,

$c_{3,Pi}$, $c_{p,Vj}$, $c_{p,Sw}$, c_{Ht}, positive definite diagonal mass matrices m_{Vj}, m_{Sw}, the pump characteristic f_{Pu} and the enthalpy function $B_\star$ ($\star \in \{Vj, Lj, Re\}$) as defined in [6].

Under the additional Assumption 2 (cf. [6]), the unique solvability of the DAE (3) can be characterized in Theorem 1.

Assumption 2 (Network Solvability) *Let $\mathcal{N}$ be a network as defined in (1).*

- *$\mathcal{N}$ contains no cycles of pumps.*
- *$\mathcal{N}$ contains no paths of pumps between two reservoirs.*
- *For each junction, the mass flow does not vanish, i.e. $\sum |q_i| > 0$ for all q_i adjacent to the junction.*

Theorem 1 *Let $\mathcal{N}$ be a network given by (1), meeting the requirements of Assumptions 1 and 2 with positive definite coefficient matrices m_{Sw}, $c_{p,Sw}$ and c_{Ht_S}. Let $n_{Re} > 0$, where n_{Re} denotes the number of reservoirs Re in the network. Then, the following statements hold.*

1. *The DAE (3) is regular and has strangeness index $\mu = 1$ (d-index 2).*
2. *The DAE (3) is uniquely solvable for every feasible initial condition condition fulfilling (3) at $t = t_0$ and the solution is continuous differentiable.*

Proof In [6] it is shown, that a network consisting only of fluid elements $\mathcal{N}_F = \{Vj, Lj, Re, Pi, Pu, De\}$ yields a uniquely solvable system of DAEs with strangeness index 1. Theorem 2 requires a fixed temperature in order to obtain existence and uniqueness of the solution. Since the fixed temperature is provided by the condition $n_{Re} > 0$ in the network $\mathcal{N}$, the unique solvability follows for the DAE (3). In [6], it is shown that the mass flow related part q_E ($E \in \mathcal{E}$) and p_V ($V \in \mathcal{V}$) causes the strangeness index 1 condition, while under Assumption 2, the energy flow related part H_E ($E \in \mathcal{E}$), and T_V ($V \in \mathcal{V}$) obtains a strangeness index 0 condition. Since the extension to the thermal elements $\mathcal{N}_S = \{Sw, Lw, Tb, Ht, Hs\}$ only effects the energy part due to Assumption 1, and the thermal elements obtain analogous strangeness index 0 conditions (cf. Theorem 2), the proof of [6] can be easily extended to the network $\mathcal{N}$. Hence, the result follows as a natural extension from [6] with the results obtained in the proof of Theorem 2. □

Theorem 1 guarantees existence and uniqueness of solutions for the coupled multi-physical system. Following [6] an index reduced surrogate model can be deduced, which has strangeness index $\mu = 0$ (d-index 1). The surrogate model can be assembled based on the network information only without the need for further algebraic manipulations. Due to strangeness index $\mu = 0$ the surrogate model is suited to be solved with a standard time integration scheme. Having a look at the multi-physical characteristic of the problem it is notable, that the topological criteria only depends on elements in the fluid network $\mathcal{N}_F$ and not on elements of $\mathcal{N}_S$. Indeed the original cause of this criteria and its effects on further manipulations in multi-physical context is investigated in the next section.

3 Topology Based Automatic Decomposition of Multi-Physical Networks

In this section the coupled model is decomposed into submodels according to their physical nature. The subsystems are stated in an input-output form, which structure is motivated by standardized approaches like [1, 14] or their software representation in form of a Functional Mock-up Unit [11]. For this purpose, the coupling variables u for the input to the system and y for the output of the system are introduced to enable the exchange of information between the domains. We demonstrate, that the choice of the decomposition has an effect on the solvability of the individual subsystems. Restoring the unique solvability of the individual domains is critical, if individual solvers (standard time integration schemes) are applied, e.g., in a multi-rate or co-simulation procedure, see, e.g., [2, 3]. Furthermore feasible coupling conditions emerge from the analysis as topological criteria based on the input-output structure. Using the derived coupling conditions, a system of coupled DAEs can be stated, which obtains the same solution as the original DAE (3).

3.1 A Solid Network

We consider a solid network

$$\mathcal{N}_S = \left\{ Ht_S, Hs, Sw, Lw, Tb, \overline{Hs}_S, \overline{Tb}_S \right\}, \tag{4}$$

that is composed of heat transfers Ht_S, heat sources Hs, solid walls Sw, lumped walls Lw, temperature boundaries Tb_S, heat source inputs $\overline{Hs}_S$ and temperature boundary inputs $\overline{Tb}_S$. The input elements $\overline{Hs}_S$ and $\overline{Tb}_S$ are introduced to enable generic couplings between different physical domains. Their corresponding variables are denoted by $u_{\overline{Hs}_S}$ and $u_{\overline{Tb}_S}$ and serve as inputs from other domains. Furthermore output variables are introduced where each variable corresponds to an input variable. Temperatures of solid walls y_{Sw} and lumped walls y_{Lw} as well as heat transfer elements y_{Ht_S} are exposed and provide their information for other domains. The selection of the possible coupling outputs is shown in Eqs. (5d)–(5f). The basic network assumptions of Assumption 1 carry over to the solid network $\mathcal{N}_S$ as well. The connectivity of the in- and outputs within the thermal network is described with the corresponding incidence matrices, denoted by $A_{Sw,\overline{Hs}_S}$, $A_{Lw,\overline{Hs}_S}$ and $A_{\overline{Tb}_S,Ht_S}$, which are natural extensions of the incidence matrix (2).

The DAE for the network $\mathcal{N}_S$ in input-output form is given by: For given continuous inputs $(u^T_{\overline{Hs}_S}, u^T_{\overline{Tb}_S})^T$, find the temperatures $(T^T_{Sw}, T^T_{Lw})^T$, the heat fluxes $(H^T_{Ht_S})^T$ and the outputs $(y^T_{Sw}, y^T_{Lw}, y^T_{Ht_S})^T$, such that

$$m_{Sw} c_{p,Sw} \frac{dT_{Sw}}{dt} = A_{Sw,Ht_S} H_{Ht_S} + A_{Sw,Hs} H_{Hs} + A_{Sw,\overline{Hs}_S} u_{\overline{Hs}_S} \tag{5a}$$

$$0 = A_{Lw,Ht_S} H_{Ht_S} + A_{Lw,Hs} H_{Hs} + A_{Lw,\overline{Hs}_S} u_{\overline{Hs}_S} \tag{5b}$$

$$H_{Ht_S} = c_{Ht_S}\big(A^T_{Sw,Ht_S} T_{Sw} + A^T_{Lw,Ht_S} T_{Lw} + A^T_{Tb,Ht_S} T_{Tb} + A^T_{\overline{Tb}_S,Ht_S} u_{\overline{Tb}_S}\big) \tag{5c}$$

$$y_{Sw} = |(A^T_{Sw,\overline{Hs}_S} + A_{\overline{Tb}_S,Ht_S} A^T_{Sw,Ht_S})| T_{Sw} \tag{5d}$$

$$y_{Lw} = |(A^T_{Lw,\overline{Hs}_S} + A_{\overline{Tb}_S,Ht_S} A^T_{Lw,Ht_S})| T_{Lw} \tag{5e}$$

$$y_{Ht_S} = A_{\overline{Tb}_S,Ht_S} H_{Ht_S}, \tag{5f}$$

for given boundary conditions $H_{Hs} = \bar{H}_{Hs}$ and $T_{Tb} = \bar{T}_{Tb}$ and given diagonal positive definite coefficient matrices m_{Sw}, $c_{p,Sw}$ and c_{Ht_S}. For practical reasons, the sign of the outputs is controlled via the absolute value of a matrix $B = (b_{ij})$, defined via $|B| := (|b_{ij}|)$. The unique solvability of the network DAE (5) can be characterized via the graph and the input network characteristic.

Theorem 2 *Let $\mathcal{N}_S$ be a network given by (4) fulfilling Assumption 1 with positive definite coefficient matrices m_{Sw}, $c_{p,Sw}$ and c_{Ht_S}. Let $n_{Sw} + n_{Tb} + n_{\overline{Tb}_S} > 0$, where n_{Sw} denotes the number of solid walls Sw, n_{Tb} denotes the number of temperature boundaries Tb, and $n_{\overline{Tb}_S}$ denotes the number of temperature boundary inputs $\overline{Tb}_S$. Then, the following statements hold:*

1. *The DAE (5) is regular and has strangeness index $\mu = 0$ (d-index 1).*
2. *The DAE (5) is uniquely solvable for every feasible initial condition fulfilling (5) at $t = t_0$ and the solution is continuous differentiable.*
3. *The outputs y_{Sw} and y_{Lw} are continuous differentiable.*

Proof

1. To show regularity and strangeness index $\mu = 0$, it is sufficient to transform the DAE (5) to its explicit form. This concerns just the lumped wall characteristic (5b), since all other equations are already given in their explicit representation. First we substitute H_{Ht_S} in the lumped wall equation (5b) by the right hand side of the heat transfer characteristic (5c). The equation reads as

$$0 = A_{Lw,Ht_S} c_{Ht_S} A^T_{Lw,Ht_S} T_{Lw} + c_{Ht_S}\big(A^T_{Sw,Ht_S} T_{Sw} + A^T_{Tb,Ht_S} T_{Tb} + A^T_{\overline{Tb}_S,Ht_S} u_{\overline{Tb}_S}\big) + A_{Lw,Hs} H_{Hs} + A_{Lw,\overline{Hs}_S} u_{\overline{Hs}_S}.$$

   This system needs to be solved according to T_{Lw}, which results in the solvability condition that $A_{Lw,Ht_S} c_{Ht_S} A^T_{Lw,Ht_S}$ needs to be regular. Due to the assumption that c_{Ht_S} is positive definite, it is possible to apply a Cholesky decomposition $c_{Ht_S} = GG^T$ with a regular matrix G. Hence,

$$A_{Lw,Ht_S} c_{Ht_S} A^T_{Lw,Ht_S} = (A_{Lw,Ht_S} G)(A_{Lw,Ht_S} G)^T.$$

According to the assumption $n_{Sw} + n_{Tb} + n_{\overline{Tb}_S} > 0$, A_{Lw,Ht_S} is a reduced incidence matrix, cf. [9, p. 141], implying $\operatorname{rank}(A_{Lw,Ht_S}) = n_{Lw}$. Combining the results yields

$$\operatorname{rank}(A_{Lw,Ht_S} c_{Ht_S} A_{Lw,Ht_S}^T) = \operatorname{rank}(A_{Lw,Ht_S} G) = \operatorname{rank}(A_{Lw,Ht_S}) = n_{Lw}.$$

2. Since the DAE (5) has been transformed to an explicit formulation, the uniqueness and solvability is covered by the theory of ordinary differential equations, i.e. the Picard-Lindelöf theorem.
3. Since y_{Sw} and y_{Lw} are linear combinations of continuous differentiable functions, it holds that y_{Sw} and y_{Lw} are continuous differentiable as well.

□

Theorem 2 has the consequence, that the topological conditions in order to guarantee existence and uniqueness of a solution for the solid subsystem (5) does not only depend on the actual network structure $\mathcal{N}_S$, but also on the chosen partition via the exposed variables $(u_{\overline{Hs}_S}^T, u_{\overline{Tb}_S}^T)^T$ and $(y_{Sw}^T, y_{Lw}^T, y_{Ht_S}^T)^T$. Indeed, the unique solvability can either be controlled via the coupling variable $u_{\overline{Tb}_S}$, (i.e. $n_{\overline{Tb}_S} > 0$) or via the network configuration $n_{Sw} + n_{Tb} > 0$. In the following this specific restriction of the coupling variables has to be considered for a proper model partitioning.

3.2 A Fluid Network

We consider a fluid network

$$\mathcal{N}_F = \left\{ Pi, Pu, De, Vj, Lj, Re, Ht_F, \overline{Hs}_F, \overline{Tb}_F \right\} \tag{6}$$

that is composed of pipes Pi, pumps Pu, demands De, volume junctions Vj, lumped junctions Lj, reservoirs Re, heat transfers Ht_F, heat source inputs $\overline{Hs}_F$ and temperature boundary inputs $\overline{Tb}_F$. As in the solid network special input elements $\overline{Hs}_F$ and $\overline{Tb}_F$ are introduced with their corresponding variables $u_{\overline{Hs}_F}$ and $u_{\overline{Tb}_F}$. In addition the output variables of solid walls, lumped walls and heat transfer elements are given by y_{Sw}, y_{Lw} and y_{Ht_F}. The basic network assumptions of Assumption 1 carry over to the fluid network $\mathcal{N}_F$ as well. The connectivity in the network is described with the corresponding incidence matrices, denoted by $A_{Vj,\overline{Hs}_F}$, $A_{Lj,\overline{Hs}_F}$ and $A_{\overline{Tb}_F,Ht_F}$, which are formulated equivalently to the solid network as a natural extension of the incidence matrix (2).

For given continuous inputs $(u_{\overline{Hs}_F}^T, u_{\overline{Tb}_F}^T)^T$, find the pressures $(p_{Lj}^T, p_{Vj}^T)^T$ the mass flows $(q_{Pi}^T, q_{Pu}^T)^T$, the heat fluxes $(H_{Ht_F}^T, H_{Pu}^T, H_{Pi}^T)^T$, the temperatures

$(T_{Vj}^T, T_{Lj}^T)^T$ and the outputs $(y_{Vj}^T, y_{Lj}^T, y_{Ht_F}^T)^T$, such that

$$\begin{aligned}
\frac{dq_{Pi}}{dt} &= c_{1,Pi}\left(A_{Jc,Pi}^T p_{Jc} + A_{Re,Pi}^T p_{Re}\right) \\
&\quad + c_{2,Pi}\mathrm{diag}\left(|q_{Pi}|\right) q_{Pi} + c_{3,Pi} \\
f_{Pu}(q_{Pu}) &= A_{Jc,Pu}^T p_{Jc} + A_{Re,Pu}^T p_{Re} \\
0 &= A_{Jc,Pi} q_{Pi} + A_{Jc,Pu} q_{Pu} + A_{Jc,De} q_{De} \\
m_{Vj} c_{p,Vj} \frac{dT_{Vj}}{dt} &= A_{Vj,Pi} H_{Pi} + A_{Vj,Pu} H_{Pu} + A_{Vj,De} H_{De} \\
&\quad + A_{Vj,Ht_F} H_{Ht_F} + A_{Vj,\overline{Hs}_F} u_{\overline{Hs}_F} \\
0 &= A_{Lj,Pi} H_{Pi} + A_{Lj,Pu} H_{Pu} + A_{Lj,De} H_{De} \\
&\quad + A_{Lj,Ht_F} H_{Ht_F} + A_{Lj,\overline{Hs}_F} u_{\overline{Hs}_F} \\
H_{Pi} &= B_{Jc}(q_{Pi}) T_{Vj} + B_{Jc}(q_{Pi}) T_{Lj} + B_{Jc}(q_{Pi}) T_{Re} \\
H_{Pu} &= B_{Jc}(q_{Pu}) T_{Vj} + B_{Jc}(q_{Pu}) T_{Lj} + B_{Jc}(q_{Pu}) T_{Re} \\
H_{Ht_F} &= c_{Ht_F}\left(A_{Vj,Ht_F}^T T_{Vj} + A_{Lj,Ht_F}^T T_{Lj} + A_{\overline{Tb}_F,Ht_F}^T u_{\overline{Tb}_F}\right) \\
y_{Vj} &= |(A_{Vj,\overline{Hs}_F}^T + A_{\overline{Tb}_F,Ht_F} A_{Vj,Ht_F}^T)| T_{Vj} \\
y_{Lj} &= |(A_{Lj,\overline{Hs}_F}^T + A_{\overline{Tb}_F,Ht_F} A_{Lj,Ht_F}^T)| T_{Lj} \\
y_{Ht_F} &= A_{\overline{Tb}_F,Ht_F} H_{Ht_F}
\end{aligned} \tag{7}$$

for given boundary conditions $q_{De} = \bar{q}_{De}$, $H_{De} = \bar{H}_{De}$ $p_{Re} = \bar{p}_{Re}$ and $T_{Re} = \bar{T}_{Re}$. Following [5], the solvability of the network DAE (7) can be characterized via the graph structure.

Theorem 3 *Let $\mathcal{N}_F$ be a network given by (6) which fulfills Assumptions 1 and 2. Let $n_{Re} > 0$. Then, the following statements hold:*

1. *The DAE (7) is regular and has strangeness index $\mu = 1$ (d-index 2).*
2. *The DAE (7) is uniquely solvable for every feasible initial condition fulfilling (7) at $t = t_0$ and the solution is continuous differentiable.*
3. *The outputs y_{Vj} and y_{Lj} are continuous differentiable.*

Proof See [5]. □

Theorem 3 shows, that in the fluid network, the choice of the partition with respect to the exposed variables $(u_{\overline{Hs}_F}^T, u_{\overline{Tb}_F}^T)^T$ and $(y_{Vj}^T, y_{Lj}^T, y_{Ht_F}^T)^T$ does not enter the solvability or index condition. This has the consequence, that regarding unique solvability, the coupling conditions can be chosen arbitrary within the specified

input and output relations. Furthermore the condition $n_{Re} > 0$ is not only crucial for the coupled problem (cf. Theorem 1), but already for the fluid problem. In the following this additional degree of freedom in the coupling variables is utilized for a proper model partitioning.

3.3 The Coupled Network

We consider a coupled network $\mathcal{N}_C$

$$\mathcal{N}_C = \{\mathcal{N}_F, \mathcal{N}_S\}, \tag{8}$$

consisting of a single fluid network $\mathcal{N}_F$ and a single solid network $\mathcal{N}_S$. In general Assumption 1 does not imply, that the subnetworks $\mathcal{N}_F$ and $\mathcal{N}_S$ are connected. In this work, we assume that both are connected, i.e., the network $\mathcal{N}_C$ consist of one non-empty connected subnetwork $\mathcal{N}_F$ and one non-empty connected subnetwork $\mathcal{N}_S$. Each element $\mathcal{N}_F$ and $\mathcal{N}_S$ exposes inports $(u_{\overline{Hs}_S}, u_{\overline{Tb}_S}, u_{\overline{Hs}_F}, u_{\overline{Tb}_F})$ and outports $(y_{Sw}, y_{Lw}, y_{Ht_S}, y_{Vj}, y_{Lj}, y_{Ht_F})$ according to the definition in (5) and (7). The connection structure of $\mathcal{N}_C$ is assumed to satisfy the following assumptions.

Assumption 3 (Network Coupling Assumption) *Let $\mathcal{N}_C$ be a network as defined in (8).*

1. *Elements of type $\overline{Hs}_S$ are connected to elements of type Ht_F.*
2. *Elements of type $\overline{Hs}_F$ are connected to elements of type Ht_S.*
3. *Elements of type $\overline{Tb}_S$ are connected to elements of type Vj or Lj.*
4. *Elements of type $\overline{Tb}_F$ are connected to elements of type Sw or Lw.*

An example for $\mathcal{N}_C$ is displayed in Fig. 2. Using Assumption 3 and sorting the inports and outports with respect to their types, we obtain a matrix representation

$$\begin{bmatrix} u_{\overline{Hs}_S} \\ u_{\overline{Tb}_S} \\ u_{\overline{Hs}_F} \\ u_{\overline{Tb}_F} \end{bmatrix} = \begin{bmatrix} 0 & 0 & 0 & 0 & 0 & C_{\overline{Hs}_S, Ht_F} \\ 0 & 0 & 0 & C_{\overline{Tb}_S, Vj} & C_{\overline{Tb}_S, Lj} & 0 \\ 0 & 0 & C_{\overline{Hs}_F, Ht_S} & 0 & 0 & 0 \\ C_{\overline{Tb}_F, Sw} & C_{\overline{Tb}_F, Lw} & 0 & 0 & 0 & 0 \end{bmatrix} \begin{bmatrix} y_{Sw} \\ y_{Lw} \\ y_{Ht_S} \\ y_{Vj} \\ y_{Lj} \\ y_{Ht_F} \end{bmatrix}. \tag{9}$$

Therefore the coupling of the networks is linear.

Using (5) and (7) as well as the coupling condition (9), the coupled problem can be stated: Find the fluid states $(q_{Pi}^T, q_{Pu}^T, p_{Vj}^T, p_{Lj}^T, H_{Pi}^T, H_{Pu}^T, T_{Vj}^T, T_{Lj}^T, H_{Ht_F}^T)$, the solid states $(H_{Ht_S}^T, T_{Sw}^T, T_{Lw}^T)^T$, the inputs $(u_{\overline{Hs}_S}^T, u_{\overline{Tb}_S}^T, u_{\overline{Hs}_F}^T, u_{\overline{Tb}_F}^T)^T$, and the

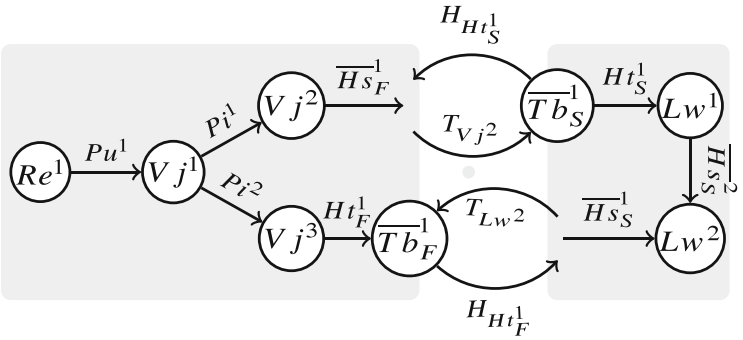

Fig. 2 Example of a graph of a coupled multi-physical network

outputs $(y_{Sw}^T, y_{Lw}^T, y_{Ht_S}^T, y_{Vj}^T, y_{Lj}^T, y_{Ht_F}^T)^T$,such that

$$
\begin{aligned}
\frac{dq_{Pi}}{dt} &= c_{1,Pi}\left(A_{Jc,Pi}^T p_{Jc} + A_{Re,Pi}^T p_{Re}\right) \\
&\quad + c_{2,Pi}\,\mathrm{diag}\left(|q_{Pi}|\right) q_{Pi} + c_{3,Pi} \\
f_{Pu}(q_{Pu}) &= A_{Jc,Pu}^T p_{Jc} + A_{Re,Pu}^T p_{Re} \\
0 &= A_{Jc,Pi} q_{Pi} + A_{Jc,Pu} q_{Pu} + A_{Jc,De} q_{De} \\
m_{Vj} c_{p,Vj} \frac{dT_{Vj}}{dt} &= A_{Vj,Pi} H_{Pi} + A_{Vj,Pu} H_{Pu} + A_{Vj,De} H_{De} \\
&\quad + A_{Vj,Ht_F} H_{Ht_F} + A_{Vj,\overline{Hs}_F} u_{\overline{Hs}_F} \\
0 &= A_{Lj,Pi} H_{Pi} + A_{Lj,Pu} H_{Pu} + A_{Lj,De} H_{De} \\
&\quad + A_{Lj,Ht_F} H_{Ht_F} + A_{Lj,\overline{Hs}_F} u_{\overline{Hs}_F} \\
H_{Pi} &= B_{Jc}(q_{Pi}) T_{Vj} + B_{Jc}(q_{Pi}) T_{Lj} + B_{Jc}(q_{Pi}) T_{Re} \\
H_{Pu} &= B_{Jc}(q_{Pu}) T_{Vj} + B_{Jc}(q_{Pu}) T_{Lj} + B_{Jc}(q_{Pu}) T_{Re} \\
H_{Ht_F} &= c_{Ht_F}\left(A_{Vj,Ht_F}^T T_{Vj} + A_{Lj,Ht_F}^T T_{Lj} + A_{\overline{Tb}_F,Ht_F}^T u_{\overline{Tb}_F}\right) \\
y_{Vj} &= |(A_{Vj,\overline{Hs}_F}^T + A_{\overline{Tb}_F,Ht_F} A_{Vj,Ht_F}^T)| T_{Vj} \\
y_{Lj} &= |(A_{Lj,\overline{Hs}_F}^T + A_{\overline{Tb}_F,Ht_F} A_{Lj,Ht_F}^T)| T_{Lj} \\
y_{Ht_F} &= \big(A_{\overline{Tb}_F,Ht_F} + A_{Lj,\overline{Hs}_F}^T A_{Lj,Ht_F}^T \\
&\quad + A_{Vj,\overline{Hs}_F}^T A_{Vj,Ht_F}^T\big) H_{Ht_F}
\end{aligned}
\tag{10}
$$

$$
\begin{aligned}
m_{Sw}c_{p,Sw}\frac{dT_{Sw}}{dt} &= A_{Sw,Ht_S}H_{Ht_S} + A_{Sw,Hs}H_{Hs} + A_{Sw,\overline{Hs}_S}u_{\overline{Hs}_S}\\
0 &= A_{Lw,Ht_S}H_{Ht_S} + A_{Lw,Hs}H_{Hs} + A_{Lw,\overline{Hs}_S}u_{\overline{Hs}_S}\\
H_{Ht_S} &= c_{Ht_S}\big(A^T_{Sw,Ht_S}T_{Sw} + A^T_{Lw,Ht_S}T_{Lw}\\
&\qquad + A^T_{Tb,Ht_S}T_{Tb} + A^T_{\overline{Tb}_S,Ht_S}u_{\overline{Tb}_S}\big)\\
y_{Sw} &= |(A^T_{Sw,\overline{Hs}_S} + A_{\overline{Tb}_S,Ht_S}A^T_{Sw,Ht_S})|T_{Sw}\\
y_{Lw} &= |(A^T_{Lw,\overline{Hs}_S} + A_{\overline{Tb}_S,Ht_S}A^T_{Lw,Ht_S})|T_{Lw}\\
y_{Ht_S} &= A_{\overline{Tb}_S,Ht_S}H_{Ht_S}\\
u_{\overline{Hs}_F} &= C_{Hs_F,Ht_S}y_{Ht_S}\\
u_{\overline{Tb}_F} &= C_{Tb_F,Sw}y_{Sw} + C_{Tb_F,Lw}y_{Lw}\\
u_{\overline{Hs}_S} &= C_{Hs_S,Ht_F}y_{Ht_F}\\
u_{\overline{Tb}_S} &= C_{Tb_S,Vj}y_{Vj} + C_{Tb_S,Lj}y_{Lj}
\end{aligned}
$$

for given boundary and initial conditions.

The main result summarizes, that not only the fully coupled problem (10) is uniquely solvable, but also the decomposed problems are unique solvable with respect to the chosen decomposition and the DAE index results are conserved for the decoupled problems.

Corollary 1 *Let $\mathcal{N}_C$ be a network as given in (8) with $\mathcal{N}_F$ fulfilling Assumptions 1 and 2 as well as $\mathcal{N}_S$ satisfying Assumption 1 with positive definite coefficient matrices m_{Sw}, $c_{p,Sw}$ and c_{Ht_S}. Furthermore let $n_{Re} > 0$, $n_{\overline{Tb}_S} > 0$ and $\mathcal{N}_C$ meet the network coupling assumption, i.e. Assumption 3. Then,*

1. *The coupled DAE (10) is regular and has strangeness index $\mu = 1$ (d-index 2).*
2. *The coupled DAE (10) is uniquely solvable for feasible initial condition fulfilling (10) at $t = t_0$ and the solution is continuous differentiable.*
3. *The coupled DAE (10) and the original DAE (3) have the same solution.*

4 Application in the Software Design for Multi-Physical System Calculations

System simulation software is typically designed in a way, that the topological representation of a physical model is separated from the transient solution procedure of the model. Considering feasible network DAEs, existence and uniqueness results are already of importance in the topological representation of the model, in order to restrict the set of feasible network models to valid ones. In order to achieve this and limit the full degree of freedom it is convenient to introduce *modeling paradigms*. Modeling paradigms, determine how a real physical process can be built up in

a network-technological way and therefore represent the topological criteria, that have been developed in Sect. 3. Consequently modeling paradigms are an additional extension of the basic network assumption in Assumption 1 and they support the topological representation in a way, that the setup of invalid model topologies is prevented in advance.

On the other hand, coupling paradigms indicate how an existing overall network can systematically be separated into its physical parts without changing the actual model and gaining additional results for the individual physical parts. Therefore coupling paradigms can be used for an automated decomposition of multi-physical networks. Furthermore, they guarantee a stable and robust simulation of the physical model. From a practical point of view it is desirable, that coupling paradigms don't modify modeling paradigms.

In the following we state certain modeling paradigms and coupling paradigms.

4.1 Modeling Paradigms

In the following two different model paradigms are formulated. The specific choice of the modeling paradigm has a certain effect on the modeling restrictions in the topological representation of the physical model on the one hand and the complexity of the solution procedure on the other hand.

Modeling paradigm 1 *If a heat transfer is adjacent to a wall and a junction, then the wall is a solid wall and the junction is a volume or a lumped junction.*

Following Modeling paradigm 1, the mass of the solid wall is always taken into account in the solid network. This consideration has a direct consequence on the solvability of the subsystems. Thus in coupled solid systems there is always at least one solid wall, i.e. $n_{Sw} > 0$. The assumptions of Theorem 2 are fulfilled and therefore the solid subsystem is uniquely solvable. Since the fluid part only depends on the requirements of the overall network, no special solvability criteria need to be checked during partitioning. This approach guarantees always a valid decomposition for the solution procedure, without taking any coupling considerations into account.

Modeling paradigm 2 *If a heat transfer is adjacent to a wall and a junction, then the wall is a lumped wall and the junction is a lumped or a volume junction.*

Using Modeling paradigm 2 the existence of a mass is not guaranteed in the solid network. Hence additional constraints imposed on the network structure may arise. In this case, an according coupling is required in order to guarantee a stable decomposition.

4.2 Coupling Paradigms

In this part we state three different coupling paradigms and describe the consequence of their application to the resulting coupled problem.

Coupling paradigm 1 *If a heat transfer is adjacent to a wall and a junction, then the heat transfer is considered in the solid network.*

A partitioning according to Coupling paradigm 1 means that the solid system is fed by the fluid network by means of the temperature of the junction, i.e. $u_{\overline{Tb_S}} = (y_{Vj}^T, y_{Lj}^T)^T$. On the other hand, the solid domain provides the heat flow of the heat transfer as input, i.e. $u_{\overline{Hs_F}} = y_{Ht_F}$. This approach is beneficial regarding the solvability of the decomposed subsystems. As $n_{\overline{Tb_S}} > 0$ for each coupled solid system, the assumptions of Corollary 1 are fulfilled. No further topological checks are necessary for the decomposed physical domains. The splitting of the global network given in Fig. 1 with respect to this partitioning strategy is shown in Fig. 3.

Coupling paradigm 2 *If a heat transfer is adjacent to a wall and a junction, then the heat transfer is considered in the fluid network.*

In contrast, when dividing according to Coupling paradigm 2, the heat exchange between the two domains is taken into account in the fluid network. Unfortunately following this coupling paradigm the solid model might not be solvable on its own. An example is shown in Fig. 4 where no reference temperature is given in the solid part.

Coupling paradigm 3 *If a heat transfer is adjacent to a wall and a junction, then the heat transfer is considered in both networks.*

Following the coupling strategy of Coupling paradigm 3 is special contrary to the first two possibilities. The heat transfer is solved in both domains, i.e. $Ht_S = Ht_F$, and the temperatures of the attached nodes are passed as outputs to the other domain, cf. Fig. 5. Although additional computational effort is necessary it might be

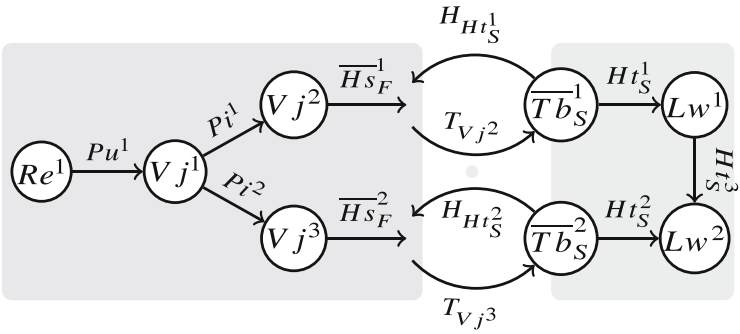

Fig. 3 Decoupled version of network $\mathcal{N}$ from Fig. 1 using coupling paradigm 1

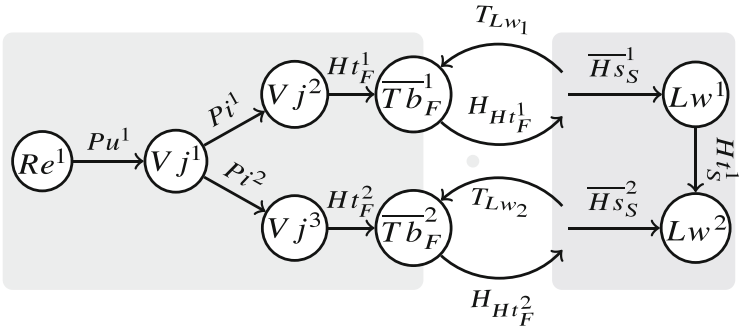

Fig. 4 Decoupled version of network $\mathcal{N}$ from Fig. 1 using coupling paradigm 2

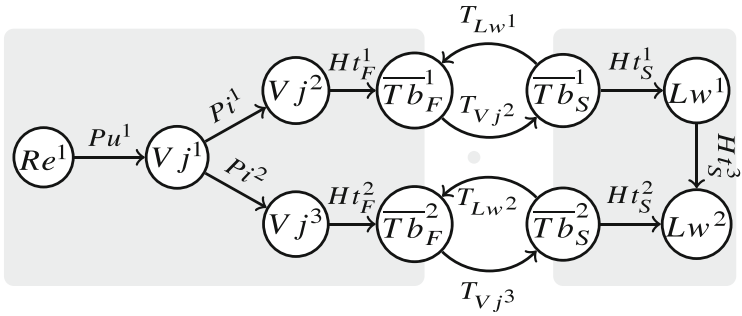

Fig. 5 Decoupled version of network $\mathcal{N}$ from Fig. 1 using coupling paradigm 3

beneficial. If we consider the networks as state transfer patterns, we can interpret the nodes as energy storage whereas the edges as energy flows. In the first two strategies, an energy transfer and an energy state between the circuits has to be handled. In order to allow energy-conserving simulations, the flows must be considered differently to storage. Thus, this approach could be preferred throughout.

Summarized, the coupling paradigms have different effects on the solvability of the solid system. In addition to the basic solvability, attention must also be paid to their effects on the numerical stability and energy conservation in the overall system.

5 Application to Co-simulation in Multi-Physical System Calculations

Under specific conditions we obtain solvable partitions of equation systems which can clearly be assigned to a specific domain, fluid and solid. Due to their different physical significance and stiffness, these systems therefore require various integration schemes, in particular various step sizes. Since all domains have their predefined input and output variables, all physical subsystems can be parametrized

with their own solver settings and form co-simulation components. A crucial point is now handling the interaction of all physical domains and their in- and outputs. First, there exists a broad variety of strategies for exchanging the data. In literature there is a fundamental distinction between event driven or asynchronous and synchronous communication, cf. [3, 12]. Furthermore, it has to be decided whether the overall system should be solved iteratively, i.e. implicit co-simulation, or whether each component should only be evaluated once per time step, i.e. explicit co-simulation. For both constellations, Gauss-Seidel-type or Jacobi-type approaches are possible. Regardless of which strategy is applied, an inter- or extrapolation of the coupling variables is necessary.

State-of-the-art modeling and simulation packages such as AVL CRUISE™M,[1] provide implemented software solutions for co-simulation following different goals. For instance AVL CRUISE™M is adapted to the needs of automotive system simulation based on physical networks.

As an example we consider a BEV (battery electric vehicle) with cooling system as given in Fig. 6. The central part of this model is an electrical network (in orange) responsible for the propulsion and is therefore coupled to a mechanical network (in green). On the other hand the electrical part is coupled to two fluid network, which act as cooling circuits. An oil circuit is used for cooling the electric machine and a water circuit is used for cooling the battery pack and the inverter. In total the model forms a multi-physical network with about 500 network elements. Due to the physical nature of the network elements, the full multi-physical network consists of multiple simply-connected networks of various types. There is one electric network, three mechanic networks, two fluid networks, fourteen gas networks and eight solid networks, which are coupled via thermal or mechanical coupling conditions. Additionally several control components communicate within the multi-physical network via databusses.

The results provided in Sect. 3 can be applied, for example, in the battery pack, cf. Fig. 7. Solid networks (in red) are coupled to a fluid network (in blue) via heat transfer connections. The fluid-solid networks comply with the assumptions of Assumption 1 and Modeling paradigm 1. The solvability of the solid networks is guaranteed and any coupling paradigm out of Coupling paradigm 1–3 can be chosen. In the case, that the fluid-solid network complies with Modeling paradigm 2, the solvability of the solid network can be achieved by choosing an appropriate coupling procedure, i.e. Coupling paradigm 1. Again the solvability of the solid network is guaranteed, since now $n_{\overline{Tb}_S} > 0$. The main result, that any valid network $\mathcal{N}$ can be partitioned into fluid and solid networks, where the solvability of the subnetworks is covered by the developed theory, is summarized in Corollary 2.

Corollary 2 (Feasible Decomposition) *Let $\mathcal{N}$ be a network given by (1) fulfilling Assumption 1. Let $n_{Re} > 0$, then there exists a decomposition $\{\mathcal{N}_F, \mathcal{N}_s\}$ and a coupling strategy as defined in (9), such that Corollary 1 is applicable.*

[1] https://www.avl.com/de/cruise-m.

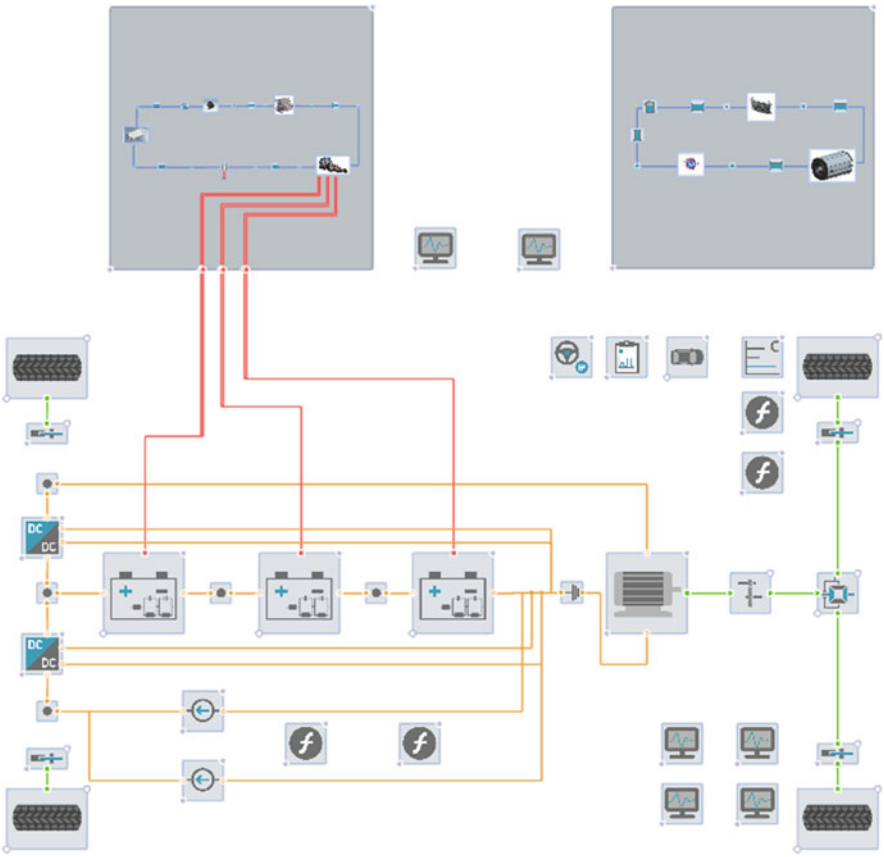

Fig. 6 Schematic representation of a BEV with cooling system

Corollary 2 implies, that in any case the solvability is guaranteed for both, the coupled multi-physical network DAE and the partitioned solid and fluid network DAEs. No further restrictions on the topology or modifications of the topology for the global model are required. Since Corollary 1 provides the corresponding solvability results, either a single-rate solver can be applied to the coupled DAE or individual (implicit or explicit) time integration schemes can be applied to the solid and fluid DAEs in order to set up a multi-rate co-simulation.

This motivates the following procedure in order to establish feasible single-rate and multi-rate models:

> Multi-Physical Topological Analysis Receipt

1. Analyze the fluid-solid network and determine the actual *modeling paradigms*.

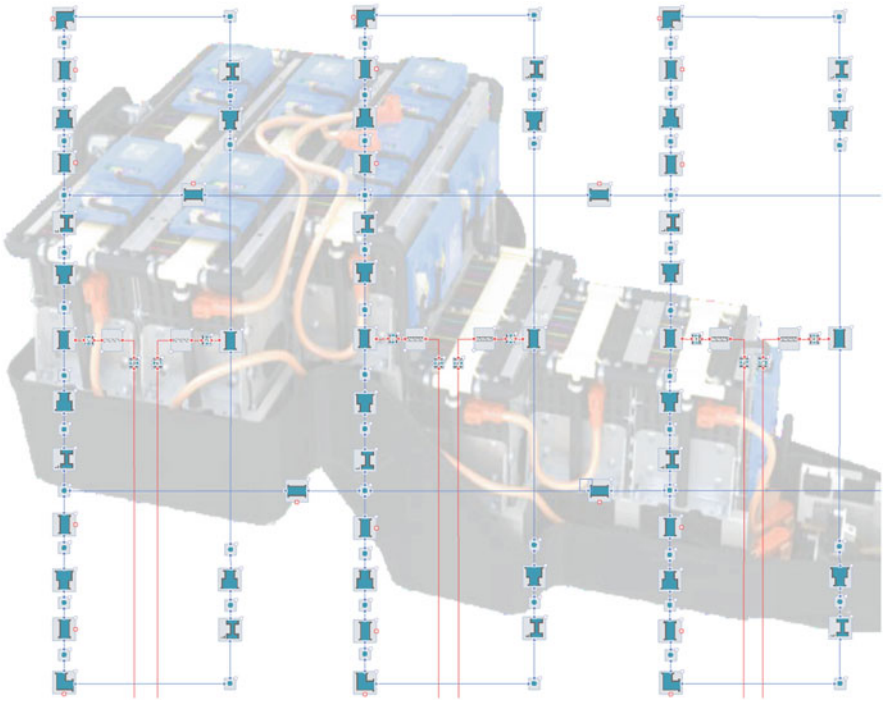

Fig. 7 Battery pack model of the BEV with cooling system from Fig. 6

2. Based on the detected *modeling paradigms*, choose suitable *coupling paradigms*.

In order to analyze the solvability of the entire model, the theory must be extended to couplings containing additionally electrical, mechanical and gas networks.

6 Conclusion and Outlook

Extending existing topology based methods to multi-physical networks seems to be a promising technique for the analysis of multi-physical systems stemming from automated generated DAEs from system simulation software. The main steps for the analysis of coupled problems have been described in terms of a fluid-solid coupled network. The selection of an appropriate coupling paradigm provides both the solvability of the coupled system and that of the subparts. Hence, both, single-rate and multi-rate approaches are well defined, if the entire network is solvable. Indeed, the thermal coupling of different physical networks is a crucial task in

system simulation in order to calculate and optimize the energy distribution within an entire vehicle. Consequently the presented analysis for the fluid-solid coupling has to be extended to electric-solid, gas-solid and mechanic-solid couplings. While the gas-solid coupling is similar to the presented fluid-solid coupling in terms of coupling conditions, the electric-solid and mechanic-solid couplings are more challenging. In those constellations, the coupling is done via material properties (e.g. resistance, capacitance), where additional DAE index problems may arise. Tackling a complete thermal coupled multi-physical system model via topological methods requires further research.

Acknowledgement Part of this work has been supported within the framework "FTI Struktur" of the Upper Austrian government.

References

1. Arnold, M.: Modular time integration of block-structured coupled systems without algebraic loops. In: Progress in Differential-Algebraic Equations. Springer, Berlin (2014)
2. Bartel, A., Günther, M.: PDAEs in refined electrical network modeling. SIAM Rev. **60**(1), 56–91 (2018)
3. Bartel, A., Günther, M.: Multirate schemes, an answer of numerical analysis to a demand from applications. Preprint BUW-IMACM 19/12, Institute of Mathematical Modelling, Analysis and Computational Mathematics, Bergische Universität Wuppertal, Germany (2019)
4. Baum, A.-K., Kolmbauer, M.: Solvability and topological index criteria for thermal management in liquid flow networks. Technical Report RICAM-Report 2015–21, Johann Radon Institute for Computational and Applied Mathematics, Austrian Academy of Sciences, 2015
5. Baum, A.-K., Kolmbauer, M., Offner, G.: Topological solvability and DAE-index conditions for mass flow controlled pumps in liquid flow networks. Electr. Trans. Num. Anal. **46**, 395–423 (2017)
6. Baum, A.-K., Kolmbauer, M., Offner, G.: Topological index analysis applied to coupled flow networks. In: Applications of Differential-Algebraic Equations: Examples and Benchmarks. Differential-Algebraic Equations Forum. Springer, Cham (2018)
7. Biggs, N.: Algebraic Graph Theory. Cambridge Mathematical Library. Cambridge University Press, Cambridge (1974)
8. Brenan, K.E., Campbell, S.L., Petzold, L.R.: Numerical Solution of Initial-Value Problems in Differential-Algebraic Equations, 2nd edn. SIAM Publications, Philadelphia (1996)
9. Deo, N.: Graph Theory with Applications to Engineering and Computer Science. Prentice-Hall Series in Automatic Computation. Prentice-Hall of India, Delhi (1974)
10. Diestel, R.: Graduate Texts in Mathematics: Graph Theory. Springer, Heidelberg (2000)
11. FMU. Functional Mock-up Interface. https://fmi-standard.org/
12. Gomes, C., Thule, C., Broman, D., Larsen, P., Vangheluwe, H.: Co-simulation: a survey. ACM Comput. Surv. **51**(3), 49:1–49:33 (2018)
13. Grundel, S., Jansen, L., Hornung, N., Clees, T., Tischendorf, C., Benner, P.: Model order reduction of differential algebraic equations arising from the simulation of gas transport networks. In: Progress in Differential-Algebraic Equations, pp. 183–205. Springer, Berlin (2014)
14. Kübler, R., Schiehlen, W.: Modular simulation in multibody system dynamics. Multibody Syst. Dyn. **4**(2), 107–127 (2000)
15. Mehrmann, V.: Index Concepts for Differential-Algebraic Equations, pp. 676–681. Springer, Berlin (2015)

16. Thulasiraman, K., Swamy, M.N.S.: Graphs: Theory and Algorithms. Wiley, New York (2011)
17. Tischendorf, C.: Topological index calculation of differential-algebraic equations in circuit simulation. Surv. Math. Ind. **8**, 187–199 (1999)

Price Modelling on Heavy-Duty Assistance Contracts

S. Barroso, M. B. Cruz, S. F. Ramos, and M. Pina

Abstract Assistance contracts of heavy-duty vehicles can be described as integrated maintenance and repair packages that allows companies to have a complete cost control through a fixed monthly fee. Almost all the regular maintenance or repairing costs are considered in these contracts, and their expected value is associated with a margin determined by the product manager, resulting in the final price of the contract. This paper presents a methodology that accounts for several factors arising from an analysis of existing data to estimate the prices of assistance contracts negotiated at NORS group. The developed methodology is based on probabilistic modelling of accumulated repair and maintenance costs. The probability density functions are chosen from a given set of known distributions or using kernel density estimators based on the minimization of the global error criteria. The total cost of the contract can be a function of the execution period (time or kilometres) and the quantiles of interest of the adjusted distributions. To define the final value of the contract the margin defined by the business manager can be added to the estimated cost. The proposed methodology has been implemented in the group allowing the business manager to simulate contract prices considering different risk levels.

S. Barroso (✉) · M. Pina
Nors Group, Porto, Portugal
e-mail: sbarroso@nors.com

M. B. Cruz
LEMA—Engineering Mathematics Laboratory, School of Engineering, Polytechnic of Porto, University of Porto, Porto, Portugal
e-mail: mbc@isep.ipp.pt

S. F. Ramos
LEMA—Engineering Mathematics Laboratory, School of Engineering, Polytechnic of Porto, University of Lisbon, Porto, Portugal

CEAUL—Faculty of Sciences, University of Lisbon, Porto, Portugal
e-mail: sfr@isep.ipp.pt

M. Cruz et al. (eds.), *Progress in Industrial Mathematics: Success Stories*,
SEMA SIMAI Springer Series 5, https://doi.org/10.1007/978-3-030-61844-5_11

1 Introduction

Nowadays is common to subscribe to some type of guarantees and assistance contracts to protect our goods. The automotive business is not different. When one buys a vehicle, it is obligated by law to subscribe an insurance contract, but some brands offer the possibility to subscribe also an assistance contract. An assistance contract can be defined as integrated package of maintenance and repair services where problems like defects or failures are rectified by an external service provider for an agreed period of time. The service provider will charge a price for such service, usually collected by means of a fixed monthly fee.

In recent years, assistance contracts have received significant attention due to the increased profits for service providers and also because of the reduction of risk for their subscribers. However, in a competitive environment, the customers compare several offers from multiple service providers looking for the better deal. As so, service providers that offer competitive contracts may expect to have a better market share. With this thoughts in mind, the service providers constantly seek to have an aggressive strategy, ensuring certain objectives like the maximization of customers or the global financial return for their business.

This paper aims to present a mathematical model for estimating prices for assistance contracts of the Group NORS (Auto-Sueco and Galius companies) that take into account the risk associated to the estimation of the costs. NORS is a company in the automotive industry world that focus in the import, sale and assistance services of heavy-duty vehicles of the Volvo Trucks and Renault Trucks brands. In fact, NORS is considered a specialist in heavy-duty vehicle assistance. Auto-Sueco and Galius are the main importers and service providers for Volvo Trucks and Renault Trucks brands, respectively. These companies sell assistance contracts where each vehicle maintenance is included and fully planned to take into account the activity and function of the new acquired truck. When the business manager designs a new contract, he plans all the maintenance schedule taking into account the most appropriate components to each truck (e.g. type of oil, specific filters). In general, these contracts include all the repairs, except for accidents or other events that may be covered by regular insurances. Consequently, the covered repairs may occur at any time and their values have a big variability that accounts for the risky part of the contract. Due to these specifications, the proposed model takes into account for each period of the contract, both the repair costs and the maintenance costs as independent random variables and fits adequate probability distributions to these random variables according with the historical data available in the company. Once the probability distributions have been fitted, the empirical probability distribution of total contract cost is obtained by throughout the simulations of random samples from the probability distributions fitted. As so, total contract cost is modelled as a function of period (time or kilometres) and quantiles of interest of the probability distributions. In order to define the final value of the contract the product manager can add a profit margin to the estimated value of the costs.

Recent literature was reviewed to understand current and future practices in cost estimation models for maintenance and service contracts (see, for example, [1, 11] and [4]). Those authors report different perspectives for cost estimation both from a qualitative and quantitative (stochastic or deterministic approaches) point of view. Models for component and system level degradation and assessment along with life cycle "big data" analytics were referred as the two most important knowledge and skill. The solution presented in this paper for cost estimation in assistance contracts is based on the business knowledge and literature. According to the business knowledge, the costs were split into two groups mutually exclusive—the maintenance costs, which are related with the regular maintenance programmed by the constructor and the ones that are not included on that set, the repair costs—which were modelled, in each group, regarding the regular maintenance intervals. By default, both groups were modelled by parametric methods, but in the case of data with nonstandard features Kernel methods were applied, as the literature generally suggests.

Section 2 is devoted to describe and analyse some of the historical data available in the group. Section 3 describes the methodology followed to estimate the overall cost of the contracts. The definition of contract price is presented in Sect. 4, while in Sect. 5 the first results of applying this model to the historical data available in two companies of NORS group are presented. Finally, in Sect. 6 we refer to the main conclusions of this approach as well as some possible further lines of research related to this subject.

2 Historical Data

The NORS Group is a Portuguese group whose vision is to be a world leader in transport solutions, construction equipment and agriculture equipment. In its genesis are 86 years of history and activity in Portugal, which started with the representation of the Volvo brand in 1933. In 2017, the NORS Group was present in 17 countries across 4 continents with more than 3,700 employees and sales exceeding 1.6 billion Euros. In order to proceed with this work, we were granted access to the relevant financial data as well as to the maintenance and repairs data, related with 1478 and 1520 assistance contracts from Company A and Company B signed in the last 4/5 years. For confidentiality reasons the monetary unities provided on this work were rescaled and only the data prior to 2018 was considered. The provided data set for each contract includes its temporal duration, the identification of the truck, the truck model, as well as all the interventions applied to the vehicle chargeable to the contract. For each intervention, a repair sheet was provided that included the repairing date, the mileage of the truck, the services and parts applied and their costs. In this paper, that introduces an initial approach to modelling activity within the group, we will disregard the technical information about each which parts and services were applied in each repair, concentrating only in their financial costs.

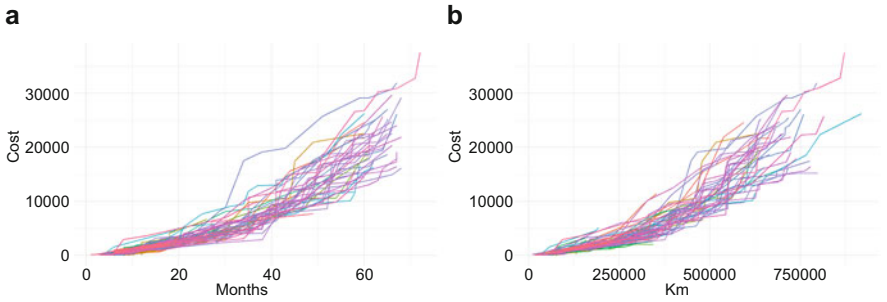

Fig. 1 Cumulative total costs versus months (**a**) and Cumulative total costs versus km (**b**)

In order to have a first view of the data provided, a graphical representation of a subset of the data provided is represented in Fig. 1. On the left, the cumulative repair costs for each contract available on the database is plotted against the contract temporal length. On the right subplot, the same costs are plotted against each vehicle mileage at the time of each repairing. Each line represents a different contract (vehicle), and all the contracts represented are related with the same truck model. It can be seen that the costs variability increases along the x-axis, being wider in the temporal scale (**a**) than within the spatial scale (**b**).

For each truck model, the regular maintenance intervals and their operations are preset by the vehicle constructor and its execution is mandatory according to the contract terms (e.g., oil changing, filters or timing belts replacements, regular inspections). Complementarily, there are other replacements and services that may be made under the contract agreement, but those are not considered on the regular maintenance scheme defined by the constructor (e.g., parts failures, consumables). As so, in this work we classified each cost related with the maintenance contract in a two-folded way: the *maintenance costs*, which are related with the regular maintenance programmed by the constructor and the ones that are not included on that set that we label as *repair costs*. Additionally, we consider also that the estimate of annual mileage travelled by each vehicle/contract, and the model regular maintenance intervals are known inputs and they will be considered in the definition of the contract's price.

Figure 2 shows the cumulative *maintenance costs* (left) and cumulative *repair costs* (right) against the vehicle mileage. A significant positive linear correlation between the maintenance cumulative costs and the mileage of the truck seems to arise from the first subplot ($r^2 = 0.92$). Concerning the *repair costs*, it can be seen that the values are small in the first kilometres travelled by the truck and that they increase very quickly with the mileage of the contract. On the other hand, the order of magnitude for maintenance and repair costs are significantly different.

As stated before, maintenance costs are related with the spare parts and services associated with each periodic maintenance recommended by the car constructor to a given truck model. As will be properly defined in (1), for each truck model, and regarding the maintenance costs, the developed model assigns one random variable

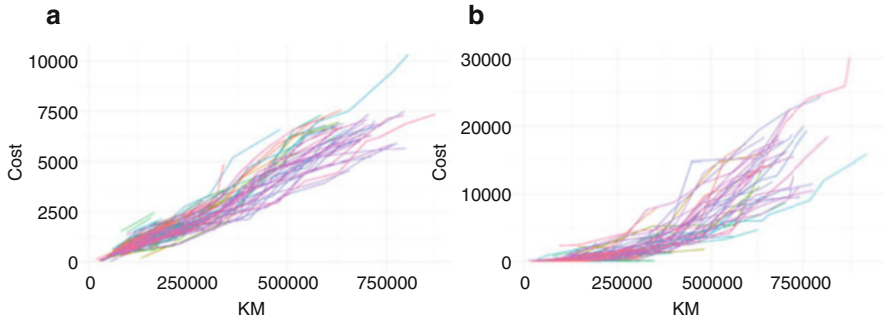

Fig. 2 Cumulative maintenance costs versus vehicle mileage (**a**) and cumulative repair costs versus vehicle mileage (**b**)

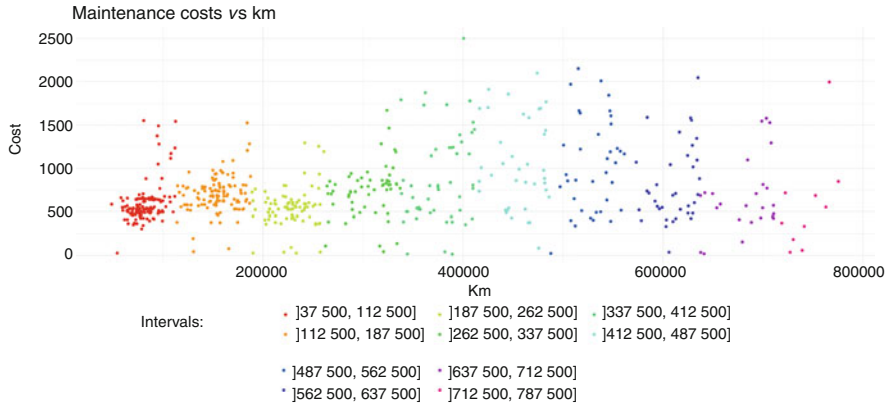

Fig. 3 Maintenance costs vs mileage for a model of truck with maintenance periodicity of 75,000 km

to each mileage interval, that is centred in multiples of the maintenance periodicity, and with an amplitude of half of the periodicity. We consider the same mileage partition for the repair costs, adding an extra initial interval, that covers the [0, "half maintenance periodicity"], that is not needed for modelling the maintenance costs, as the trucks don't have any maintenance costs in that initial period. Figures 3 and 4 represent the maintenance and repair costs as function of the mileage, for a given truck model. The periodic maintenance for this type of truck occur at each 75,000 km, and each interval is marked in the figures.

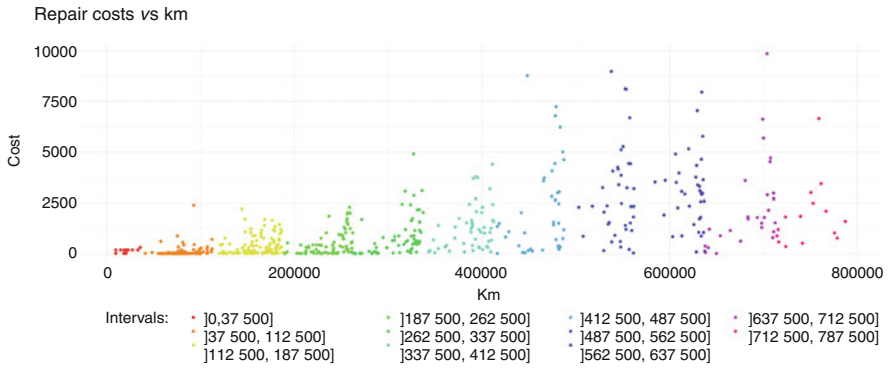

Fig. 4 Repair costs vs mileage for a model of truck with maintenance periodicity of 75,000 km

3 Estimating the Costs of Contracts

This section describes the development of a conceptual cost model considering a probabilistic approach. The contract includes provision for maintenance activities and repair actions, therefore the total cost of the contract is given as the sum of the costs of each intervention in the different mileage intervals.

3.1 Total Cost

The duration of an assistance contract may depend on the time or on the number kilometres travelled by the vehicle (or both). Some previous analysis on the historical data showed that for the NORS clients, the mileage is time dependent and the costs showed a high correlation with the mileage. As so, in this work the costs will be modelled as function of the number of kilometres. As previously found in Sect. 2, the costs have large variability in each interval and either the maintenance costs as well as the repair costs take very different values in the same interval. In the other hand, the previous analysis shows that the Pearson correlation coefficient for the costs of two consecutive intervals is low (less than 0.5), indicating the absence of "strong" positive correlation between the costs of two consecutive intervals. All of this confirms our idea that is possible to obtain the total cost of the contract for the truck of model k by the sum of a set of independent random variables that represent the costs of each intervention (maintenance and repair) in different intervals of kilometres:

$$C_n = \sum_{i=1}^{n} M_i + \sum_{i=0}^{n} R_i \,, \tag{1}$$

where M_i is a random variable that represents the maintenance costs in the interval I_i, $i = 1, \ldots, n$; R_j is a random variable that represents the repair costs in the interval I_j, $j = 0, \ldots, n$ with $I_i = I_j =](i - 0.5) \times A_k,\ (i + 0.5) \times A_k]$, $i, j = 1, \ldots, n$, the interval of kilometres, and, in particular, for repairs is considered $I_0 =]0,\ 0.5 \times A_k]$. A_k is the periodicity of the maintenance of truck of the model k.

As was considered that the total cost of the contract for the truck of model k is a linear function of the independent random variables M_i and R_j, this cost is also a random variable whose (unknown) distribution depends on probability distributions of these random variables. Taking into account the estimated density distribution of C_n, it is possible to obtain a set of statistical quantities of interest. If the distributions of M_i and R_j are known, Monte Carlo methods (see, for example, [13]) allow us to simulate the total cost distribution. The Monte Carlo procedure uses algorithmically generated pseudo-random numbers which are then transformed to follow a prescribed probability distribution. Figure 5 schematically represents the input variables simulated form a probability distribution, the functional relationship that then provides the output (total cost) and the probability distribution of the output.

As stated, Monte Carlo simulations of the total costs distribution require the knowledge of the distributions of the random variables M_i and R_j. The initial descriptive study made with the maintenance and repair costs historical data using this intervalar formulation, indicates that the distributions, truncated Normal, Gamma, Log-normal and Weibull are good options for modelling most of those variables. All of these distributions have $\mathbb{R}^+$ as support. In the cases where the cost in each interval does not have a simple analytical representation, it was considered the kernel density estimation (KDE) methods.

When possible, the parameters of parametric distributions were estimated using the maximum likelihood, otherwise the method of moments was used [7]. The

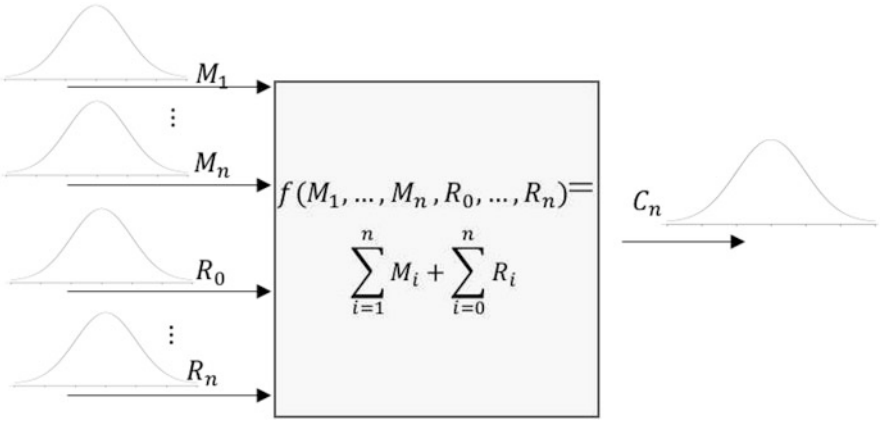

Fig. 5 Monte Carlo simulation

Anderson-Darling goodness of fit test (AD-Test) was used to select the theoretical distribution with the best adherence to the data in each interval.

KDE approach was used in the instances where the cost in each interval did not had a simple analytical representation. Essentially, this method consists in the sum of bumps placed in the observation with some shape and a fixed width

$$\hat{f}(x) = \frac{1}{nh} \sum_{n}^{i=1} K\left(\frac{x - X_i}{h}\right), \tag{2}$$

where $\mathbf{X} = (X_1, \ldots, X_n)$ is an i.i.d random sample from an unknown distribution with density function $f(x)$, the kernel function, $K(.)$, is a smooth function and h is the smoothing bandwidth. In other words, the function $K(.)$ is the shape and h is the width of the bumps. As kernel function we considered the most common option, the Gaussian kernel defined by:

$$K(x) = \frac{e^{\frac{-\|x\|^2}{2}}}{\int e^{\frac{-\|x\|^2}{2}} dx}. \tag{3}$$

For the estimation of the bandwidth we consider the estimator

$$\hat{H} = \frac{0.9 \times \min(S, IQ/1.34)}{n^5}, \tag{4}$$

where S be the standard-deviation of $\mathbf{X}$ and IQ the inter-quantile range of $\mathbf{X}$.

Before starting the description of simulation procedure, is important to notice that the M_i, $i = 1, \cdots, n$, were seen as absolutely continuous random variables, while the R_j, $j = 0, \cdots, n$, were seen as mixture random variables. This classification is due to the existence of maintenance costs at all intervals I_i, $i = 1, \cdots, n$, as well as to the fact that not every truck needs a repair assistance in all the intervals.

Concerning the repair costs, let R_j^c be a continuous random variable that represents the positive repair costs in the interval j, $j = 0, \cdots, n$, with the probability density function given by

$$f(r_j^c) = \begin{cases} f_D(r_j^c), \ r_j^c > 0 \\ 0, \ \text{otherwise} \end{cases}, \tag{5}$$

were $f_D(.)$ is the probability density function of one theoretical distributions referred above or is the result of the application of the KDE method for positive repairing cost's. Finally, the repairing cost in the interval j, R_j, $j = 0, \cdots, n$, is related to R_j^c through

$$R_j = g(R_j^c) = \begin{cases} R_j^c, \ R_j^c > 0 \\ P(R_j = 0), \ R_j^c = 0 \end{cases} \tag{6}$$

At this stage, every random variable (cost) in a certain interval has already a probability distribution function associated to it (parametric or non-parametric). The distribution for the total costs will be sum of the distributions associated with each independent random variable. For simulation purposes, we assume that every random variable $M_i \sim F_{M_i}(\theta_{M_i})$ and $R_i \sim F_{M_j}(\theta_{R_j})$, $i = 1, \ldots, n$, $j = 0, \ldots, n$, where θ_{M_i} and θ_{R_j} represent the distribution parameter vectors, define the vector $(M_1^{1,*}, \cdots, M_n^{1,*}, R_0^{1,*}, \cdots, R_n^{1,*})$ and allow to obtain the total cost for the first realization, which is defined by $C_n^{1,*} = M_1^{1,*} + \cdots + M_n^{1,*} + R_0^{1,*} + \cdots + R_n^{1,*}$. This procedure is repeated N times, where N is a large number, in order to create the resample $C_n^{1,*}, C_n^{2,*}, \cdots, C_n^{N,*}$. The obtained distribution is the Monte Carlo evaluation of the distribution of total cost of the contract.

The sample of the distribution of total cost of the contract allows to obtain several quantities of interest such as probabilities, quantiles, etc. In this work, we consider the quantile $\alpha \times 100\%$, $q_{F_{C_n^*}}(\alpha)$, to estimate the contact cost, where $1-\alpha$ represents some measure of risk.

With this approach, the contract costs are only dependent of the limit of kilometres. But, in fact, sometimes the duration of the contract depends on time. In order to include this possibility, we defined the function $f_{km}(t)$ that relates the contract time and the truck mileage. Accordingly to the data provided by the company (see Fig. 6), this relation seems to be reasonable fitted by a linear function, so we considered the function

$$f_{km}(t) = a \times t + b \tag{7}$$

to define the expected travelled distance ran by a truck as function of the months in the contract, where a and b are the coefficients of the linear regression.

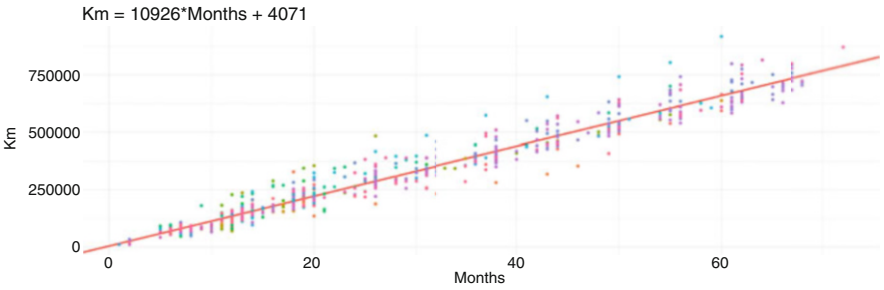

Fig. 6 Travelled distance vs time (months), for one truck model

3.2 An Illustrative Example

The illustration of the proposed method is based on truck model with maintenance periodicity of 75,000 km and a contract with duration of 300,000 km.

For practical purpose, the methodology proposed was implemented in R software [9] by means of a Graphical User Interface (GUI). To fit the truncated Normal distribution was used the package `truncnorm` [2, 8]. The Gamma, Log-normal and Weibull distributions parameters were estimated using the function `fitdist` from the package `fitdistrplus` [5]. In the execution of the AD-Tests was used the package `goftest` of R [6, 10].

As kernel function we consider a Gaussian kernel, and the bandwidth estimative was calculated using (4). In this case, the estimation was carried out with the functions `density` and `bw.nrd0` from *R* [3, 12].

For this work, $N = 1000$ Monte Carlo simulations were performed. Typically, the number of Monte Carlo simulations is defined taking into account the desired accuracy. Thus, it is desirable to determine a value of N that obtains a suitable level of accuracy for a given problem at hand. There are several methods for determining N that guarantees a specified level of accuracy for standard error estimates, confidence intervals, confidence regions, hypothesis tests or bias correction. As this work aimed to obtain the sampling distribution of total cost, N was chosen based on the histogram regularity of the samples. Different histograms were produced by varying the number of simulations. For $N = 1000$ the histogram of the samples turned out to be regular beyond any reasonable doubt.

Table 1 provides, for each interval and for both type of intervention, the intervals of kilometres considered, the fitted distributions and the empirical probability of the repairing occurrences. The results showed that in the first interval only 6% of the contracts lead to repair costs, while in the other intervals this probability exceeded 50%. As stated before, the maintenance costs for the I_0 interval are not simulated, as there is no periodic intervention in that mileage range given that the first maintenance intervention is schedule by the constructor to the 75,000 km, and according to the company engineers and historical data, none anticipates the first intervention by 37,500 km.

Taking into account the fitted distributions presented in the Table 1 and the procedure described in Sect. 3.1, a sample of the distribution of the total contract cost was achieved. Figure 7 represents the estimated histogram with smooth

Table 1 Fitted distribution for costs and empirical probability of repair occurrences

i	Interval	Maintenance	Repair	Probability of repair
0	]0, 37,500]	–	Weibull	0.06
1	]37,500, 112,500]	Gamma	Kernel	0.68
2	]112,500, 187,500]	Kernel	Weibull	0.63
3	]187,500, 262,500]	Kernel	Weibull	0.62
4	]262,500, 375,000]	Gamma	Weibull	0.54

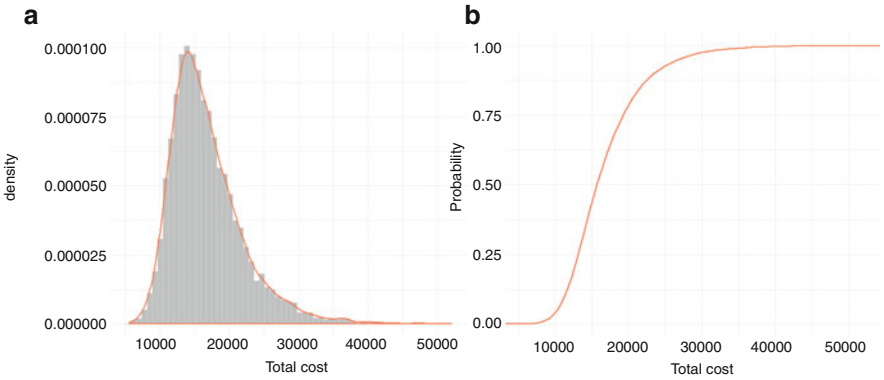

Fig. 7 Histogram (**a**) and empirical cumulative distribution plot (**b**) for the contract total cost of the given example

probability density function and the plot of the empirical distribution function of the random variable that represents the total cost of the contract.

This allows the manager to have some risk related estimate for the total contract cost. For example, given $\alpha = 0.95$, the cost estimate is $q_{F_{C_4^*}}(0.95) = 25{,}857$ monetary units, while for $\alpha = 0.05$ the value achieved was around $q_{F_{C_4^*}}(0.05) = 12{,}840$ monetary units.

4 The Price

This section presents a procedure to define the price of an assistance contract which is based on the idea that this price is a linear function of the estimated costs.

4.1 The Price of the Contract

The price of an assistance contract can be defined as the estimated costs to which was added a profit margin. To define the price of the contract is necessary to choose the model of the truck, the periodicity of the regular maintenance defined by the constructor, the maximum mileage covered by the contract or the duration of the contract. If the duration is a limit of time, then consider $K = f_{km}(t)$ km for t months. If the duration is a limit of kilometres, say K km, then it's no necessary to adjust the value. As so, and considering A (km) the periodicity of the regular maintenance defined by the constructor, we define $m = \max\{i : K \leq (i + 0.5) \times A, i = 1, \ldots, n\}$ as the number of intervals to be considered for this contract. Therefore, the total cost for this generic contract will be $q_{F_{C_m^*}}(\alpha)$ with a

risk $1-\alpha$. The true limit of kilometres for this contract will be $K_{max} = (m+0.5) \times A$ kilometres. Finally, the price of the contract will be given by:

$$\text{Price}(\alpha, \beta) = \beta \times q_{F_{C_m^*}}(\alpha) \ , \tag{8}$$

where β is the margin defined by the business manager and $1 - \alpha$ the risk.

4.2 Penalty

For the type of assistance contracts that this paper refers to, is usual to set a limit of kilometres that a truck can travel, and it is not plausible for a truck to stop at the exact moment the contract ends. When the trucks passes that limit, a monetary value (penalty cost) is applied for the extra kilometres travelled. We modelled the total cost of a contract as the cost for m intervals and the penalty cost as an adjustment to a cost of a contract with $m + 1$ intervals. As so, the penalty cost is then defined by,

$$C_P(n, \alpha, A_k) = \frac{q_{F_{C_{n+1}^*}}(\alpha) - q_{F_{C_n^*}}(\alpha)}{A_k} \tag{9}$$

monetary units per kilometre, for contracts with n intervals and periodicity of maintenance of A_k kilometres.

5 Results

The approach explained in this paper was implemented in two companies at NORS, regarding the historical data available on closed contracts. Both Figs. 8 and 9 represent the real and estimated profit margin for the all range of the real duration of assistance contracts on both companies. The numbers inside each cell represent the number of contracts of that type. For comparison terms, the beta value in (8) was settled to $\beta = 1.05$ for both companies. It may be observed that contracts with longer duration and more kilometres travelled tend to have a smaller margin, or even turned into losses.

It is important to notice that, as expected, the contracts with longer duration and with more kilometres have much more variance on the costs, and therefore their risks are significantly higher. Nevertheless, the other contracts are reasonably stable within this model parametrization, and a detailed analysis should be made by the management in order to consider whether to assign the same risk factor for all the contracts or to make it depend on the longevity of the contract.

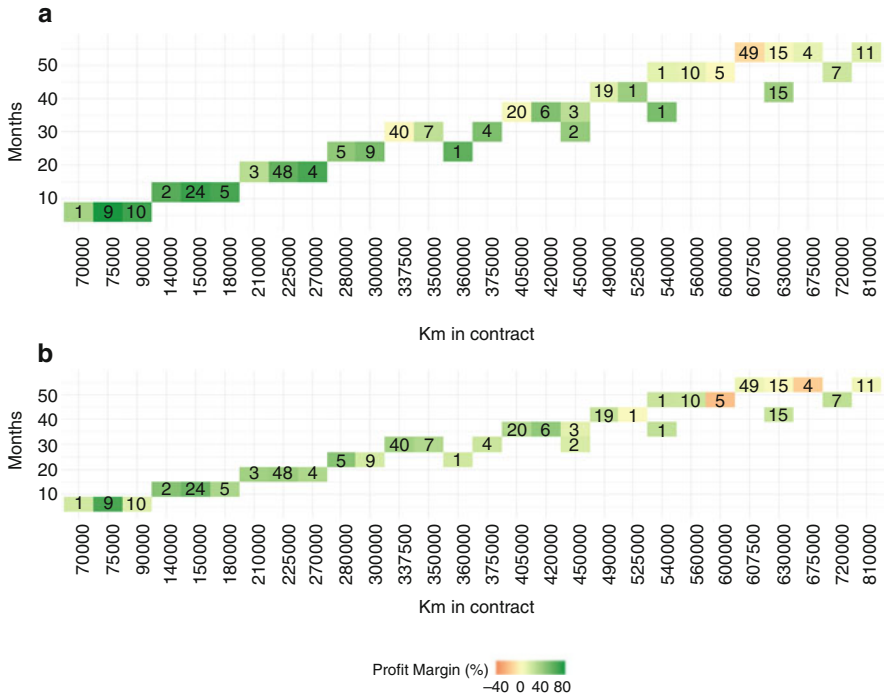

Fig. 8 Real (**a**) and estimated (**b**) profit margins of Company A versus duration of the assistance contracts

In other perspective, in Figs. 10 and 11, which represents the real and estimated margins of the assistance contracts of both companies. It can be observed that the profit has a large variability and extended contracts tend to decrease the margin.

This project was developed in an industrial company with the purpose to help the management of the assistance contracts to estimate and simulate their risks and prices. In fact, we went a little further, as besides the developed mathematical model, a graphical user interface (GUI) was built in order to implement the model and to give additional information to the management as presented in Fig. 12. This GUI, allows the business manager to estimate contract price proposals according to the model presented, to compare it with the ones that were previously settled by the company, as well as to explore and graphically analyse all current situations of all the contracts regarding one particular type of truck, and, of course be aware of the risk level he is taking when making the proposal. Finally, the parametrization of the model regarding, for example, the best fitted distributions is almost automatic and it is monthly updated with the new information from the on-going contacts, leading to as much as possible adherence to the reality.

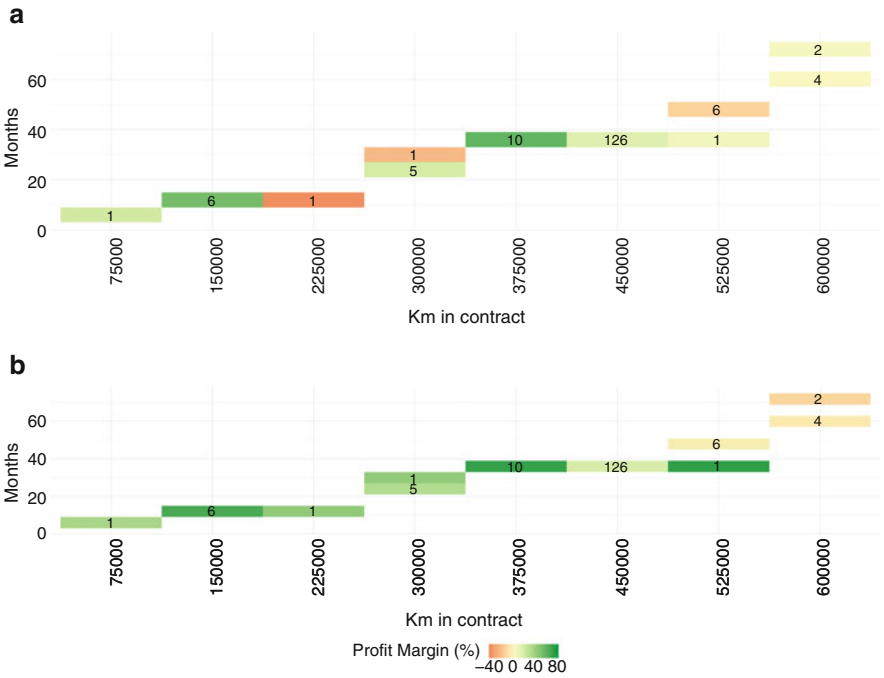

Fig. 9 Real (**a**) and estimated (**b**) profit margins of Company B versus duration of the assistance contracts

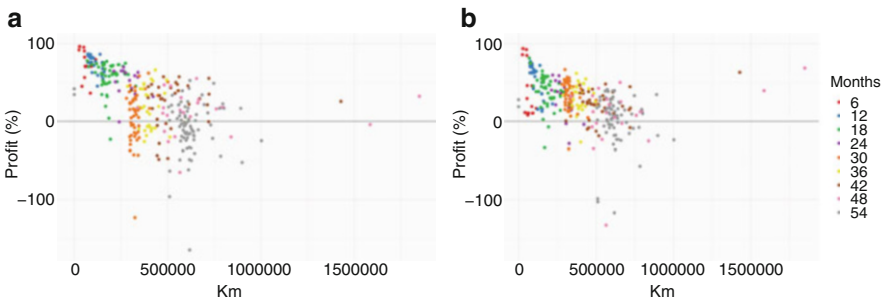

Fig. 10 Real (**a**) and estimated (**b**) profit margins of Company A versus mileage

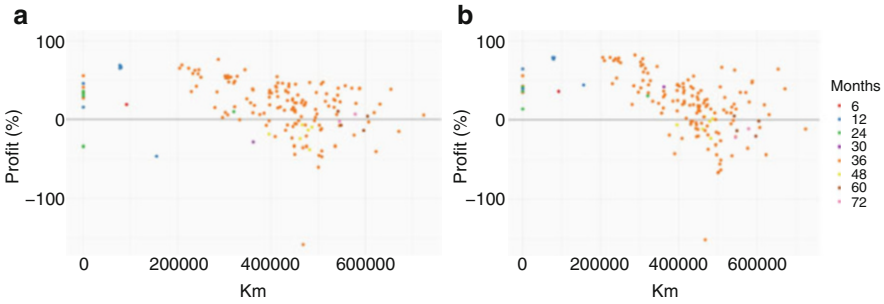

Fig. 11 Real (**a**) and estimated (**b**) profit margins of Company A versus mileage

Fig. 12 Snapshot of the developed Graphic User Interface

6 Conclusions

In this paper we address a challenge made by two NORS group companies regarding the costs and risks related with their assistance contracts for trucks. We built a stochastic model using the Monte Carlo simulation for estimating, at a certain risk, the contracts total cost. The price of the contracts is a function of the total cost. The resulting model was applied to two different models of trucks, belonging to different segments.

In the short term, the results indicate that the existing parameterization lead to good results without significant losses. However, for long range contracts, there is an increased risk of losses. The model was implemented on the company, via a Graphical User Interface that allows the managers to estimate contract price proposals according to this formulation, to compare them with the ones that were previously settled by the company, as well as to explore and graphically analyse the

historical data, that is, take an overview of the current situation regarding all the contracts for each particular type of truck, and, of course be aware of the risk level when making a particular proposal to a new client.

As this is an ongoing project, further work is to be done. One point of interest will be in optimizing the margin, β (8), of the contract for the risk taken. At this point, the margin is chosen by the business manager and takes into account some client segmentation. Other point of interest would be to explore the references of truck parts. For example, there are some type of single repairs that costs about 1.1 times the total value of the contract. According to historical data, these repairs are very rare but these situations must be covered by the profit margin in the other contracts. On the other hand, if the *life* of the truck parts are modelled, it is possible to anticipate costs, or even enable more information on eventual contracts renewals.

Acknowledgments The authors would like to thank to: the management team from Auto-Sueco and Galius companies, for all their support and business clarifications; the LAB MI team for all the fruitful discussion about this model; the anonymous reviewers for the insightful comments to the first version of this paper.

References

1. Ashgarizadeh, E., Murthy D.N.P.: Service contract: a stochastic model. Math. Comput. Modell. **31**, 11–20 (2000)
2. Burkardt, J.: The truncated normal distribution. Department of Scientific Computing Website, Florida State University (2014)
3. Chen, Y.C.: A tutorial on kernel density estimation and recent advances. Biostat. Epidemiol. **1**, 161–187 (2017). https://doi.org/10.1080/24709360.2017.1396742
4. Dattaa, P.P., Rajkumar, R.: Cost modelling techniques for availability type service support contracts: A literature review and empirical study. CIRP J. Manuf. Sci. Technol. **3**(2), 142–157 (2010)
5. Delignette-Muller, M.L., Dutang, C.: fitdistrplus: An R package for fitting distributions. J. Stat. Software **64**(4), 1–34 (2015). http://www.jstatsoft.org/v64/i04/
6. Faraway, J., Marsaglia, G., Marsaglia, J., Baddeley, A.: goftest: Classical Goodness-of-Fit Tests for Univariate Distributions (2017). https://CRAN.R-project.org/package=goftest
7. Kaas, R., Goovaerts, M., Dhaene, J., Denuit, M.: Modern Actuarial Risk Theory: Using R, vol. 128. Springer, Berlin (2018)
8. Mersmann, O., Trautmann, H., Steuer, D., Bornkamp, B.: truncnorm: Truncated Normal Distribution (2018). https://CRAN.R-project.org/package=truncnorm
9. R Core Team: R: A Language and Environment for Statistical Computing. R Foundation for Statistical Computing, Vienna, Austria (2017). https://www.R-project.org/
10. Razali, N.M., Wah, Y.B.: Power comparisons of Shapiro-Wilk, Kolmogorov-Smirnov, Lilliefors and Anderson-Darling tests. J. Stat. Model. Anal. **2**(1), 21–33 (2011)
11. Rinsaka, K., Sandoh, H.: A stochastic model on an additional warranty service contract. Comput. Math. Appl. **51**, 179–188 (2006)
12. Silverman, B.W.: Density estimation for statistics and data analysis. In: Monographs on Statistics and Applied Probability. Chapman and Hall, London (1986)
13. Thomopoulos, N.T.: Essentials of Monte Carlo Simulation: Statistical Methods for Building Simulation Models. Springer, New York (2013)

Tsunami-HySEA: A Numerical Model Developed for Tsunami Early Warning Systems (TEWS)

J. M. González-Vida, M. J. Castro, J. Macías, M. de la Asunción, S. Ortega, and C. Parés

Abstract The aim of this work is to present the collaboration between the EDANYA research group of the University of Málaga and several international institutions regarding the implementation of computational tools in the framework of the TEWS (Tsunami Early Warning Systems). These collaborations have resulted in the development of the first GPU-based finite volumes numerical model, known as Tsunami-HySEA, able to accelerate tsunami numerical simulations to become a real operational tool in TWC (Tsunami Warning Centres). In this way, tsunami-HySEA is able to compute large tsunami scenarios with good accuracy in only few minutes, which has produced a change of paradigm in the operational assessment of tsunami risks and is making substantial improvements in the current alert systems and therefore, to our citizens security.

1 Introduction

If numerical models are to be used as predictive tools in Natural Disasters such as tsunamis, this requires extremely fast computations. Less than a decade ago, nobody could expect real-time computing in the framework of Tsunami Early Warning Systems (TEWS). Nevertheless, in recent years, EDANYA Group has set a new paradigm in Tsunami Science. Aiming saving lives in the context of TEWS, the EDANYA Group has developed Tsunami-HySEA, a GPU-based numerical model with the objective of producing faster than real time (FTRT) numerical simulations of tsunami events. Based on high efficient, reliable and robust

J. M. González-Vida (✉) · S. Ortega
Department Applied Mathematics, Industrial Engineering School, University of Málaga, Málaga, Spain
e-mail: jgv@uma.es; sergio.ortega@uma.es

M. J. Castro · J. Macías · M. de la Asunción · C. Parés
Department Math. Analysis, Statistics and Op. Research and App. Mathematics, Faculty of Sciences, University of Málaga, Málaga, Spain
e-mail: mjcastro@uma.es; jmacias@uma.es; marcah@uma.es; pares@uma.es

M. Cruz et al. (eds.), *Progress in Industrial Mathematics: Success Stories*,
SEMA SIMAI Springer Series 5, https://doi.org/10.1007/978-3-030-61844-5_12

mathematical algorithms, together with the computational power of NVIDIA GPUs, Tsunami-HySEA is able to simulate a tsunami event with the required spatial and time resolution in only few minutes [1–5].

Nowadays one of the main challenges in Tsunami Science is producing accurate assessments of the tsunami waves impact, mainly in populated areas, and just some minutes after the generating earthquake was triggered. This timely prediction would save many lives in the occurrence of such events. Before the arrival of GPU computations to tsunami prediction, no numerical code was able to do so, and TEWS relied on the conservative, rough and now obsolete method based on Decision Matrices. More complex TEWS used precomputed databases as computational component, but they were extremely hard to generate and require a huge amount of computational resources. Prior to Tsunami-HySEA, and then other models, no system in the world was able to compute, solving the model equations and, in just few minutes, the evolution of a tsunami and predict its impact on land.

A second issue was the cost of the hardware required to perform such numerical simulations, unaffordable for many countries and governmental institutions (especially in developing countries). However, the new technology based on graphics cards results in an affordable hardware easy to run. Thus, Tsunami-HySEA came to propose a solution to these issues in nowadays Tsunami Science challenges: the cost of the computational system and the possibility of real time computations in this area.

The collaboration with different countries government agencies related with tsunami hazards, as well as with other interdisciplinary scientists during the implementation and improving process of Tsunami-HySEA has been a very rewarding collaboration as will be shown here.

This papers organizes as follows. Section 2 is devoted to describe the Tsunami-HySEA model, features, model equations and numerics, nested meshes implementation and time integration. Section 3 describes different computational techniques used in the operational version of Tsunami-HySEA as the load balancing algorithm used to equilibrate computational load, the multi-GPU implementation of the code. In Sect. 4, some numerical results corresponding to field cases are presented and in terms of computational time and numerical scheme efficiency. Then, Sect. 5 presents several collaborations and experiences with different institutions that currently are using Tsunami-HySEA in their tsunami systems. Finally some concluding remarks and comments close the paper.

2 The Tsunami-HySEA Model

The computational simulation of a tsunami event essentially involves three steps: generating the initial wave from the ocean surface, propagating along the ocean, and finally flooding coastal areas. Tsunami-HySEA was born with the idea of creating a numerical model capable of bringing these three steps together into a single numerical model. But providing these results on an operational system, where

response time is limited, is a great challenge. Tsunami-HySEA qualifies for a good balance between efficiency, robustness and reliability of tsunami simulations while producing these results in short computation times, much faster than real time in the case of Tsunami Early Warning Systems.

Tsunami-HySEA has been implemented using CUDA and MPI in order to take advantage of the massive parallel architecture of multi-GPU clusters, so that the computing time required could be dramatically reduced with respect to the use of a single CPU core or even a multi-core processor and, at the same time, numerical resolution could be increased still computing extremely fast. Many features are included in Tsunami-HySEA, such as the possibility of using nested meshes, direct output of time series, the computation of the initial seafloor deformation using the Okada [6] model (which is also carried out in GPU), support for rectangular or triangular faults, resuming a stored simulation with the possibility of adding new grids and new points for the time series, and asynchronous writing of the output NetCDF files, so that the computations are not awaiting while the data output are still being written on disk. A 2D domain decomposition is performed, and load balancing techniques are also used taking into account the wet and dry zones and the nested meshes, so that the computational load of all the MPI processes is as similar as possible. The entire numerical computation is carried out in multi-GPUs, using double numerical precision, including the nested meshes processing. Multiple CUDA kernels have been implemented, and CUDA streams are used to compute in parallel different meshes in a same level of the grid hierarchy. Furthermore, the MPI communications can overlap with kernel computations and memory transfers between CPU and GPU memory in order to increase the efficiency of the solver. By means of this very efficient implementation, the model is able to simulate 8 h of real time tsunami in the Mediterranean Sea (in a mesh with 10 million volumes and a resolution of 30 arc-sec) in 259 s using 6 computation nodes with a total of 12 NVIDIA GeForce GTX Titan Black or more recently, with the NVIDIA Tesla P100, in 257 s but using only 2 of them, or even in 284 s with a NVIDIA Tesla V100.

Besides, the Tsunami-HySEA model has been severely tested using specifically designed tsunami model benchmarks. In particular, it has passed all the tests compiled at [7] and all the benchmarks proposed at the "2011 NTHMP model benchmarking workshop" [8] for inundation and propagation (see [9]). Tsunami-HySEA has also participated in the "NOAA/NTHMP MMS Benchmarking Workshop: Tsunami Currents", see [10] in [11] (also to appear in [12] for laboratory experiments and in [13] for field data), and see [14] for a participating models intercomparison. Detailed information about all these benchmarks can be found at the HySEA models web page [15]. Tsunami-HySEA is being used in the Italian TEWS (CAT/INGV) since 2014 and is currently the reference code at GDACS at the Joint Research Centre of the European Commission, has recently been implemented in the Spanish TEWS at IGN at Madrid and it is being evaluated by other TEWS, as SHOA-UTFSM (Chile), SINAMOT (Costa Rica) or the Puerto Rico Seismic Network (US).

2.1 Model Equations

Tsunami-HySEA solves the 2D non-linear shallow water equations in spherical coordinates. For the sake of simplicity, the equations in Cartesian coordinates are presented here:

$$\begin{cases} \dfrac{\partial h}{\partial t} + \dfrac{\partial q_x}{\partial x} + \dfrac{\partial q_y}{\partial y} = 0 \\ \dfrac{\partial q_x}{\partial t} + \dfrac{\partial}{\partial x}\left(\dfrac{q_x^2}{h} + \dfrac{g}{2}h^2\right) + \dfrac{\partial}{\partial y}\left(\dfrac{q_x q_y}{h}\right) = gh\dfrac{\partial H}{\partial x} + S_x \\ \dfrac{\partial q_y}{\partial t} + \dfrac{\partial}{\partial x}\left(\dfrac{q_x q_y}{h}\right) + \dfrac{\partial}{\partial y}\left(\dfrac{q_y^2}{h} + \dfrac{g}{2}h^2\right) = gh\dfrac{\partial H}{\partial y} + S_y \end{cases} \tag{1}$$

In the previous system, $h(x, y, t)$ denotes the thickness of the water layer at point $(x, y) \in D \subset \mathbb{R}^2$ at time t, being D the horizontal projection of the 3D domain where the earthquake and tsunami take place. $H(x, y)$ is the depth of the bottom at point (x, y) measured from a fixed level of reference. The function $\eta(x, y, t) = h(x, y, t) - H(x, y)$ denotes the sea water free surface and $\boldsymbol{q}(x, y, t) = \big(q_x(x, y, t),\ q_y(x, y, t)\big)$ the mass-flow of the water at point (x, y) at time t. The mass-flow is related to the height-averaged velocity $\boldsymbol{u}(x, y, t)$ by means of the expression: $\boldsymbol{q}(x, y, t) = h(x, y, t)\,\boldsymbol{u}(x, y, t)$.

The terms S_x and S_y parameterize the friction effects between the fluid and the ocean bottom surface, and are given by a Manning law:

$$\begin{cases} S_x(W) = -gh\,\dfrac{n^2}{h^{4/3}}\,u_x\,\|\boldsymbol{u}\| \\ S_y(W) = -gh\,\dfrac{n^2}{h^{4/3}}\,u_y\,\|\boldsymbol{u}\| \end{cases}$$

where $n > 0$ is the Manning coefficient.

2.2 The Tsunami-HySEA Model Numerical Scheme

To discretize system (1), the domain D is divided into L cells or finite volumes $V_i \subset \mathbb{R}^2$, $i = 1, \ldots, L$. The values h, q_x and q_y at each cell represent cell averages of the water depth and mass-flow.

Tsunami-HySEA solves the two-dimensional shallow water system (1) by processing separately the propagation of the tsunami wave in the deep ocean and the inundation of the coastal areas, but both integrated in a single code. For the propagation step, it implements a fast, two-step scheme similar to leap-frog written under a finite volume framework. In the inundation step, a second order TVD-WAF

flux-limiter scheme, described in [16], is used. The combination of both schemes provides a smooth transition when the waves arrive to the coast, guarantees the mass conservation and prevents the generation of spurious high-frequency oscillations near discontinuities generated by leap-frog type numerical schemes.

A CFL (Courant-Friedrichs-Lewy) condition is imposed to ensure the linear stability of the scheme. In practice, this condition implies a restriction on the time step. In order to deal with wet-dry transitions, Tsunami-HySEA implements the 2D extension of the 1D numerical treatment described in [17]. The resulting scheme is well-balanced for the water at rest stationary solution ($\boldsymbol{q} = \mathbf{0}$ and η constant), that is, it exactly preserves the lake at rest solutions and are second or third order accurate, depending on the reconstruction operator and the time stepping method.

The Okada model [6] is used to predict the initial bottom deformation caused by the earthquake, which is transmitted instantaneously to the sea surface, thus generating the tsunami wave. Triangular faults [18] are also supported to compute the initial bottom deformation. Optionally, the Kajiura filter [19] can be applied to the result of this deformation. Several fault segments can be considered and it is possible to apply the deformation on them in asynchronous time instants. Furthermore, the initial deformation of the seafloor can be applied to the entire spatial domain or locally in a subdomain.

2.3 Nested Meshes

Tsunami-HySEA supports nested meshes in order to spatially refine and compute more accurately the impact of the tsunami in coastal areas. The grid hierarchy consists of N levels, $l_0, l_1, \ldots l_{N-1}$, each one having one or more submeshes. The root level l_0 is formed by one grid that covers all the spatial domain using the coarsest spatial resolution. The grids of level l_i, $i > 0$, have r_i times the spatial resolution of the level l_{i-1}, where r_i is the ratio of refinement of the level l_i. An unlimited number of levels are supported, with a power-of-two ratio of refinement between levels and, eventually, different ratios of refinement at each level. The grid hierarchy should fulfill the proper nested conditions defined in [20], which are also in [21]:

1. A fine grid starts and ends at the corner of a cell in the next coarser grid.
2. There must be at least one level l_{i-1} cell in some level l_{i-1} grid separating a grid cell at level l_i from a cell at level l_{i-2}, in the north, south, east, and west directions, unless the cell abuts the physical boundary of the domain.

Besides, it is also required that a grid of level l_i, $i > 0$, should be contained in only one coarser grid of level l_{i-1}.

2.4 Time Integration

The numerical scheme described in Sect. 2 is applied separately in each grid. Since each level has a different spatial resolution, the time step applied at each level should be modified accordingly. Specifically, in [21] a unique time step is used to process all the submeshes of a same level, which is defined as $\Delta t_i = \Delta t_{i-1}/r_i$ for $i > 0$, being Δt_i the time step applied at level l_i. However, in Tsunami-HySEA a local time stepping strategy is used, that is, a local time step in each grid is computed.

S_i denotes the number of submeshes of the level l_i, and $s_{k,i}$ is the k-th submesh of the level l_i, with $0 \leq i \leq N-1$. $\Delta t^n_{s_{k,i}}$ is the n-th time step applied in the submesh $s_{k,i}$. Figure 1 shows in circled numbers the order of the main steps in the nested meshes processing using an example with three levels and $r_1 = r_2 = 2$. Note that the time steps can be different in a same submesh and there is not any regridding step like in [21], since all the submeshes are fixed during all the simulation.

2.5 Interpolation, Projection of Fine Solutions and Flux Correction

Tsunami-HySEA follows the same approach based on the fluctuations of the state values that is used in [21] for the interpolation of the fine ghost cells and the projection of the fine solutions to the next coarser level. A flux correction step at the boundaries of the submeshes is also needed to ensure mass conservation. All these steps are performed as described in [21] for the two layer case. See the former reference for a detailed description of these steps and mathematical proofs of how the stationary solutions are preserved.

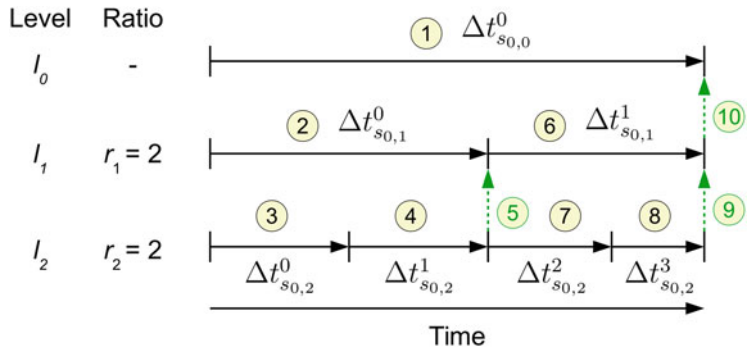

Fig. 1 Order of the main steps of the nested meshes processing using three levels and one submesh at each level. Black arrows: time integration; green arrows: projection of fine solutions and flux correction

3 Computational Techniques

In this section several computational techniques and algorithms used in Tsunami-HySEA are briefly described. All details will be available in [22].

Load Balancing Algorithm
A 2D domain decomposition is performed to divide the domain into subdomains. In order to get a balanced partition of the domain, in the sense that the computational load of all the subdomains is similar, the 1D static load balancing algorithm presented in [23] is used. This algorithm has been extended to 2D including nested meshes and also considering non-homogeneous GPUs.

Multi-GPU Implementation
The Tsunami-HySEA numerical scheme, the nested meshes processing, the Okada model and the Kajiura filter are implemented in CUDA and MPI using double numerical precision.

Asynchronous File Writing
A synchronous file writing approach could have a big impact in the performance, since the computations should stop until the current data have been written to disk. To solve this issue, Tsunami-HySEA allows writing the NetCDF files asynchronously, so that computations can continue while data are being written to the disk.

Activation of the Nested Meshes Processing
Note that it is unnecessary to process the nested meshes until a movement of the water is detected in the region covered by them, since they will remain in water at rest stationary state if no movement of the water occurs. For this reason, at the beginning of the simulation only the coarsest level is processed until a movement of the water is detected in the area covered by the nested meshes.

4 Numerical Results

In this section we analyze the efficiency of the Tsunami-HySEA multi-GPU implementation described in Sect. 2 using several problems with real topobathymetric data. For a summary of the Tsunami-HySEA model validation and verification, the reader is referred to [1, 9].

All the simulations in this section have been carried out in the CTE-POWER cluster of the Barcelona Supercomputing Centre (BSC). This cluster is based on IBM POWER9 processors and it consists of 52 computing nodes, each one having 40 cores and four Tesla V100, with an Infiniband interconnection network. We have used up to 64 GPUs. For each number of GPUs, we have tested different domain decompositions and the best runtime has been selected.

4.1 Mediterranean Sea

This example simulates a tsunami in the Mediterranean Sea using a mesh of 10,029,541 volumes with a spatial resolution of 30 arc-sec. The topobathymetric data have been provided by the National Institute of Geophysics and Volcanology (INGV) of Italy. The simulation time is 8 h.

Table 1 and Fig. 2a show the runtimes obtained. Figure 3 shows an image of the simulation. Using 64 Tesla V100, the simulation runs in only 18 s, and a speedup of 15.6 is reached with respect to one GPU (see Fig. 7).

4.2 2011 Tohoku Earthquake

This problem simulates the tsunami caused by the earthquake occurred on March 11, 2011, in Tohoku (Japan), using a mesh of 84,180,240 volumes covering all the Pacific Ocean with a spatial resolution of 1 arc-min. The data have been provided by the NOAA Centre for Tsunami Research (NCTR). The simulation time is 24 h.

Table 1 and Fig. 2b show the runtimes obtained. Figure 4 shows an image of the simulation at 4 h. In this case, a speedup of 44.4 is reached with respect to one GPU (see Fig. 7), much larger than the speedup obtained in the Mediterranean Sea problem because the mesh is much bigger and therefore the computing power of the GPUs can be better exploited.

Table 1 Execution times in seconds and speed-up over 1 GPU for all the problems using up to 64 Tesla V100

GPUs	Mediter.	Speed-up over 1 GPU	Tohoku	Speed-up over 1 GPU	LANTEX 2013	Speed-up over 1 GPU	1755	Speed-up over 1 GPU
1	286.5	1.00	7547.5	1.00	8108.4	1.00	4322.4	1.00
4	83.3	3.44	1963.0	3.84	2313.6	3.50	1430.8	3.02
8	48.6	5.89	1016.2	7.43	1322.5	6.13	1209.2	3.57
16	31.5	9.09	535.6	14.09	822.6	9.86	945.8	4.57
24	25.8	11.10	371.0	20.34	616.1	13.16	640.9	6.74
32	23.2	12.35	290.6	25.97	520.2	15.59	657.0	6.57
40	21.3	13.45	241.8	31.21	459.6	17.64	615.4	7.02
48	20.1	14.25	211.1	35.75	403.6	20.09	595.3	7.26
56	19.3	14.84	187.5	40.25	401.6	20.19	540.6	7.99
64	18.3	15.65	170.0	44.40	374.5	21.65	501.1	8.83

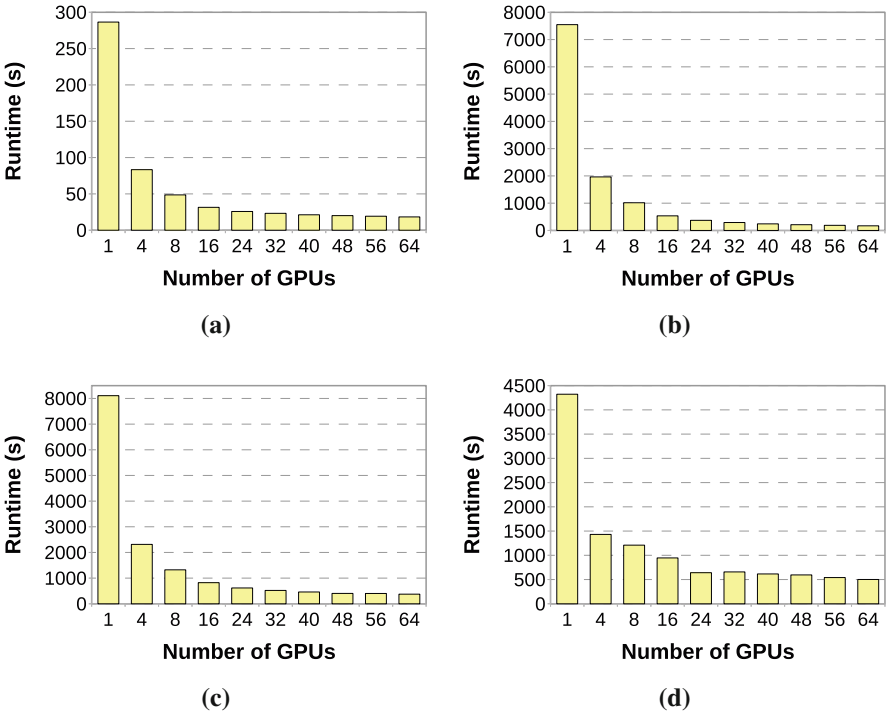

Fig. 2 Execution times in seconds for all the problems using up to 64 Tesla V100: (**a**) Mediterranean Sea, (**b**) 2011 Tohoku earthquake, (**c**) LANTEX 2013, (**d**) 1755 Lisbon earthquake

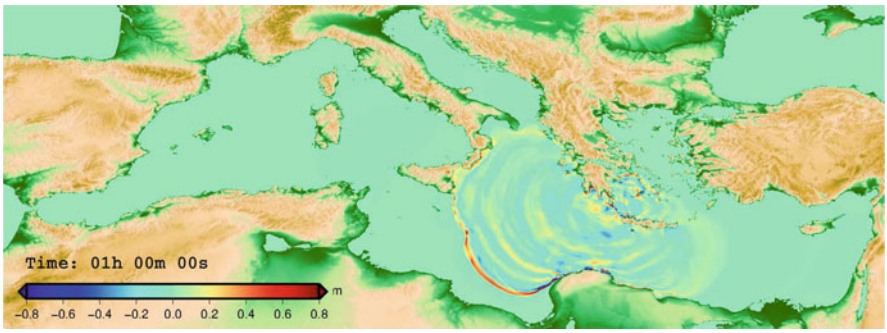

Fig. 3 Simulation of the Mediterranean Sea problem

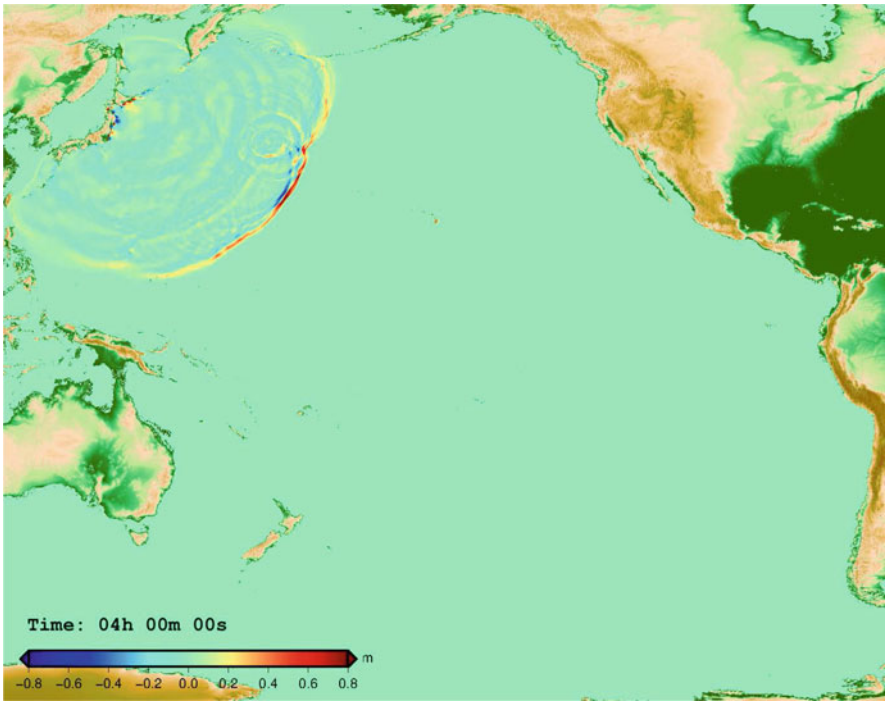

Fig. 4 Simulation of the 2011 Tohoku tsunami problem

4.3 LANTEX 2013

This problem is based on the LANTEX scenario proposed in the Caribbean Wave LATEX 2013 exercise. The data have been provided by the NOAA Centre for Tsunami Research and the National Geophysical Data Centre Digital Elevation Model for Puerto Rico. A three nested level mesh configuration is used in this case. The level l_0 mesh has 253,350 volumes and a spatial resolution of 64 arc-sec, the level l_1 mesh has 1,202,224 volumes, $r_1 = 8$. The third resolution level, l_2, has a mesh of 22,129,536 volumes and $r_2 = 8$. The simulation time is again 4 h.

Figure 5a depicts the initial state and the nested meshes, represented as black rectangles. Figure 5b shows the impact of the tsunami in Puerto Rico using the l_2 mesh. Table 1 and Fig. 2c show the runtimes obtained. Again, the best runtime has been reached with 64 GPUs, achieving a speedup of 21.6 with respect to one GPU. For a detailed analysis of the results obtained with this simulation and a comparison with the MOST tsunami model [24], see [1].

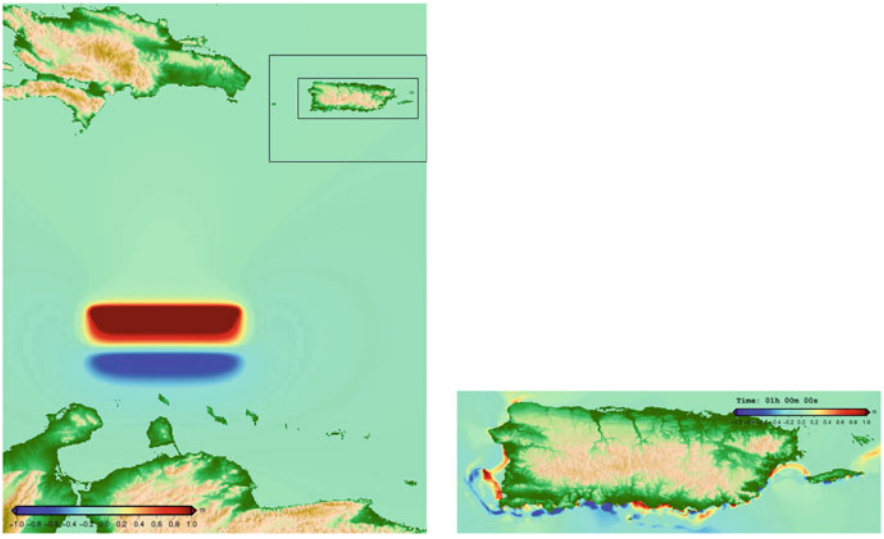

Fig. 5 Simulation of the LANTEX 2013 problem: (**a**) Initial state and nested meshes, (**b**) Impact of the tsunami in Puerto Rico using the finest mesh

4.4 1755 Lisbon Earthquake

This example simulates the tsunami caused by the Lisbon earthquake occurred on November 1, 1755, which caused great damage and many causalities in the south of Portugal, Lisbon, Spain and Morocco. The bathymetric data have been obtained from the European Marine Observation and Data Network (EMODnet) and also data were provided by the Spanish Institute of Oceanography. Three resolution levels have been used, where the level l_0 mesh has 6,033,600 volumes and a spatial resolution of 1/8 arc-min (approx. 225 m), the level l_1 mesh has 18,066,496 volumes with $r_1 = 4$ (approx. 56 m), and the finest level has two meshes covering the cities of Cádiz and Huelva with a total of 20,317,440 volumes and $r_2 = 4$ (approx. 14 m). The simulation time is 1.5 h.

Figure 6a depicts the initial state and the nested meshes. Figure 6b shows the arriving of the tsunami to the city of Cádiz using the finest resolution level. Table 1 and Fig. 2b show the runtimes obtained. The best runtime has been reached with 64 Tesla V100, achieving a speedup of 8.6 with respect to one GPU (Fig. 7).

Finally, in Fig. 8 we can see that, in the Mediterranean and Tohoku problems, there have been processed approximately 18,000 and 43,000 millions of volumes per second, respectively, using 64 GPUs.

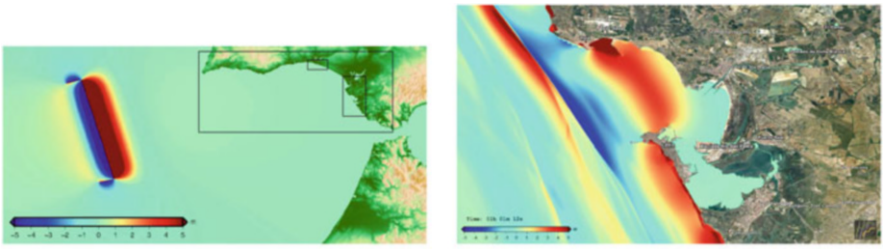

Fig. 6 Simulation of the 1755 tsunami problem: (**a**) Initial state and nested meshes, (**b**) Arrival of the tsunami to Cádiz using the finest resolution level

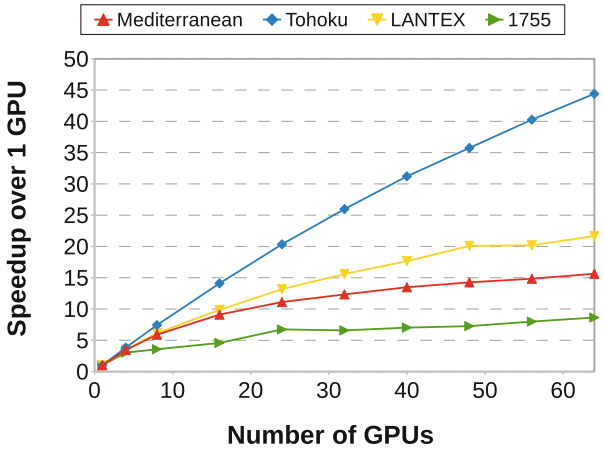

Fig. 7 Speedup with respect to one Tesla V100 in all the problems

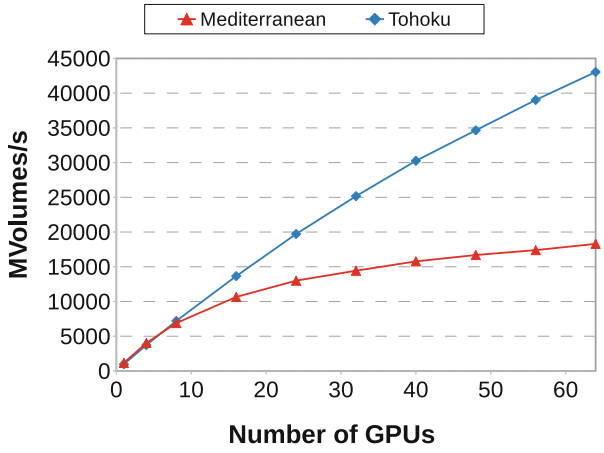

Fig. 8 Millions of volumes processed per second for some problems

5 Collaborations, Research Agreements with Industry

5.1 CAT-INGV, Italy

Although any researcher working on Tsunami Science can benefit from using fast, robust and reliable tsunami models, when computing time it is reduced to such limits, the main beneficiaries of this kind of models is the community devoted to early warning and faster than real time predictions. Our initial collaborations started with the CAT-INGV (Tsunami Alert Centre of the INGV, Italy) by means of a Memorandum of Understanding signed in 2012. The main aim of this agreement was to collaborate in the development of customized and improved versions of Tsunami-HySEA designed according to their specifications.

The implementation of the CAT-INGV is based on the North-eastern Atlantic, the Mediterranean and connected seas Tsunami Warning System (NEAMTWS) decision Matrix (DM): alert levels are set based exclusively on earthquake location and magnitude. The use of a DM allows a rapid implementation of a Tsunami Warning System (TWS) but it not considers important features to better characterize a tsunami forecast as earthquake focal mechanism, anisotropy of tsunami propagation and the morphology of the coast. The CAT also uses a database of pre-calculated scenarios and they were exploring the possibility of simulating the tsunami on the fly by using a Faster than real time (FTRT) GPU-based model.

Tsunami-HySEA is playing an important role in boosting research at INGV in the last two issues: (1) generate a database of thousands of pre-calculated scenarios, and (2), to compute scenarios in real time (see [25]). The used grid for the Mediterranean Sea is the one described in Sect. 4.1 and it is depicted in Fig. 9. The grid resolution considered is 30 arc-sec, with $5{,}221 \times 1{,}921 = 10{,}029{,}541$ cells. The initial conditions are based on synthetic examples and the total simulation time considered in the alert system is 8 h for a tsunami in the Mediterranean Sea.

As output of the model, free surface elevation time series are saved every 15 s at 17,000 selected locations throughout the Mediterranean.

In Table 2 are presented the computational time, speed-ups and the number of times faster than real time (FTRT) for the current multi-GPU version of Tsunami-HySEA.

It can be observed that 8 h of simulation can be computed in less than 5 min in just one GPU, that means capacity of computing around 100 times faster than real time. With this GPU architecture it is possible to compute 900 times faster than real time using 16 GPUs. This computation power can be used not only to provide results for events occurring in real time, but also to generate a pre-computed database of hundred of thousands of cases, or more recently it is being used in the context of Probabilistic Tsunami Hazard Assessment, where a huge number of scenarios must be computed to provide a probabilistic distribution of solutions for different scenarios, taking into account the uncertainties associated to this kind of natural hazards.

Fig. 9 Global domain considered by the INGV (Italy) for the Mediterranean Sea

Table 2 Computational times

N. GPUs	Comput. time (s)	Speed-up	Times FTRT
1	286.51	1.00	100.52
4	83.35	3.44	345.53
8	48.62	5.89	592.35
16	31.49	9.10	914.57

5.2 Other Tsunami Early Warning Centres

Our collaboration has been especially intense and fruitful with the NCTR (NOAA Centre for Tsunami Research) in the U.S.A. Starting in 2012 with a Research Contract where another of the numerical models of the HySEA family, Landslide-HySEA, was introduced in the NCTR tsunami tsunami prediction capabilities as initial conditions generator in cases of landslide generated tsunamis. Later, in 2016 a Memorandum of Understanding was signed between the National Oceanic and Atmospheric Administration of the United States (NOAA) and the University of Málaga focusing in a research collaboration with the U.S. Oceanic and Atmospheric Research Dpt. in tsunami modelling and related activities. During this collaboration, the numerical model used by the Tsunami Warning Centres (TWC) of the United States, MOST, was recoded for GPU architecture and several of the computational techniques described in the previous sections were applied in order to improve the MOST model performance. Currently, Tsunami-HySEA is being adapted to be

Fig. 10 Global Disaster Alert Coordination System main webpage

included in the SIFT system (Short-term Inundation Forecasting for Tsunamis) to be used in the Tsunami Warning Centres of the United States.

Other important collaboration was initiated with the SHOA (Servicio Hidrográfico y Oceanográfico de la Armada) of Chile through an Agreement signed with the UTFSM University. Currently they are evaluating Tsunami-HySEA in order to be integrated in the Chilean Tsunami Warning System.

In Spain, an Agreement between the IGN (Instituto Geográfico Nacional) and de University of Málaga has been also signed to include a customized version of Tsunami-HySEA in the Spanish Tsunami Warning System, that is being currently developed.

5.3 Other Institutions, International Projects and Awards

In 2015 an Agreement was signed between the Institute for the Protection and Security of the Citizen of the Joint Research Centre of the European Union and UMA. This Agreement established the basis of a collaboration that aimed, as first step, the installation of Tsunami-HySEA in the GDACS (Global Disaster Alert Coordination System), that is a cooperation framework between the United Nations, the European Commission and disaster managers worldwide to improve alerts, information exchange and coordination in the first phase after major sudden-onset disasters. In this system (see Fig. 10) tsunami events are computed in real time using one GPU dedicated in exclusive for this system.

In 2018, Tsunami-HySEA and Landslide-HySEA codes were selected as European flagship codes for tsunami simulations. The main objective of ChEESE is to establish a new Centre of Excellence (CoE) in the domain of Solid Earth targeting the preparation of 10 Community flagship European codes for the upcoming pre-Exascale (2020) and Exascale (2022) supercomputers. Some preliminary results for Tsunami-HySEA in this project have been several improvements in the numerical model efficiency obtained thanks to the interdisciplinary collaboration between specialists in Geophysics, Numerical Modelling, Computer Science and Tsunami Alert Systems.

More recently, since October 2019, Tsunami-HySEA has been integrated in the ARISTOTLE-ENHSP European project. ARISTOTLE project is a scalable system that can provide new hazard-related services to the ERCC (European Emergency Responding Coordination System). A pool of experts in the field of Meteorology and Geophysics of Europe has been created and they can assess the ERCC in crisis situations. In this system, a computation platform has been designed where a final operator (an expert in tsunamis field) can run multiple tsunami computations according to earthquake data provided in real time by the hazard alert systems.

Finally, we would like to add in this section that Tsunami-HySEA was awarded in 2018 with the NVidia Global Impact Award. This award, endowed with $100,000 USD, is defined by NVidia as a groundbreaking work that addresses the world's most important social and humanitarian problems. The award goes to researchers or institutions using NVidia technology to achieve breakthrough results with broad impact.

6 Conclusions

Traditionally, TEWS have worked, and continue working, with Decision Matrices. This represents actually an old system with some advantages but also many disadvantages and drawbacks. As the calculation in real time was unattainable, the use of precomputed scenario databases was proposed to improve predictions and warnings. This method traditionally required months to years of numerical computations and a huge effort to build them up. Besides, this approach presents problems related to unexpected events or where non-linear effects are important and the linear combination of results is clearly non enough.

EDANYA Group decided to address the specific problem of performing real time simulations of tsunamis to be used in the context of TEWS and anywhere in the world. In the Pacific Ocean, for the far-field prediction, this kind of warning systems can be less fast-computing-demanding but, in the near-field or, for example in the Mediterranean, the response is needed in just a few minutes. In this challenging scenario, the required ingredients are difficult to combine in a single resulting numerical tool: efficiency, robustness, reliability and an extremely fast response. In the context of tsunami simulations in large domains and deeper waters, the scientific community agree on the use of the non-linear Shallow-Water equations

as basic modeling tool. They serve to reproduce the propagation and inundation of seismic generated tsunamis with a suitable degree of precision. Tsunami-HySEA solves this set of equations, based on innovative numerical algorithms developed by the EDANYA Research Group. Tsunami-HySEA combines two numerical models (the first one focused on the simulation of the propagation of the tsunami—far-field simulation—) and the other one focused on the simulation in close to coast shallower areas and inundation processes, but both models are fully integrated in a single code. It was necessary to get a good balance between accuracy and low dissipation with an extremely efficient and fast code.

Tsunami-HySEA has been tested with a wide number of analytical solutions, laboratory experiments, and field and benchmark experiments with very satisfactory results presented in important meetings. Tsunami-HySEA has been defined as a game changer in the context of Tsunami Warning Systems due to the revolution that was introduced by the aforementioned computational efficiency in the GPU architecture.

This numerical model has been adopted and included in several Tsunami Warning Centres around the world as well as in other information systems (GDACS) and Early Warning Projects (ARISTOTLE-ENHSP Project). Tsunami-HySEA was selected as flagship code in the H2020 ChEESE project in order to create the future European Centre of Excellence for Exascale in Solid Earth. A future European centre dedicated to the simulation and mitigation of geohazards by using the new exascale computers that will be available in the next years.

Acknowledgments This research has been partially supported by the Spanish Government research project MEGAFLOW (RTI2018-096064-B-C21), SIMURISK (MTM2015-70490), Junta de Andalucía/FEDER (UMA18-FEDERJA-161), Universidad de Málaga, Campus de Excelencia Andalucía TECH and ChEESE project (EU Horizon 2020, grant agreement N. 823844), https://cheese-coe.eu/. The work presented here has been possible thanks to the close collaboration with our colleagues at CAT-INGV Rome, PMEL-NOAA at Seattle and JRC-EC at Ispra. Thank you to the Barcelona Supercomputing Centre (BSC) for their support with the CTE-POWER access program.

References

1. Macías, J., Mercado, A., González, J.M., Ortega, S., Castro, M.J.: Comparison and computational performance of Tsunami-HySEA and MOST models for LANTEX 2013 scenario: Impact assessment on Puerto Rico coasts. Pure Appl. Geophys. **173**(12), 3973 (2016)
2. Castro, M.J., García, J.A., González, J.M., Parés, C.: Solving shallow-water systems in 2D domains using finite volume methods and multimedia SSE instructions. J. Comput. Appl. Math. **221**(1), 16 (2008)
3. Lastra, M., Mantas, J.M., Ureña, C., Castro, M.J., García, J.A.: Simulation of shallow-water systems using graphics processing units. Math. Comput. Simul. **80**(3), 598 (2009)
4. Castro, M.J., de la Asunción, M., Mantas, J.M., Ortega, S.: On the benefits of using GPUs to simulate shallow flows with finite volume schemes. Bol. Soc. Esp. Mat. Apl. **50**, 27 (2010)
5. de la Asunción, M., Mantas, J.M., Castro, M.J.: In: D'Ambra, P., Guarracino, M., Talia, D. (eds.) Euro-Par 2010 - Parallel Processing, pp. 353–364. Springer, Berlin, Heidelberg (2010)

6. Okada, Y.: Internal deformation due to shear and tensile faults in a half-space. Bull. Seismol. Soc. Am. **82**(2), 1018 (1992)
7. Synolakis, C.E., Bernard, E.N., Titov, V.V., Kânoğlu, U., González, F.I.: Validation and verification of tsunami numerical models. Pure Appl. Geophys. **165**(11), 2197 (2008)
8. NTHMP (National Tsunami Hazard Mitigation Program): In: Proceedings and Results of the 2011 NTHMP Model Benchmarking Workshop. Tech. rep., Boulder: U.S. Department of Commerce/NOAA/NTHMP; (NOAA Special Report) (2012)
9. Macías, J., Castro, M.J., Ortega, S., Escalante, C., González-Vida, J.M.: Performance benchmarking of Tsunami-HySEA model for NTHMP's inundation mapping activities. Pure Appl. Geophys. cs **174**(8), 3147 (2017)
10. Macías, J., Castro, M.J., Ortega, S., Escalante, C., González-Vida, J.M.: Tsunami currents benchmarking results for Tsunami-HySEA. Tech. rep., Portland, Oregon (2016). https://doi.org/10.13140/RG.2.2.22999.47527
11. NTHMP (National Tsunami Hazard Mitigation Program): Report on the 2015 NTHMP Current Modeling Workshop. Tech. rep., Portland, Oregon (2016)
12. Macías, J., Castro, M.J., Escalante, C.: Performance assessment of Tsunami-HySEA model for NTHMP tsunami currents benchmarking. Lab data. Coastal Engineering **158**(103667) (2020)
13. Macías, J., Ortega, S., Castro, M.J., González-Vida, J.M.: Performance assessment of Tsunami-HySEA model for NTHMP tsunami currents benchmarking. Field cases. Ocean Modeling **152**, 101645 (2020). https://doi.org/10.1016/j.ocemod.2020.101645
14. Lynnet, P.J., et al.: Inter-model analysis of tsunami-induced coastal currents. Ocean Modelling **114**, 14 (2017). https://doi.org/10.1016/j.ocemod.2017.04.003
15. EDANYA Reseach Group: HySEA project web page. benchmarks minisite (2021). https://edanya.uma.es/hysea/index.php/benchmarks
16. de la Asunción, M., Castro, M.J., Fernández-Nieto, E.D., Mantas, J.M., Ortega, S., González, J.M.: Efficient GPU implementation of a twowaves TVD-WAF method for the two-dimensional one layer shallow water system on structured meshes. Comput. Fluids **80**, 441 (2013)
17. Castro, M.J., Ferreiro, A.M., García, J.A., González, J.M., Macías, J., Parés, C., Vázquez-Cendón, M.E.: The numerical treatment of wet/dry fronts in shallow flows: applications to one-layer and two-layer systems. Math. Comput. Modell. **42**(3–4), 419 (2005)
18. Meade, B.J.: Comput. Geosci. **33**(8), 1064 (2007)
19. Kajiura, K.: The leading wave of a tsunami. Bull. Earthquake Res. Ins. **41**, 535 (1963)
20. Berger, M.J., Colella, P.: Local adaptive mesh refinement for shock hydrodynamics. J. Comput. Phys. **82**(1), 64 (1989)
21. de la Asunción, M., Castro, M.J.: Simulation of tsunamis generated by landslides using adaptive mesh refinement on GPU. J. Comput. Phys. **345**, 91 (2017)
22. de la Asunción, M., Castro, M.J., Macías, J., González-Vida, J.M.: In preparation (2020)
23. de la Asunción, M., Castro, M.J., Mantas, J.M., Ortega, S.: Numerical simulation of tsunamis generated by landslides on multiple GPUs. Adv. Eng. Software **99**, 59 (2016)
24. Titov, V.V., González, F.I.: Implementation and testing of the method of splitting tsunami (MOST) model. Tech. rep., NOAA Technical Memorandum ERL PMEL-112 (1997)
25. Molinari, I., Tonini, R., Lorito, S., Piatanesi, A., Romano, F., Melini, D., Hoechner, A., Gonzàlez Vida, J.M., Maciás, J., Castro, M.J., de la Asunción, M.: Fast evaluation of tsunami scenarios: uncertainty assessment for a mediterranean sea database. Nat. Hazards Earth Syst. Sci. **16**(12), 2593 (2016). https://doi.org/10.5194/nhess-16-2593-2016. https://www.nat-hazards-earth-syst-sci.net/16/2593/2016/

Wildfire Resources Management: A Decision Support Tool Created with R to Solve Optimisation Models in Logistics for Fighting Forest Fires

Jorge Rodríguez Veiga, María José Ginzo Villamayor, and Balbina Virginia Casas Méndez

Abstract The first part of this work reviews several mathematical programming models dedicated to resource allocation and planning problems in the context of extinguishing large forest fires. These problems have been studied as part of the research projects *Lumes* and *Enjambre*, which involve both the public and private sectors in Spain. The objective of *Lumes* and *Enjambre* is to develop advanced technologies for fighting forest fires. Moreover, the projects address other tasks such as the design of algorithms to prevent aircraft collisions and estimating the perimeters of forest fires using techniques such as estimating sets from thermal images. The second part of this work is focused on the `R` package and corresponding graphic interface, Wildfire Resources Management (`wrm`), which are designed to offer a user-friendly model interface in terms of the introduction of the necessary data, resolution, and presentation of the results, according to the needs of the interlocutors in the company dedicated to the extinction of forest fires. The auxiliary package uses various solvers, such as `symphony` and `gurobi`. This work presents the various components of `wrm` (which can be viewed in the GitHub repository), a computational study, and a procedure for its use.

1 Introduction

In recent years, Spain has been one of the European Union countries that is the most affected by forest fires. This problem poses one of the most serious threats to the forest heritage of the country, affecting the integrity of material assets and human lives. Moreover, it is a problem that may intensify owing to the effects of climate

J. Rodríguez Veiga · M. José Ginzo Villamayor · B. Virginia Casas Méndez (✉)
Department of Statistics, Mathematical Analysis and Optimization, Institute of Mathematics, IMAT, Technological Institute of Industrial Mathematics, ITMATI, Group of Optimization Models, Decision, Statistics and Applications, MODESTYA, University of Santiago de Compostela, Santiago, Spain
e-mail: jorge.rodriguez.veiga@usc.es; mariajose.ginzo@usc.es; balbina.casas.mendez@usc.es

M. Cruz et al. (eds.), *Progress in Industrial Mathematics: Success Stories*,
SEMA SIMAI Springer Series 5, https://doi.org/10.1007/978-3-030-61844-5_13

change. Various reports by the Ministry of Agriculture, Fisheries and Food (MAPA) of Spain in 2018 [4] reflected the severity of the situation.

In the past decade, an average of 12,573 fires occurred per year, of which two thirds were *conatos*.[1] Although *conatos* do not cause significant damage and the affected areas usually recover naturally, they are also relevant. Although the number of fires and *conatos* has been decreasing in the past decade, effective resource management remains essential. The magnitude of the problem results in an expenditure of millions of Euros by state, regional, and local administrations for the prevention and extinction of forest fires. According to the latest numbers from MAPA, 44.4% of the fires in 2019 occurred in the northwest area of the country, which includes the communities of Galicia, Asturias, Cantabria, and the Basque Country, as well as the Castilian provinces of León and Zamora.

Furthermore, although the total number of fires per year is decreasing, there is an increasing threat of large wildfires,[2] against which extinction services are ineffective. This significant threat results in the need for large-scale decisions to be made, taking into account numerous variables that affect the decision-making process.

As an example of how dramatic the situation may be, a wave of fires occurred in Galicia between Friday 13 October 2017 and Sunday 15 October 2017, when more than 100 forest fires were active simultaneously. Among the resources involved in the extinction operation, there were 500 soldiers, 35 brigades, 220 motor pumps, 40 blades, and 20 air resources; 45,000 ha of land burned, and there were 3 deaths and 20 injured.

In general, the design of decision support systems for logistics is an extremely active field of research and applications in modern operations. Within the forest fire control framework, it is also essential for efficient decisions to be made. Furthermore, budgets and fire resources are limited in this context [6]. In this sense, it is worth mentioning that economic theory plays a central role in the management of forest fires. The first works to engage in the economic study of forest fires were [5] and [14], which described the establishment of an optimum fire management programme. A theoretical framework has been used to identify the most efficient means of managing wildfire costs, namely the Cost Plus Net Value Change, (C+NVC, [3]). This framework is intended to minimise the cost of the use of resources in fire fighting plus the cost produced by the hectares of land burned, taking into account the material losses in the fire (such as trees and urban goods) as well as the restocking or reconstruction of these areas. Three types of problems associated with forest fire management have been distinguished in the literature: prevention, detection, and the management of resources for forest fire containment [8].

In the case of Spain, different research projects have emerged in light of this growing problem. In 2010, the *Prometeo* project arose, with the goal of improving

[1] *Conatos* are fires affecting an area of less than 1 ha.

[2] Large wildfires are fires in which more than 500 ha of surface burn.

the efficiency of fire fighting. *Prometeo* was one of the largest applied research projects awarded to a business consortium in Spain to fight forest fires. The project involved more than 16 companies and active government participation, with the aim of achieving the following objectives: mitigating the environmental damage in case of fire in an efficient manner, reducing the number and size of large wildfires, and ensuring the safety of extinguishing devices.

Following the *Prometeo* project, the *Lumes* and *Enjambre* projects were implemented in 2013 and 2015, respectively, which again involved various companies in the public and private sectors, and were funded by the Spanish Centre for the Development of Industrial Technology. Among those involved in these projects was the public consortium the Technological Institute of Industrial Mathematics (ITMATI), which includes three universities of Galicia, Coremain, a computer consulting company located in Santiago de Compostela, and Spain Babcock International, a leading provider of air emergency services and aircraft maintenance. The main objective of these projects is to develop new advanced technologies for comprehensively fighting major forest fires, reducing the number and surface size of these fires, and generating a security enclosure in operations that can significantly reduce the accident rate of the participants (technical, brigade, and pilots).

Various activities have been of substantial interest in projects of this magnitude. These activities include image processing, which provides information regarding the vegetation structure and evolution of the fire (according to which resources are selected), the study of the feasibility of unmanned aircraft in this context, algorithms and strategies to ensure the safety of terrestrial environments, analyses of night extinction operations, and the coordination of air traffic. In particular, the tasks that are of greatest relevance within the *Enjambre* project can be classified as follows:

- An algorithm to estimate the perimeters of forest fires using techniques for estimating sets from thermal images.
- An algorithm to prevent collisions between aircraft that are working on the same forest fire.
- An algorithm to calculate the efficiency of water discharges by air resources in the extinction of forest fires.
- An algorithm to manage resources, taking into account the regulations in force in Spain (such as rest times and the minimum number of resources in the area).

This paper details the final point mentioned above, the efficient management of resources involved in the extinction of a forest fire, and the corresponding computer tools that are designed. Three problems that are of significant relevance can be differentiated:

1. The selection of resources necessary for the containment of a forest fire.
2. The assignment of each air resource to an area of unloading and loading for the retarders used to contain the forest fire.
3. The allocation of air resources to re-fuelling points.

As these problems are strongly interconnected, the following paragraphs explain the integration and use of each of the problems to facilitate the understanding and scope thereof.

To understand the management of a forest fire, it is first necessary to define the roles of certain agents. The extinguishing director is in charge of the entire forest fire management operation. To this end, the director has the support of the air resources air coordinator (who aims to achieve the safety of the operation and optimise the times of the air resources), the air resources land coordinator (who aims to control the fuel available in re-fuelling bases and plans the use of these bases), and the land resources coordinator (who aims to manage the operation of the land resources and ensure their safety).

When a forest fire is detected, the extinguishing director needs to determine a subset of the available resources that will be used to contain the fire (a model has been designed for this purpose, which is referred to as Mathematical Model 1). Once the resources have been selected and their periods of action on the fire have been established, as well as the rest periods, the air resources are allocated to the flight routes (which are defined as the elliptical aerial routes that the aircraft must follow between the points of discharge and retardant loading). In particular, for each set of aircraft working in the same period, the air resources air coordinator carries out the assignment of aircraft to the flight routes (Mathematical Model 2). Moreover, because the air resources land coordinator already knows the time assignments of the air resources for each rest period, Mathematical Model 3 for the assignment of the aircraft to the re-fuelling points must be executed. Thus, with this distribution of tasks, the extinguishing director has assured control over the resources that are working in the fire and those that are re-fuelling. This also allows for the correct management of re-fuelling points, thereby avoiding collapses or shortages. Figure 1 provides a schematic description of the entire process.

In this paper, the implementation of a mathematical programming model that responds to the interest of the company Spain Babcock International in automating the selection and temporary allocation of resources in the extinction of a forest fire is presented. The collaboration is carried out within the *Lumes* and *Enjambre* projects. The company does not have a similar tool at present and currently uses a human-based method aided by GIS tools. The new tool will serve as a support system for the recommendation of resources to be used by the extinction coordinators, and therefore, according to the computation study carried out, they will be more efficient. The company Coremain, which also participates in the projects, is in charge of integrating this tool with other algorithms created in the project, such as that providing the evolution of the fire perimeter. All of this constitutes an important knowledge transfer for the company. In Sect. 2, a basic model existing in the literature is presented. Section 3 outlines the model created in the projects for the selection and temporary allocation of resources. Sections 4 and 5 present complementary models created to assign aerial resources to flight routes and re-fuelling bases, respectively. Section 6 explains the implementation programmed with `R`, which solves the main model.

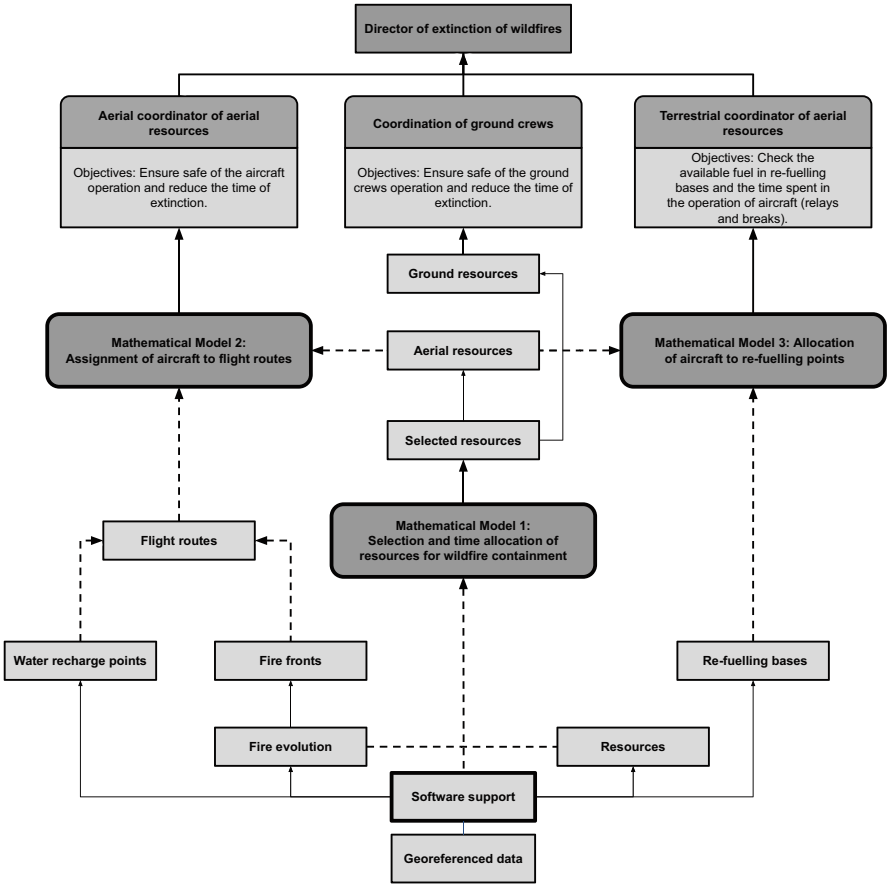

Fig. 1 Workflow of three resource allocation models considered in paper

2 Seminal Model to Select Resources

A seminal study that investigated the optimal initial selection of extinction resources for forest fires using integer linear programming is that of [2]. The approach of this study, with several modifications, was considered to be adequate in responding to any problems arising in the *Lumes* and *Enjambre* projects.

With respect to data, [2] began with information regarding the forest fire, specifically with an estimate of the fire evolution. The authors also used information relating to the resources, regarding both their description and position at the time of the initial planning.

Given the underlying decision problem, the variables used in the developed model are associated with resources and fires.

However, there is an important restriction relating to the fire. It must be able to be contained with the available resources at some point in the considered time horizon. Moreover, restrictions are in place that represent the logical relationships among the model variables.

Several parameters of the model are introduced below.

To include the information of the estimation of the forest fire evolution, for each period of time $t \in T := \{1, \ldots, m\}$, where m is the number of time periods constituting the time horizon for which the temporary planning is performed, the following notation is used:

SP_t **Fire perimeter**, *i.e.* the line surrounding the burning surface (km).
PER_t **Increment of the perimeter** (km).
NVC_t **Increment in the cost** of the burned land (monetary units).

For each resource $i \in I := \{1, \ldots, n\}$, where n is the number of available resources, the following parameters are considered:

C_i **Cost per period** of the use of a resource (monetary units).
P_i **Fixed cost** by resource selection (monetary units).
PR_i **Resource performance**, *i.e.* extinguished fire perimeter (km/h).

In terms of the information regarding the resources, for each resource $i \in I := \{1, \ldots, n\}$, the starting position of the resource is represented as follows:

A_i **Number of periods** required to reach the fire from the base where the resource is located.

Considering these parameters, the first question to address is: How can these parameters be obtained? To answer this question, it is necessary to take into account the available historical fire data, from which it is possible to obtain estimates of the costs associated with the use of resources and damaged land, as well as the performance of the resources. For example, in Galicia, reports are available on all fires that have occurred since 1 January 1999, in which all of the data relating to each fire are recorded, including the affected area, instants at which the fire started, whether it was controlled and completely extinguished, causes, type of attack, and resources used. Both the public and private entities dedicated to extinction possess historical data on the operations. These data, together with fire simulators and weather forecasts, can be used to obtain estimates of the increase in the fire perimeter and area. The data also provide useful information for computer applications with geographic information related to the location of the resource bases, re-fuelling points, hydrographic network, arrival times between different locations, aerial photos, and loss valuation. In Galicia, the *GIS* application *Xeocode2* is available for the authorities.

Regarding the model decision variables of the model, the first group is associated with the resources. For each resource $i \in I$ and each period $t \in T$:

d_{it} Binary variable that takes a value of 1 if the resource is used **until this period**.
z_i Binary variable that takes a value of 1 if the resource is **selected** to work on the forest fire.

The interpretation is that the value of d_{it} is 1 for the resources i that together can extinguish the fire working until a certain period $t' \geq t$.

A second group of variables is associated with the fire. For each period $t \in T$:

y_t Binary variable that takes a value of 1 if the fire is **not contained** in the period (with $y_0 = 1$).

The objective function involves minimising the cost of the use of resources and the cost associated with the burned land, which is formulated as follows:

$$\min \sum_{i \in I, t \in T} C_i \cdot t \cdot d_{it} + \sum_{i \in I} P_i \cdot z_i + \sum_{t \in T} NVC_t \cdot y_{t-1}$$

To complete the model presentation, the restrictions are explained below. These restrictions represent the fact that the fire will be extinguished at some point and also that the logical relationships among the variables must be fulfilled.

Fire Containment At a certain moment of time, the perimeter 'built' by the resources must cover the fire perimeter.

$$\sum_{i \in I} \sum_{t \in T} (t - A_i) \cdot PR_i \cdot d_{it} \geq \sum_{t \in T} PER_t \cdot y_{t-1}$$

Logical Relationships Among Variables A resource is selected only if it works up to a certain period. Moreover, the fire is considered to be **not extinguished** only if the resources have not covered the entire perimeter.

$$\forall i \in I, \sum_{t \in T} d_{it} \leq z_i$$
$$\forall t \in T, SP_t \cdot y_{t-1} - \sum_{t' \leq t} \sum_{i \in I} (t' - A_i) \cdot PR_i \cdot d_{it'} \leq M \cdot y_t$$

In the above, M denotes a sufficiently large constant.

[2] illustrated their model using an example. The authors employed different tools for the construction and resolution. The inputs related to the fire behaviour were obtained using a fire simulation program known as FARSITE,[3] the fire-fighting resource containment rates were based on [9], and the exact solution of the model was obtained using the LINGO solver.

To solve the problems of the *Enjambre* project, another interesting tool is [15], whereby a study is carried out on the estimation of the costs of the forest fire extinction operations.

[3] https://www.fs.usda.gov/treesearch/pubs/4617.

3 Model to Select and Temporally Allocate Resources

The companies in the *Enjambre* project are not only interested in the selection of resources at the initial moment, but also require a time schedule that takes into account the current regulation on flight and pilot rest times [13], known as 16B. Furthermore, it is desirable to go beyond the initial selection and aspire to employ a methodology involving a *rolling horizon*, which enables the possibility of execution at any instant. According to the interlocutors in the company, it is interesting to have a plan that explicitly includes the rest, flight, and work times for the resources fighting the fire. Moreover, for each resource group (aircraft, machines, and brigades), the extinction coordinators require the minimum and maximum number of resources. Thus, [10] proposed a new model that includes novel variables. For each resource $i \in I$, each period $t \in T$, and each group $g \in G := \{1, \ldots, r\}$, where r is the number of different groups of resources:

- s_{it} Binary variable that takes a value of 1 if the resource **starts to work** in the period.
- fl_{it} Binary variable that takes a value of 1 if the resource **flies (travels) without working** in the period.
- r_{it} Binary variable that takes a value of 1 if the resource **rests** in the period.
- er_{it} Binary variable that takes a value of 1 if the resource **ends a break** in the period.
- e_{it} Binary variable that takes a value of 1 if the resource **ends its work** in the period.
- w_{it} Binary variable that takes a value of 1 if the resource **is containing the wildfire** in the period.
- u_{it} Binary variable that takes a value of 1 if the resource **is used** in the period; that is, $u_{it} = fl_{it} + r_{it} + w_{it}$.
- z_i Binary variable that takes a value of 1 if the resource is **selected** in a certain period.
- μ_{gt} Integer variable that counts the number of **missing** group resources to reach the minimum in the period.

In the new model, the objective function minimises the cost of the use of the resources as well as the cost associated with the burned land. Furthermore, the objective function penalises non-compliance with the minimum number of resources of each group that must be present. The objective function is formulated as follows:

$$\min \sum_{i \in I, t \in T} C_i \cdot u_{it} + \sum_{i \in I} P_i \cdot z_i + \sum_{t \in T} NVC_t \cdot y_{t-1} + \sum_{g \in G, t \in T} M' \cdot \mu_{gt}$$

Here, M' denotes a large constant. The restrictions of this model are as follows:

Fire Containment At a certain point, the extinction will progress sufficiently to end the tasks of the resources.

Start of the Activity If a resource is used, it is selected in a certain period. The resources acting on the fire at the time of executing the algorithm continue to act or fail to act for the entire period considered.

Start and End of the Activity If a resource is selected, it must fly (in general, travel) from the base to the fire. At the end of the intervention, the resource must have sufficient time to return to the base.

Logical Relations Among the Variables

Number of Resources The minimum and maximum number of resources cannot be violated as long as the fire is not contained.

Breaks This is the main difference from the model in [2]. It is useful to create a variable that **acts as a counter** of the number of periods that have been spent without rest for each resource in each period.

The formulation of the restrictions is not included in this setup, but they can be viewed in [10].

4 Model for Allocation of Aerial Resources to Flight Routes

As mentioned in Section 1, once the resources that will participate in the extinction during a set of periods have been selected, one task of the aerial coordinator of aerial resources is the allocation of resources that are assigned to identical periods to the flight routes.[4]

It is appropriate to mention the words of [7]: 'In the case of amphibious airtankers, the air attack officer must decide from which water body each airtanker will pick up water and when and where each airtanker will drop its load'.

In [12], a mixed integer linear programming model was introduced to automate this task. The notations P and K are used for the sets of water recharging points and fire fronts, respectively. Moreover, P_i, G_i, and K_i are the set of water points, group of aerial resources, and fire fronts that are assigned to resource i.

[4] A flight route is a circular path that follows a set of air resources and is associated with a certain point of water loading and a fire front on which water is discharged.

Subsequently, given a resource $i \in I$, a resource group $g \in G$, a water recharge point $p \in P$, and a fire front $k \in K$, new parameters are introduced:

CAP_i **The carrying capacity**.
DOI_{gpk} The number of **downloads** per hour performed by an aerial resource of group g in the flight route, given by the fire front k and water point p.
DIS_{ik} **The distance** from the current position of aerial resource i to fire front k.

Taking into account the new decision problem to be solved, the following variables are used:

a_{ipk} Binary variable that takes a value of 1 if the aerial resource is **assigned** to a flight route given by water point p and fire front k.
m_k Real variable that measures the **lack of water** used on the fire front relative to the amount initially assigned.
f_k Binary variable that takes a value of 1 if fire front k is left **unattended**.

In this allocation problem, the objective is to maximise the discharged water/retardant per time unit. This criterion can produce ties when selecting the resources, in which case the closest resources will be prioritised. Moreover, a front being left unattended and/or receiving fewer downloads than those planned will result in a penalty. Thus, the objective function is formulated as follows:

$$\max \sum_{i\in I}\sum_{g\in G_i}\sum_{p\in P_i}\sum_{k\in K} DOI_{gpk}\cdot CAP_i\cdot a_{ipk} - \sum_{i\in I}\sum_{k\in K_i}\sum_{p\in P_i}\frac{DIS_{ik}}{\max\limits_{i'\in I,k'\in K} DIS_{i'k'}}\cdot a_{ipk}$$
$$- \sum_{k\in K} M\cdot(m_k + f_k)$$

The main restrictions of this model are that the maximum number of air resources on each flight route should not be exceeded and that no front should be disregarded. The remaining restrictions refer to the logical relationships among the variables.

The model [12] was programmed using the `AMPL` language and solved with `gurobi`. Part of the corresponding computational study is presented below. Different potentially realistic instances were designed (from 1 to 11) considering a different number of air resources, water[5] recharging points, and fronts in each case. The model was solved, and the average and maximum times obtained for 100 samples from each instance were recorded.

Table 1 describes the instances and Fig. 2 presents the computation times (s). The execution times (top line) were less than 5 min in each case, with most of these executions being less than 1 min. The average times were always less than 20 s and reached a value of 1 s only with a number of aircraft equal to 12 or 15.

[5]In this paper, the term water is used for simplicity, but in general reference will be made to any kind of retardant used in extinguishing a forest fire.

Table 1 Several instances considered in study of model for allocation of resources to flight routes

Instance number	1	2	3	4	5	6	7	8	9	10	11
Number of aircraft	3	3	3	3	3	6	6	9	9	12	15
Number of water points	3	6	6	9	9	3	6	3	9	6	6
Number of fire fronts	3	3	6	3	6	3	3	3	3	6	6

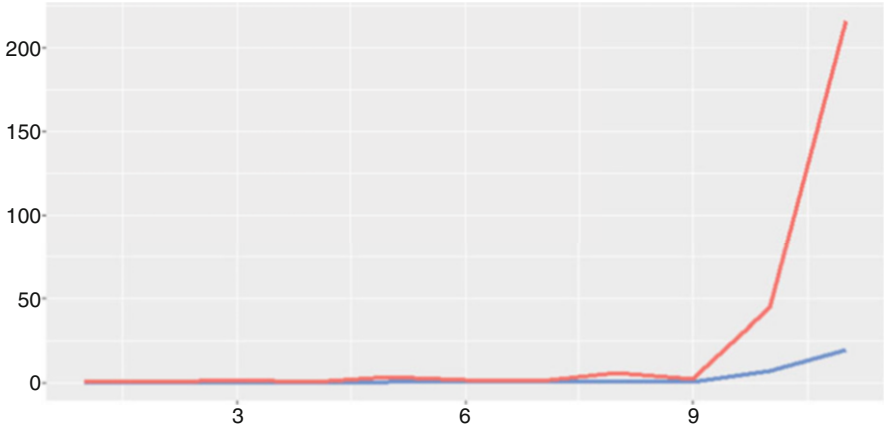

Fig. 2 Average and maximum computation times (s) of model for resource allocation to flight routes in several instances

5 Model for Allocation of Aerial Resources to Re-fuelling Points

As also mentioned in Sect. 1, once the resources that will participate in the extinction during a set of periods have been selected, a task of the terrestrial coordinator of aerial resources involves the allocation of air resources to the re-fuelling points in periods when the air resources are not indicated to work on the fire.

Therefore, a second model was introduced in [12]. In this case, it is a binary linear programming model to automate this other tasks. Accordingly, it becomes necessary to consider new sets:

B Set of **re-fuelling bases**.
B_i Set of re-fuelling bases **assigned to resource** $i \in I$.

Given a resource $i \in I$, base $b \in B$, and period $t \in T$, new parameters are introduced:

LOI_i Fuel **load** of the aerial resource.
REF_i Re-fuelling **time** of the aerial resource.
FUE_b Current quantity of the **fuel available** in the base.
NUM_b Number of aerial resources that **can refuel simultaneously** at the base.

TIM_{ib} **Time** required to move an aerial resource from its current location to the base.

ATI_t **Accumulated time** since the start of the re-fuelling planning process up to the period.

Two new sets of decision variables are also used:

s_{ibt} Binary variable that takes a value of 1 when the aerial resource **starts re-fuelling** at the base in the corresponding period.

e_{ibt} Binary variable that takes a value of 1 when the aerial resource **ends** re-fuelling at the base in the corresponding period.

In this allocation problem, the objective is to allocate the air resources to the different re-fuelling points in such a manner that the time spent in the operation is minimised, taking into account the re-fuelling itself and the round trip displacements from the work point to the re-fuelling base.

$$\min \sum_{i \in I} \sum_{b \in B_i} \sum_{t \in T} (ATI_t + TIM_{ib}) \cdot e_{ibt}$$

Regarding the restrictions, the fuel availability at each base, number and type of resources that can be used at each base simultaneously, re-fuelling times of the different resource types, and various logical relationships between the variables and parameters must be considered. The waiting times in the bases can be tackled in this manner.

The model was programmed using `AMPL` and solved with `gurobi`. Different realistic instances (from 1 to 11) were designed, with a different number of air resources and re-fuelling bases considered in each case. The model was solved, and the average and maximum times obtained for 100 samples from each of the instances were recorded.

Table 2 describes the instances and Fig. 3 presents the corresponding computation times (s). The execution times (top line) were less than 10 min in each case, with most of these executions being less than 5 min. The average times never exceeded 3 min, and the maximum times did not exceed 3 min, provided that the number of aircraft was less than 9.

Table 2 Several instances considered for allocation of resources to re-fuelling points

Instance number	1	2	3	4	5	6	7	8	9	10	11
Number of aircraft	3	3	3	3	3	6	6	6	6	9	12
Number of re-fueling bases	3	6	9	12	15	3	6	9	12	6	9

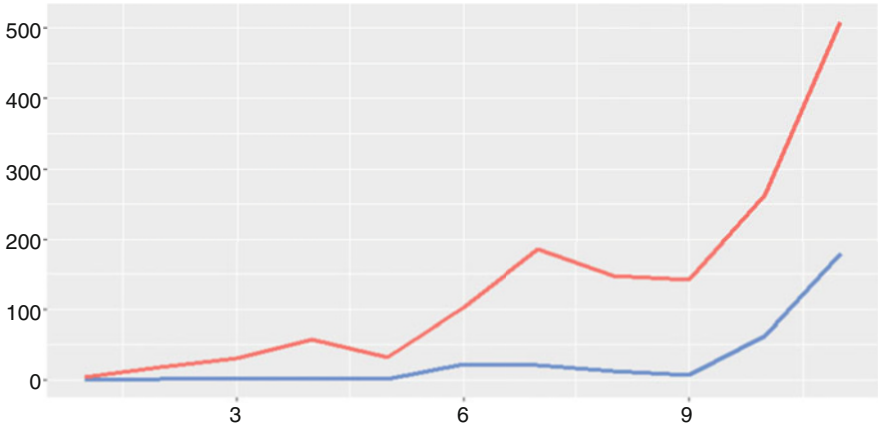

Fig. 3 Average and maximum computation times (s) of model for the resource allocation to refuelling points in several instances

6 `Wrm` in Practice

In this section, the Wildfire Resources Management (`wrm`) package [11], created using the `R` software, is explained. It is a decision support tool created to solve optimization models in logistics for fighting forest fires. The `shinydashboard` library [1] provides an interface for friendly use of the model presented in Sect. 3. `wrm` is an open-source package stored in the `GitHub` repository. The main libraries are the following:

`Shiny`	This library enables easy construction of interactive web applications
`Shinydashboard`	This library creates dashboards with 'Shiny'
`Plotly`	This library translates 'ggplot2' graphs into an interactive web-based version
`Shinyjs`	This library performs common `JavaScript` operations in the `Shiny app`

6.1 Installation and Input Data

It is recommended to install the `wrm` package from the `GitHub` repository. For this reason, the first step is to install the 'devtools' package of `R`. Thereafter, it is necessary to install the below packages by using the following commands in the `R` console:

```
devtools::install_github('jorgerodriguezveiga/romo')
devtools::install_github('jorgerodriguezveiga/WildfireResources')
devtools::install_github('jorgerodriguezveiga/wrm')
```

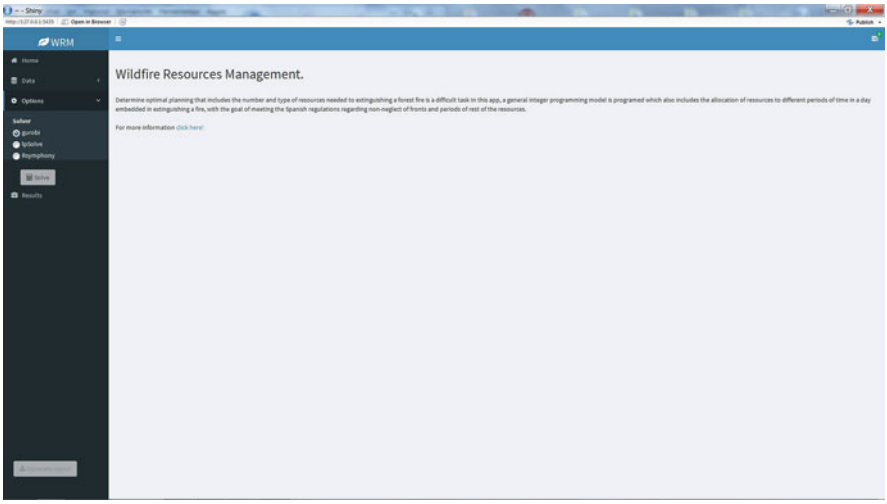

Fig. 4 `wrm` interface appearance

Once the installation is complete, the following command line statement loads the interface:

```
wrm::shinyapp().
```

The interface automatically offers the appearance illustrated in Fig. 4.

To verify the installation, an example dataset can be downloaded from the example folder. Firstly, it is advisable to use the example from the feasible subfolder.

Regarding the input data, the following information (parameters and corresponding descriptions) for each of the available resources should be provided:

Name	Resource name
G	Resource group name
ITW	True if the resource is working on the wildfire
IOW	True if the resource is working on other wildfires
A	Total time required by the resource to reach the forest fire (min)
CWP	Total current time since the last resort break (min)
CRP	Total current rest time if the resource is on a break (min)
CUP	Total time of the current use in the day (min)
BPR	Maximum performance of the resources; that is, kilometres maintained in 1 h (km/h)
P	Fixed cost per use of the resource (Euros)
C	Cost per hour of the use of the resource (Euros/h)
TRP	Time required by the resource to travel to the fire from the rest area and vice versa (min)
WP	Maximum working time without interruption (min)
RP	Required rest time (min)
UP	Maximum daily working time including breaks (min)

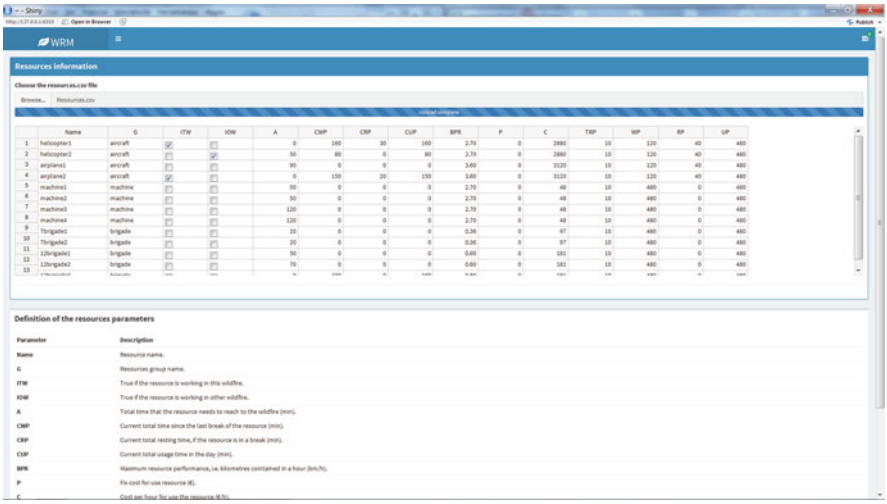

Fig. 5 Appearance of interface after entering input data corresponding to resources

The input data can be written to a `.csv` file. Figure 5 presents an example of the interface appearance after entering the input data of the resources in `wrm`. In this example, two helicopters are considered, together with two aeroplanes and nine ground resources, among which six are brigades.

Furthermore, the following information for the fire should be provided:

Period	Time period
PER	Increased perimeter of the forest fire (km) in the period
NVC	Increased costs of the forest fire (costs of the affected area, reforestation, and urban damage) in the period
$EF.r$	Resource efficiency in the period (a number in [0,1])
$nMin.g$	Minimum number of resources of the 'g' group working on the forest fire in the period
$nMax.g$	Maximum number of resources of the 'g' group working on the forest fire in the period

The appearance of the data files corresponding to a fire in the interface following its incorporation is similar to that for the resources.

6.2 *Performance and Results*

After loading the data files for the resources and fire, the solver used to solve the model should be selected: `gurobi`, `lpSolve` or `Rsymphhony`. The solver is

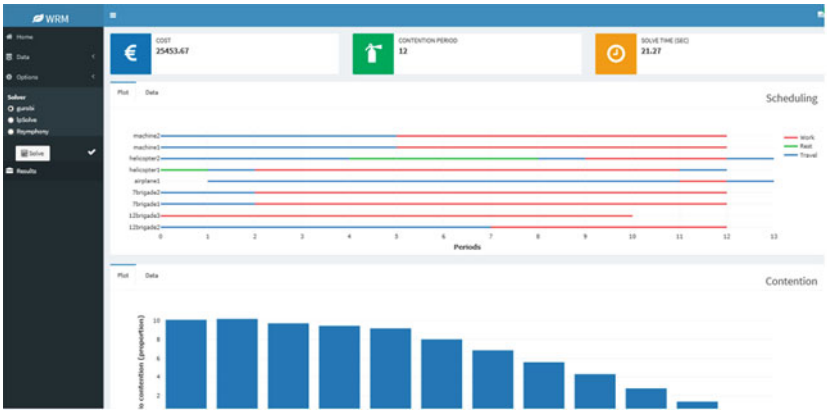

Fig. 6 Appearance of `wrm` results

executed by selecting 'Solve' in the interface and then waiting several seconds until the model is resolved, following which an 'OK' message will appear.

The results are obtained by selecting 'Results' in the interface. The obtained results include the cost, period in which the fire is contained, execution time, planning for the periods and resource type, and percentage of containment by period, as can be observed in the example of Fig. 6.

It can be observed from Fig. 6 that the computation time was 21.27 s and the fire was contained in period 12. Regarding the temporal planning of resources, the first terrestrial resource required five time periods to move from its current location to the fire, and the remaining time was spent working. The first helicopter required the four initial time periods for its displacement, rested for the following four periods, moved during another period, and worked for three periods until the extinction of the fire, at which point a new displacement began. Regarding the containment speed, it was possible to contain 10% of the fire in the first period.

Moreover, an alternative description of the number and type of resources used in each period is obtained, as illustrated in the case of Fig. 7. For example, one air resource, five brigades, and two other land resources were operating in period 8.

6.3 Computing Results

To illustrate the costs and time required by `wrm`, a simulation study with potentially realistic data was performed.

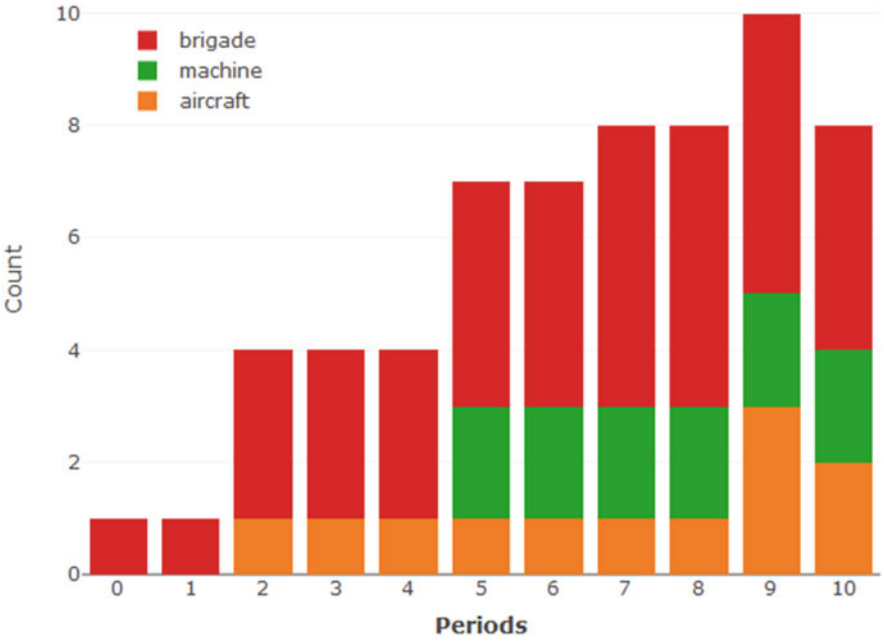

Fig. 7 Appearance of results corresponding to number of resources used

We created 24 cases by combining the resource groups indicated by Air.(aircraft), Mach. (machines), and Brig. (brigades) with 5 or 10 members for 20, 30 or 40 time periods. A total of 50 realistic instances were randomly constructed from each case.

All of the computations included in this paper were performed on a personal computer with an Intel(R) Core(TM) i7-7700HQ 2.80 GHz CPU processor and 8.00 GB of memory.

In Table 3, the average information of the selected resources is displayed, distinguished by cases. The table presents the costs (Euros) of the operation, differentiating the costs of the use of resources and those for the hectares of land affected by the fire. It can be observed that the cost increased considerably when the number of periods increased.

Moreover, Table 4 indicates that the runtime was shorter for a smaller number of periods. In particular, if the number of time periods was as high as 30 (equivalent to 5 h), the execution times were short, with all of the instances resolved in less than 2 min.

Table 3 Mean operating costs obtained with `wrm`

Case	Air.	Mach.	Brig.	Periods	Resources	Fire	Total
1	5	5	5	20	895869.0	319879.8	1215748.8
2	10	5	5	20	1486565.4	314567.3	1801132.7
3	5	10	5	20	865444.4	287148.5	1152592.9
4	10	10	5	20	1564649.0	299793.1	1864442.1
5	5	5	10	20	854955.4	258997.2	1113952.6
6	10	5	10	20	1388193.4	281408.7	1669602.1
7	5	10	10	20	944578.4	281366.4	1225944.8
8	10	10	10	20	978959.6	246404.0	1225363.6
9	5	5	5	30	1707375.6	521991.5	2229367.1
10	10	5	5	30	2470270.2	381142.7	2851412.9
11	5	10	5	30	1677948.4	481234.3	2159182.7
12	10	10	5	30	1958495.8	346409.7	2304905.5
13	5	5	10	30	1651833.8	417261.5	2069095.3
14	10	5	10	30	3283654.6	436526.0	3720180.6
15	5	10	10	30	1392073.6	416127.4	1808201.0
16	10	10	10	30	3194804.2	406712.3	3601516.5
17	5	5	5	40	2441557.9	655377.6	3096935.5
18	10	5	5	40	3059774.8	347869.5	3407644.3
19	5	10	5	40	3750399.6	933170.7	4683570.3
20	10	10	5	40	2830142.6	389734.8	3219877.4
21	5	5	10	40	2648602.7	496788.5	3145391.2
22	10	5	10	40	2328978.2	256745.1	2585723.3
23	5	10	10	40	3362878.8	756016.1	4118894.9
24	10	10	10	40	5173332.1	452019.8	5625351.9

7 Conclusions

The first conclusion that can be rapidly drawn from this work is that operational research produces useful techniques for the optimal management of resources in fire-fighting problems. In particular, the model introduced in [2] is extended to meet the requirements of the partners in the company dedicated to fire-fighting. In this manner, academic advances can create powerful tools that are capable of producing results that can be transferred to industry.

For the specific problem studied, the results offer economic benefits and, importantly, enable an improvement in the efficiency of extinction tasks, thereby making the tasks safer and more powerful for the defence of the natural environment.

The models of Sects. 4 and 5 are less complex than that of Sect. 3. The introduction of the data, modelling, and resolution have been addressed with `AMPL` and `gurobi`. However, the greater complexity of the model in Sect. 3 motivated the creation of an interface using `R`, which facilitates the introduction of data and displays the results graphically.

Table 4 Mean execution time obtained with `wrm`

Case	Air.	Mach.	Brig.	Periods	Total time (s)
1	5	5	5	20	5.0
2	10	5	5	20	18.1
3	5	10	5	20	11.3
4	10	10	5	20	19.1
5	5	5	10	20	10.3
6	10	5	10	20	27.5
7	5	10	10	20	15.2
8	10	10	10	20	20.3
9	5	5	5	30	61.3
10	10	5	5	30	107.9
11	5	10	5	30	91.6
12	10	10	5	30	99.1
13	5	5	10	30	85.7
14	10	5	10	30	155.3
15	5	10	10	30	104.2
16	10	10	10	30	167.4
17	5	5	5	40	210.9
18	10	5	5	40	357.6
19	5	10	5	40	289.0
20	10	10	5	40	340.9
21	5	5	10	40	232.3
22	10	5	10	40	359.5
23	5	10	10	40	253.3
24	10	10	10	40	424.1

It should be noted that tools are required that provide adequate values for the model parameters. Historical fire data are also necessary to obtain useful research results. Of course, a tool to support the decision making of extinction coordinators is provided, but the experience of the pilots and brigades as well as their knowledge of the terrain is essential for appropriate extinguishing operations in a safe environment.

Regarding the work in progress, it is worth mentioning the interest in improving the graphic interface designed, including new utilities. Moreover, its correct integration with other tools for different project requirements is important. Finally, from the perspective of current academic findings that are potentially transferable to industry, it is worth studying the application of modern decomposition techniques to solve large problems involving resource selection and time planning. Moreover, the incorporation of uncertainty into the problem (stochastic programming) via modelling uncertainty (two-stage problem/multistage problem), the use of algorithms to solve integer stochastic problems, and possible parallel programming should be investigated.

Acknowledgments The authors are grateful for the interesting comments made by Alfonso Lorenzo and José Luis Sáiz Díaz, from the Spain Babcock International, as well as Manuel Febrero Bande, Wenceslao González Manteiga, and Beatriz Pateiro López from the University of Santiago de Compostela. This work has been supported by ITMATI, the ERDF (MINECO/AEI grants MTM2016-76969-P and MTM2017- 87197-C3-3-P), and Xunta de Galicia (Competitive Reference Group ED431C 2017/38).

References

1. Chang, W., Borges-Ribeiro, B.: Shinydashboard. Create Dashboards with Shiny. R Package Version 0.7.0. http://rstudio.github.io/shinydashboard/ (2018). Accessed 19 September 2018
2. Donovan, G.H., Rideout, D.B.: An integer programming model to optimize resource allocation for wildfire containment. For. Sci. **49**, 331–335 (2003)
3. Gorte, J.K., Gorte, R.W.: Application of economic techniques to fire management-a status review and evaluation. Gen. Tech. Rep. INT-GTR-53. Ogden, UT, US Department of Agriculture, Forest Service. Intermountain Research Station **53**, 26 p. (1979)
4. Gobierno de España. Ministerio de Agricultura, Pesca y Alimentación: Los Incendios Forestales en España: 1 enero–31 diciembre 2018. Avance Informativo. https://www.mapa.gob.es/es/desarrollo-rural/estadisticas/iiff_2018_tcm30-507741.pdf (2019). Accessed 11 November 2019
5. Headley, R.: Fire Suppression, District 5. USDA-Forest Service, pp. 1–57 (1916)
6. Kim, Y.-H., Bettinger, P., Finney, M.: Spatial optimization of the pattern of fuel management activities and subsequent effects on simulated wildfires. Eur. J. Oper. Res. **197**, 253–265 (2009)
7. Martell, D.L.: A review of recent forest and wildland-fire management decision support systems research. Curr. For. Rep. **1**, 128–137 (2015)
8. Miller, C., Ager, A.A.: A review of recent advances in risk analysis for wildfire management. Int. J. Wildland Fire **22**, 1–14 (2013)
9. National Wildfire Coordinating Group Fireline Handbook: NWCG Handb. 3. PMS 410-1. NFES 0065 (1998)
10. Rodríguez-Veiga, J., Ginzo-Villamayor, M.J., Casas-Méndez, B.V.: An integer linear programming model to select and temporally allocate resources for fighting forest fires. Forests **9**, 1–18 (2018)
11. Rodríguez-Veiga, J., Ginzo-Villamayor, M.J., Casas-Méndez, B.V.: Wildfire resources management (wrm). GitHub Repository. https://github.com/jorgerodriguezveiga/wrm (2018). Accessed 12 December 2019
12. Rodríguez-Veiga, J., Gómez-Costa, I., Ginzo-Villamayor, M.J., Casas-Méndez, B.V., Saiz-Díaz, J.L.: Assignment problems in wildfire suppression: Models for optimization of aerial resource logistics. For. Sci. **64**, 504–514 (2018)
13. Spanish Ministry of Development: Operational Circular 16-B. http://www.aecaweb.com/informes/documentos/INFORMES_Y_ESTUDIOS/circular_operativa_16_b.doc (1995). Accessed 18 June 2018
14. Sparhawk, W.N.: The Use of Liability Ratings in Planning Forest Fire Protection. National Emergency Training Center, United States of America (1925)
15. Vázquez-Vázquez, M.C., Chas-Amil, M.L., Touza, J.M.: Estimación de los costes de las operaciones de extinción de incendios forestales: Estudio de caso en el Distrito Forestal de A Limia. Revista Galega de Economía **23**(1), 99–113 (2014)

Index

M. Cruz et al. (eds.), *Progress in Industrial Mathematics: Success Stories*,
SEMA SIMAI Springer Series 5, https://doi.org/10.1007/978-3-030-61844-5